ISTANBUL TECHNICAL UNIVERSITY ★ GRADUATE SCHOOL

NUMERICAL SIMULATION OF TRANSIENT SANDFACE AND WELLBORE TEMPERATURE BEHAVIORS OF WELLS IN MULTILAYER SINGLE-PHASE OIL AND GEOTHERMAL RESERVOIRS

Ph.D. THESIS

Cihan ALAN

Department of Petroleum and Natural Gas Engineering

Petroleum and Natural Gas Engineering Programme

FEBRUARY 2022

ISTANBUL TECHNICAL UNIVERSITY ★ GRADUATE SCHOOL

NUMERICAL SIMULATION OF TRANSIENT SANDFACE AND WELLBORE TEMPERATURE BEHAVIORS OF WELLS IN MULTILAYER SINGLE-PHASE OIL AND GEOTHERMAL RESERVOIRS

Ph.D. THESIS

Cihan ALAN
(505112503)

Department of Petroleum and Natural Gas Engineering

Petroleum and Natural Gas Engineering Programme

Thesis Advisor: Assoc. Prof. Dr. Murat ÇINAR

FEBRUARY 2022

ISTANBUL TEKNİK ÜNİVERSİTESİ ★ LİSANSÜSTÜ EĞİTİM ENSTİTÜSÜ

ÇOK TABAKALI, TEK-FAZLI PETROL VE JEOTERMAL REZERVUARLARDAKİ KUYULARIN KARARSIZ KUYU CİDARI VE KUYU İÇİ SICAKLIK DAVRANIŞLARININ SAYISAL SİMÜLASYONU

DOKTORA TEZİ

Cihan ALAN
(505112503)

Petrol ve Doğal Gaz Mühendisliği Anabilim Dalı

Petrol ve Doğal Gaz Mühendisliği Programı

Tez Danışmanı: Doç. Dr. Murat ÇINAR

ŞUBAT 2022

Cihan ALAN, a Ph.D. student of ITU Graduate School student ID 505112503, successfully defended the thesis/dissertation entitled "NUMERICAL SIMULATION OF TRANSIENT SANDFACE AND WELLBORE TEMPERATURE BEHAVIORS OF WELLS IN MULTILAYER SINGLE-PHASE OIL AND GEOTHERMAL RESERVOIRS", which he prepared after fulfilling the requirements specified in the associated legislations, before the jury whose signatures are below.

Thesis Advisor :	**Assoc. Prof. Dr. Murat ÇINAR** İstanbul Technical University	.....
Jury Members :	**Prof. Dr. Mustafa ONUR** University of Tulsa	.....
	Prof. Dr. Ö. İnanç TÜREYEN Istanbul Technical University	.....
	Assoc. Prof. Dr. Gürşat ALTUN Istanbul Technical University	.....
	Dr. İhsan Murat GÖK National Energy Services Reunited Corp. (NESR)	.....

Date of Submission : 07 January 2022
Date of Defense : 18 February 2022

To my parents,

FOREWORD

Firstly, I am thankful to my advisor Assoc. Prof. Dr. Murat ÇINAR for his guidance and huge efforts. Secondly, I thank Prof. Dr. Mustafa ONUR of the University of Tulsa for his valuable contribution and endless support from the beginning to the end. I also thank to my Ph.D. dissertation committee and jury members Assoc. Prof. Dr. Gürşat ALTUN, Dr. İhsan Murat GÖK and Prof. Dr. Ö. İnanç TÜREYEN for their valuable comments and suggestions that helped to improve the content of my Ph.D. dissertation.

February 2022

Cihan ALAN
(Petroleum and Natural Gas Engineer, M.Sc.)

TABLE OF CONTENTS

Page

FOREWORD ..... **ix**
TABLE OF CONTENTS ..... **xi**
ABBREVIATIONS ..... **xiii**
SYMBOLS ..... **xv**
LIST OF TABLES ..... **xvii**
LIST OF FIGURES ..... **xix**
SUMMARY ..... **xxv**
ÖZET ..... **xxvii**
1. INTRODUCTION **1**
1.1 Literature Review 1
1.2 Scope and Purpose of the Thesis 4
2. NUMERICAL IMPLEMENTATION FOR SLIGHTLY COMPRESSIBLE FLUID FLOW IN A COUPLED 1-D (*r*) RESERVOIR AND 1-D (*z*) WELLBORE SYSTEM … **7**
2.1 Initial and Boundary Conditions 7
2.1.1 Reservoir 7
2.1.2 Wellbore 8
2.1.3 Heat losses 9
2.1.4 Discretization 9
2.1.5 Coupling reservoir and wellbore 10
2.2 Comparison of Pressure and Temperature Solutions 11
2.3 Impact of Gauge Distances 16
2.4 Impact of Parameters 20
2.4.1 Effect of porosity 21
2.4.2 Effect of permeability 24
2.4.3 Effect of heat loss 25
2.4.4 Effect of well radius 27
2.4.5 Effect of flow rate 29
2.4.6 Effect of skin 31
2.5 Parameter Estimation Using Transient Drawdown Temperature Data 40
2.6 History Matching Field Data 47
2.7 Discussions and Recommendations 54
3. NUMERICAL IMPLEMENTATION FOR SLIGHTLY COMPRESSIBLE FLUID FLOW IN A COUPLED 2-D (*r*-*z*) RESERVOIR AND 1-D (*z*) WELLBORE SYSTEM **61**
3.1 Boundary Conditions and Coupling 62
3.2 Numerical Solution 63

3.3 Comparison of Transient Pressure and Temperature Solutions 66
3.4 Multi-Layer Reservoir and Wellbore System 72
3.4.1 Model initialization 72
3.4.2 Comparison of drawdown pressure and temperature solutions 74
3.4.2.1 Heat loss effect on drawdown 77
3.4.3 Impact of parameters 78
3.4.3.1 Effect of J-T coefficient 80
3.4.3.2 Effect of porosity 81
3.4.3.3 Effect of permeability and flow rate 81
3.4.3.4 Effect of viscosity 83
3.4.3.5 Effect of volumetric heat capacity of rock and specific heat capacity of reservoir fluid 83
3.4.3.6 Effect of well radius 84
3.4.3.7 Effect of the product of mobility and layer thickness (kh/μ) 84
3.4.3.8 Effect of distance between producing zones 88
3.4.4 Impact of skin effects 89
3.4.4.1 Comparison of drawdown pressure and temperature solutions 89
3.4.4.2 Sensitivity analysis 92
3.4.4.3 Effect of drawdown time in the presence of skin effects 92
3.4.5 Applications of multi-layer system 94
3.4.5.1 Variable rate test 94
3.4.5.2 Plugged perforations 96
3.4.5.3 Parameter estimation 97
4. CONCLUSIONS 103
REFERENCES 107
APPENDICES 113
CURRICULUM VITAE 191

ABBREVIATIONS

AI	**:** Artificial Intelligence
BU	**:** Buildup Period
DD	**:** Drawdown Period
DGA	**:** Downhole Gauge Assembly
DST	**:** Drill Stem Testing
DTS	**:** Distributed Temperature Sensors
FIT	**:** Functional Iteration Technique
GUI	**:** Graphical User Interface
PC	**:** Personal Computer
PDE	**:** Partial Differential Equation
PLT	**:** Production Logging Tool
PSS	**:** Pseudo Steady State
PVT	**:** Pressure Volume Temperature

SYMBOLS

A_r **:** Surface area of a gridblock, L^2, m^2
A_w : Cross-sectional area of a gridblock, L^2, m^2
API : American Petroleum Institute gravity, degree
B : Formation volume factor of fluid, L^3/ L^3, m^3/sm^3
c : Isothermal compressibility of fluid, Lt^2/m, Pa^{-1}
c_m : Isothermal compressibility of rock, Lt^2/m, Pa^{-1}
c_p : Specific heat capacity of fluid, L^2/t^2T, J/kg·K
$c_{p,m}$: Specific heat capacity of rock, L^2/t^2T, J/kg·K
c_t : Isothermal compressibility of fluid-saturated rock, Lt^2/m, Pa^{-1}
c_v : Control volume of gridblock, L^3, m^3
C : Wellbore storage, mL^2/t^2 , m^3/MPa
D : Diameter of wellbore gridblock, L, m
f : Friction factor, unitless
g : Gravitational acceleration, L/t^2, m/s^2
GOR : Producing gas oil ratio, L^3/ L^3, sm^3/sm^3
h_{res} : Reservoir thickness, L, m
H : Specific enthalpy of fluid, L^2/t^2, J/kg
H_m : Specific enthalpy of rock, L^2/t^2, J/kg
k : Permeability, L^2, mD [m^2]
n_p : Number of pressure points in observed data, unitless
n_T : Number of temperature points in observed data, unitless
N_r : Number of gridblocks in radial direction for reservoir, unitless
N_{rz} : Number of gridblocks in axial direction for reservoir, unitless
N_z : Number of gridblocks in axial direction for wellbore, unitless
p : Pressure, m/Lt^2, MPa
p_{in} : Pressure at initial condition, m/Lt^2, MPa
p_r : Pressure in reservoir domain, m/Lt^2, MPa
p_{obs} : Observed pressure, m/Lt^2, MPa
p_{ref} : Pressure at reference condition, m/Lt^2, MPa
q_{sc} : Surface flow rate, L^3/t, sm^3/D
q_r : Volumetric flow rate in the radial direction for wellbore, L^3/t, sm^3/D
q_w : Volumetric flow rate in the axial direction for wellbore, L^3/t, sm^3/D
Q_{loss} : Heat loss term, mL/t^3, J/s·m
r_e : Radius of outer reservoir boundary, L, m
r_w : Radius of wellbore, L, m
r_{wb} : Effective radius of wellbore, L, m
r_s : Radius of skin zone, L, m

r_e : Radius of outer reservoir, L, m
R_e : Reynolds number, unitless
R_h : Coefficient defined in heat loss term, t^3T/mL, s·m·K/J
S : Entropy of fluid, mL^2/t^2T, J/K
s : Skin, unitless
t : Time, t, hour
t^n : Time at time step (n), t, hour
t^{n+1} : Time at time step (n+1), t, hour
T : Temperature, T, K
T_e : Earth temperature at corresponding depth, T, K
T_{in} : Temperature at initial condition, T, K
T_{obs} : Observed temperature, T, K
T_r : Temperature in reservoir domain, T, K
T_{ref} : Temperature at reference condition, T, K
u : Velocity in the radial direction, L/t, m/s
$\boldsymbol{u_{c_r}}$: Darcy's velocity in radial direction, L/t, m/s
$\boldsymbol{u_{c_z}}$: Darcy's velocity in axial direction, L/t, m/s
U : Specific internal energy, L^2/t^2, J/kg
U_t : Overall heat transfer coefficient, m/t^3T, J/s·m^2·K
v : Velocity in the axial direction, L/t, m/s
V : Volume, L^3, m^3
w_p : Weights used for pressure, unitless
w_T : Weights used for temperature, unitless
x_f : Half fracture length, L, m
z : Depth above the top of the producing horizon, L, m
z_w : Wellbore depth, L, m
β : Isobaric thermal expansion coefficient of fluid, T^{-1}, K^{-1}
β_m : Isobaric thermal expansion coefficient of rock, T^{-1}, K^{-1}
β_t : Isobaric thermal expansion coefficient of fluid-saturated rock,T^{-1},K^{-1}
ε_{JT} : Joule-Thomson coefficient, mT/Lt^2, K/Pa
ϑ : Roughness of the pipe, L, m
λ : Thermal conductivity of fluid, mL/t^3T, J/m·s·K
λ_r : Thermal conductivity of fluid in radial direction, mL/t^3T, J/m·s·K
λ_z : Thermal conductivity of fluid in axial direction, mL/t^3T, J/m·s·K
λ_m : Thermal conductivity of rock, mL/t^3T, J/m·s·K
λ_t : Thermal conductivity of fluid-saturated rock, mL/t^3T, J/m·s·K
$\boldsymbol{\lambda_{t_r}}$: Thermal conductivity of fluid-saturated rock in radial direction, mL/t^3T, J/m·s·K
$\boldsymbol{\lambda_{t_z}}$: Thermal conductivity of fluid-saturated rock in axial direction, mL/t^3T, J/m·s·K
μ : Viscosity of fluid, m/Lt, Pa·s
ρ : Density of fluid, m/L^3, kg/m^3
ρ_m : Density of rock, m/L^3, kg/m^3
$(\rho c_p)_m$: Volumetric heat capacity of rock, L^2/t^2T, J/kg·K
$(\rho c_p)_t$: Volumetric heat capacity of fluid-saturated rock, L^2/t^2T, J/kg·K
φ : Coefficient of isentropic expansion, mT/Lt^2, K/Pa
ϕ : Porosity, fraction

LIST OF TABLES

Page

Table 2.1: Simulation input data used for comparison example. 12
Table 2.2: Parameters used in synthetic cases for sensitivity analysis. 21
Table 2.3: Parameters used in synthetic cases for sensitivity analysis in the presence of skin effects. 32
Table 2.4: Parameters used in synthetic cases for nonlinear regression (NR). 42
Table 2.5: Regression results of parameters; NR Case 1. 45
Table 2.6: Regression results of parameters; NR Case 2. 45
Table 2.7: Regression results of parameters; NR Case 3. 46
Table 2.8: Regression results of parameters; NR Case 4. 46
Table 2.9: Parameters used in history matching. 48
Table 2.10: Buildup PTA results of field data from the analytical model. 49
Table 2.11: Regression results of parameters; History matching case. 51
Table 3.1: Description of perforations for the multi-layer system having partially/fully penetrated well. 67
Table 3.2: Simulation input data used for comparison of multi-layer system. 73
Table 3.3: Description of layers for multi-layer system. 73
Table 3.4: Parameters effecting numerical solutions for multi-layer system. 79
Table 3.5: Description of different completions for multi-layer system. 85
Table 3.6: Regression of layer permeability with no skin effects using temperature alone. 100
Table 3.7: Regression of layer permeability with no skin effects using both pressure and temperature together. 100
Table 3.8: Regression of layer permeability with no skin effects using pressure alone. 100
Table 3.9: Regression of layer skin value using temperature alone. 101
Table 3.10: Regression of layer skin value using both pressure and temperature together. 101
Table 3.11: Regression of layer permeability and skin values. 101

LIST OF FIGURES

Page

Figure 1.1: Schematic view of the coupled non-isothermal wellbore and reservoir system. 6
Figure 2.1: Comparison of sandface and wellbore temperatures with skin effects for entire flow history. 14
Figure 2.2: Comparison of sandface and wellbore pressures with skin effects for entire flow history. 15
Figure 2.3: Comparison of sandface and wellbore temperatures with skin effects for drawdown on semi-log plots. 15
Figure 2.4: Comparison of sandface and wellbore temperatures with skin effects for buildup on semi-log plots. 16
Figure 2.5: Effect of gauge location in the wellbore on drawdown temperature derivative. 18
Figure 2.6: Effect of gauge location in the wellbore on drawdown temperature. 18
Figure 2.7: Derivative of pressure and temperature and surface flow rate during drawdown. 19
Figure 2.8: Effect of gauge location in the wellbore on buildup temperature derivative. 19
Figure 2.9: Effect of gauge location in the wellbore on buildup temperature. 20
Figure 2.10: Effect of porosity in the wellbore on drawdown temperature. 23
Figure 2.11: Effect of porosity in the wellbore on buildup temperature. 23
Figure 2.12: Effect of permeability in the wellbore on drawdown temperature. .24
Figure 2.13: Effect of permeability in the wellbore on buildup temperature. 25
Figure 2.14: Effect of heat losses in the wellbore on drawdown temperature. 26
Figure 2.15: Effect of heat losses in the wellbore on buildup temperature. 26
Figure 2.16: Effect of heat losses across the wellbore at the end of drawdown. .27
Figure 2.17: Effect of effective well radius in the wellbore on drawdown temperature. 28
Figure 2.18: Effect of the effective well radius in the wellbore on buildup temperature. 28
Figure 2.19: Effect of flow rates in the wellbore and sandface on drawdown temperatures. 30
Figure 2.20: Effect of flow rates in the wellbore and sandface on buildup temperatures. 30
Figure 2.21: Effect of flow rates across the wellbore at the end of drawdown. ..31
Figure 2.22: Effect of skin permeability with positive skin in the wellbore on drawdown temperature. 33

Figure 2.23: Effect of skin permeability with positive skin in the sandface on drawdown temperature. 34
Figure 2.24: Effect of skin radius with positive skin in the wellbore on drawdown temperature. 34
Figure 2.25: Effect of skin radius with positive skin in the sandface on drawdown temperature. 35
Figure 2.26: Effect of the positive skin value in the wellbore on drawdown temperature. 35
Figure 2.27: Effect of the positive skin value in the sandface on drawdown temperature. 36
Figure 2.28: Effect of the negative skin value in the wellbore on drawdown temperature. 37
Figure 2.29: Effect of the negative skin value in the sandface on drawdown temperature. 38
Figure 2.30: Effect of the positive skin value in the wellbore on buildup temperatures. 38
Figure 2.31: Effect of the positive skin value in the sandface on buildup temperatures. 39
Figure 2.32: Effect of the negative skin value in the wellbore on buildup temperature. 39
Figure 2.33: Effect of the negative skin value in the sandface on buildup temperature. 40
Figure 2.34: Effect of gauge location in the wellbore on drawdown temperature with noise; NR - Case 1. 44
Figure 2.35: Effect of gauge location in the wellbore on drawdown temperature with noise; NR - Case 3. 44
Figure 2.36: Buildup pressure derivative of field data. 48
Figure 2.37: Drawdown temperatures of field data. 50
Figure 2.38: Comparison of temperature for the drawdown period; HR case. ... 52
Figure 2.39: Comparison of pressure for the drawdown period; HR case. 52
Figure 2.40: Comparison of temperature for entire flow history; HR case. 53
Figure 2.41: Comparison of pressure for the drawdown; HR case. 53
Figure 2.42: Buildup temperatures of field data. 54
Figure 2.43: Effect of J-T coefficient (changing only in the reservoir) on drawdown wellbore temperature (z=110m). 57
Figure 2.44: Effect of J-T coefficient (changing only in the wellbore) on drawdown wellbore temperatures(z=30m). 57
Figure 2.45: Drawdown temperatures of field data (HM case). 59
Figure 3.1: Schematic view of the coupled wellbore and reservoir gridblocks representation for multi-layer system. 61
Figure 3.2: Nonsymmetrical highly sparse coefficient matrix for coupled reservoir/wellbore system (N_r=N_z=N_{rz}=3). 65
Figure 3.3: Comparison of sandface/wellbore pressures for entire history, Case 1. 68
Figure 3.4: Comparison of sandface/wellbore temperatures during DD, Case 1. 68
Figure 3.5: Comparison of sandface/wellbore temperatures during BU, Case 1. 69
Figure 3.6: Comparison of sandface/wellbore pressures for entire history, Case 2. 69

Figure 3.7: Comparison of sandface/wellbore temperatures during DD, Case 2. 70
Figure 3.8: Comparison of sandface/wellbore temperatures during BU, Case 2. 70
Figure 3.9: Comparison of sandface/wellbore pressures for entire history, Case 3. 71
Figure 3.10: Comparison of sandface/wellbore temperatures during DD, Case 3. 71
Figure 3.11: Comparison of sandface/wellbore temperatures during BU, Case 3. 72
Figure 3.12: Schematic view of layer permeability on 2-D (*r*-*z*) plot for comparison case with no skin effects. 74
Figure 3.13: Comparison of wellbore/reservoir pressures and temperatures across the wellbore from numerical simulator developed and CMG-STARS at the end of drawdown. 75
Figure 3.14: Inflow production profile across the wellbore from numerical simulator developed at the end of drawdown. 75
Figure 3.15: Reservoir pressure distribution (*r*-*z*) areal view from numerical simulator developed at different time steps during drawdown. 76
Figure 3.16: Reservoir temperature distribution (*r*-*z*) areal view from numerical simulator developed at the end of drawdown. 77
Figure 3.17: Comparison of wellbore/sandface temperatures across the wellbore for different overall heat loss coefficient values from numerical simulator developed and CMG-STARS at the end of drawdown. 78
Figure 3.18: Schematic view of layer permeability on 2-D (*r*-*z*) plot for sensitivity. 79
Figure 3.19: Comparison of wellbore/reservoir temperature profiles for Cases 1 and 2 at the end of drawdown. 85
Figure 3.20: Comparison of wellbore/reservoir temperature profiles for Cases 3 and 4 at the end of drawdown. 86
Figure 3.21: Comparison of wellbore/reservoir pressure profiles for Cases 1 and 2 at the end of drawdown. 86
Figure 3.22: Comparison of wellbore/reservoir pressure profiles for Cases 3 and 4 at the end of drawdown. 87
Figure 3.23: Inflow production profile across the wellbore for all cases at the end of drawdown. 87
Figure 3.24: Comparison of wellbore/sandface temperatures and inflow production profile across the wellbore for all unperforated distances at the end of drawdown. 89
Figure 3.25: Comparison of wellbore/reservoir pressures and temperatures across the wellbore from numerical simulator developed and CMG-STARS for skin case 1 at the end of drawdown. 90
Figure 3.26: Comparison of wellbore/reservoir pressures and temperatures Across the wellbore from numerical simulator developed and CMG-STARS for skin case 2 at the end of drawdown. 91
Figure 3.27: Inflow production profile across the wellbore from numerical simulator developed at the end of the drawdown for skin cases 1 and 2. 91
Figure 3.28: Comparison of wellbore temperature profile at different time steps during drawdown with no skin effects. 93

Figure 3.29: Comparison of transient wellbore and sandface temperatures in the middle layers of the lower zone (left) and the upper zone (right) in semi-log plot during drawdown with no skin effects. 93
Figure 3.30: Comparison of inflow production profile across the wellbore at different time steps during drawdown for no skin effects (left) and with skin (s=20 only in the upper zone) (right). 94
Figure 3.31: Surface flow rate history of variable rate test. 95
Figure 3.32: Wellbore temperatures and pressures during drawdown period of variable rate test. 95
Figure 3.33: Comparison of wellbore and sandface temperature (left) and pressure (right) profile at different time steps for a variable rate test. 96
Figure 3.34: Comparison of wellbore temperature profile at different time steps during drawdown with plugged perforations after 2 years. 97
Figure 3.35: Histogram of layer permeability in the lower zone (left) and in the upper zone (right). 98
Figure 3.36: Schematic view of layer permeability on 2-D (*r*-*z*) plot. 99
Figure 3.37: Comparison of wellbore pressures and temperatures and inflow production profile at the end of drawdown for Case 3. 102
Figure E.1: Comparison of wellbore/sandface temperatures and pressures for different J-T coefficient values for both zones at the end of drawdown. 157
Figure E.2: Comparison of wellbore/sandface temperatures and pressures for different J-T coefficient values in the upper zone at the end of drawdown. 158
Figure E.3: Comparison of wellbore/sandface temperatures and pressures for different J-T coefficient values in the lower zone at the end of drawdown. 159
Figure E.4: Comparison of wellbore/sandface temperatures and pressures for different porosity values for both zone at the end of drawdown. 160
Figure E.5: Comparison of wellbore/sandface temperatures and pressures for different porosity values in the upper zone at the end of drawdown. 161
Figure E.6: Comparison of wellbore/sandface temperatures and pressures for different porosity values in the lower zone at the end of drawdown. 162
Figure E.7: Comparison of wellbore/sandface temperatures and pressures for different permeability values for both zones at the end of drawdown (q_{sc} = 500 sm^3/D). 163
Figure E.8: Comparison of wellbore/sandface temperatures and pressures for different permeability values in the upper zone at the end of drawdown (q_{sc} = 500 sm^3/D). 164
Figure E.9: Comparison of wellbore/sandface temperatures and pressures For different permeability values in the lower zone at the end of drawdown (q_{sc} = 500 sm^3/D). 165
Figure E.10: Comparison of wellbore/sandface temperatures and pressures for different permeability values in the upper zone at the end of drawdown (q_{sc} = 100 sm^3/D). 166

Figure E.11: Comparison of wellbore/sandface temperatures and pressures for different permeability values in the lower zone at the end of drawdown (q_{sc} = 100 sm^3/D). 167
Figure E.12: Comparison of wellbore/sandface temperatures and pressures For different permeability values in the upper zone at the end of drawdown (q_{sc} = 1000 sm^3/D). 168
Figure E.13: Comparison of wellbore/sandface temperatures and pressures for different permeability values in the lower zone at the end of drawdown (q_{sc} = 1000 sm^3/D). 169
Figure E.14: Comparison of wellbore/sandface temperatures and pressures for different surface flow rates at the end of drawdown. 170
Figure E.15: Comparison of wellbore/sandface temperatures and pressures for different viscosity values for both zones at the end of drawdown. 171
Figure E.16: Comparison of wellbore/sandface temperatures and pressures for different viscosity values in the upper zone at the end of drawdown. 172
Figure E.17: Comparison of wellbore/sandface temperatures and pressures for different viscosity values in the lower zone at the end of drawdown. 173
Figure E.18: Comparison of wellbore/sandface temperatures and pressures for different volumetric heat capacity of rock values for both zones at the end of drawdown. 174
Figure E.19: Comparison of wellbore/sandface temperatures and pressures for different volumetric heat capacity of rock values in the upper zone at the end of drawdown. 175
Figure E.20: Comparison of wellbore/sandface temperatures and pressures for different volumetric heat capacity of rock values in the lower zone at the end of drawdown. 176
Figure E.21: Comparison of wellbore/sandface temperatures and pressures for different fluid specific heat capacity values for both zones at the end of drawdown. 177
Figure E.22: Comparison of wellbore/sandface temperatures and pressures for different fluid specific heat capacity values in the upper zone at the end of drawdown. 178
Figure E.23: Comparison of wellbore/sandface temperatures and pressures for different fluid specific heat capacity values in the lower zone at the end of drawdown. 179
Figure E.24: Comparison of wellbore/sandface temperatures and pressures for different well radius values for both zones at the end of drawdown. 180
Figure E.25: Comparison of wellbore/sandface temperatures and pressures for different well radius values in the upper zone at the end of drawdown. 181
Figure E.26: Comparison of wellbore/sandface temperatures and pressures for different well radius values in the lower zone at the end of drawdown. 182
Figure E.27: Comparison of wellbore/sandface temperatures and pressures for unperforated distance of 5 m between producing zones at the end of drawdown. 183

Figure E.28: Comparison of wellbore/sandface temperatures and pressures for unperforated distance of 10 m between producing zones at the end of drawdown. 183
Figure E.29: Comparison of wellbore/sandface temperatures and pressures for unperforated distance of 20 m between producing zones at the end of drawdown. 184
Figure E.30: Comparison of wellbore/sandface temperatures and pressures for unperforated distance of 30 m between producing zones at the end of drawdown. 184
Figure E.31: Comparison of wellbore/reservoir pressures and temperatures for different skin values for both zones at the end of drawdown (q_{sc} = 100 sm^3/D). 185
Figure E.32: Comparison of wellbore/reservoir pressures and temperatures For different skin values in the upper zone at the end of drawdown (q_{sc} = 100 sm^3/D). 186
Figure E.33: Comparison of wellbore/reservoir pressures and temperatures for different skin values in the lower zone at the end of drawdown (q_{sc} = 100 sm^3/D). 187
Figure E.34: Comparison of wellbore/reservoir pressures and temperatures for different skin values for both zones at the end of drawdown (q_{sc} = 1000 sm^3/D). 188
Figure E.35: Comparison of wellbore/reservoir pressures and temperatures for different skin values in the upper zone at the end of drawdown (q_{sc} = 1000 sm^3/D). 189
Figure E.36: Comparison of wellbore/reservoir pressures and temperatures for different skin values in the lower zone at the end of drawdown (q_{sc} = 1000 sm^3/D). 190

NUMERICAL SIMULATION OF TRANSIENT SANDFACE AND WELLBORE TEMPERATURE BEHAVIORS OF WELLS IN MULTILAYER SINGLE-PHASE OIL AND GEOTHERMAL RESERVOIRS

SUMMARY

The interpretation of dynamic temperature data acquired during well tests and distributed temperature sensors (DTS) has grown increasingly in the last decade. While research studies are ordinarily based on sandface solutions, actual field measurements are made in the wellbore, generally at a certain distance above the sandface for conventional well tests. There is still a need for further fundamental studies to emphasize the apparent differences between sandface and wellbore temperature responses especially when it comes to history matching and production optimization applications.

The objective of this study is to develop and present applications of a two-dimensional (2-D) r-z, fully implicit, single-phase non-isothermal, transient coupled reservoir/wellbore model with a single well located at the center of a cylindrical reservoir. The model accounts for the Joule-Thomson (J-T), isentropic expansion, conduction and convection effects for predicting the transient temperature behavior and computing the wellbore temperature at different gauge depths. In this study, single phase fluid flow of oil or geothermal brine from a fully penetrating vertical or inclined well in an infinite-acting homogeneous reservoir is modeled. The coupled simulator solves mass, momentum, and energy conservation equations simultaneously for both reservoir and wellbore. The functional iteration procedure is used that updates fluid properties based on available correlations as a function of pressure and temperature at a given time step. Comparisons of the developed model for several syntetic cases with a commercial simulator are provided.

We identify diagnostic characteristics of temperature transients at gauge locations at the sandface and above the sandface that may arise during a well test, we examine the sensitivity of the model parameters appearing in the coupled non-isothermal reservoir/wellbore model through synthetically generated test data sets and history matched field application. The drawdown and buildup sandface transient temperature data are obtained from the coupled model and used to interpret and analyze temperature transients. In addition to the J-T coefficient of fluid, we show that history matching transient temperature data provides estimates for the skin zone radius and permeability when analyzed jointly with the conventional pressure test analysis (PTA). An investigation on the effect of gauge location on temperature data shows that the early-time response is influenced by the wellbore phenomena while the J-T effects are clearly identified at later times at typical gauge locations up to 100 m above the top of

the producing horizon (refers to total pay zone). Logarithmic time derivative of temperature transients is found as a useful diagnostic tool to differentiate the wellbore phenomena from the reservoir response. It is also shown that the temperature transient is more reflective of the properties of the near wellbore region (e.g., skin zone) than the pressure transient. For this reason, analyzing temperature transients together with the pressure transients could add more value to the analysis to better examine near wellbore characteristics.

A comprehensive sensitivity study conducted for multi-layer systems by constructing a 2-D (*r*-*z*) coupled model indicates beneficial remarks on PLT data. We provide well profile outputs of pressure, temperature, and flow distributions along the wellbore to identify most influential parameters, such as the layer petrophysical properties and the layer thermal parameters. Several examples of regression on temperature and pressure from multi-layer systems are considered for demonstrating the utility of the developed simulator. Due to high number of parameters involved in multi-layer systems, a robust characterization on thermal and rock properties is required to be able to achieve a realistic regression on temperature profiles to compute inflow rates of individual layers.

ÇOK TABAKALI, TEK-FAZLI PETROL VE JEOTERMAL REZERVUARLARDAKİ KUYULARIN KARARSIZ KUYU CİDARI VE KUYU İÇİ SICAKLIK DAVRANIŞLARININ SAYISAL SİMÜLASYONU

ÖZET

Kuyu içi ve rezervuar sistemlerinin karakteristik özellikleri, endüstride yaygın olarak kuyu testi uygulamaları ile belirlenir. Kuyu testlerinin amacı, yüzeyde üretim debisinde geçici ve kontrollü değişiklikler yaratarak, kuyu yüzeyine yakın yerlere konumlandırılan basınç ve sıcaklık ölçerlerden elde edilen basınç verilerini analiz etmektir. Rezervuar karakterizasyonu çalışmalarının çoğu, problemi basitleştirmek adına rezervuarda izotermal bir akış olduğu varsayımına dayanır. Böyle bir varsayım, rezervuardaki sıcaklık değişikliklerini ihmal eder ve pratik açıdan doğrudur, çünkü üretim boyunca gözlemlenen sıcaklık değişimleri, basınç değişimlerine oranla genellikle küçüktür. Ancak, basınç düşümlerinin fazla olduğu durumlarda yüksek sıcaklık değişimleri gözlemlenebilir. Örneğin yüksek debiyle veya çok düşük geçirgenlikli tabakalardan üretim yapılması ya da kuyuya yakın civarda hasar bulunduğu durumlarda, petrol veya jeotermal su üretilen rezervuarlarda kararsız akış dönemindeki sıcaklık davranışlarının izotermal olmayan koşullarda altında incelenmesine ihtiyaç vardır.

Fiziksel ve termodinamik süreçler dikkate alındığında, aslında, kuyu içi ve rezervuar sistemlerinde üretim veya enjeksiyonla birlikte izotermal olmayan akış koşullarının oluştuğu ve sıcaklığın zamanla değiştiği gözlemlenir. Yazındaki son çalışmalarda, bu sıcaklık değişikliklerine, izentropik genleşmenin yanı sıra Joule-Thomson etkisinin sebep olduğu gösterilmiştir. Dolayısıyla, bu tür etkileri içeren kararsız akış dönemi boyunca kaydedilen sıcaklık verileri, rezervuar ve akışkan özellikleriyle ilgili önemli bilgiler içerebilir. Örneğin, rezervuar geçirgenliği, gözeneklilik, zar bölgesi yarıçapı ve geçirgenliği, kayaç ve akışkan sistemin ısı kapasitesi ve ısıl iletkenlik gibi parametreler sıcaklık davranışlarını etkiler. Bu yüzden, kuyu testlerinden veya dağıtılmış sıcaklık sensörlerinden (DTS) elde edilen dinamik sıcaklık verilerinin yorumlanması son yıllarda giderek yaygınlaşmıştır. Araştırmalar genellikle rezervuar çözümlerine dayalı olsa da aslında konvansiyonel kuyu testlerinden elde edilen saha ölçümleri, kuyu içinde genellikle rezervuarın belirli bir mesafe üzerinde gerçekleştirilir. Özellikle tarihsel çakıştırma uygulamaları söz konusu olduğunda, kuyu yüzeyindeki ve kuyu içindeki sıcaklık ölçümleri arasındaki belirgin farklılıkları vurgulamak için daha fazla temel araştırmaya ihtiyaç vardır.

Bu çalışmanın amacı doğrultusunda, iki boyutlu (2-D) r-z, tek fazlı, izotermal olmayan, kararsız akış döneminde kuyu içi ve rezervuar modellerini birleştiren, silindir bir rezervuarın merkezinde tek kuyuya sahip, tamamıyla kapalı bir halde

(implicit) sayısal çözümler üreten bir rezervuar simülatörü geliştirilmiştir. Kararsız akış dönemindeki sıcaklık davranışları, Joule-Thomson, izentropik sıkışma/genleşme, ısı iletimi ve taşınması gibi fiziksel etkiler değerlendirilerek modellenir ve rezervuarın yanı sıra kuyu içinde farklı ölçüm derinliklerinde sıcaklık ve basınç hesaplanabilir. Homojen ya da heterojen, tek ya da çok tabakalı bir rezervuarda, rezervuarın kalınlığı boyunca bütünüyle veya kısmen tamamlanmış dikey bir kuyudan petrol veya jeotermal suyun tek fazlı sıvı akışı, yüzey koşullarında tanımlanmış sabit veya değişken debili üretim testleri ve kapama dönemleri için modellenmiştir. Geliştirilen simülatör hem rezervuar hem de kuyu içinde kütle, momentum ve enerji korunumu denklemlerini kuyu içi ve rezervuar modellerini birleştirerek beraber çözer. Belirli bir zaman adımında, basıncın ve sıcaklığın bir fonksiyonu olarak mevcut korelasyonları kullanarak akışkan özelliklerini güncelleyen fonksiyonel yineleme prosedürü ile çözümler geliştirilmiştir. Geliştirilen sayısal modelin endüstride kullanılan ticari izotermal olmayan bir simülatör ile karşılaştırılması sağlanmıştır.

Kuyu yüzeyine yakın yerlere konumlandırılan basınç ve sıcaklık ölçerlerden elde edilen sıcaklık verilerinin, kararsız akış dönemi davranışlarını tanımlamak için sentetik olarak kuyu testi verileri oluşturulmuş ve gerçek saha verilerine tarihsel çakıştırma yapılmıştır. Sentetik veriler, izotermal olmayan kuyu içi ve rezervuar birleşik simülatörümüzden elde edilmiştir. Üretim ve kapama sırasında kararsız akış dönemindeki sıcaklık davranışlarının model parametrelerine olan duyarlılığı incelenmiştir. Akışkanın Joule-Thomson katsayısının bulunabilmesine ek olarak, tarihsel çakıştırma yapılan kararsız sıcaklık verileri, geleneksel basınç testi analizi (PTA) ile birlikte kullanıldığında zar bölgesi yarıçapı ve geçirgenliği için tahminler sağlar. Kuyu testleri esnasında özellikle üretim dönemi boyunca genellikle yüzeyde ya da kuyu dibindeki operasyonel etkiler, ölçüm aletlerinde kaydedilen verilere olumsuz yansımaktadır. Bu sebeple, üretim boyunca kaydedilen basınç verileri, bu karakteristik özellikleri taşıması sebebiyle, kuyu testleri analizi yapılırken çoğu zaman değerlendirilmez. Fakat üretim boyunca kaydedilen sıcaklık verileri bu çalışmada gösterildiği gibi yararlı bilgiler sağlayabilir. Saha verilerine tarihsel çakıştırma örneğinde ayrıntılı olarak gösterildiği gibi, kapama dönemi basınç verileri, üretim boyunca kaydedilen sıcaklık verileriyle birlikte analiz edildiğinde, kuyu içi ve rezervuar sistemini anlamamıza yardımcı olabilir. Ayrıca, iyi bir tarihsel sıcaklık çakıştırması için, etkin kuyu yarıçapı adıyla yeni bir parametre tanımlanmasına ihtiyaç duyulmuştur. Konvansiyonel kuyu testleri operasyonlarında, kuyu dibinde kuyu yüzeyine yakın yerlere birçok mekanik alet yerleştirilmektedir. Fakat, bu aletler, sıvı akışının kuyu yüzeyinin üzerinde nispeten daha küçük bir hacimde gerçekleşmesine sebep olmaktadır. Kuyu dibinde akışkan hacminin sıcaklık tepkisi üzerine etkisi çok kritik olduğundan, bu yeni parametre (etkin kuyu yarıçapı) saha verileriyle tarihsel çakıştırma gerçekleştirilirken bir bilinmeyen olarak değerlendirmeli ve tahmin edilerek bulunmalıdır.

Kararsız akış döneminde gözlemlenen sıcaklık verilerinin logaritmik türevi, kuyu içi etkilerinin rezervuar tepkisinden ayırt edilmesine faydalı bir teşhis aracı olduğu görülmüştür. Kuyu yüzeyine belirli bir uzaklığa yerleştirilen ölçüm aletlerinden elde edilen kararsız sıcaklık davranışları analiz edildiğinde, kuyu içi etkilerinin bu çalışmada önerilen logaritmik türev analizinde tümsek oluşturulduğu gözlemlenir. Bu çalışmada sunulan çözümler, tüm bu ölçüm aletlerinden gelen basınç ve sıcaklık verilerinin ne tip bir bilgi içerebileceğini araştırmamıza olanak sağlamıştır. Ölçüm aletlerinin kuyu dibine yerleştirildikleri konumun sıcaklık verileri üzerindeki etkisine ilişkin bir araştırmamız, sıcaklığın erken zaman tepkisinin, kuyu içi akıştan

etkilendiğini göstermiştir. Rezervuardaki Joule-Thomson etkilerinin ise daha sonraki zamanlarda kuyu yüzeyinden 100 metreye kadar uzağa konumlandırılan ölçüm aletlerinden elde edilen verilerde açıkça gözlemlenebildiğini gösterilmiştir. Bu sebeple, kuyu testleri boyunca ölçüm aletlerinin kuyu yüzeyine en yakın konuma yerleştirilmesi hedef alınır, fakat bu bazen mümkün olmayabilir. Radyal akış rejimi dönemleri için yarı logaritmik ve logaritmik türev analiz metotları kullanılarak kuyu yüzeyinden oldukça uzakta ölçülen sıcaklık verilerinin, güvenilir bilgiler içermeyebileceği anlaşılmıştır. Tipik konumlara yerleştirilen ölçüm aletlerinden elde edilen üretim dönemi sıcaklık verilerinde, kuyu içi etkilerinin sonrasında rezervuar tepkisi görülür. Ancak, kapama dönemi sıcaklık verileri ise daha çok kuyu içi etkilerini takiben, ölçüm aletlerinin yerleştirildiği konumu çevreleyen kayaç formasyonuna olan ısı kayıplarının etkisinde kalır.

Kararsız akış döneminde gözlemlenen sıcaklık verilerinin, basınç verilerine nazaran, yakın kuyu bölgesinin (örneğin, zar bölgesi) özelliklerini daha fazla yansıttığı da gösterilmiştir. Sıcaklık verileri incelenirse basınca göre daha yavaş ilerlediği gözlemlenir. Bu durum, sıcaklık verilerinin, özellikle kuyu civarıyla ilgili, basıncın göremediği daha fazla bilgiyi yansıtmasını sağlar. Bu nedenle, kararsız zamandaki sıcaklık ve basınç verilerini birlikte analiz etmek, kuyuya yakın bölgelerin özelliklerini daha iyi incelememizi sağlayabilir. Basınç türev analizine benzer şekilde, sıcaklık verilerinin türevlerinden sıcaklığa özgü davranışları belirlemek mümkündür. Zar faktörü etkisi olmadığında, erken zamanlarda kuyu içi etkilerini ve bunu takip eden Joule-Thomson katsayısıyla ilişkili olan geç zaman davranışını görmekteyiz. Zar faktörü etkin olduğunda ise süresi zar bölgesinin geçirgenliği ve yarıçapıyla ilişkili olan ara bir sıcaklık davranışı belirmektedir. Sonrasında zar bölgesi etkileri sona erdiğinde, zar bölgesi dışındaki özellikleri gösteren geç zaman sıcaklık davranışı belirmektedir.

2-boyutlu (r-z) birleşik kuyu içi ve rezervuar modelleri oluşturarak çok katmanlı sistemler üzerinde kapsamlı parametre duyarlılığı çalışmaları sunulmuştur. Kuyu içi basınç ve sıcaklık profilleri ile akış debi (PLT) profilleri, bu sonuçları kontrol eden en etkin parametreleri (katmanların petrofiziksel ve termal özellikleri gibi) belirleyebilmek amacıyla ayrıntılı şekilde gösterilmiştir. Endüstride PLT saha operasyonlarından elde edilen veriler, kuyu içi akışkan tipi tanımlamalarını ve katmanların akış debilerinin yüksek çözünürlüklü ölçümlerini sağlayarak, kuyuların performansını değerlendirmek amacıyla kullanılır. Tipik bir PLT aleti, kuyunun temsili bir üretim veya enjeksiyon profilini oluşturmak için kuyu dibinde fiziksel ölçümler yapan birçok sensör ve mekanik aletten oluşur. Bu aletler, kuyu içinde belirli konumlarda sıcaklık ve basınç ölçümlerini, akışkan tipi tanımlamasını, akışkan hacimlerini ve birbirleriyle oranlarını, katmanlara özel akışkan debilerini sunmaktadır. Bu mekanik aletler, kuyu içinde akış sırasında çok düşük ya da çok yüksek debili rezervuar katmanlarının bulunduğu ölçüm noktalarında düzgün çalışmayabilir ve katmanlara özel akışkan debilerini, doğru bir şekilde hesaplayamayabilir. Bu yüzden, PLT operasyonu boyunca, kuyu içinde yapılan basınç ve sıcaklık ölçümleri ve kuyu içi akış debi (PLT) profillerinin oluşturulması üzerinde çalışılmıştır. Bu sebeple, geliştirilen simülatörün faydasını da göstermek amacıyla çok katmanlı sistemlerden sentetik olarak oluşturulmuş basınç ve sıcaklık profili verileri kullanılarak birçok regresyon örneği ele alınmıştır. Bu örneklerde, kuyu boyunca her bir katmanın debisini sıcaklık ve basınç profillerinden bulunan parametrelerle hesaplayarak, kuyu içi akış debi (PLT) profillerinin bulunması hedeflenmiştir. Fakat, çok katmanlı sistemlerde parametre sayısının fazla olması sebebiyle, gerçekçi bir regresyon yapabilmek için, ısıl

özelliklerin doğru tespit edilmesi gerektiği görülmüştür. Geliştiren simülatörle, çok katmanlı sistemlerin davranışları; farklı rezervuar ve kuyu parametrelerine sistemin verdiği tepkiler araştırılmıştır. Bu tip bilgiler, PLT testlerinin dizayn edilmesinde kullanılabilir. Bir diğer uygulama da kuyu içine yerleştirilen dağıtılmış sıcaklık ve basınç sensörlerinin toplayacağı verilerin analizi olabilir. Gerçekleştirilen bir örnekte, bir perforasyonun tıkanmasının sıcaklık verileri üzerine etkisi gösterilmiştir. Ayrıca, geliştiren simülatörün, gelecekte gerçekleştirilebilecek olası yapay zekâ uygulamaları için çok hızlı ve efektif çıktılar üretmesi hedeflenmiştir.

1. INTRODUCTION

The characteristic properties of the wellbore/reservoir systems are typically inferred in the industry by conventional well testing applications. The objective of well testing is to create temporary and controlled changes in surface production rate to acquire measurements of transient-pressure responses which are usually accompanied with corresponding temperature data. Most of the reservoir characterization studies are simplified by a common assumption of isothermal fluid flow in conventional reservoirs. Such an assumption neglects temperature changes in the reservoir and is correct from a practical point of view as the changes in temperature with production for conventional reservoirs are usually small when compared to changes in pressure. Nevertheless, high temperature changes may be observed in wells producing under drawdown which would be the case if the well is produced with high production rates or highly damaged or completed in a tight formation. Therefore, there is a need to study the temperature transients behaviors of reservoirs producing oil and geothermal water under nonisothermal conditions. Indeed, physical and thermodynamic concepts prove non-isothermal flow in wellbore/reservoir systems and produce transient-temperature responses alone and jointly with production or injection.

Recent studies show that if the drawdown at the well is significant due to high production rate or due to presence of a skin zone around the wellbore, the temperature changes caused by isentropic expansion as well as Joule-Thomson effects could be significant and hence, the temperature transients due to such effects can reveal some important characteristics of the formation and fluid properties; e.g., reservoir permeability, porosity, skin zone radius and permeability, volumetric thermal capacity of the rock and fluid system, and even thermal conductivity during buildup periods.

1.1 Literature Review

A conventional well testing operation is generally divided into two groups: exploration/appraisal well tests that are performed following the drilling operations, and production well tests that are performed in an existing well usually after a long

shut-in. For exploration well tests, temperature measurements are valuable for flow history and fluid losses estimation while for production tests, temperature measurements have been shown to be useful to provide information such as completion and reservoir characteristics (Sidorova et al., 2015). Conventional well test analysis relies on the assumption that the process is isothermal in spite of the fact that temperature changes occur due to pressure decline in a negligible extend for PTA. Non-isothermal behavior stems from fundamental physical phenomenon such as J-T, isentropic expansion/compression, conduction and convection (Onur and Cinar, 2017a).

Early research studies in the literature focused on investigating sandface temperatures analytically through decoupling the pressure diffusivity and the thermal energy balance equations (Chekalyuk, 1965; Garg and Pritchett 1977, 1984; Ramazanov and Nagimov, 2007; Duru and Horne 2010a, 2010b, 2011a, 2011b). A number of researchers in the last decade (App, 2010; Palabiyik et al. 2013, 2015; Sidorova et al., 2015; Onur and Cinar, 2016; Palabiyik et al., 2016) have developed non-isothermal reservoir models which couple both mass and energy balance equations. Some of these studies typically verified their work with commercial non-isothermal flow simulators, such as TOUGH2 (Pruess et al, 1999) for geothermal reservoirs, and CMG-STARS (2020) for oil and gas reservoirs that use fully implicit numerical procedures to simulate transient temperature and transient pressure. In all these studies, temperature measurements are conducted at the sandface. Yet, generally in almost all well testing field applications, downhole pressure and temperature gauges are placed at a shallower depth in the wellbore, usually dozens of meters above the top of the reservoir.

Modelling dynamic features of flow in the wellbore requires the solution of conservation equations for mass, momentum and energy through multi-dimensional formulation of wellbore with the compressible Navier-Stokes equations. This computationally expensive solution requires challenging coupling conditions at boundaries with reservoir (Amara et al., 2009). Since changes in the radial direction in the wellbore are negligible when compared to changes along the wellbore, a one-dimensional axial model can correctly simulate the transient wellbore behaviors with simplified coupling techniques that may include proper source terms in the mass, momentum and energy balance equations (Forouzanfar et al., 2015). Therefore, the

task is to couple 1-D (z) wellbore model, solving mass, momentum, and energy equations, together with 2-D (r-z) non-isothermal reservoir model.

Earlier research studies used Ramey's traditional work (1962) that predicts wellbore temperature distribution by an analytical temperature equation that solves the transient heat conduction equation under transient conditions while ignoring the momentum effects. An overall heat transfer coefficient was introduced for the heat loss to formation by resistances to heat flow in the wellbore caused by tubing wall, tubing insulation, fluid in the casing/tubing, annulus, casing wall, and cement. Willhite (1967) provides a method to estimate overall heat transfer coefficient for wellbore. Numerous investigators such as Curtis and Witterholt (1973), Wu and Pruess (1990), Alves et al. (1992), Hasan and Kabir (1994, 2002), Hagoort (2004) proposed enhancements to Ramey's model. There are many studies mainly intended to serve full field reservoir simulations with various wells by developing general purpose numerical reservoir simulators which are capable of solving non-isothermal multiphase flow problems based on compositional models, black-oil models or both, e.g., Pourafshary et al. (2009) compared their results with compositional simulator called general-purpose adaptive simulator (GPAS) (Wang et al., 1997, 1999; Han et al., 2005) developed at The University of Texas at Austin whereas Semenova et al. (2010) and Livescu et al. (2010) used Stanford's general-purpose research simulator (GPRS) (Cao, 2002; Jiang, 2007).

In this study, we divert the focus on investigating well-testing problems which demands a single well coupled with a reservoir model as in earlier works which are typically based on developing semi-analytical coupled wellbore/reservoir models for describing the wellbore non-isothermal transient effects. Hasan et al. (2005) presented the first transient analytical single phase wellbore temperature equation for predicting transient temperatures along the wellbore for drawdown and buildup tests, and verified it with their rigorous model (Hasan et al., 1997). Izgec et al. (2007) proposed a hybrid numerical-differentiation scheme to substitute the constant overall-heat-transfer-coefficient introduced in the analytical wellbore temperature equation of Hasan et al. (2005). Spindler (2011) presented a dimensional analysis to modify the analytical and semi-analytical solutions of Hasan et al. (2005) and Izgec et al. (2007), and also proposed an analytical temperature solution which considers conduction along the wellbore for the first time in literature. Duru and Horne (2010a) modified transient

wellbore temperature solutions of Hasan et al. (2005), and predicted sandface temperature as a function of time from their non-isothermal reservoir flow model developed without momentum balance. Sui et al. (2008) discretized non-isothermal wellbore model but with the assumption of steady-state mass, momentum and thermal energy balance equations in their non-isothermal reservoir flow model. Onur et al. (2016a) used transient mass, momentum, and thermal energy balance equations to propose a semi-analytical non-isothermal reservoir flow model that can simulate bottomhole temperature with wellbore storage and skin effects, and a transient analytical wellbore model based on decoupling of transient isothermal mass-momentum balance equations and transient wellbore temperature model of the modified versions of Hasan and Kabir equations for drawdown and shut-in periods. In a series of papers, Onur et al. (2016a, 2016b, 2017) and App (2017) aimed to investigate the information content of transient temperature measurements made under single-phase flow of slightly compressible fluid within a vertical wellbore during drawdown and buildup tests. Furthermore, Onur (2017) provided additional analyses based on their previous studies. Onur et al. (2019) used the similar solution method and included skin effects to identify the information content of such transient wellbore data.

1.2 Scope and Purpose of the Thesis

The interpretation of dynamic temperature data acquired during well tests and distributed temperature sensors (DTS) has grown increasingly in the last decade. While research studies are ordinarily based on sandface solutions, actual field measurements are made in the wellbore, generally at a certain distance above the sandface for conventional well tests. There is still a need for further fundamental studies to emphasize the apparent differences between sandface and wellbore temperature responses especially when it comes to history matching applications.

The objective of this project is to develop and present applications of a two-dimensional (2-D) *r-z*, fully implicit, single-phase non-isothermal, transient coupled reservoir/wellbore model model with a single well located at the center of a cylindrical reservoir. The model accounts for the Joule-Thomson (J-T), isentropic expansion, conduction and convection effects for predicting the transient temperature behavior and computing the wellbore temperature at different gauge depths. In this study, single

phase fluid flow of oil or geothermal brine from a fully penetrating vertical well in an infinite-acting homogeneous single layer reservoir is modeled. The coupled simulator solves mass, momentum and energy conservation equations simultaneously for both reservoir and wellbore. We use the functional iteration procedure that updates fluid properties based on available correlations as a function of pressure and temperature at a given time step. Comparisons of the developed model with a commercial simulator is provided.

To understand and identify diagnostic characteristics of temperature transients at gauge locations at the sandface and above the sandface that may arise during a well test, we examine the sensitivity of the model parameters appearing in the coupled non-isothermal reservoir/wellbore model through synthetically generated test data and history matched field application. The drawdown and buildup sandface/wellbore transient temperature data are obtained from the coupled model and used to interpret and analyze temperature transients. In addition to the J-T coefficient of fluid, history matching transient temperature data provides estimates for the skin zone radius and permeability when analyzed jointly with the conventional pressure test analysis (PTA). An investigation on the effect of gauge location on temperature data shows that the early-time response is influenced by the wellbore phenomena while the J-T effects are clearly identified at later times at typical gauge locations up to 100 m above the top of the producing horizon. Logarithmic derivative of temperature transients is found as a useful diagnostic tool to differentiate the wellbore phenomena from the reservoir response. It is also shown that the temperature transient is more reflective of the properties of the near wellbore region (e.g., skin zone) than the pressure transient. For this reason, analyzing temperature transients together with the pressure transients could add more value to the analysis to better examine near wellbore characteristics.

In this study, we emphasize the value of transient wellbore temperature responses for a conventional well testing configuration where the actual pressure and temperature field measurements are acquired at gauges that sit on downhole gauge assembly (DGA) located generally at a certain distance, from 30 m up to 100 m above the top of reservoir (Sidorova et al., 2014). Thus, a fully implicit coupled 1-D wellbore and 2-D reservoir numerical simulator have been developed by solving the equations of mass, momentum, and energy conservation along axial z coordinate for wellbore, and cylindrical r-z coordinate for reservoir along with the appropriate initial and boundary

conditions. The numerical simulator developed is able to generate pressure and temperature transients resulting from production in a vertical well for single-phase fluids (water or oil) in a single layer reservoir where the inner zone adjacent to the wellbore may represent a skin zone (Figure 1.1). First, the mathematical formulation of both 1-D (z) wellbore and 1-D (r) and 2-D (r-z) reservoir models and their coupling technique are presented with the definition of the initial and boundary conditions followed by the solution algorithm of the coupled system (refer to Appendix). Secondly, comparison of numerical solutions with those computed from a well-known commercial simulator CMG-STARS (2020) is provided. Then, a thorough sensitivity study on different parameters affecting temperature transients is considered and followed by nonlinear regression techniques to investigate the effect of gauge location on parameters estimates based on temperature response. Finally, parameter estimation cases are performed followed by a history matching of a well test from an oil reservoir.

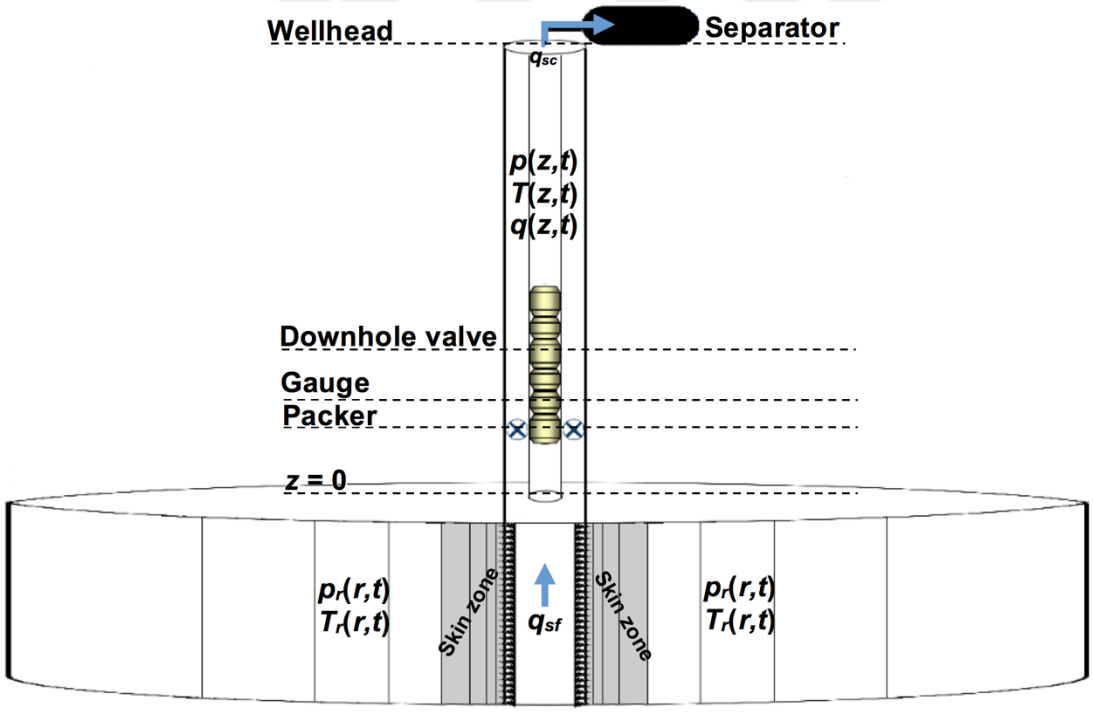

Figure 1.1: Schematic view of the coupled non-isothermal wellbore and reservoir system.

2. NUMERICAL IMPLEMENTATION FOR SLIGHTLY COMPRESSIBLE FLUID FLOW IN A COUPLED 1-D (r) RESERVOIR AND 1-D (z) WELLBORE SYSTEM

Mathematical model formulations described in the Appendix refer to physical processes such as the flow of fluids in porous media and in wellbore characterized by PDEs describing spatial and temporal changes of temperature and pressure based on conversation of mass and energy for reservoir whereas mass, momentum and energy for wellbore. Therefore, pressures, temperatures, and rates at any wellbore depth as well as pressure and temperatures at any location within the reservoir are simultaneously calculated for any given time. In this work, finite difference approach is used to convert PDEs into a numerical model by discretizing with geometrically spaced radial grid system for reservoir and user defined spaced for wellbore with respect to appropriate initial and boundary conditions for each domain. The numerical simulator developed considers block-centered grid system in which temperature and pressure variables are defined at the center of the gridblocks whereas flow rate variables are defined at the gridblock faces. In addition, bottomhole rates and wellhead flowing pressure/temperature are calculated by the simulator for design purposes of such tests.

2.1 Initial and Boundary Conditions

In the reservoir model, the initial pressure and temperature represent the pressure and temperature at the midpoint of all reservoir gridblocks and also at the bottommost wellbore gridblock which is adjacent to the reservoir. For wellbore gridblocks above the sandface, pressure is calculated by use of the hydrostatic gradient of the fluid where temperatures are dependent upon the geothermal gradient (see Figure 3.1).

2.1.1 Reservoir

Here, p_r and T_r denotes pressures and temperatures in the reservoir domain. The outer reservoir boundary conditions at $r=r_e$ in the reservoir model are a no-flow (insulated) for pressure ($\partial p_r/\partial r=0$) and the constant earth temperature (T_e) at the corresponding

depth based on geothermal gradient. Note that for the physical system considered, while r goes to infinity, temperature would reach T_e at the corresponding depth. In order to model infinite acting flow, the reservoir outer radius (r_e) is taken so large that the effect of outer temperature boundary cannot be observed throughout the entire flow history. The inner boundary conditions for temperature and pressure at $r=r_w$ in the reservoir correspond to $(\partial p_r/\partial r)_{r=r_w}$ and $(\partial T_r/\partial r)_{r=r_w}$ terms of second order derivatives in mass and energy conservation equations given in Appendix A (Equations A.38 and A.75). The inner-boundary condition for temperature assumes that heat flux is continuous at the boundary, according to the relationship given in Equation 2.3. The inner-boundary condition for pressure requires information from wellbore gridblock ($p_{w\,j}$) that is adjacent to the first reservoir gridblock ($p_{r_{1,j}}$) for a layer j, and given as:

$$\left(ru_{c_r}\right)_{r=r_w} = -\left(r\frac{k_r}{\mu}\frac{\partial p_r}{\partial r}\right)_{r=r_w} = -r_w\left(\frac{k_r}{\mu}\right)_{r=r_w}\left(\frac{p_{r_{1,j}} - p_{w\,j}}{r_1}\right) \tag{2.1}$$

2.1.2 Wellbore

We consider a no flow boundary at the bottom of the well by setting the velocity to zero (q_{w0}=0). The boundary condition at the top of the well is the specified constant surface flow rate ($q_{wNz}=q_{sc}$) which is the only constraint to start the flow in coupled system of the numerical simulator developed. During a buildup, the well can be shut-in from any preferable wellbore gridblock simply setting its flow rate to zero and excluding the overlying wellbore gridblocks from computations. In addition, the second order derivatives of energy balance equation require definitions at upper and lower boundaries. One may simply consider insulated boundary conditions for temperature ($\partial T/\partial z$=0) as the conductive heat transfer along the wellbore has negligible effects. Otherwise, a ghost gridblock at the top of the wellbore is required to be added to the model and to the solution matrix to be solved simultaneously for temperature (and also for pressure) with a simple linear interpolation between the first two neighbor gridblocks. A ghost gridblock at the bottom of the wellbore is not required because convective terms cancel out (q_{w0}=0) and heat conduction to underburden layer is not considered due to insulated boundary condition for temperature at the bottom of the wellbore ($\partial T/\partial z$=0).

2.1.3 Heat losses

The well-known basic equation used widely to calculate the wellbore heat losses per unit length of pipe is given as $Q_{loss}=(T_e-T_w)/R_h$ in which R_h is typically represented as $1/(2\pi r_w U_t)$ where U_t is the overall coefficient of heat transfer for a wellbore system composed of tubing, annulus, casing and cement (Ramey, 1962). In the derivations of wellbore equations (see Appendix C), the second order derivative of the conduction term in radial axis (λ_r) of Equation C.27 which is defined by thermal conductivity of fluid at the boundary between wellbore gridblock and its surrounding rock is replaced by overall coefficient of heat transfer (U_t) as:

$$\left(\lambda_r \frac{\partial T_w}{\partial r}\right)_{r=r_w} = \underbrace{\left(\frac{\lambda_r}{\Delta r}\right)}_{U_t} (T_w - T_e) \tag{2.2}$$

where T_e depends on the geothermal gradient for the corresponding depth. U_t may be recalculated to account for changes in wellbore design due to different tubing, annulus, casing or cement. In the derivations of reservoir equations (see Appendix A), the calculated value of overall coefficient of heat transfer U_t at the boundary between bottommost wellbore gridblocks that are adjacent to the first reservoir gridblocks replaces the thermal conductivity of the fluid-saturated rock in radial direction (λ_{t_r}) which appears in the second order derivative (Equation A.75). This also conforms with the reservoir inner boundary condition by assuming constant heat flux at the interface.

$$\left(\lambda_{t_r} \frac{\partial T_r}{\partial r}\right)_{r=r_w} = \underbrace{\left(\frac{\lambda_{t_r}}{\Delta r}\right)}_{U_t} (T_r - T_w) \tag{2.3}$$

2.1.4 Discretization

A fully implicit discretization of equations is applied for both reservoir and wellbore domains in which a backward difference in time derivative is considered. Functional iteration method is chosen for solving the reservoir and wellbore equations iteratively in a single solution matrix from time step t^n to t^{n+1} by starting with an initial guess at t^n and then by updating the all unknown pressure, temperature, rates as well as all terms that are dependent on pressure and temperature until convergence is achieved.

For discretizing the spatial derivatives in conservation equations of the reservoir model, a forward first-order finite-difference scheme is used. Therefore, discretized

terms containing the convective heat transfer coefficients (see Appendix B) for a production well are all negative as the pressure solution propagates from outer boundary to inner boundary for producing from a cylindrically shaped reservoir as given in Equation B.6 through B.9. Reservoir gridblocks are numbered from the inner-most to outer-most gridblocks with respect to wellbore.

A backward first-order finite-difference scheme is used for discretizing spatial derivatives of the conservation equations for the wellbore (see Appendix D). Thus, the convective terms do not require information from outside the domain at the upper-most gridblocks. As mentioned earlier, convective terms cancel out for the bottom-most gridblock as we define no flow boundary at the bottom of the well ($q_{w0}{}^{n}$=0). As wellbore gridblocks are numbered in an increasing order from the bottom-most to the surface (*j*th gridblock is above (*j*-1)th gridblock), convective derivatives discretized about the jth gridblock for temperature as $\left(\frac{\partial T_w}{\partial z}\right)_j = \frac{T_{w_j}{}^{n+1} - T_{w_{j-1}}{}^{n+1}}{z_j - z_{j-1}}$ and for pressure as $\left(\frac{\partial p_w}{\partial z}\right)_j = \frac{p_{w_j}{}^{n+1} - p_{w_{j-1}}{}^{n+1}}{z_j - z_{j-1}}$.

There exist (N_z-1) unknown rates from momentum conservation equations as $q_{sc}{}^{n}$ defined at the top of the well is the only well constraint that controls the entire coupled model from the wellhead. Therefore, a forward first-order finite-difference scheme is required to account for the boundary information when discretizing spatial derivative of pressure in momentum balance given in Appendix D such as $\left(\frac{\partial p_w}{\partial z}\right)_j = \frac{p_{w_j}{}^{n+1} - p_{w_{j+1}}{}^{n+1}}{z_j - z_{j+1}}$.

2.1.5 Coupling reservoir and wellbore

Coupling occurs at the boundary in radial direction between the bottom-most wellbore gridblock and the first reservoir gridblock that is adjacent to it. The continuity of pressure and temperature is achieved through this boundary which requires pressures and temperatures from both domains for heat transfer (Equations 2.2 and 2.3), inner-boundary for pressure (Equation 2.1) and convection in radial direction within wellbore mass and energy balance (Equations A.38 and A.75). As stated earlier, volumetric rate calculated by Darcy's law for a layer *j*, and given as:

$$q_{r_j}{}^{n+1} = 2\pi\Delta z_j \left(\frac{r_w}{r_1 - r_w}\right)\left(\frac{k_r}{\mu}\right)_{r=r_w,j}\left(p_{r_{1,j}}{}^{n+1} - p_{w_j}{}^{n+1}\right) \tag{2.4}$$

This method is more rigorous as no manipulation (such as setting $q_{r_j}^{n+1}$=0 during buildup) is required to prevent cross-flow between reservoir and wellbore.

2.2 Comparison of Pressure and Temperature Solutions

Several synthetic examples were used to benchmark numerical solutions with those generated from the commercial non-isothermal simulator CMG-STARS (2020), which can simulate transient pressure and temperature responses for an arbitrary sequence of production and shut-in periods in a coupled reservoir and wellbore model in which there exists a one-to-one correspondence between reservoir and wellbore gridblocks (i.e., an equal number of reservoir layers and wellbore gridblocks that are adjacent to them). When comparing the commercial simulator with the model proposed in this study, water is used as the reservoir fluid. The main reason for using water is the fact that thermodynamic properties of a single component water is well established. The commercial simulator solves enthalpy in energy balance; therefore, the J-T effects are implicitly accounted for without a need for an explicit definition of the J-T coefficient. On the other hand, the numerical simulator developed solves temperature, thus an explicit definition of the J-T coefficient is required. Thus, for an accurate comparison, a pure component with well-established thermodynamic properties is needed. Water would be the obvious choice. In the case of single-phase oil, it is recommended that, if available, measured thermal properties based on experimental data should be used. Otherwise, a tuned EOS is required for the calculation of a consistent set of thermodynamic properties, a challenging task for a standard cubic EOS such as Peng-Robinson (Peng and Robinson, 1976). Explicit definition of J-T coefficient in the proposed model makes it possible to estimate this parameter through history matching which is not possible with the commercial software.

Water properties are obtained from the equation of state (IAPWS, 2018). Therefore, when modeling pressure and temperatures in the simulator, water physical and thermal properties (density, viscosity, J-T coefficient, isothermal compressibility, isobaric thermal expansion, specific heat capacity, thermal conductivity) are treated as variable with pressure and temperature. The porosity given in Equation 2.5 and formation volume factor (FVF) of water ($B=\rho_{sc}/\rho(p,T)$) are also calculated as a function of pressure and temperature.

$$\phi = \phi_{ref}\left[1 + c_m\left(p_r - p_{ref}\right) - \beta_m\left(T_r - T_{ref}\right)\right] \tag{2.5}$$

Here, the reference pressure and temperature are evaluated at initial reservoir conditions. The properties of water and solid matrix calculated at initial reservoir pressure and temperature are given in Table 2.1. Solid matrix thermal properties in numerical solutions are treated as constant at the initial pressure and temperature. The example case is based on flow rate history that consists of a 2-day production at a constant surface flow rate of 1000 sm^3/D followed by a 4-day buildup. In the numerical simulator developed, the only well constraint is the rate at the wellhead conditions. There are 41 gridblocks in the wellbore with uniform length of 25 m whereas 200 logarithmically spaced gridblocks in the reservoir. Reservoir outer radius (r_e) is taken very large to represent an infinite acting flow throughout the entire flow history. The sandface pressure and temperature refer to computed gridblock pressure and temperature of the first reservoir gridblock that is adjacent to the wellbore gridblock.

Table 2.1: Simulation input data used for comparison example.

Model Properties		Water Properties		Rock Properties	
r_w (m)	0.15	ρ (kg/m^3)	1003.9	ρ_m (kg/m^3)	2347
r_e (m)	25000	c_p (J/kg.K)	4088.4	$c_{p,m}$ (J/kg.K)	1000
h_{res} (m)	25	ε_{JT} (K.Pa)	-2.027×10^{-7}	λ_m (J/m.s.K)	3.67
z_w (m)	1025	μ (Pa.s)	0.479×10^{-3}	c_m (Pa^{-1})	4×10^{-10}
p_{in} (MPa)	50	λ (J/m.s.K)	0.678	β_m (K^{-1})	9×10^{-5}
T_{in} (K)	333.15	β (K^{-1})	5×10^{-4}		
q_{sc} (sm^3/D)	1000	c (Pa^{-1})	4.57×10^{-10}		
Geo. grad. (K/m)	0.03	B (m^3/sm^3)	0.995		
U_t (W/m.s.K)	29				
k (mD)	50				
ϕ	0.1				

Using the data presented in Table 2.1, pressures and temperatures at any given point within the reservoir as well as pressure, temperature and flow rate profiles along the wellbore with respect to time are computed by the numerical simulator developed for any given flow history, which may consist of numerous drawdown and buildup periods. Commercial simulator computes pressures and temperatures at any given point within the reservoir with respect to time as well. On the other hand, well profiles are only computed from the top to the bottom boundaries of the producing horizon. The commercial simulator does not construct any wellbore gridblocks that are not adjacent to a reservoir gridblock. Hence, comparisons are performed only at the

sandface and wellbore gridblocks that have one-to-one correspondence at the producing horizon.

Skin effects are included by incorporating a skin factor into the finite difference model by the thick skin concept of Hawkins (1956). Specifically, a skin region is represented by a zone of altered permeability adjacent to the producing horizon. The permeability of the skin zone, k_s is defined by specifying the radius of the skin region, r_s, the skin factor, s, and using the following equation:

$$s = \left(\frac{k}{k_s} - 1\right) ln\left(\frac{r_s}{r_w}\right) \tag{2.6}$$

Here, the synthetic example considered present results for a single value of skin factor (s = 5) having a radius of 1.5 m and permeability of 26 mD. In following sections, individual effects of these skin-zone parameters on both drawdown and buildup temperatures are discussed in detail.

Figures 2.1 and 2.2 compares the sandface/wellbore temperatures and pressures respectively from the numerical simulator developed and the commercial simulator for the entire flow history. Figure 2.3 compares the corresponding drawdown sandface/wellbore temperatures on a semi-log plot whereas Figure 2.4 similarly compares for buildup sandface/wellbore temperatures plotted as a function of shut-in time. As seen, all pressure and temperature solutions match quite well.

Comparing two different simulators with different numerical implementations is not a trivial task for such complex processes since numerical parameters could affect the output significantly. It is not a focus of this study to present an exact match with the commercial simulator. The implementation for numerical simulator developed is primarily different from the commercial simulator in solving the energy equation and coupling wellbore and reservoir gridblocks. Commercial simulators are black box software and our reach of their implementation is limited with their user manual. Thus, the numerical details of their implementation are not available to us. There are still a lot of gray area and to our knowledge, there is no commercially available software that rigorously solves the problem described. The coupling part of the commercial simulator used in this study is still under development as 2017 and 2020 versions produce different results in temperature for the case considered at the very early times. Thus, inconsistencies observed in figures are acceptable. The absolute differences in

temperature are very small, i.e., in the range of 0.1 K. This might well be explained with numerical errors.

Considering the temperature response in this example, the J-T expansion leads to heating during drawdown at late times, and cooling during buildup due to its negative sign for the fluid considered. Figure 2.3 allows us to have a closer look at the match on a semi-log plot where the J-T expansion takes place at the later times of drawdown period. On the other hand, the isentropic expansion and compression mechanism leads to a cooling effect during drawdown while causing a heating effect during buildup, which occurs due to the fluid expansion near wellbore at very early times of drawdown and buildup. The difference in drawdown temperature responses between the sandface and the wellbore block adjacent to the reservoir is caused by the extra pressure drop in the wellbore.

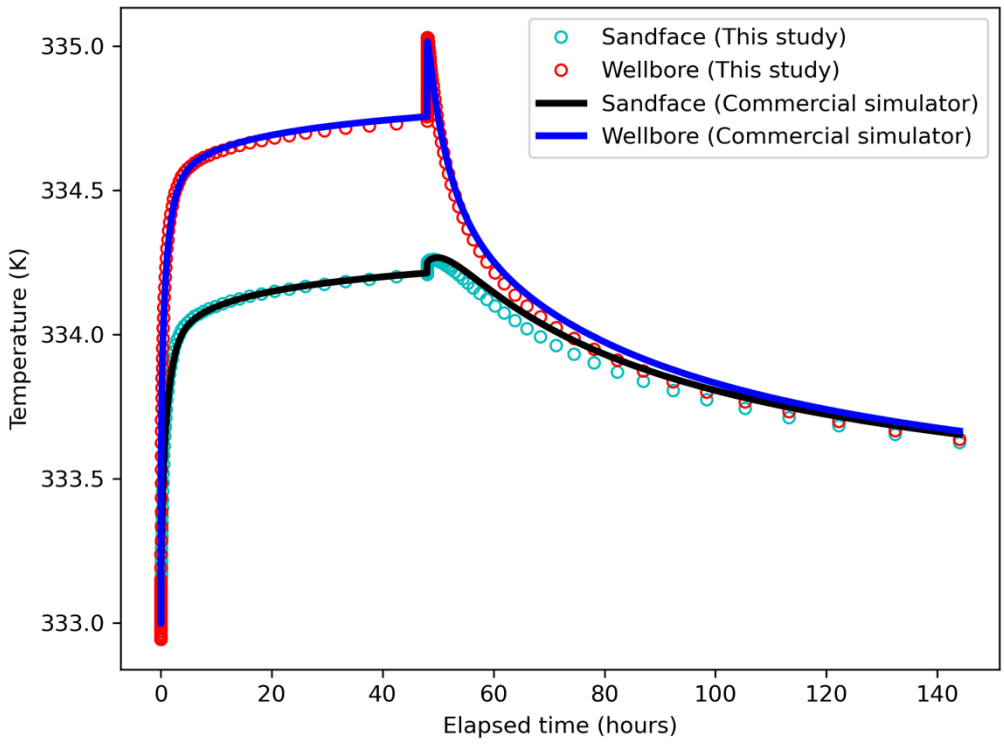

Figure 2.1: Comparison of sandface and wellbore temperatures with skin effects for entire flow history.

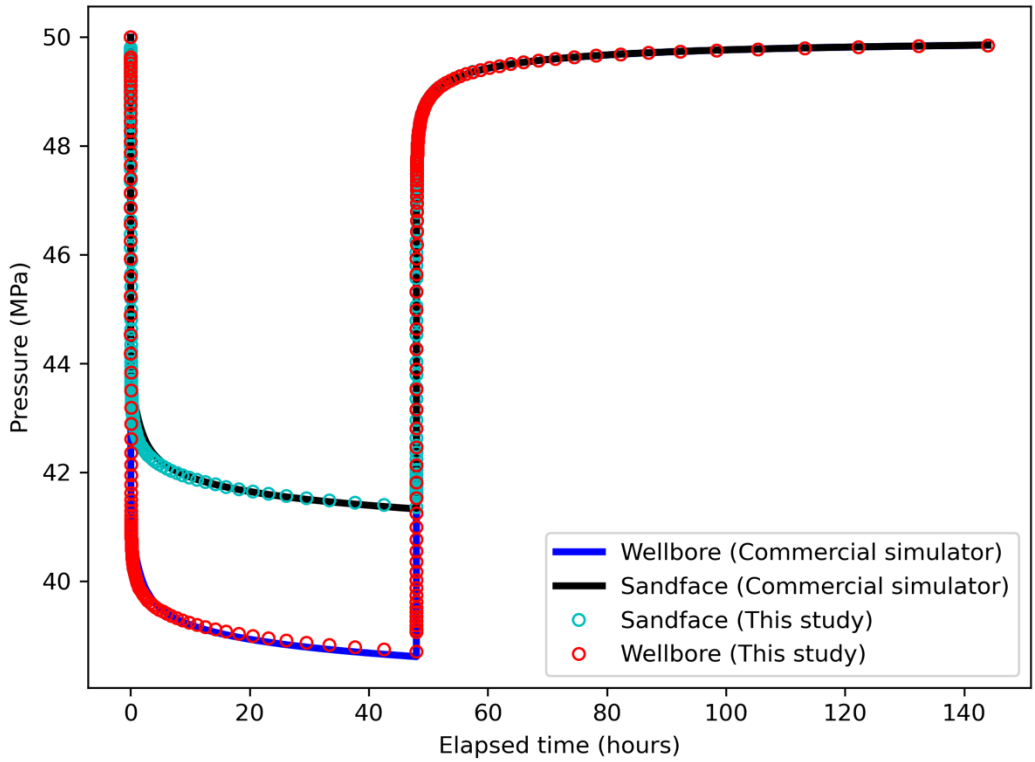

Figure 2.2: Comparison of sandface and wellbore pressures with skin effects for entire flow history.

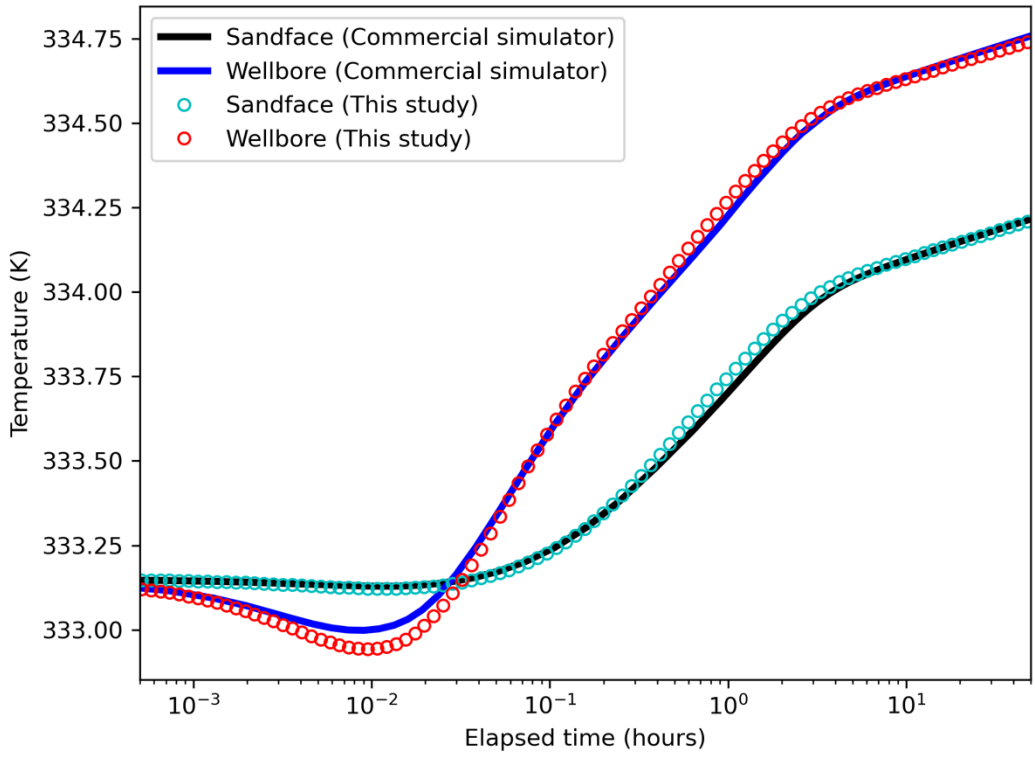

Figure 2.3: Comparison of sandface and wellbore temperatures with skin effects for drawdown on semi-log plots.

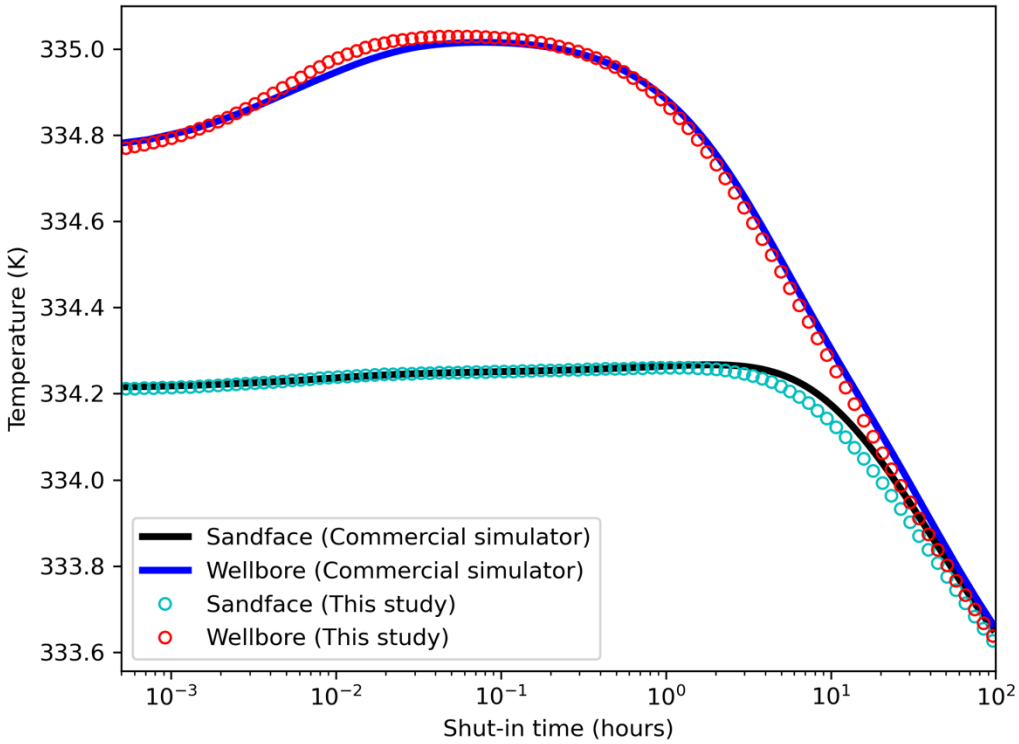

Figure 2.4: Comparison of sandface and wellbore temperatures with skin effects for buildup on semi-log plots.

2.3 Impact of Gauge Distances

Now, we investigate the transient temperature responses using numerical simulator developed for the base case described above (with no skin effects) for different gauge locations; sandface, wellbore block adjacent to sandface, z = 10 m, z = 30 m, z = 50 m and z = 90 m. Note that z = 0 refers to the top of the producing horizon throughout this chapter. In order to place the gauges exactly on these corresponding depths, the height of wellbore gridblocks is set to 20 m. Therefore, the reservoir thickness is also taken 20 m due to one-to-one correspondence at the bottomhole. Also, the durations of drawdown and buildup periods are changed to 10 and 100 hours respectively. We keep all other parameters the same as in Table 2.1.

Figure 2.5 compares drawdown temperature differences (ΔT) which is the substraction from its initial value and logarithmic derivatives of drawdown temperatures ($\partial T/\partial \ln t$) whereas Figure 2.6 compares drawdown temperatures on a semi-log plot with respect to time. In addition, the derivative of pressure change, derivative of temperature and sandface flow rate (q_r is given in Equation 2.4) are all plotted with respect to time for drawdown on a semi-log plot in Figure 2.7. Similarly, Figures 2.8 and 2.9 makes the

same comparison of Figures 2.5 and 2.6 for the buildup period as a function of shut-in time.

Considering drawdown, the derivative of the wellbore temperature exhibits a hump at all gauge locations, seen clearly on Figure 2.5 similar to the signal in pressure during wellbore storage dominated flow. When the pressure difference and temperature derivative responses are compared (Figure 2.7), a shift in time is clear between two humps. As it is well known, during wellbore storage dominated flow, the wellbore fluid expands and accounts for the difference between the sandface and wellbore rates. The wellbore storage dominated flow region ends when the sandface and wellbore rates become equal. In the wellbore temperature response, the fluid expansion in the wellbore leads to an initial decrease in temperature during the wellbore storage dominated flow, since the higher temperature fluid from the lower locations has not reached the gauge location in large quantities. Once the sandface rate starts to become larger, a transition zone where a temperature change through mixing is observed at a fixed gauge location. When the hump in the derivative disappears, the derivative becomes almost constant. In this period, temperature difference and temperature exhibit a constant slope converging to the slope of the sandface response. Thus, once the transition period ends, the reservoir response is observed at the gauge location. Note that during this period the reservoir response is caused by the J-T phenomenon. A slight decrease in temperature is observed due to heat losses.

Similarly, the wellbore buildup response exhibits a more pronounced effect of compression during early times compared to sandface. As there is no rock in the wellbore, this behavior is solely due to the wellbore fluid compression, leading to heating. Similar to drawdown, a transition zone is observed in the temperature derivative due to mixing, following a stabilization. Also, the temperature eventually becomes the same as the initial temperature at the corresponding location at later times. The only wellbore temperature converging to the sandface response is the gridblock adjacent to the reservoir. Therefore, the wellbore buildup response does not contain information regarding the reservoir at late times when temperature is measured in the wellbore above the producing horizon. The wellbore phenomena dominate buildup response in the time frame of a conventional test.

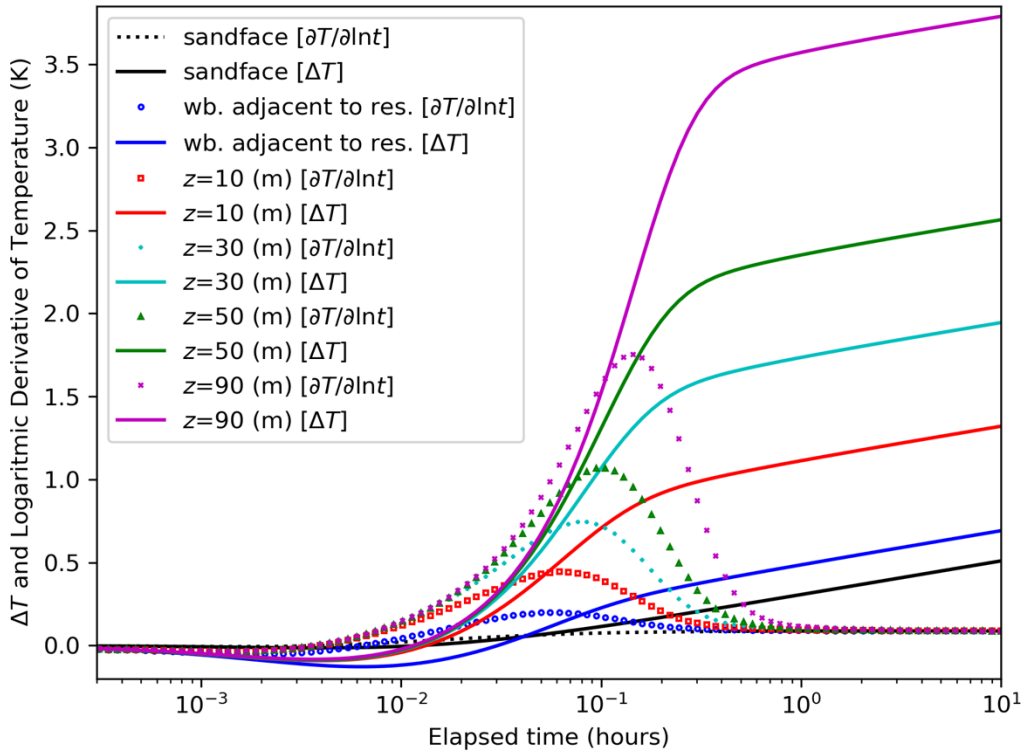

Figure 2.5: Effect of gauge location in the wellbore on drawdown temperature derivative.

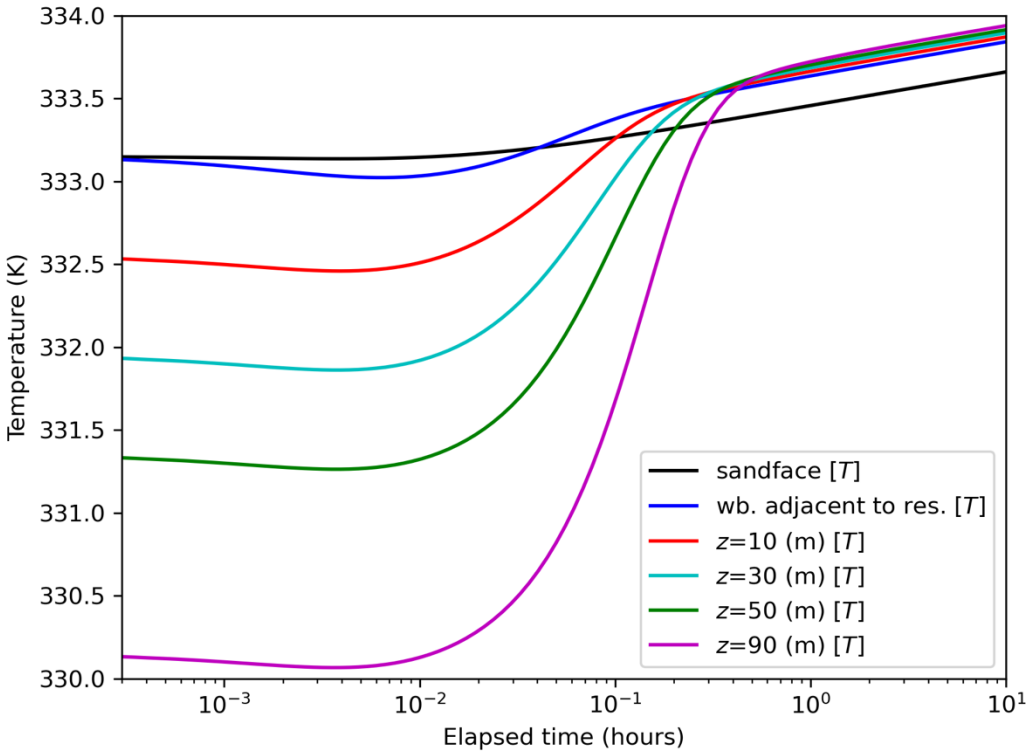

Figure 2.6: Effect of gauge location in the wellbore on drawdown temperature.

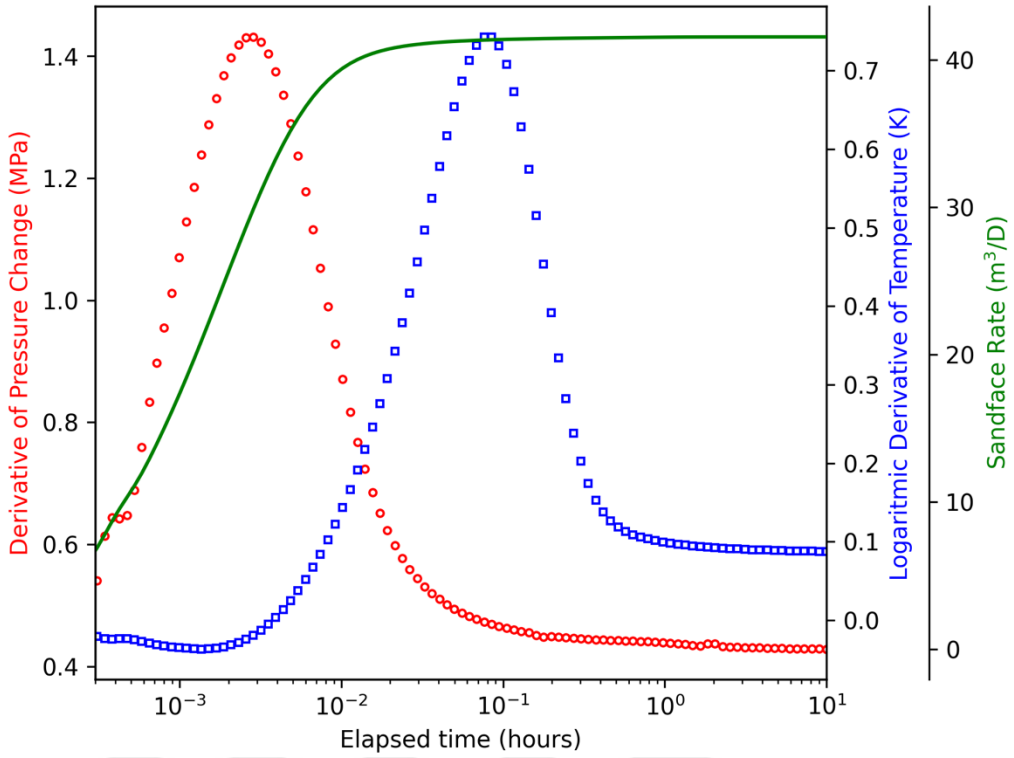

Figure 2.7: Derivative of pressure and temperature and surface flow rate during drawdown.

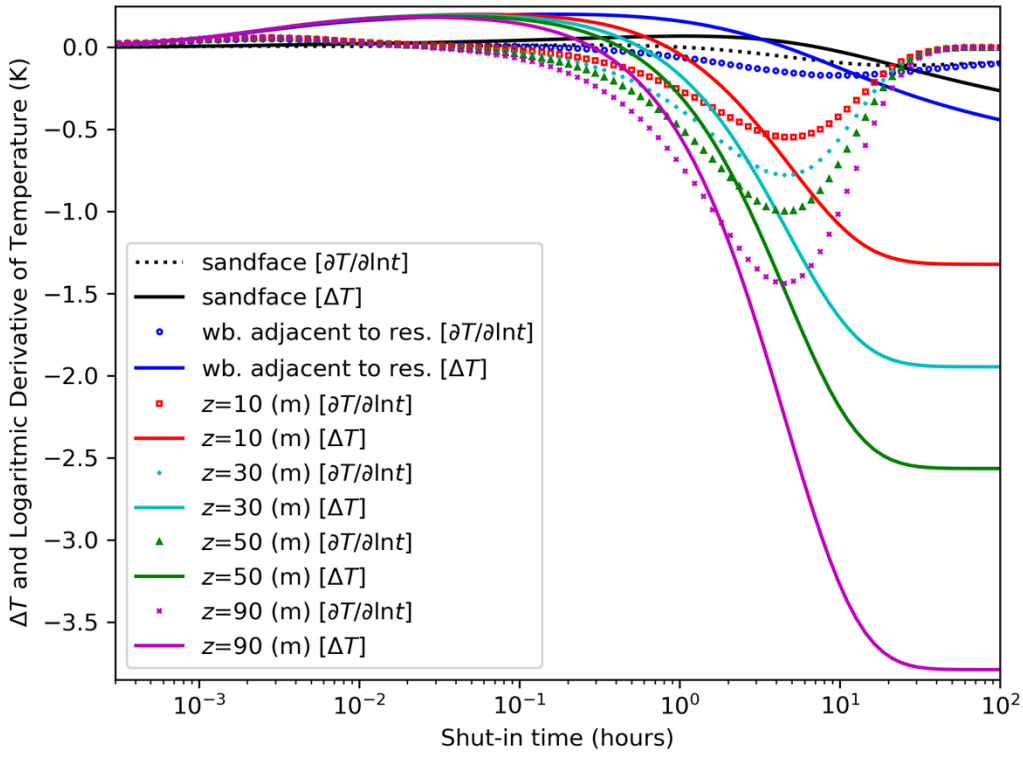

Figure 2.8: Effect of gauge location in the wellbore on buildup temperature derivative.

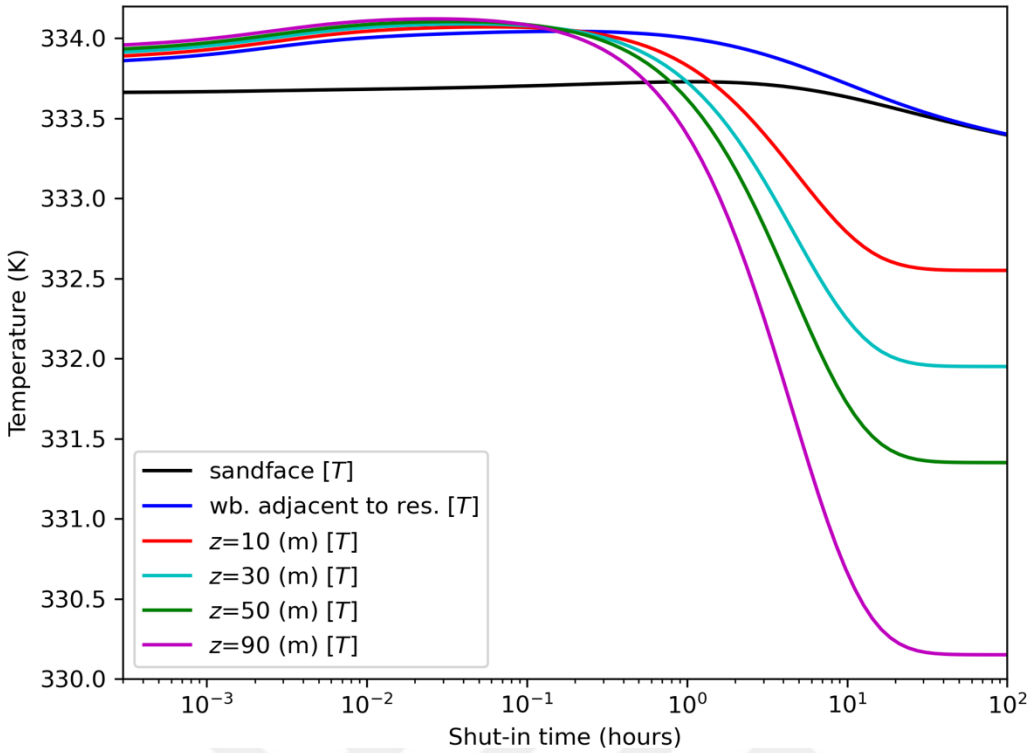

Figure 2.9: Effect of gauge location in the wellbore on buildup temperature.

2.4 Impact of Parameters

Here, we investigate the impact of the fluid and rock parameters on transient temperature responses using numerical simulator developed with no skin effects. It is important to note that the assumption of single-phase fluid flow where the gauges are located in the wellbore (z = 30 m) is endorsed. The important parameters such as porosity, permeability, heat loss coefficient, flow rate, well radius are listed in Table 2.2 and sensitivity to these values are inspected on semi-log plots of wellbore temperature differences (ΔT) and logarithmic derivative of temperatures ($\partial T/\partial \ln t$) for both drawdown and buildup period.

Since the gauge location for a typical well test is 30 m and higher above the producing horizon (Duru, 2010a), sensitivities on the magnitude of a parameter shown on semi-log plots contain wellbore temperature solutions from this gauge location only (30 m).

In Table 2.2, an effective radius of wellbore (r_{wb}) is introduced to account for volume changes in wellbore due to the placement of several operational tools (DGA, downhole valves, packer, joints, etc.) causing the fluid flow in the wellbore to occur in a relatively smaller volume above the sandface. Since the volume of the wellbore fluid is critical

for temperature response, an effective wellbore radius is introduced. Sidorova et al. (2014, 2015) showed detailed sketches of the cross section of wellbore with DST string and gauge placement.

Table 2.2: Parameters used in synthetic cases for sensitivity analysis.

Parameters	Case 1	Case 2	Case 3
ϕ	0.05	0.22	0.40
k (mD)	30	100	1000
U_t (W/s.K)	20	60	120
r_{wb} (m)	0.08	0.11	0.14

2.4.1 Effect of porosity

Figures 2.10 and 2.11 show the effect of porosity on drawdown and buildup wellbore (z = 30 m) temperatures, respectively. In the implementation of numerical simulator developed, an instant equilibrium of rock and fluid temperatures is assumed such that only a single temperature is solved. Changing porosity would result in a change in fluid and rock mass in a control volume. Rock and fluid have different heat capacities. As the pressure decreases, fluid expands and the expansion results in a temperature decrease since work is done. The energy (work) required comes from the stored energy in internal forms with different contributions of rock and fluid depending on their mass in the control volume that is controlled by porosity. Volumetric heat capacity of rock dominates the final temperatures within a time step because porosity is generally below forty percent.

During the isentropic expansion for the high-porosity case, a larger temperature decrease occurs compared to the low-porosity case since the fluid mass in the control volume is larger, requiring more energy for expansion. This deviation exhibits as a shift in temperature at later times where the J-T effects dominates since the change in pressure with respect to time becomes smaller whereas the change in pressure with respect to position becomes larger. Effect of porosity is observed through the isentropic expansion and sensitivity of porosities fades out in the J-T dominated times. This is clearly observed in the temperature derivative since, at early times when the isentropic expansion dominates, the temperature derivative changes with respect to porosity, however, in the J-T dominated period all the temperature derivatives converge to the same value. The buildup behavior is similar but reversed: At about after 10 hours the system tries to recover and reach the initial temperature through conduction. If the buildup time is unrealistically larger (for practical purposes), the

temperature goes back to the initial value and a change is observed in the temperature derivative response.

When considering the temperature response in the wellbore, the initial decrease in temperature occurs due to the isentropic expansion of the wellbore fluid. Hence, no effect of porosity is observed during this period (A negligible difference resides due to the transition). The temperature derivative exhibits a transition zone and converges to the same value. This flattening of derivative represents the period at which the reservoir response is observed in the wellbore. The buildup response in the gauge location does not reflect any reservoir response. A heating due to compression of the wellbore fluid is followed by a transition period due to mixing as explained before. Once transition period ends, as it is indicated by the derivative response, heat loss in the wellbore dominates and the temperature reaches the initial temperature. The difference observed in the graph at late times between different porosity values is caused by the temperature difference between the cases at the instant of shut-in. Since the temperature difference (ΔT) is calculated based on the temperature at shut-in, a shift is observed, however, all the temperature values go to the same initial temperature at the gauge location. The only parameter that is affected by porosity in the built-up response is the temperature at the instant of shut-in.

In this porosity example, there is a significant difference in magnitude of porosity between the lowest and highest cases (0.05-0.40). Even for such a case, the deviation in temperature with respect to porosity is not too much in the drawdown. In the buildup, however, at the gauge location, the effects are masked by the heat losses. For all practical purposes, estimating porosity from the drawdown temperatures seems to be not a trivial task since drawdown data is not clean and the changes in temperature are small. Eventually, the decrease in temperature depends on the heat capacity of rock. If it is larger, then the change in temperature difference becomes lower due to the isentropic expansion/compression, and in some cases, it is not observed.

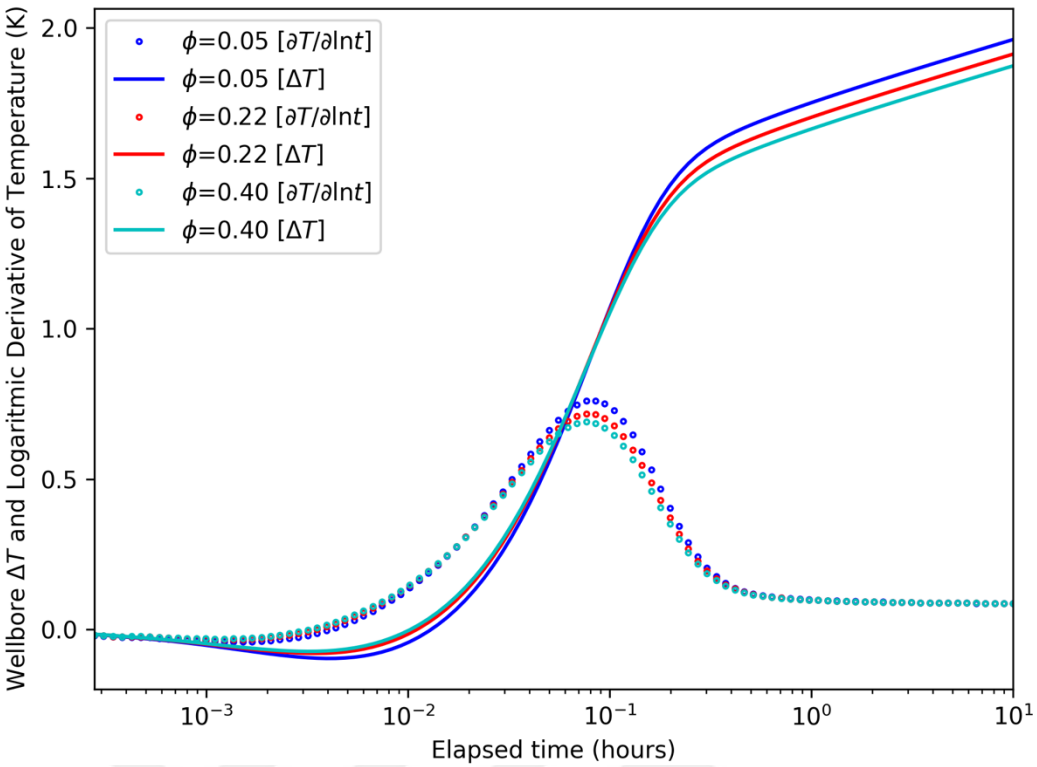

Figure 2.10: Effect of porosity in the wellbore on drawdown temperature.

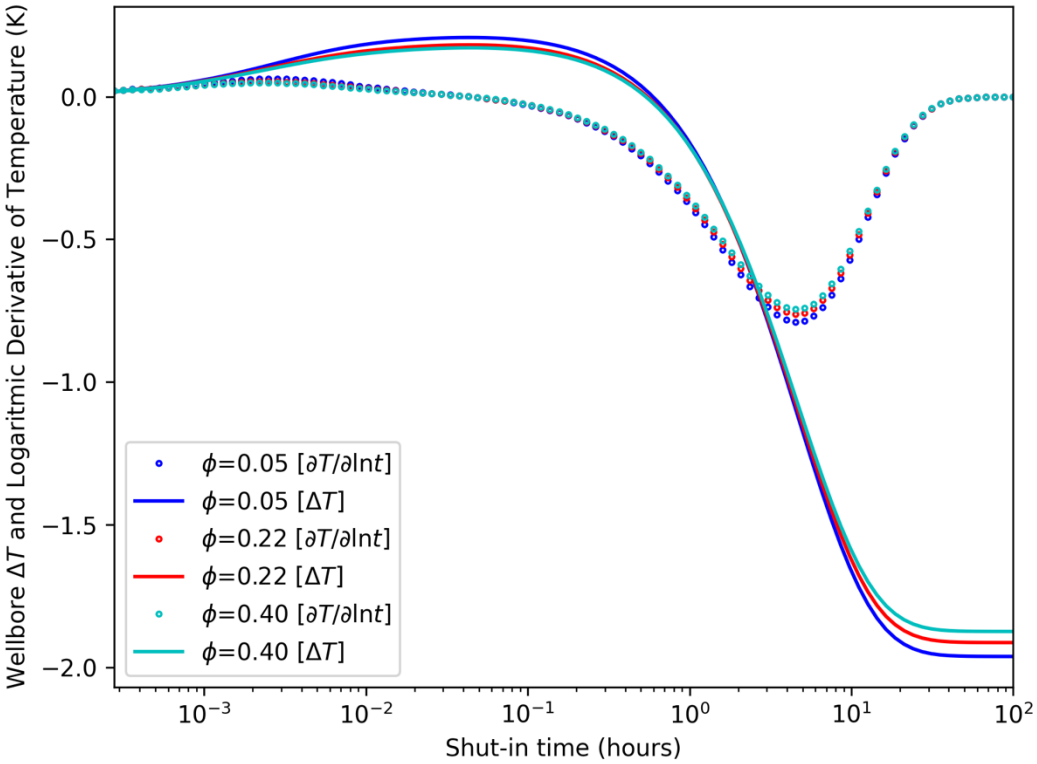

Figure 2.11: Effect of porosity in the wellbore on buildup temperature.

2.4.2 Effect of permeability

Figures 2.12 and 2.13 show the effect of permeability on drawdown and buildup wellbore (z = 30 m) temperatures, respectively. The magnitude of pressure drawdown determines how temperature changes. A higher permeability rock allows a lower pressure drawdown, which, in turn, reduces the impact of the isentropic expansion/compression and J-T heating/cooling on temperature. The temperature derivative response at the gauge location exhibits an isentropic expansion, initially depending on the wellbore pressure, then a transition zone, and later becoming constant. Clearly, the wellbore temperature derivatives exhibit a major downward shift with increasing permeability at later times. When the permeability is sufficiently high, the system behaves almost isothermal. During drawdown, the late time slope of the ΔT curve is affected by permeability. As it is shown by Onur and Cinar (2017b), the slope at late times during drawdown is controlled by the transmissibility and J-T coefficient. The buildup response at the gauge location again is not very useful since it is dominated by the wellbore phenomena.

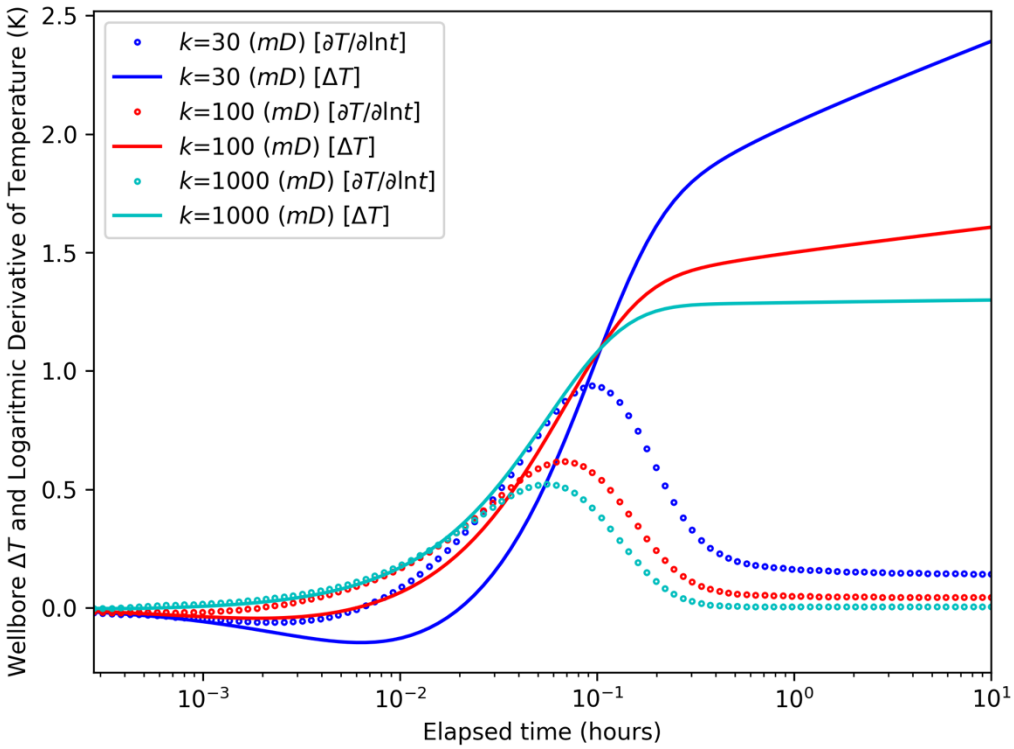

Figure 2.12: Effect of permeability in the wellbore on drawdown temperature.

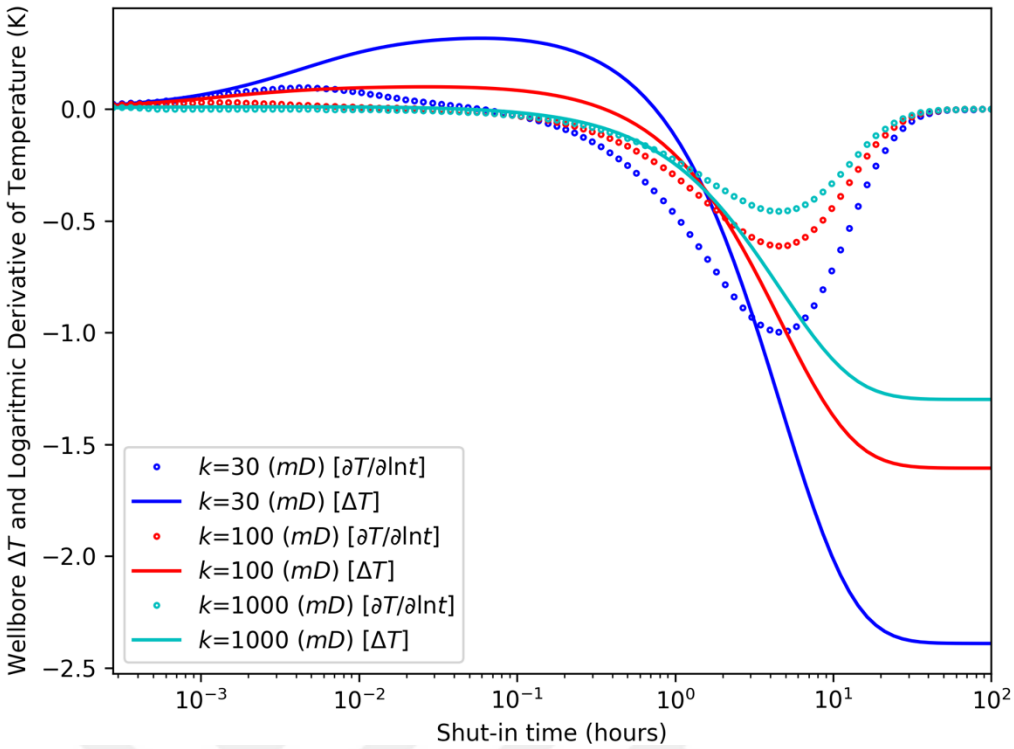

Figure 2.13: Effect of permeability in the wellbore on buildup temperature.

2.4.3 Effect of heat loss

Figures 2.14 and 2.15 show the effect of overall heat transfer coefficient on drawdown and buildup wellbore (z = 30 m) temperatures, respectively. In the treatment of numerical simulator developed, overall the heat transfer coefficient is constant. As expected, when the overall heat transfer coefficient is higher, the heat loss becomes larger, and temperature decreases at the gauge location. The drawdown temperatures and derivatives show negligible changes for different values at late-times. The duration of the transition zone does not seem to change due to heat loss. The primary difference is in the buildup case such that when the overall transfer coefficient is larger, the temperature reaches the initial temperature much more quickly as expected, leading to a shift in the temperature derivative. This shift in the derivative hump is directly correlated with the overall transfer coefficient. Figure 2.16 shows the temperature profile in the wellbore at the end of drawdown. The cooling due to heat losses is obvious when the fluid travels towards the wellhead.

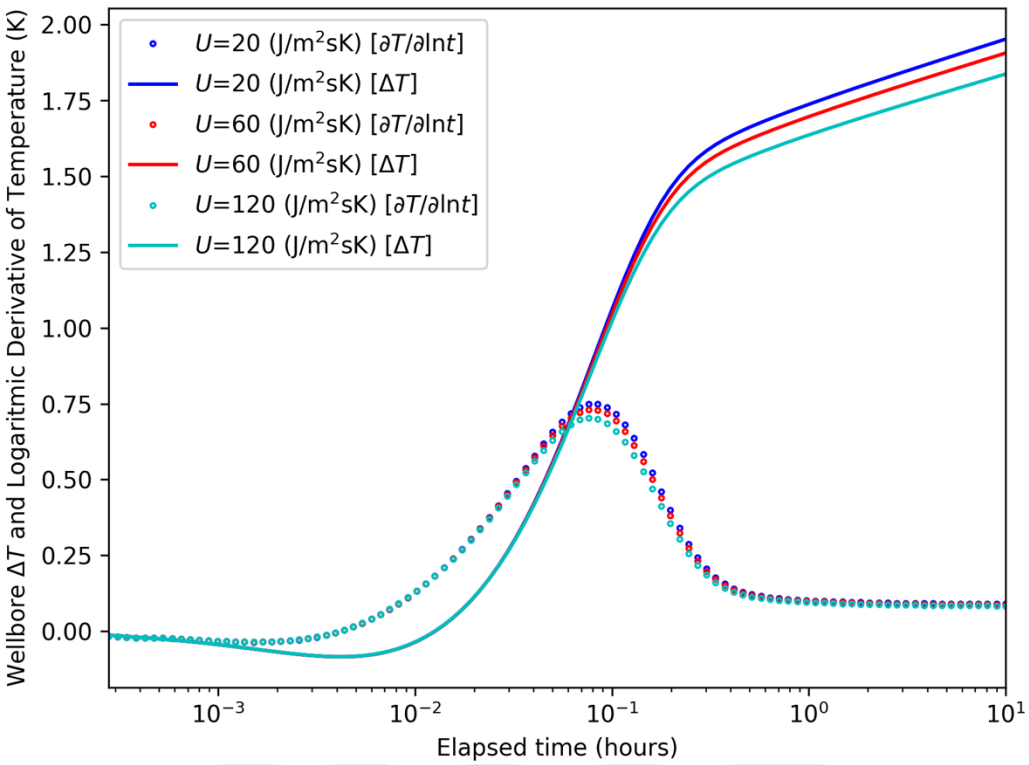

Figure 2.14: Effect of heat losses in the wellbore on drawdown temperature.

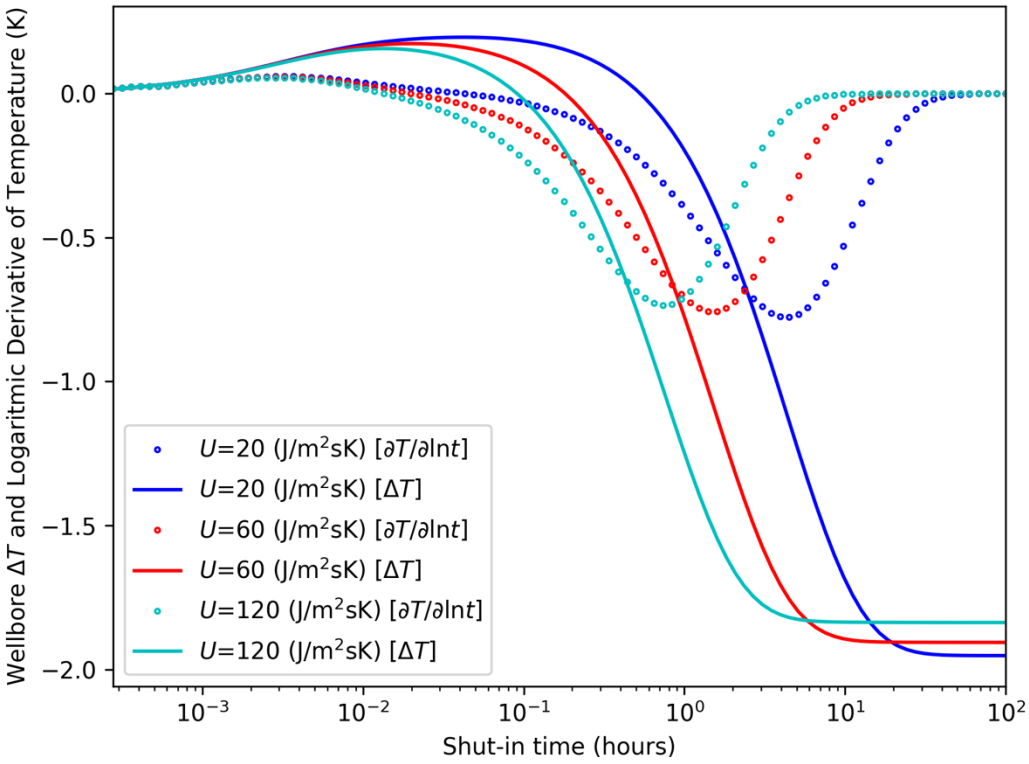

Figure 2.15: Effect of heat losses in the wellbore on buildup temperature.

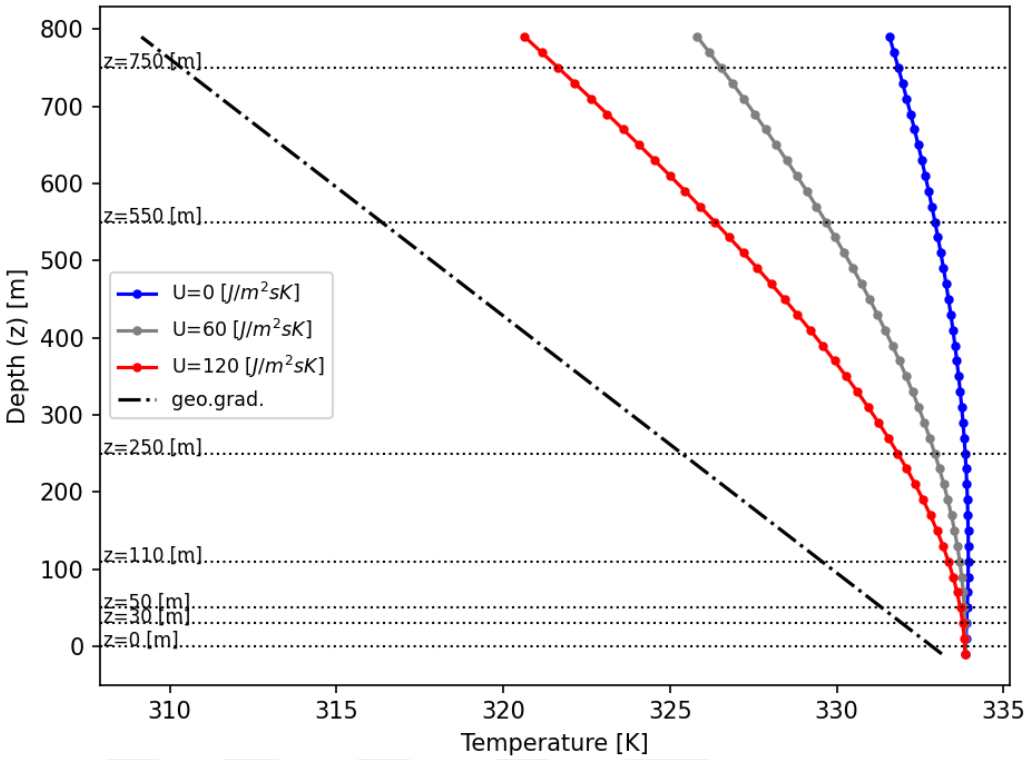

Figure 2.16: Effect of heat losses across the wellbore at the end of drawdown.

2.4.4 Effect of well radius

Here, we discuss the effect of change in well radius which causes a notable shift in wellbore temperature responses during the early times when the wellbore phenomena dominate. Therefore, the definition of an effective radius of wellbore (r_{wb}) is needed to reflect the field data correctly. Otherwise, if the same radius is considered for both wellbore and the producing horizon, a shift in temperature match is inevitable. Figures 2.17 and 2.18 show the impact of effective wellbore radius (r_{wb}) on drawdown and buildup wellbore (z = 30 m) temperatures, respectively. The temperature deviation in wellbore is dominated by the wellbore phenomena through mixing at early times, thus the effect of the volume of the wellbore fluid is investigated through well radius. For a large diameter wellbore, the isentropic expansion dominates over a larger time interval at the early times since the volume of the fluid is larger. Consequently, the transition zone shifts to later times and the reservoir response is observed later. The buildup temperature response is similar to drawdown. It takes a longer time to reach the initial temperature at the gauge location due to different fluid volumes.

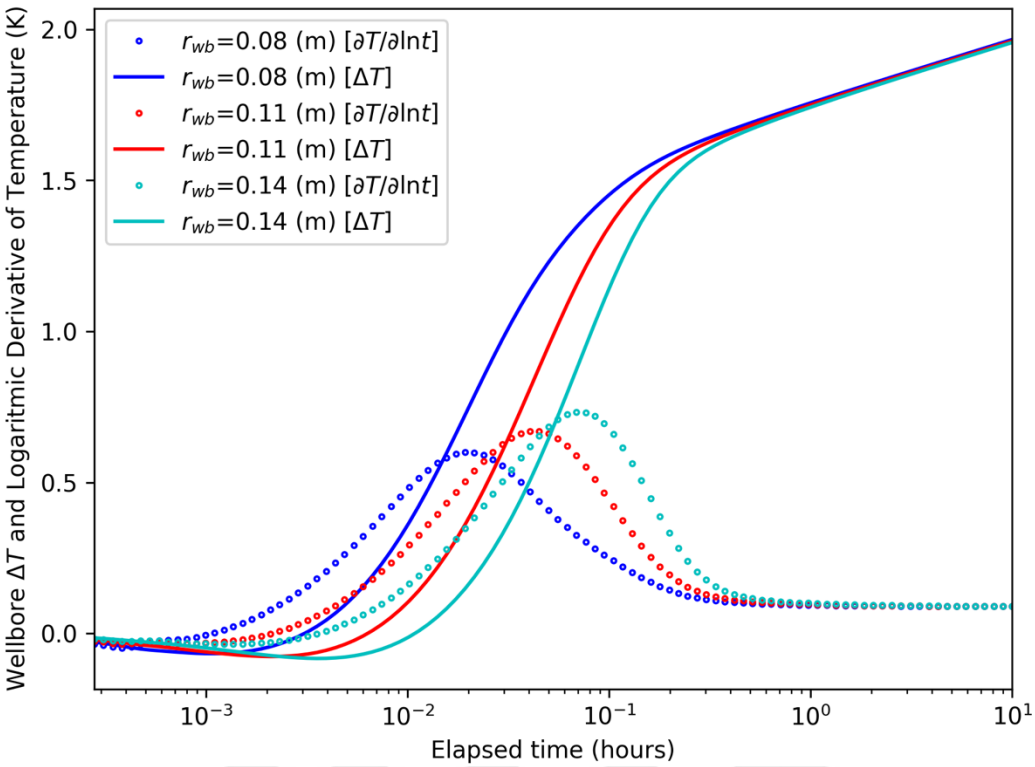

Figure 2.17: Effect of effective well radius in the wellbore on drawdown temperature.

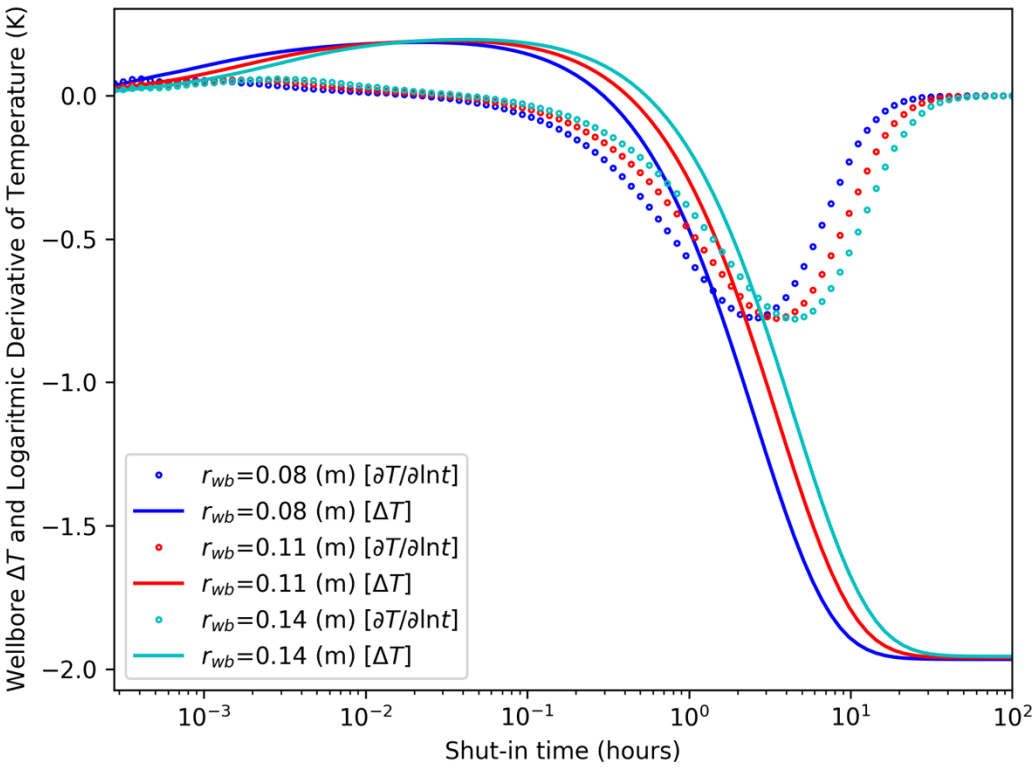

Figure 2.18: Effect of the effective well radius in the wellbore on buildup temperature.

2.4.5 Effect of flow rate

Figures 2.19 and 2.20 show the effect of flow rate on drawdown and buildup wellbore (z=30m)/sandface temperatures, respectively. The flow rate has a major effect on the temperature change since the pressure drop becomes larger with increasing flow rate. Thus, the temperature change is larger. Second, for larger flow rates, the duration of the transition zone in the wellbore temperature measurements is smaller. Since the flow rate is large, it takes less time for the fluid to mix in the wellbore. For the buildup, this same observation is not valid. The duration of the transition period is almost the same since it is controlled by heat losses in the wellbore that is a parameter assumed constant. The primary difference is the magnitude due to the value of temperature at the instant of shut-in.

Conduction has a negligible effect on the drawdown temperatures while it becomes effective on the late-time buildup sandface temperatures when the velocity becomes zero within the reservoir. Similar to pressure propagation in porous media, heat conduction is a diffusive process. It takes a substantial amount of time (more than any practical limits of a test) for the temperature to reach the initial reservoir temperature since thermal diffusivity is much smaller than the mass diffusivity. Thus, pressure propagates faster than temperature (Onur et al., 2016b). When the buildup response in the wellbore is considered, it is dominated by the wellbore phenomena. No effect of thermal conductivity of the reservoir is observed. The temperature reaches the initial temperature almost at the same time. No shift in time is observed between humps yet the magnitudes differ since the flow rate reaches to zero. Figure 2.21 shows the temperature profile at the end of drawdown. The velocity of the wellbore fluid is higher for the high flow rate case. Consequently, the temperature change along the wellbore is less. If the velocity is lower, more cooling is observed due to heat losses. This is due to the residence time of the wellbore fluid.

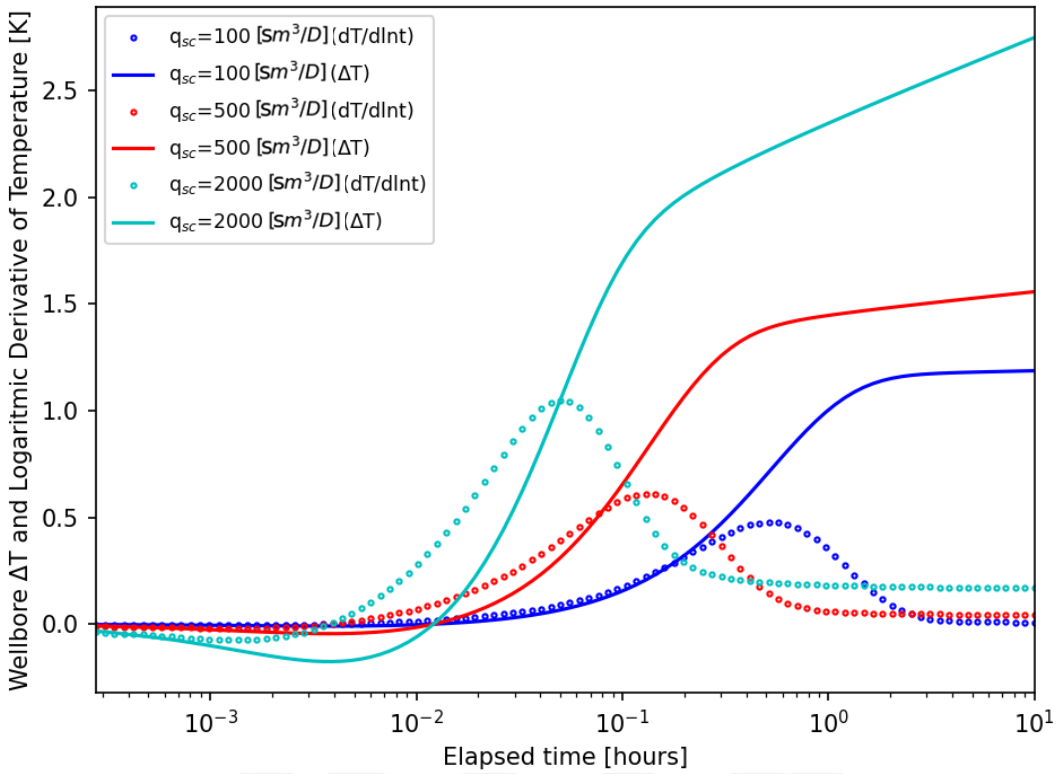

Figure 2.19: Effect of flow rates in the wellbore and sandface on drawdown temperatures.

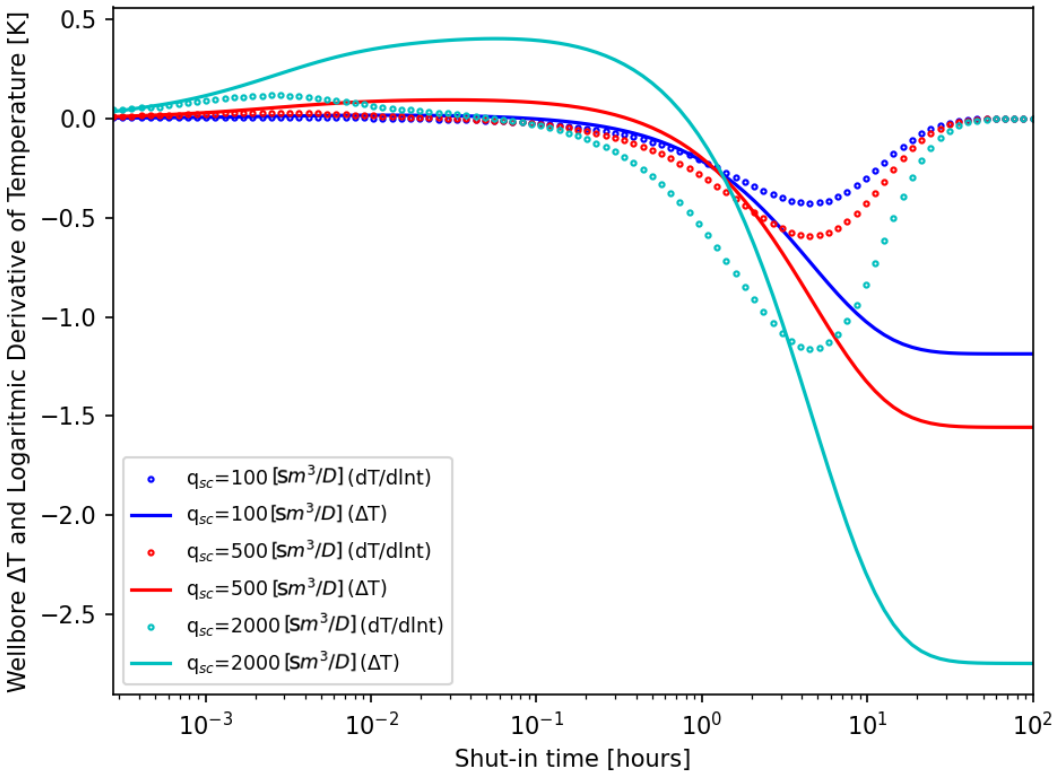

Figure 2.20: Effect of flow rates in the wellbore and sandface on buildup temperatures.

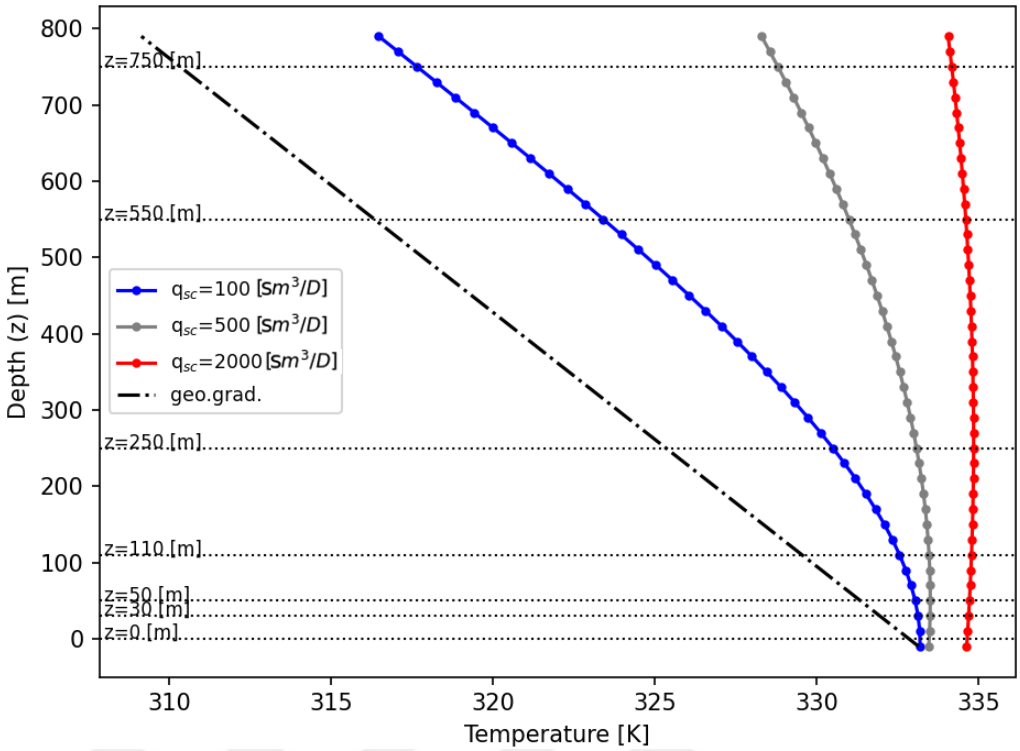

Figure 2.21: Effect of flow rates across the wellbore at the end of drawdown.

2.4.6 Effect of skin

As stated earlier, skin is modelled as a composite zone near the wellbore through the Hawkins formula (1956) given in Equation 2.6. The skin factor is a lumped parameter including many different wellbore effects including permeability alteration in near wellbore region. In this approach, an equivalent composite reservoir model is generated to account for pressure drop due to skin. In Table 2.3, the cases studied are reported, with calculated skin factor, and respective skin-zone permeability and skin-zone radius. In each case, a single parameter is kept constant to investigate the individual effects of parameters on wellbore temperature differences (ΔT) and logarithmic derivative of temperatures ($\partial T/\partial \ln t$) for both drawdown and buildup period on semi-log plots. For a better illustration of essential aspects, the reservoir permeability is increased to 100 mD, the drawdown duration is increased to 100 hours and the well radius is decreased to 0.1 m.

Table 2.3: Parameters used in synthetic cases for sensitivity analysis in the presence of skin effects.

Case No	k (mD)	k_s (mD)	r_s (m)	s
1			0.5	3
2	100	**35**	1.5	5
3			4.4	7
4		47		3
5	100	35	**1.5**	5
6		28		7
7		24	0.5	
8	100	35	1.5	**5**
9		43	4.5	
10		1471	0.5	
11	100	224	1.5	**-1.5**
12		165	4.5	

Firstly, we investigate transient wellbore and sandface temperature responses for drawdown through Figures 2.22 through 2.27. Sandface temperature solutions are also included in each figure (right) for comparison purposes. In Figures 2.22 and 2.23, the skin zone permeability is kept constant (k_s = 35 mD) while having different skin radius whereas, in Figures 2.24 and 2.25, the skin radius is taken as the same value (r_s = 1.5 m) while having different skin permeabilities. Cases 1 and 4 result in an equal low skin factor (s = 3) likewise Cases 3 and 6 result in an equal high skin factor value (s = 7) although different skin permeability and skin radius values are used as listed in Table 2.3. Figures 2.26 and 2.27 present the combined effects of these two skin zone parameters when the skin factor is kept constant (s = 5).

Onur (2017) shows that the sandface temperature-derivative data indicates an intermediate time stabilization, which reflects the skin zone properties, and a late-time stabilization, which reflects non-skin zone properties. In the new representation of temperature derivative which is the logarithmic derivative of temperature ($\partial T/\partial \ln t$) on a semi-log plot, two distinct stabilizations are identified. Likewise, two distinct slopes are identified in the temperature difference. A positive skin in the temperature derivative is recognized with two distinct stabilizations: The hump reflecting wellbore phenomena is followed by the initial stabilization indicating skin permeability followed by a second stabilization at a lower value reflecting reservoir permeability. The slope of the semilog straight line of temperature difference decreases since the permeability of the reservoir is higher than the skin zone permeability. The temperature measurements at the gauge location (30 m above the producing zone) still contains information regarding skin zone properties, however, if skin zone radius is

smaller, could be masked by the wellbore phenomena. The skin zone radius controls the duration of the skin zone dominated period: The larger the skin zone radius, the longer the effects prevail as seen in Figures 2.24 and 2.25. Thus, the contrast in permeability on the near well region is clearly observed in the drawdown transient temperature data. The pressure response does not contain such a resolution since the process is diffusive.

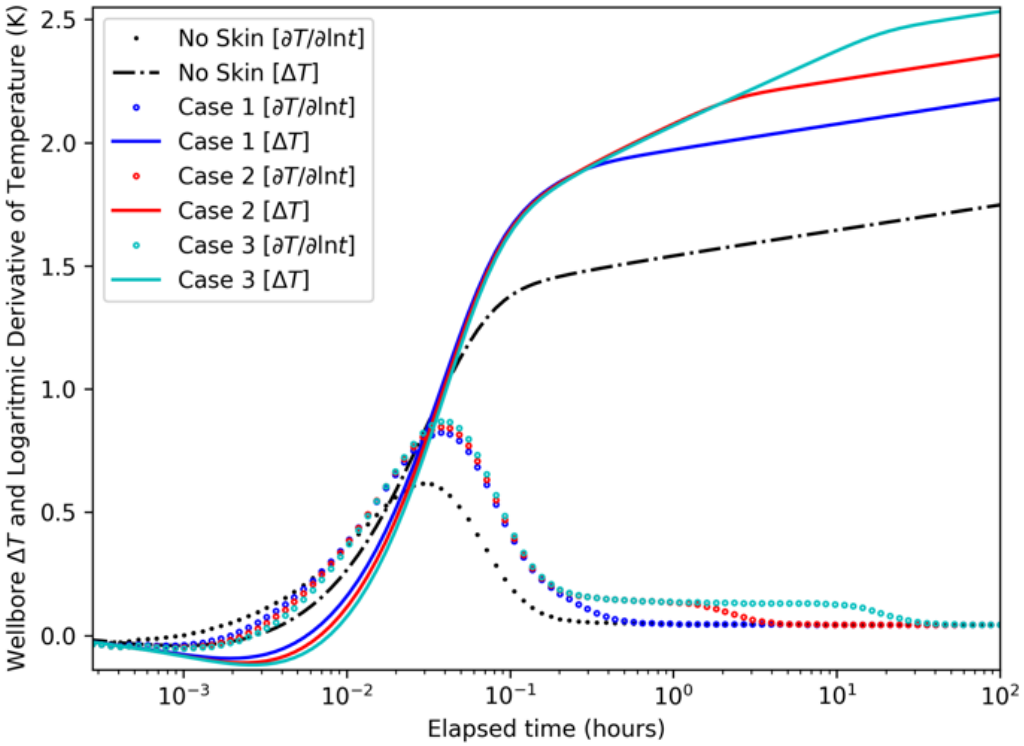

Figure 2.22: Effect of skin permeability with positive skin in the wellbore on drawdown temperature.

Figures 2.22 and 2.23 provides a comparison when skin zone permeability varies while skin radius is kept constant. As expected in all cases, the reservoir response is observed at the same time (around half hours) because all the derivatives reach the second stabilization at the same time as well. The major difference is the slope of the temperature difference. During the initial stabilization, each curve exhibits a different slope, however, during the second stabilization period, all curves converge to the same slope indicating the reservoir permeability.

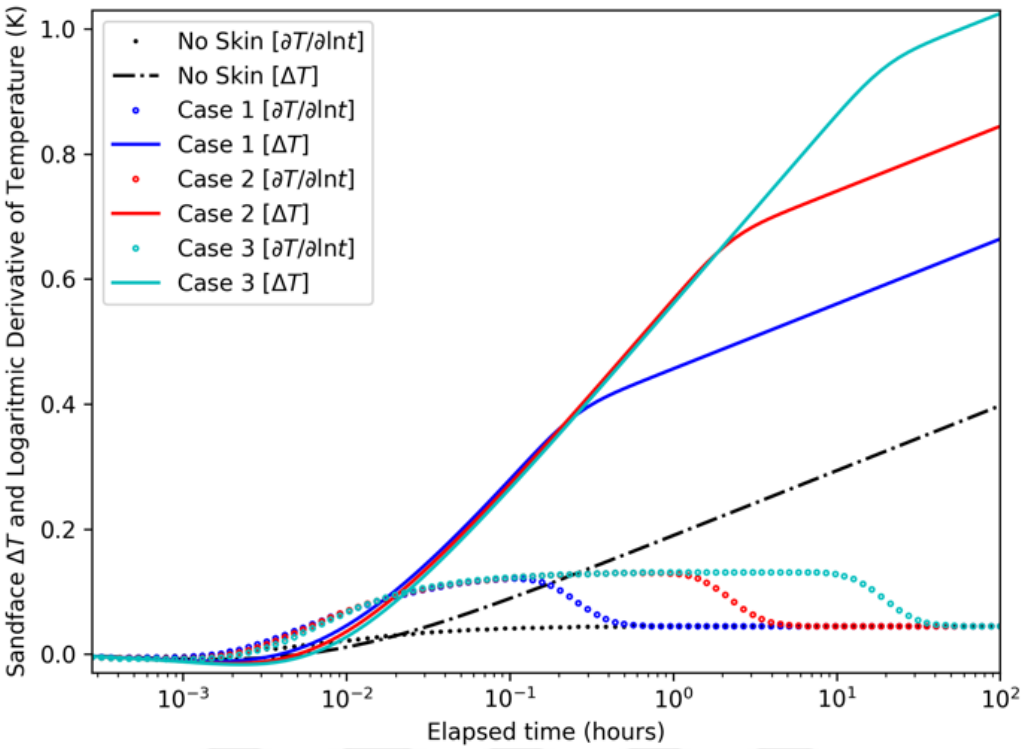

Figure 2.23: Effect of skin permeability with positive skin in the sandface on drawdown temperature.

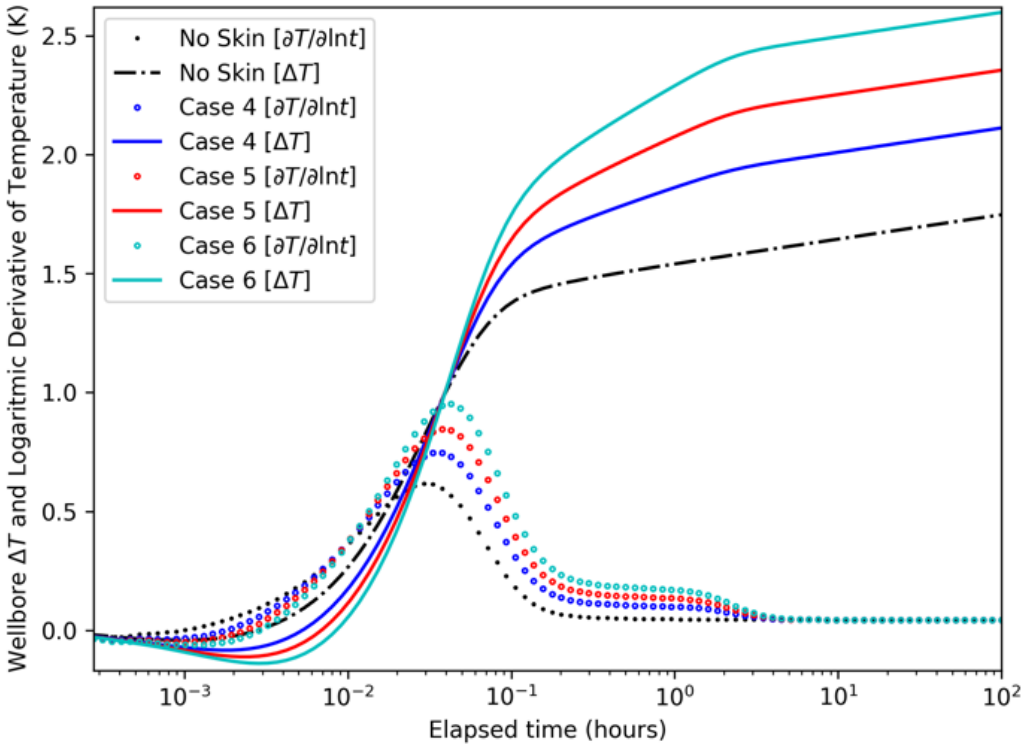

Figure 2.24: Effect of skin radius with positive skin in the wellbore on drawdown temperature.

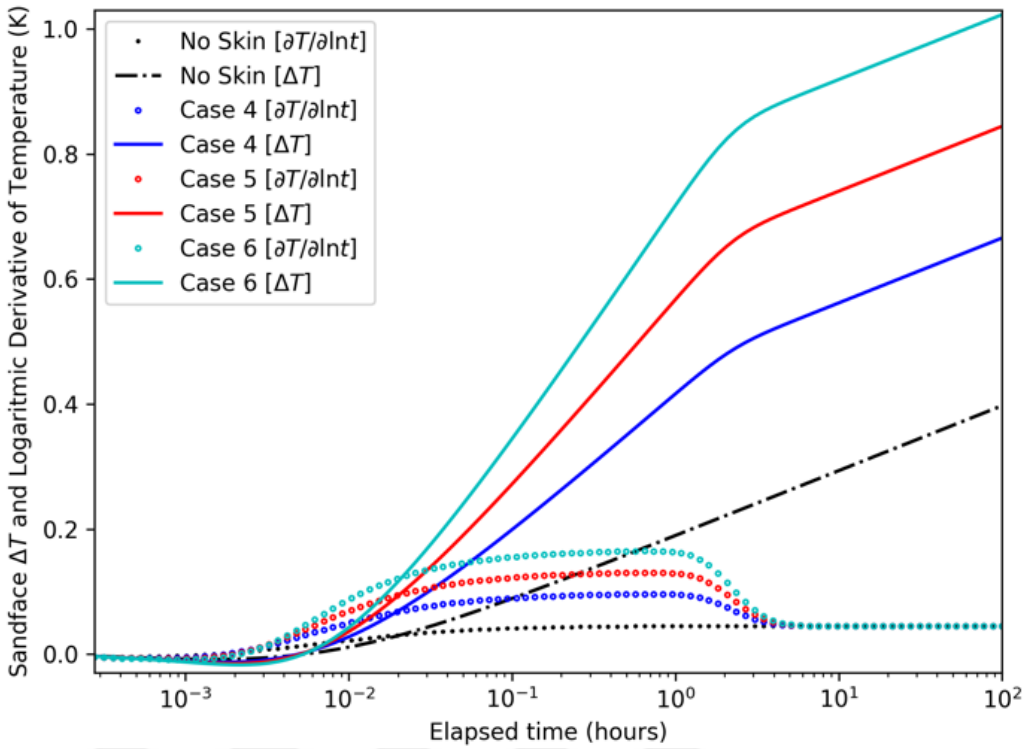

Figure 2.25: Effect of skin radius with positive skin in the sandface on drawdown temperature.

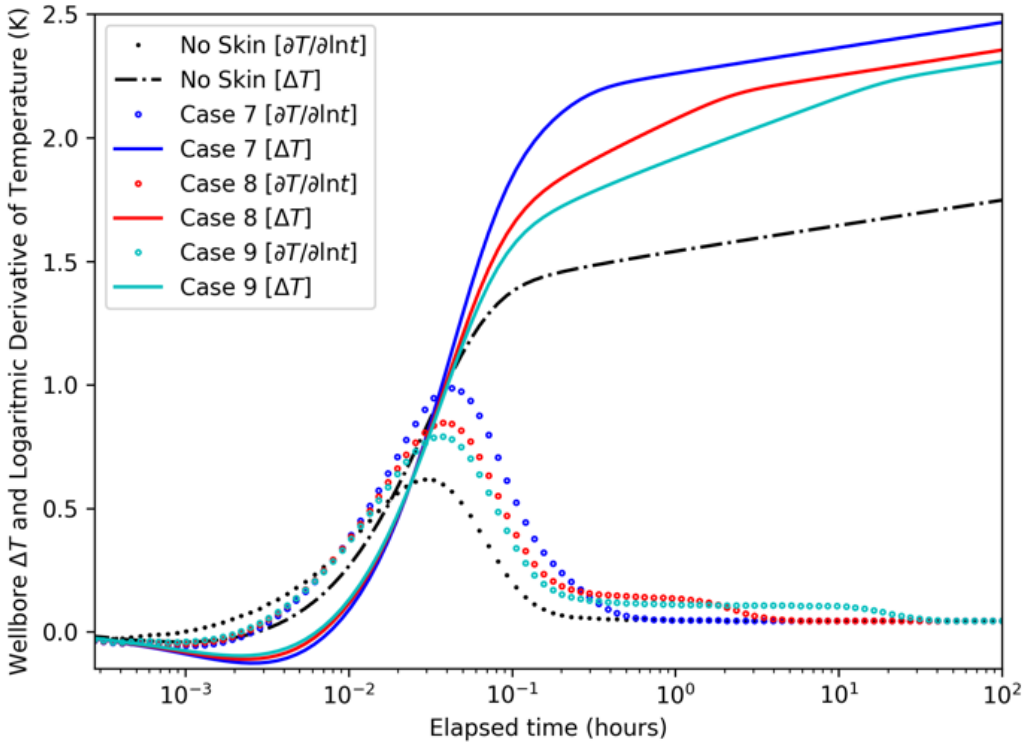

Figure 2.26: Effect of the positive skin value in the wellbore on drawdown temperature.

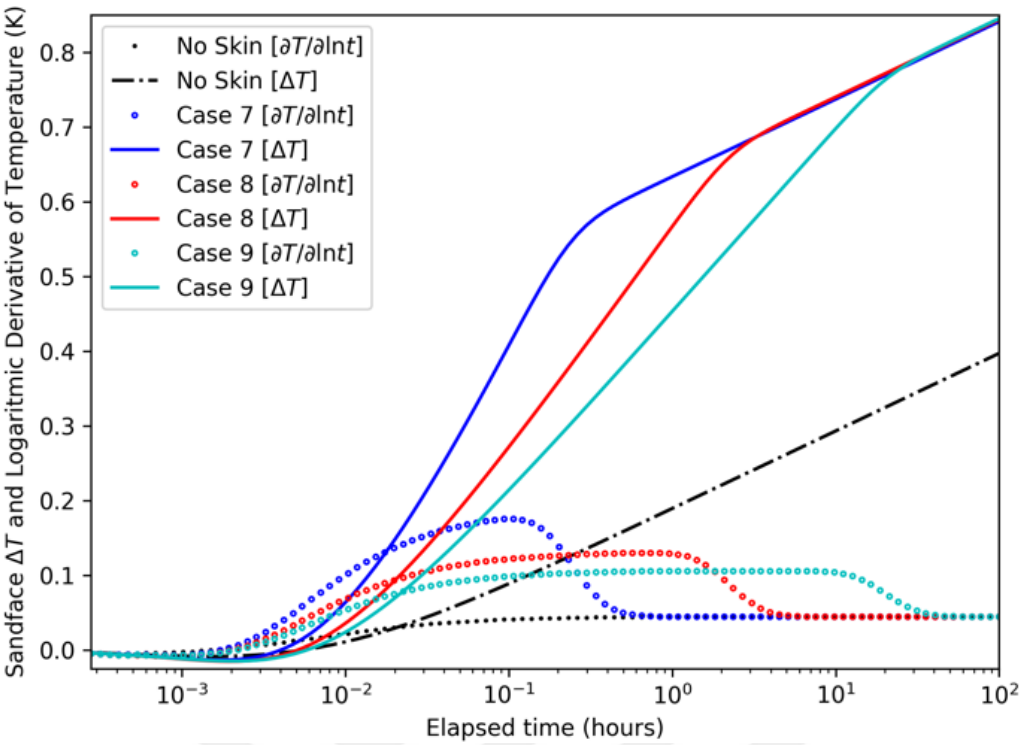

Figure 2.27: Effect of the positive skin value in the sandface on drawdown temperature.

Figures 2.24 and 2.25 clearly shows the resolution of temperature data. In all cases the skin is constant but the skin zone permeability and radius differ. Both parameters affect the temperature response as aforementioned before. Even if the skin is the same for all cases, the temperature response clearly deviates due to the changes in skin zone permeability and radius. Such a resolution is not possible for pressure since the pressure is a diffusive process; thus, near wellbore resolution is lost through averaging. Another observation worth to mention is the masking of skin zone parameters when the skin radius is small in the wellbore temperature response. In the case where skin radius is 0.5 m, the wellbore transition zone masks the first stabilization making it impossible to deconvolve any skin parameters, however, this r_s value should not be considered as a limit. We successfully generated cases where the first stabilization is observed when r_s is lower. The radius and flow rate are critical parameters that control the duration of the wellbore phenomena with regarding temperature.

In the case of negative skin (Cases 10-12), the observations are similar a seen in Figures 2.28 and 2.29. Since the permeability of the skin zone is higher than the permeability of the reservoir, the first stabilization is lower in magnitude than the second stabilization indicating an initial lower slope followed by a higher slope in

temperature difference. The wellbore response reaches to the initial temperature once the wellbore effects fade out. One particular observation, for the case with 4.5 m of skin radius, the reservoir response is not observed in the temperature signal. There seems to be a clear radius of investigation for temperature signal that is limited to near wellbore region, possibly larger than logs

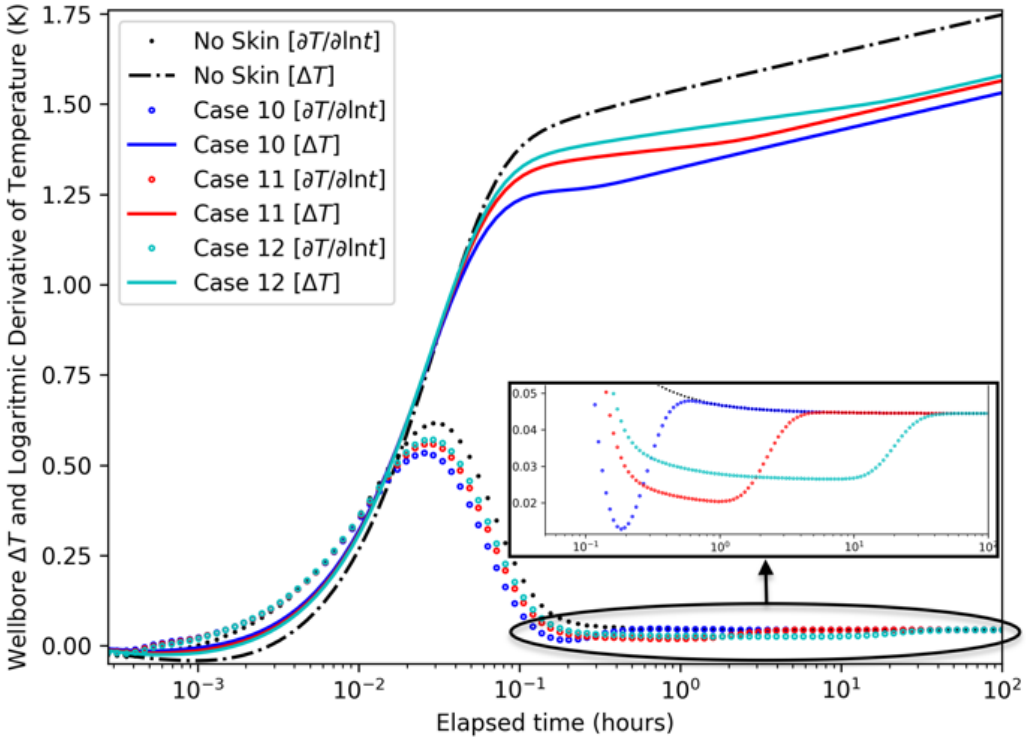

Figure 2.28: Effect of the negative skin value in the wellbore on drawdown temperatures.

Figures 2.30 through 2.33 show the temperature responses of the buildup period with respect to shut-in time in the same fashion for the positive and negative skin, respectively. Unlike sandface responses, the wellbore temperature response at the gauge location does not indicate reservoir properties during the buildup for the test durations considered. In all cases the temperature response is dominated by the wellbore phenomena.

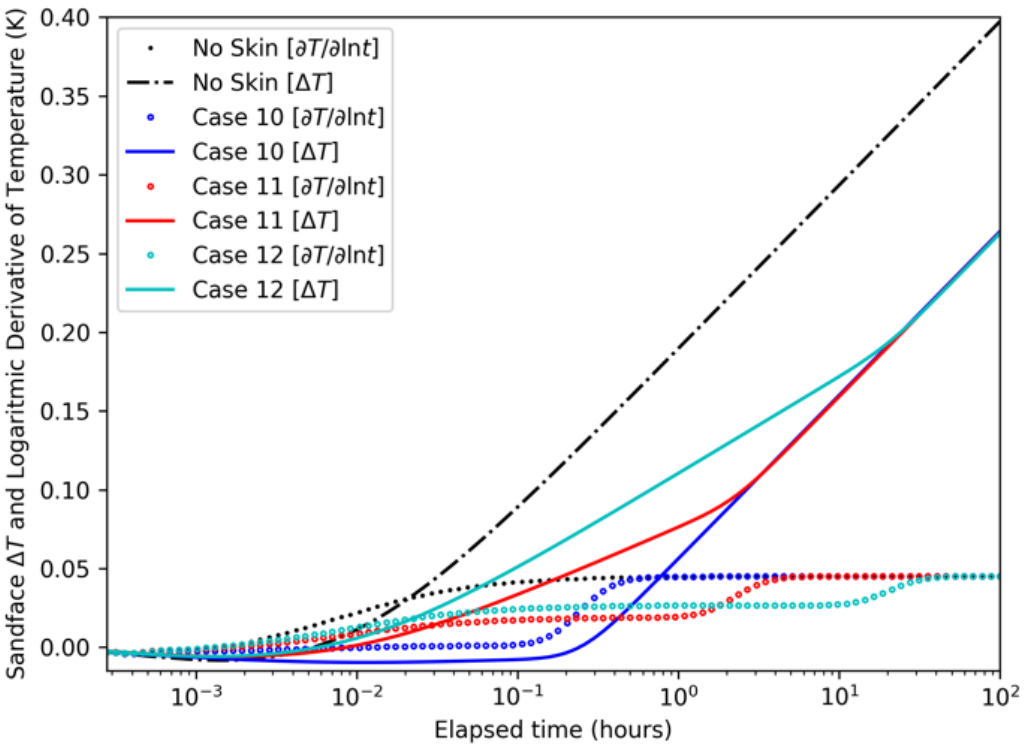

Figure 2.29: Effect of the negative skin value in the sandface on drawdown temperatures.

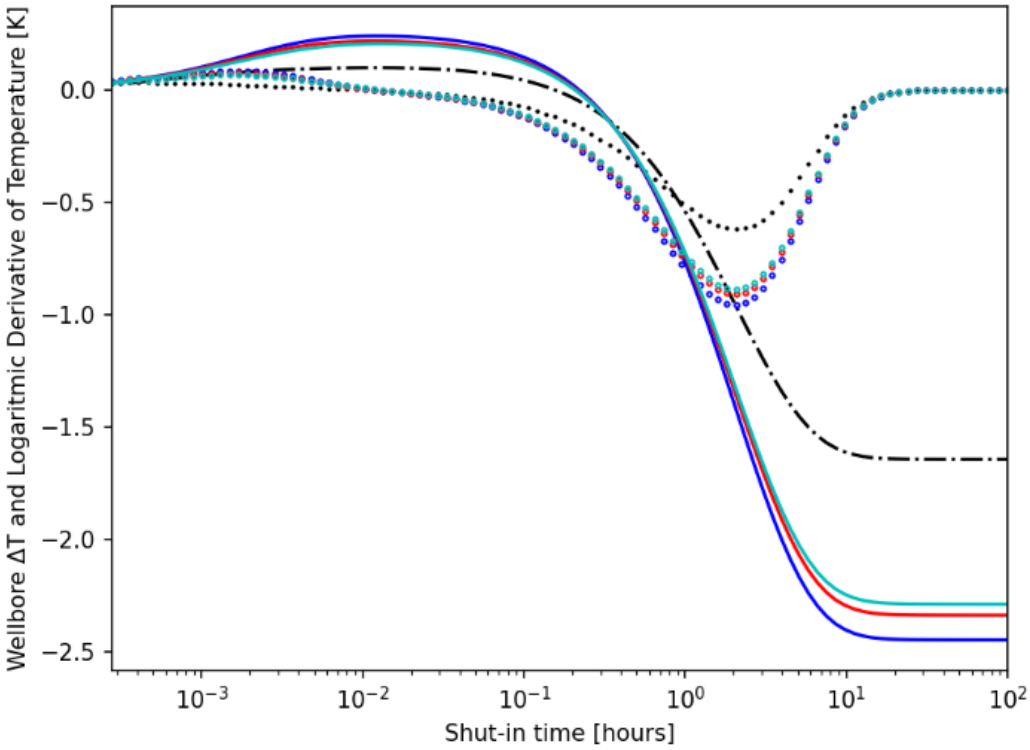

Figure 2.30: Effect of the positive skin value in the wellbore on buildup temperatures.

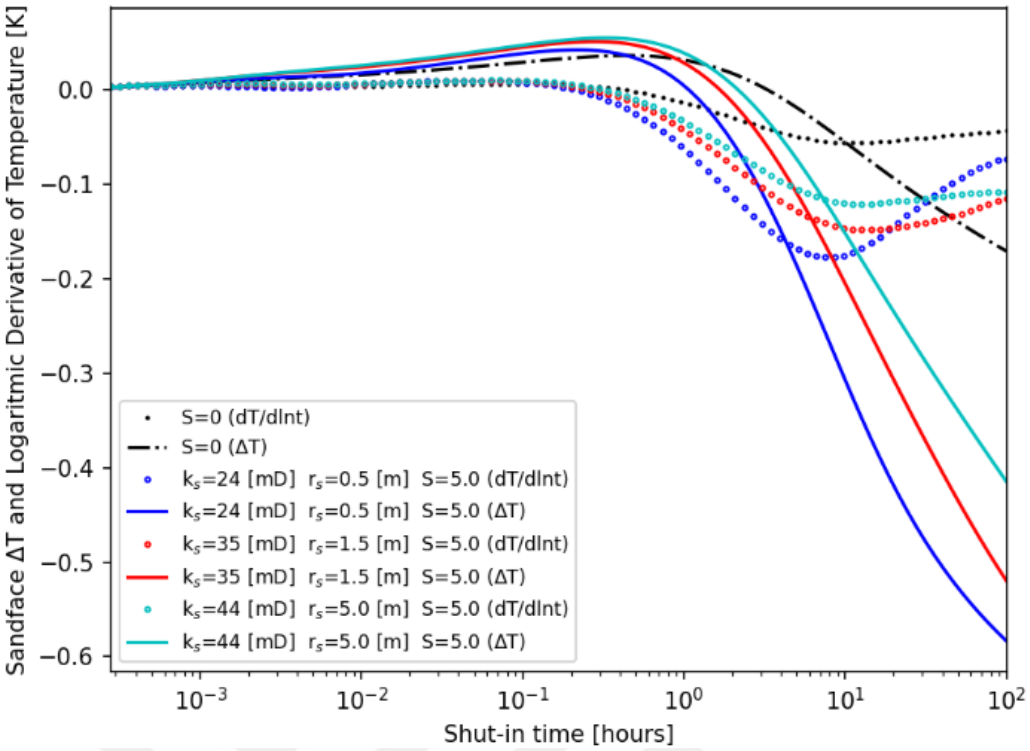

Figure 2.31: Effect of the positive skin value in the sandface on buildup temperatures.

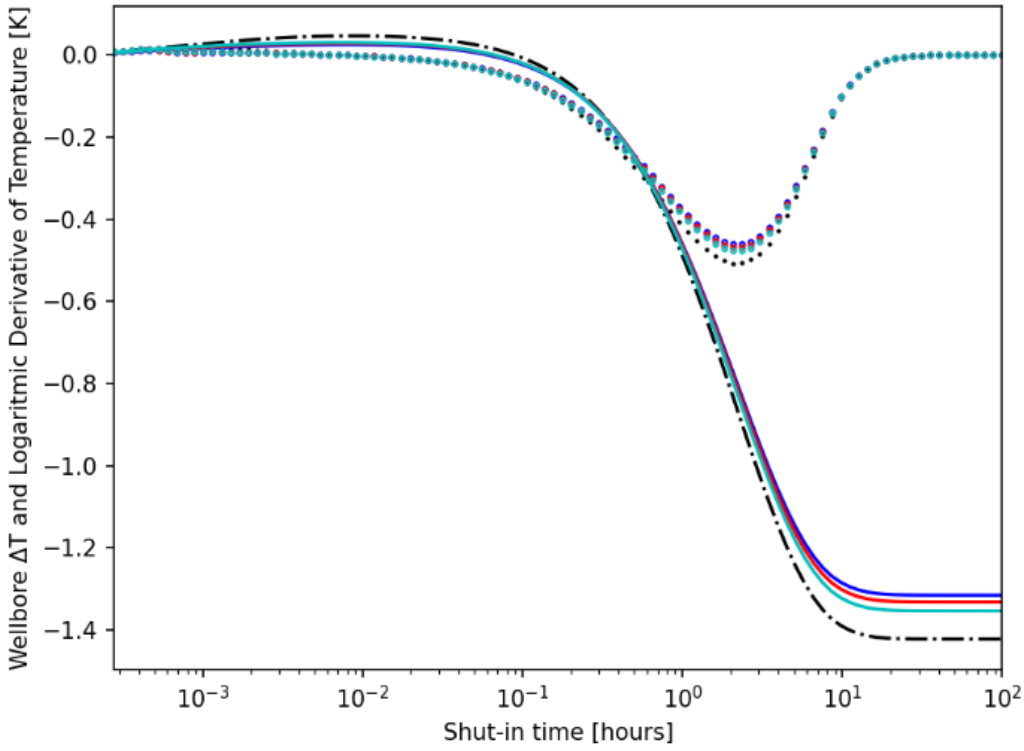

Figure 2.32: Effect of the negative skin value in the wellbore on buildup temperature.

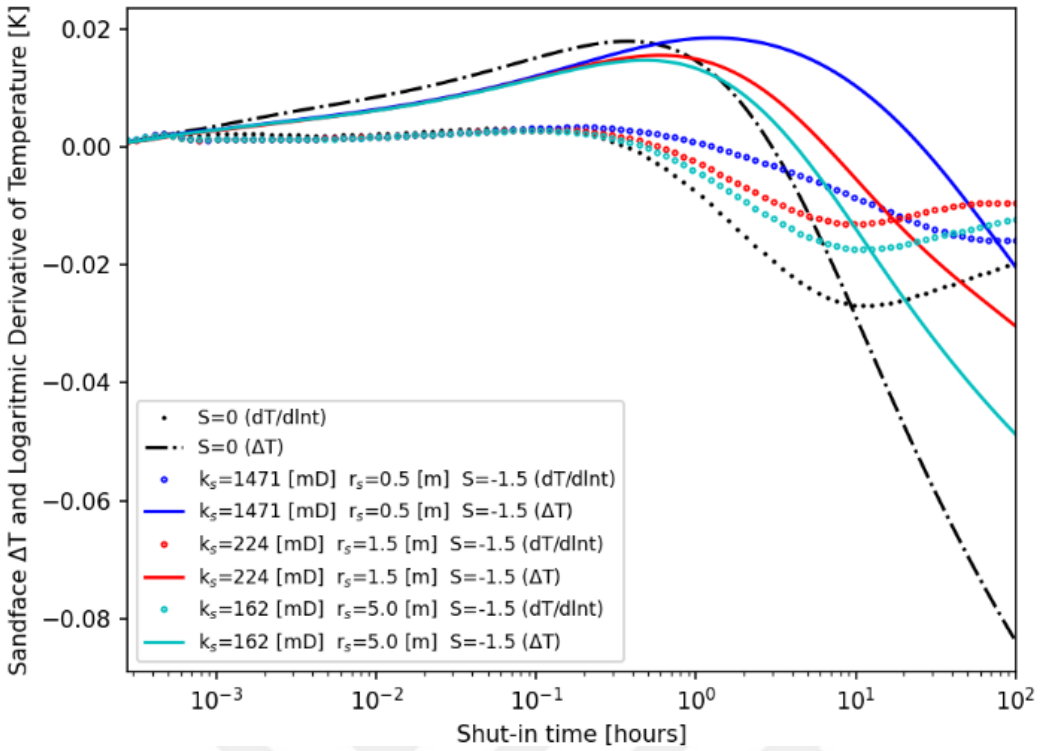

Figure 2.33: Effect of the negative skin value in the sandface on buildup temperature.

2.5 Parameter Estimation using Transient Drawdown Temperature Data

Based on analyses in the previous section the following conclusions are obtained regarding the information content of temperature transient measurements.

- The radius of investigation of temperature transients during buildup is lower than the pressure transients possibly larger than logs.
- The temperature transients during drawdown reflect contrast in reservoir properties in near wellbore region.
- Since the thermodynamic parameters ε_{JT}, β and c_p are related to each other through thermodynamic relations, any estimated thermodynamic parameter needs to be consistent with the thermodynamic parameters used as input.
- There seems to be a sensitivity to porosity, which is worth to investigate.
- The buildup temperature response reflects the wellbore phenomena in general.

Here, we emphasize to use the drawdown transient temperature data for estimation of parameters that cannot easily be acquired from conventional well test applications such as porosity and skin zone properties (skin radius and skin permeability). In addition,

unique to temperature measurements, the J-T coefficient is also included as a parameter.

We performed numerous regressions on estimating each parameter discussed throughout this study. Transient drawdown wellbore temperature data acquired not so far away from sandface (=> 90 m) provides almost exact estimates when each parameter is investigated alone. However, in real field applications, parameters are estimated as a set. Panini and Onur (2018) suggests using the permeability acquired from PTA as an initial guess in temperature regression. Similarly, reservoir permeability assumed as a known parameter from PTA, thus it is not included in the regression for synthetic cases discussed here. When J-T coefficient is included in the regression, it does not vary with pressure and temperature thus kept constant throughout each simulation run.

The nonlinear regression problem is solved using the Levenberg-Marquardt algorithm for minimizing an objective function given in Equation 2.7, in which n_t is the number of observed temperature data (T_{obs}) and the model vector m consists parameters as $\mathbf{m}=[\phi \quad \varepsilon_{JT} \quad k_s \quad r_s]$. The algorithm Lmfit (Newville et al., 2014) provides enhanced features to estimate the confidence intervals and automatically calculate correlations from the covariance matrix. Parameters can be constrained by an algebraic expression and/or with upper and/or lower bounds. The method of computing the Jacobian matrix for numerical estimations, the loss function to reduce the influence of outliers on the solution and the tolerance for termination are some of the most influential properties that can be used to improve regression results of Lmfit:

$$O(\boldsymbol{m}) = \sum_{i=1}^{n_t} [T_{obs} - T_w(\boldsymbol{m})]^2 \tag{2.7}$$

Panini and Onur (2018), discuss procedures to provide initial estimates to the nonlinear regression problem. Instead, we use the bounds for each parameter to be estimated because the minimum and maximum values that each parameter can possibly take is known. The lowest values of unknown parameters are used as initial guesses for regression. In addition, temperature responses are corrupted from numerical simulator developed to simulate observed data by using normally (Gaussian) distributed random errors with a standard deviation of 0.0025 K. It is important to note, as skin radius is

not kept constant during regression, in each run, geometrically spaced grid system for reservoir is reinitiated to represent the altered skin radius precisely.

The effect of gauge location is tested on the output of estimated parameters. The observed data (n_t = 300) are the simulated temperature responses at different gauge locations (z = 30 m, z = 50 m, z = 90 m) for a drawdown duration of 12 hours. For four different synthetic cases with skin effects are considered having the input data described so far unless otherwise stated in Table 2.4. Figures 2.34 and 2.35 present the drawdown temperature difference (ΔT) and the logarithmic derivative of drawdown temperature ($\partial T/\partial \ln t$) on a semi-log plot with respect to time from the corresponding gauge locations for Case 1 and 3, respectively. The regression results include estimates, confidence intervals and cross-correlation coefficients matrix are tabulated individually for each case in Tables 2.5 through 2.8**.**

Table 2.4: Parameters used in synthetic cases for nonlinear regression (NR).

NR Case	1	2	3	4
k (mD)	50	300	30	100
s	5	10	-2	-1
ϕ	0.10	0.22	0.07	0.30
k_s (mD)	17.6	29.7	228.3	264.1
r_s (m)	1.5	0.3	1.0	0.5
q_{sc} (sm^3/D)	500	1000	500	1000

In general, the estimated values of the J-T coefficient and skin properties such as the radius and the permeability of skin region are in good agreement with the true input values. As the gauge is placed further away from sandface, the confidence intervals keep increasing in general, meaning the information losing its reliance. As seen in Table 2.4, the first two cases investigate the positive skin effects whereas the remaining two cases explore the negative skin effects. As the first case has the largest radius of skin in all cases given, intermediate and late time slopes are easy to be identified as seen in Figure 2.34. Therefore, estimated values of the parameters obtained by the regression in Table 2.5 are good and the confidence intervals for all parameters also small, indicating all parameters are well determined by the data. Since the second case has a higher skin value with a lower radius of skin when compared with the first case, it is harder to distinguish the slopes of intermediate and late times (although not shown here) resulting in much higher cross-correlation coefficients for all parameters in Table 2.6 due to the correlation between each other. Having cross

correlation coefficients above 0.9 or below -0.9 means that parameters cannot be estimated independently. Therefore, some attempts such as reducing the number of parameters to be investigated is required for lowering these reported correlations between unknown parameters in the regression. For instance, from the conventional well testing applications, in addition to the permeability, skin value can be acquired and provided to the regression problem as a known parameter to improve the results. Apart from the high correlation coefficients, the estimates are still in good agreement with the input values except for porosity.

The last two cases investigate the parameters in the presence of negative skin effects. As seen in Figure 2.35, the third case indicating two distinct slopes for the intermediate and late times has a higher radius of skin when compared with the forth case. Although both slopes are well distinguished, the cross-correlation coefficients between the J-T coefficient and skin are still reported quite high in Table 2.7. Thus, these parameters cannot be estimated independently. It is clear that the J-T coefficient is the most influential parameter that controls the temperature changes, particularly in the late times of drawdown. Therefore, many parameters are expected to be highly correlated with it. However, in the presence of high cross correlation coefficients such as above 0.9 or below -0.9, it is recommended to decrease the number of parameters to be estimated by assuming that both permeability and skin values are determined correctly from PTA and provided to the regression problem. While the intermediate times for the forth case are mostly not seen on the wellbore temperature responses, the reported estimates in Table 2.8 are still good, and the cross-correlation coefficients are lower when compared with the third case that also has negative skin effects.

Although there is a sensitivity to porosity, for all practical purposes, it would be extremely difficult if not impossible to find porosity since the sensitivity is within the range of uncertainty of several other parameters assumed. The confidence levels of porosity are high even in a synthetic case.

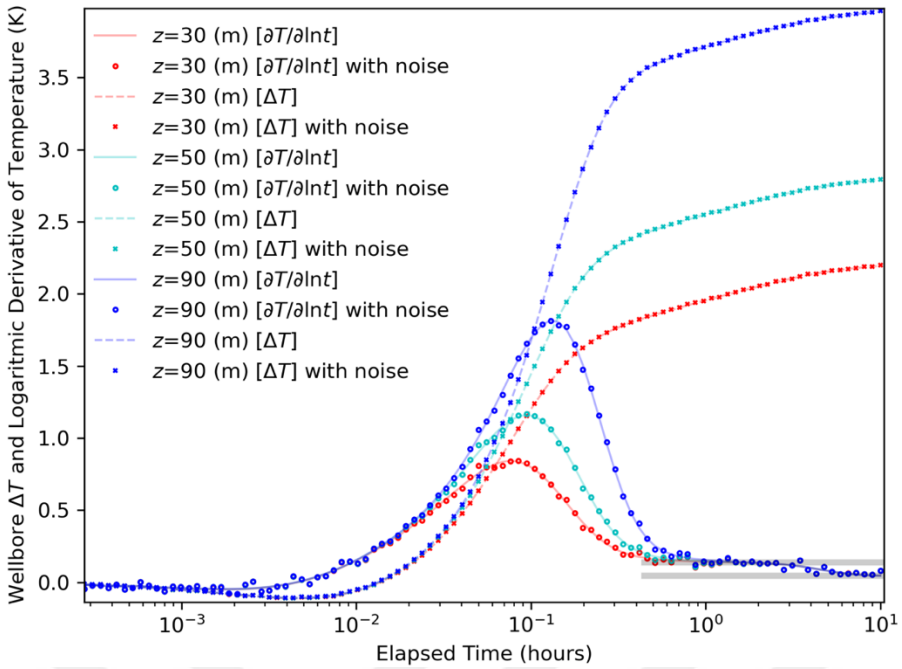

Figure 2.34: Effect of gauge location in the wellbore on drawdown temperature with noise; NR - Case 1.

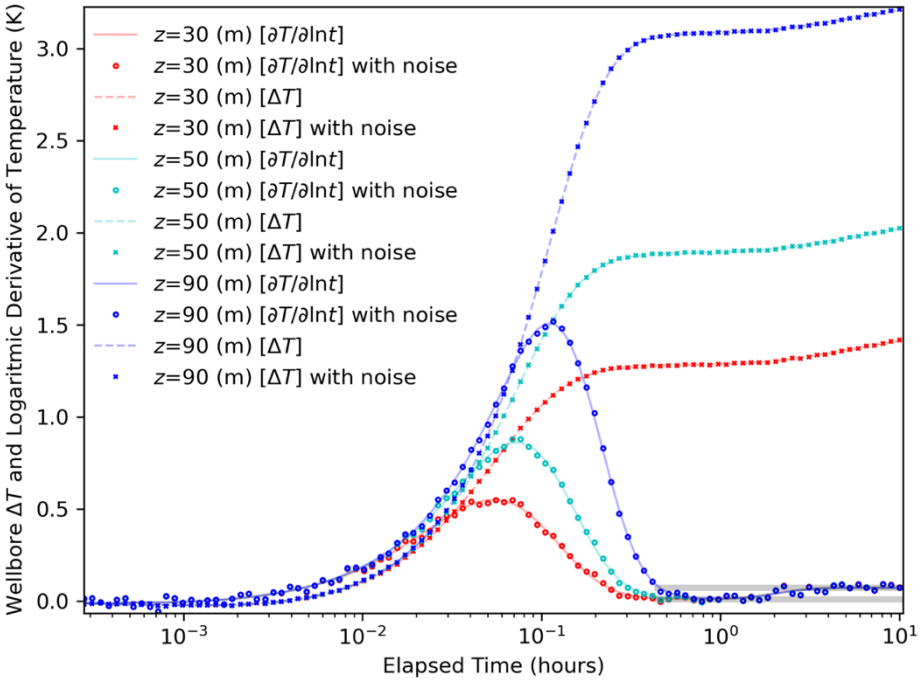

Figure 2.35: Effect of gauge location in the wellbore on drawdown temperatures with noise; NR - Case 3.

Table 2.5: Regression results of parameters; NR Case 1.

	z = 30 m				z = 50 m				z = 90 m			
	Estimated		Conf. interval (%)		Estimated		Conf. interval (%)		Estimated		Conf. interval (%)	
ϕ	0.098		2.99		0.099		3.18		0.099		3.61	
ε_{JT} (K/Pa)	-2.0262×10^{-7}		0.02		-2.0261×10^{-7}		0.02		-2.0258×10^{-7}		0.02	
r_s (m)	1.494		0.55		1.492		0.58		1.490		0.63	
k_s (mD)	17.6		0.13		17.561		0.14		17.561		0.16	
s calculated	4.99				4.99				4.99			
		ϕ	ε_{JT}	r_s	k_s		ϕ	ε_{JT}	r_s	k_s		ϕ	ε_{JT}	r_s	k_s
Cross correlation coefficients	ϕ	1	0.466	-0.711	-0.937	ϕ	1	0.540	-0.707	-0.942	ϕ	1	0.636	-0.721	-0.950
	ε_{JT}	0.466	1	-0.556	-0.635	ε_{JT}	0.540	1	-0.617	-0.686	ε_{JT}	0.636	1	-0.686	-0.749
	r_s	-0.711	-0.556	1	0.825	r_s	-0.707	-0.617	1	0.827	r_s	-0.721	-0.686	1	0.839
	k_s	-0.937	-0.635	0.825	1	k_s	-0.942	-0.686	0.827	1	k_s	-0.950	-0.749	0.839	1

Table 2.6: Regression results of parameters; NR Case 2.

	z = 30 m				z = 50 m				z = 90 m			
	Estimated		Conf. interval (%)		Estimated		Conf. interval (%)		Estimated		Conf. interval (%)	
ϕ	0.245		15.07		0.227		18.57		0.142		32.62	
ε_{JT} (K/Pa)	-2.0265×10^{-7}		0.03		-2.0263×10^{-7}		0.03		-2.0271×10^{-7}		0.05	
r_s (m)	0.297		1.57		0.299		1.82		0.311		2.16	
k_s (mD)	29.5		0.96		29.6		1.12		30.3		1.39	
s calculated	9.98				10				10.07			
		ϕ	ε_{JT}	r_s	k_s		ϕ	ε_{JT}	r_s	k_s		ϕ	ε_{JT}	r_s	k_s
Cross correlation coefficients	ϕ	1	<0.1	-0.987	-0.993	ϕ	1	0.375	-0.987	-0.993	ϕ	1	0.894	-0.986	-0.994
	ε_{JT}	<0.1	1	-0.137	-0.154	ε_{JT}	0.375	1	-0.412	-0.425	ε_{JT}	0.894	1	-0.902	-0.91
	r_s	-0.987	-0.137	1	0.998	r_s	-0.987	-0.412	1	0.998	r_s	-0.986	-0.902	1	0.998
	k_s	-0.993	-0.154	0.998	1	k_s	-0.993	-0.425	0.998	1	k_s	-0.994	-0.91	0.998	1

Table 2.7: Regression results of parameters; NR Case 3.

		z = 30 m				z = 50 m				z = 90 m			
		Estimated		Conf. interval (%)		Estimated		Conf. interval (%)		Estimated		Conf. interval (%)	
ϕ		0.073		8.63		0.073		7.44		0.071		7.37	
ε_{JT} (K/Pa)		-2.0244×10^{-7}		0.21		-2.0246×10^{-7}		0.17		-2.0257×10^{-7}		0.16	
r_s (m)		0.995		0.47		0.995		0.49		0.995		0.53	
k_s (mD)		226.3		3.59		226.6		3.15		229.6		3.30	
s calculated		-1.99				-2				-1.99			
		ϕ	ε_{JT}	r_s	k_s	ϕ	ε_{JT}	r_s	k_s	ϕ	ε_{JT}	r_s	k_s
Cross correlation coefficients	ϕ	1	0.963	-0.151	-0.980	1	0.956	-0.125	-0.973	1	0.959	-0.101	-0.968
	ε_{JT}	0.963	1	<0.1	-0.969	0.956	1	<0.1	-0.962	0.959	1	<0.1	-0.962
	r_s	-0.151	<0.1	1	<0.1	-0.125	<0.1	1	<0.1	-0.101	0.1	1	-0.104
	k_s	-0.98	-0.969	<0.1	1	-0.973	-0.962	<0.1	1	-0.968	-0.962	-0.104	1

Table 2.8: Regression results of parameters; NR Case 4.

		z = 30 m				z = 50 m				z = 90 m			
		Estimated		Conf. interval (%)		Estimated		Conf. interval (%)		Estimated		Conf. interval (%)	
ϕ		0.365		13.71		0.375		12.06		0.348		19.82	
ε_{JT} (K/Pa)		-2.0276×10^{-7}		0.06		-2.0272×10^{-7}		0.05		-2.0268×10^{-7}		0.05	
r_s (m)		0.502		1.16		0.502		1.12		0.504		1.28	
k_s (mD)		244.2		5.50		241.2		4.93		248.4		8.23	
s calculated		-0.95				-0.94				-0.97			
		ϕ	ε_{JT}	r_s	k_s	ϕ	ε_{JT}	r_s	k_s	ϕ	ε_{JT}	r_s	k_s
Cross correlation coefficients	ϕ	1	<0.1	-0.549	-0.995	1	0.122	-0.190	-0.992	1	0.507	-0.350	-0.996
	ε_{JT}	<0.1	1	0.181	<0.1	0.122	1	0.218	-0.190	0.507	1	<0.1	-0.544
	r_s	-0.549	0.181	1	0.478	-0.190	0.218	1	<0.1	-0.350	<0.1	1	0.280
	k_s	-0.995	<0.1	0.478	1	-0.992	-0.190	<0.1	1	-0.996	-0.544	0.28	1

2.6 History Matching Field Data

A nonlinear regression was performed for history matching the field temperature and pressure data, which were obtained from a DST well testing operation that involved a single production period of 20.178 hours with a stabilized surface oil flow rate of 314 sm^3/D followed by a buildup period of 48 hours. A vertical well (fully penetrated) of length 4000 m having a radius of 0.15 m was tested. The temperature and pressure measurements were recorded at the gauges placed 60.9 m above the top of the producing horizon. A pressure control valve at the bottomhole some distance above the gauge operates the flow to the surface. Similarly, in the numerical simulation, the well is shut-in two gridblocks above the gauge location during buildup. Table 2.9 summaries the model and fluid properties used in the regression. The reference pressure (77.863 MPa) and temperature (428.96 K) measured at the gauge location were used to calculate the fluid properties that were obtained from PVT correlations based on the surface measurements available during the DST operation i.e., API (45°), GOR (550 ft^3/bbl), specific gas gravity (0.83). In addition to FVF and porosity given in Equation 2.5 and FVF, the oil density is also calculated similarly as a function of pressure and temperature from Equation 2.8. The remaining oil physical and thermal properties listed in Table 2.9 are constant throughout the numerical simulation. Solid matrix thermal properties are taken same values listed in Table 2.1 and also treated as constant. The bubble point pressure was lower than the pressures recorded at the wellhead throughout the entire flow period in which the assumption of single phase flow of oil along the wellbore remained valid. A local equilibrium between wellbore and the surrounding rock is assumed prior to fluid flow, thus, the initial wellbore temperatures were identical to the surrounding rock temperatures calculated by the geothermal gradient (0.03 K/m), increasing from 298 K at the top of the well to 430.22 K at the bottom of the well that is adjacent to the first reservoir gridblock. Since the stabilization of production rate did not occur before 1.4 hours of fluid production at surface, the transient behavior of both temperature and pressure measured in the wellbore some distance above the sandface need to be represented by a transient-thermal coupled simulator.

$$\rho = \rho_{ref}\left(e^{[c(p-p_{ref})-\beta(T-T_{ref})]}\right) \tag{2.8}$$

The simulation model constructed here to represent the system described above is only able to response for an infinite acting composite reservoir system. The reservoir is represented with 100 gridblocks geometrically spaced (as default) whereas 98 gridblocks used in the wellbore with uniform length of 40.6 m which is chosen to place the gauge exactly on reported depth and also represent the entire wellbore to the surface. The bottommost gridblock in the wellbore and the reservoir gridblock that is adjacent to it have always the same thickness and the well radius for the coupling purposes. Outer diameter of the reservoir is taken very large as in the previous models discussed (r_e=25,000 m) to model infinite acting radial flow.

Table 2.9: Parameters used in history matching.

Model properties		Oil properties	
r_w (m)	0.15	ρ (kg/m^3)	686
h_{res} (m)	19.2	c_p (J/kg.K)	2050
z_w (m)	4000	μ (Pa.s)	0.6×10^{-3}
q_{sc} (sm^3/D)	1975	λ (J/m.s.K)	0.40
Geothermal grad. (K/m)	0.03	β (K^{-1})	4.65×10^{-4}
p_{in} (MPa) [z = 60.9 m]	77.863	c (Pa^{-1})	8.05×10^{-10}
T_{in} (K) [z = 60.9 m]	428.96	B (m^3/sm^3)	1.27

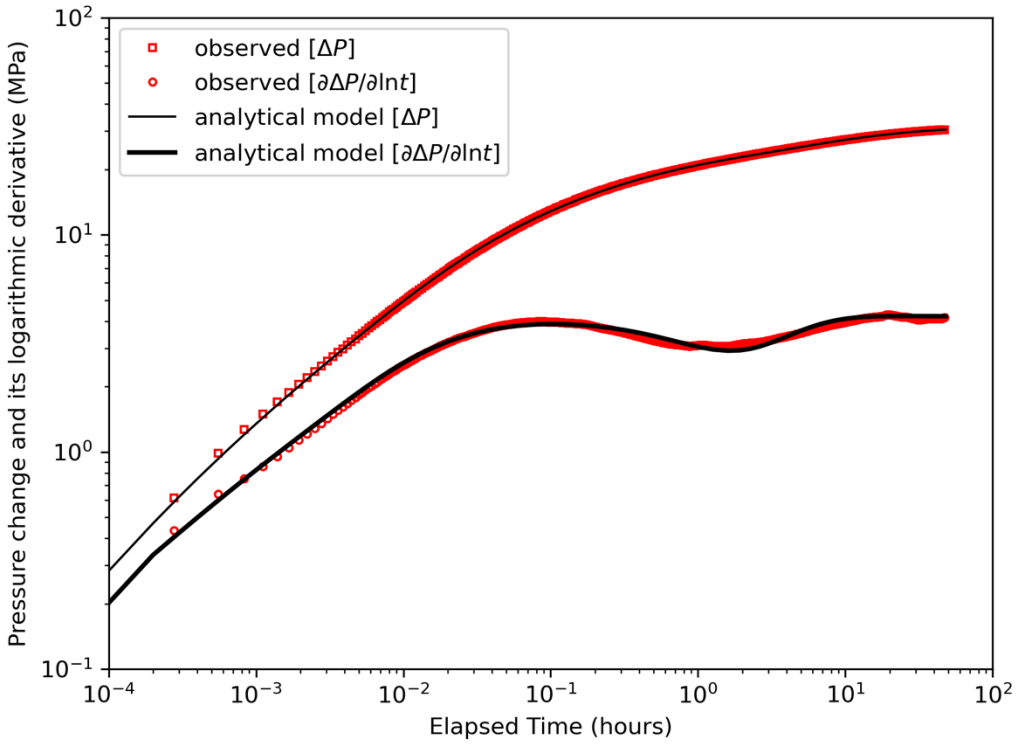

Figure 2.36: Buildup pressure derivative of field data.

Figure 2.36 shows a log-log plot of the pressure change and its derivative versus time from the buildup period following the constant-rate drawdown. The analysis is conducted using Saphir module (Kappa, 2020). Clearly, the buildup pressure-derivative data display an early time ½ slope reflecting an infinite conductivity fractured system followed by an intermediate time derivative, which suggests a double porosity behavior. The parameters estimated from the buildup pressure analysis are tabulated in Table 2.10. The high value of omega (in the order of 0.1) implies a multiple layer system rather than a naturally-fractured system (Bourdet, 2002).

Table 2.10: Buildup PTA results of field data from the analytical model.

Wellbore storage type	Constant
Well type	Vertical fractured uniform flux
Reservoir type	Dual porosity PSS
Initial reservoir pressure (MPa)	79.353
k (mD)	2.785
C (m^3/MPa)	3.0943×10^{-3}
Skin	0
x_f (m)	4.69
Omega	0.455372
Lambda	4.03251×10^{-5}

The drawdown temperature difference (ΔT) and logarithmic derivative of temperature ($\partial T/\partial \ln t$) recorded at the gauge location are shown in Figure 2.37. The derivative exhibits a wellbore transition period followed by the first and second stabilizations (highlighted as gray in Figure 2.37). The magnitude of the first stabilization, which is lower than the second stabilization indicates a negative skin. As stated earlier in the sensitivity cases, the first stabilization represents the skin region properties (such as skin radius and skin permeability) whereas the second stabilization reflects reservoir properties. Similarly, the temperature difference exhibits two distinct slopes. This is consistent with the buildup analysis in which we observe a fractured well having a small half-length in a sense that, when analyzed with a non-fractured model, the buildup gives a negative skin.

$$O(\boldsymbol{m}) = \sum_{i=1}^{n_p}\left[\left(\frac{T_{obs} - T_w(\boldsymbol{m})}{w_T}\right)^2\right] + \sum_{i=1}^{n_t}\left[\left(\frac{p_{obs} - p_w(\boldsymbol{m})}{w_p}\right)^2\right] \tag{2.9}$$

During history matching, the objective is to estimate k, r_{wb}, ε_{JT}, r_s and k_s by regressing the drawdown pressure and temperature data together. While regressing on the field

data from such a typical DST operation, in which a packer is set to isolate the tested producing horizon restricting the flow into the tubing, an effective well radius is required to be estimated for a descriptive temperature match. In the nonlinear regression, the objective function to be minimized is given in Equation 2.9 where n_p and n_t are the numbers of temperature and pressure observed data, respectively. w_T (1.235) and w_p (11.82×10^6) represent the weights used for the temperature and pressure, respectively, and are chosen such that both responses have a similar influence on regression. The results of the nonlinear regression for the unknown model vector m consisting of the parameters as $\mathbf{m} = [k\ \ r_{wb}\ \ \varepsilon_{JT}\ \ r_s\ \ k_s]$ include the estimates, confidence intervals and cross correlation coefficients listed in Table 2.11. The unknown parameters, bounded with the min and max values that they could possibly have, are also given in Table 2.11 and their lowest values are used as the initial guess. We also observe that the drawdown temperature data shows a significant sensitivity to the gauge location and geothermal gradient while not causing any major changes in its pressure response. One may also investigate these parameters through regression if there exists any uncertainty.

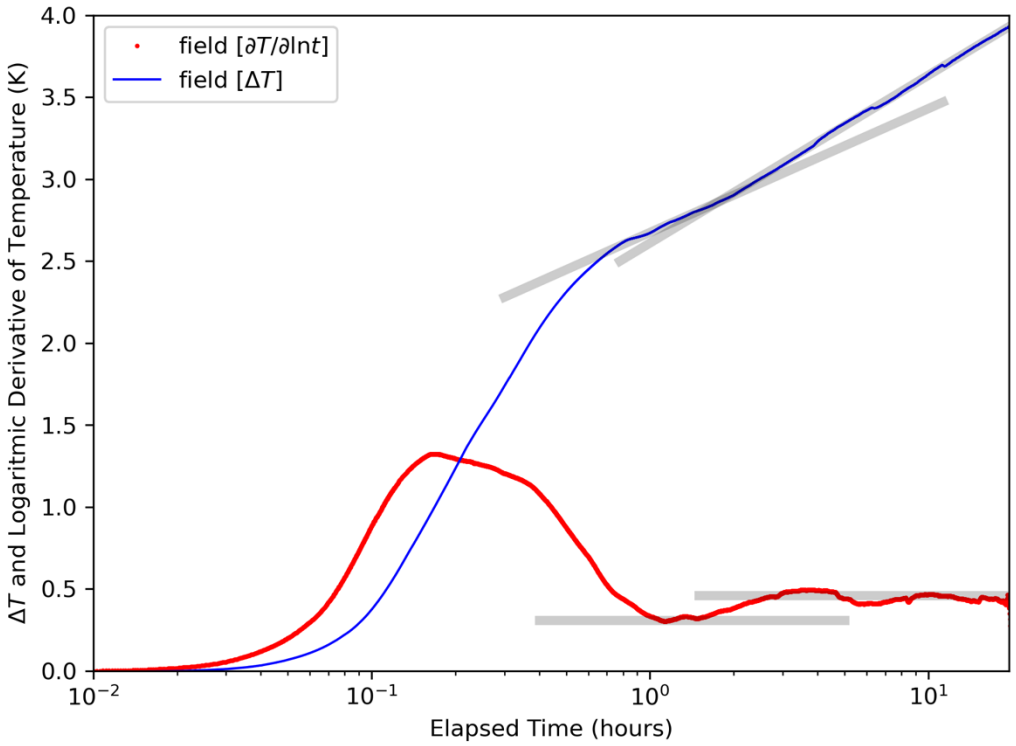

Figure 2.37: Drawdown temperatures of field data.

The skin value is calculated using the Hawkins formula (1956) with the estimates of skin permeability and radius of skin values during regression unlike the synthetic cases discussed in the parameter estimation section where the skin permeability is the calculated value. Similarly, the confidence interval of skin is reported in the results although the parameter is not regressed. All estimates seem to have acceptable values of the confidence interval. Skin is calculated as -0.6 from the estimate of skin permeability and skin radius. We also observe that the drawdown temperature data shows a significant sensitivity to the gauge location and geothermal gradient while not causing any major changes in its pressure response. One may also investigate these parameters through regression if there exists any uncertainty.

Table 2.11: Regression results of parameters; History matching case.

	Estimated	Conf. interval (%)	Bounds
k (mD)	4.97	1.34	[1 to 10,000]
ε_{JT} (K/Pa)	-1.87×10^{-7}	2.16	$[-1\times10^{-6}$ to $-1\times10^{-8}]$
r_s (m)	0.5244	6.62	[0.20 to 4]
k_s (mD)	9.52	2.19	[1 to 10,000]
r_{wb} (m)	0.1076	0.43	[0.05 to 0.15]

Cross correlation coefficients

	k	ε_{JT}	r_s	k_s	r_{wb}
k	1	0.343	-0.636	<0.1	<0.1
ε_{JT}	0.343	1	-0.701	-0.787	-0.480
r_s	-0.636	-0.701	1	0.168	0.457
k_s	<0.1	-0.787	0.168	1	0.181
r_{wb}	<0.1	-0.480	0.457	0.181	1

When the permeability values are compared between the regressed value (~5 mD) from the drawdown temperature data and the calculated value (~3 mD) from the buildup PTA results, there exists a difference although the temperature match of field and regressed drawdown temperature difference (ΔT) and logarithmic derivative of temperature ($\partial T/\partial \ln t$) data are in good agreement as seen in Figure 2.38. The main reason of the difference observed in estimated permeabilities relies on the nature of the processes. After the well is shut in, the fluid in the wellbore generally reaches a quiescent state in which bottomhole pressure increases are smooth and easy to measure by gauges. On the other hand, the drawdown data are mostly noisy at gauge level due to the variations in flow rate measurements at the wellhead. Therefore, attempts of analyzing the drawdown pressure transients fail due to the noise which corrupts the most of recorded pressure data and causes extreme difficulties for the analyst to distinguish the regions of interest. Figure 2.45 shows the drawdown pressure responses

from the field and regressed data. It is obvious that the flow rate variations at wellhead are significant when a constant specified surface flow rate is considered in the numerical simulations of regression. All in all, the buildup permeability and permeability obtained from drawdown pressure and temperature agree well (see also Figures 2.40 and 2.41).

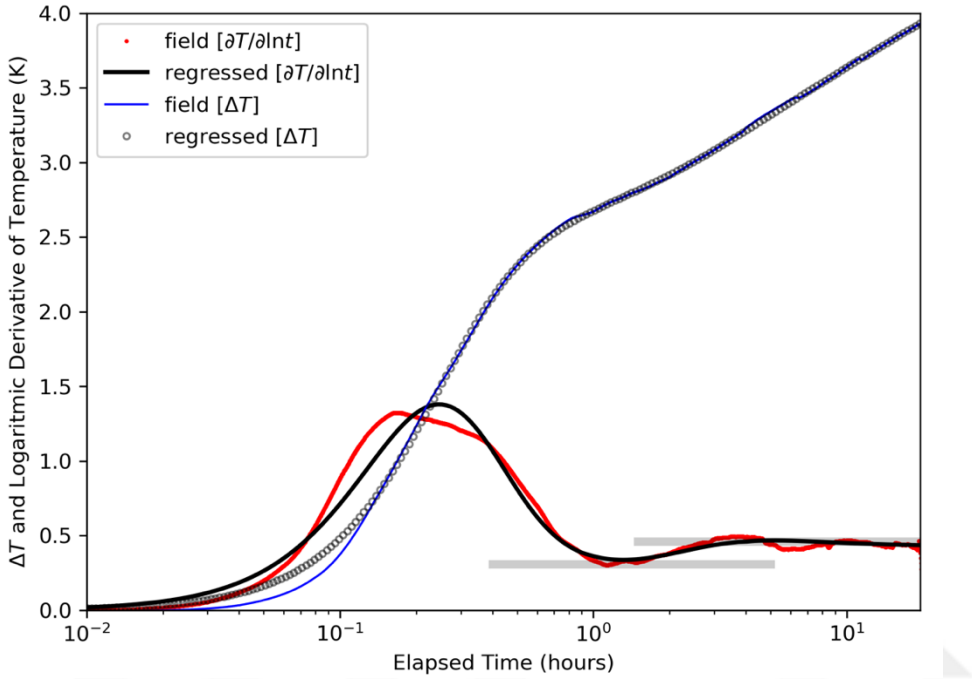

Figure 2.38: Comparison of temperature for the drawdown period; HR case.

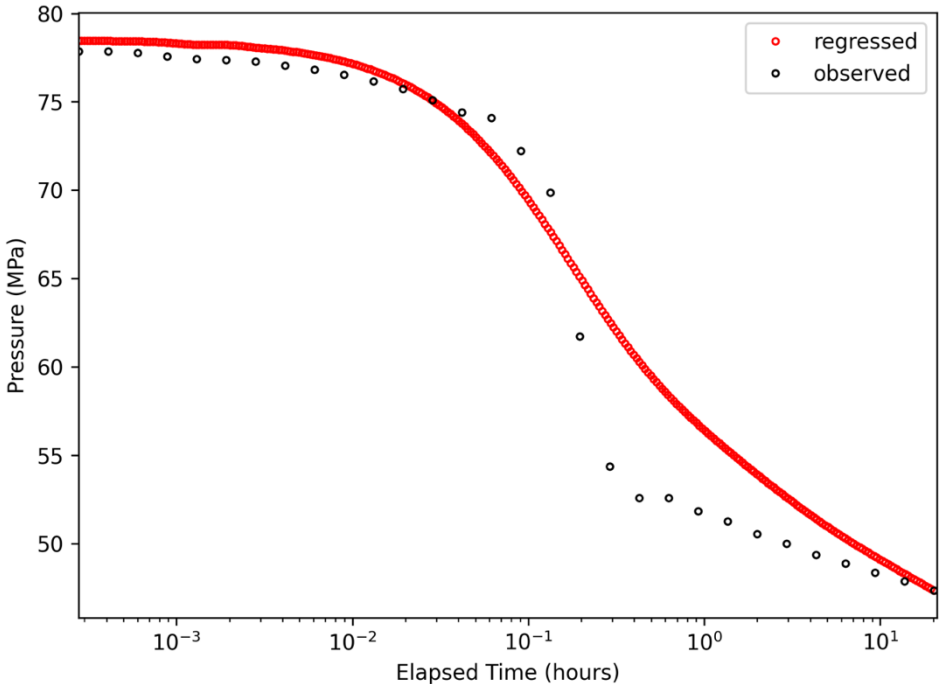

Figure 2.39: Comparison of pressure for the drawdown period; HR case.

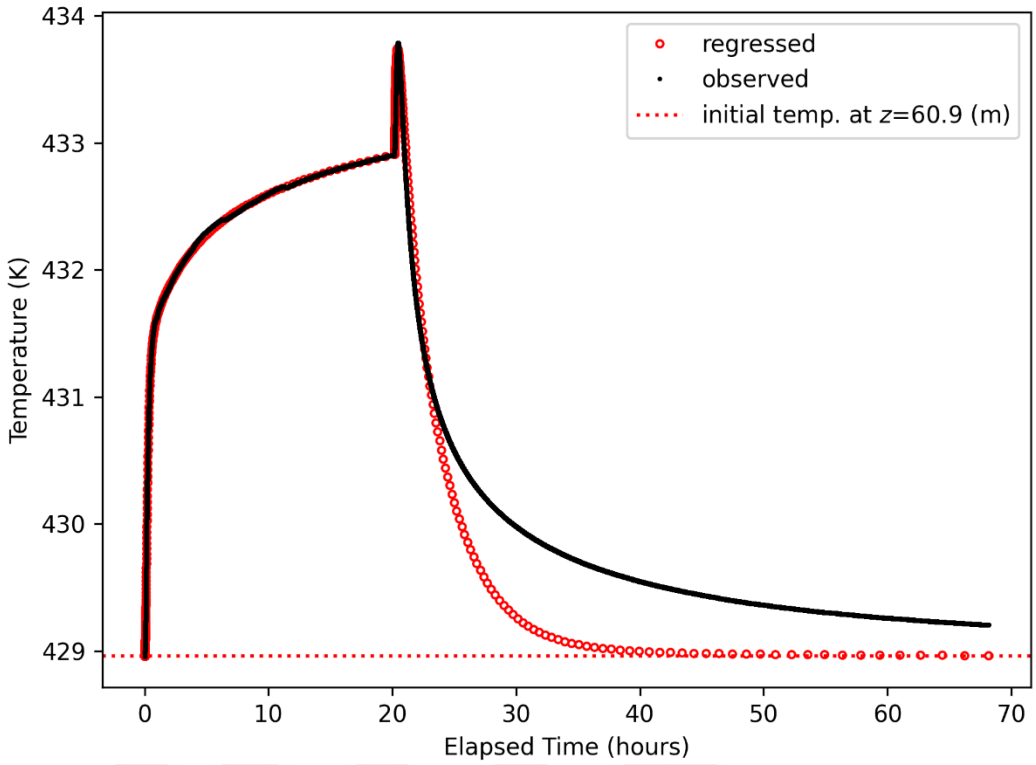

Figure 2.40: Comparison of temperature for entire flow history; HR case.

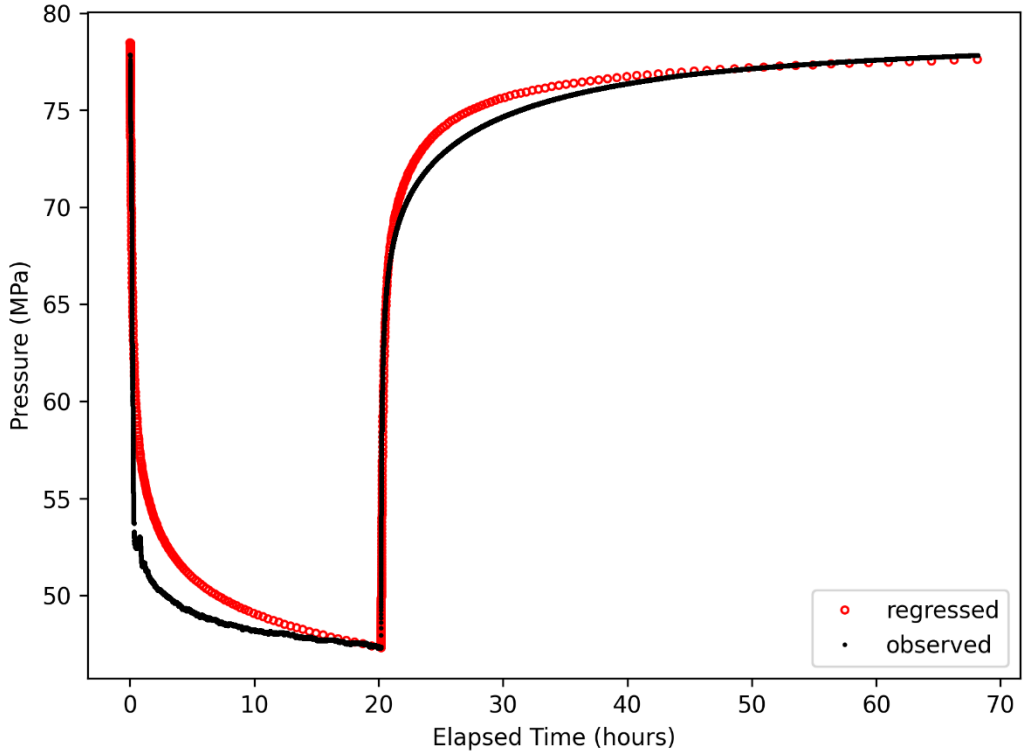

Figure 2.41: Comparison of pressure for the drawdown; HR case.

The buildup derivative field response in Figure 2.36 indicates that the temperature deviation during this period is wellbore dominated. No reservoir response is observed.

As shown in Figure 2.40, the initial temperature shoot at the instant of shut-in is represented with the model (controlled by φ), however, the sharp decline following is inconsistent with the pressure recordings. For this period, matching through optimization of overall heat transfer coefficient does not produce the same behavior. In this period, the wellbore fluid usually cools down due to heat losses, however, in this example, a set of tools having a high heat capacity are in place. It seems that the presence of these tools slows down the conductive cooling of the wellbore fluid. In this period, the model and the true system become inconsistent.

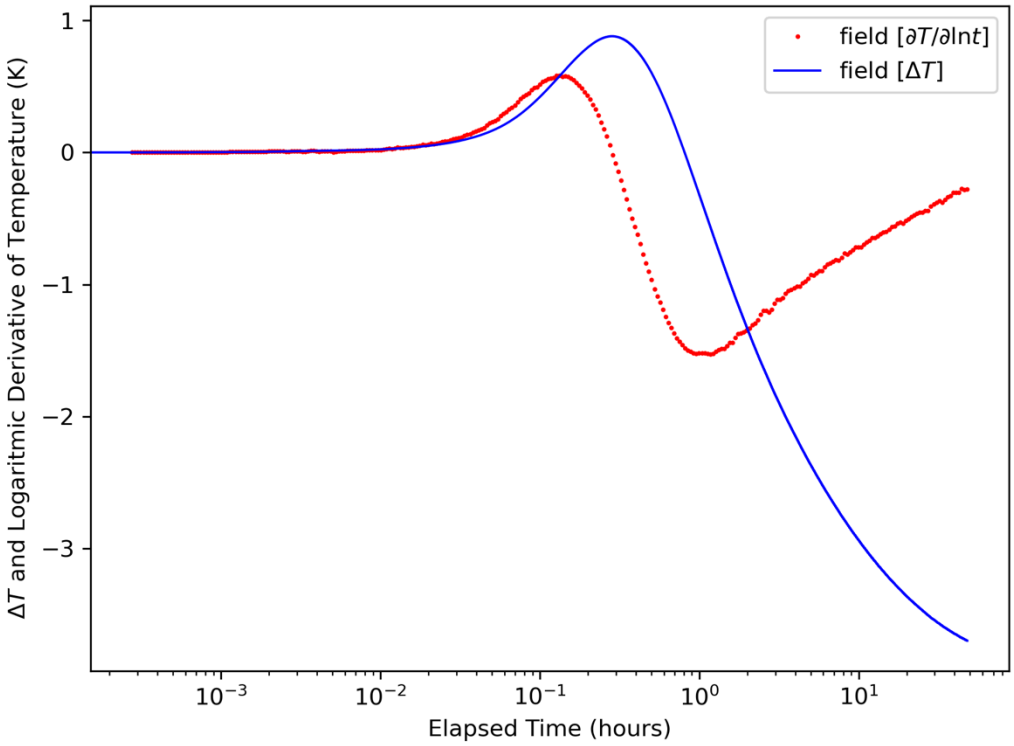

Figure 2.42: Buildup temperatures of field data.

2.7 Discussions and Recommendations

Here, further clarifications and recommendations are aimed to be discussed such as:

1. Advantages in using numerical simulator compared to analytical or semi-analytical solutions that exist in literature

Analytical and semi-analytical solutions in the literature (Onur et al, 2019 and Galvao et al. 2019) are based on decoupling of temperature and pressure solutions. In this study, the presented simulator solves the wellbore and reservoir conservation equations in a coupled manner. All the unknowns appear in the same matrix. This

allows us to perform history matching of both temperature and pressure measurements at gauge locations. Decoupling of pressure and temperature for the estimation of sandface temperatures works quite well as it is shown in the literature (Onur et al, 2016b). In such a case, pressure and temperature measurements are matched individually to estimate the parameters. On the other hand, for measurements obtained at gauge location, it is not clear to us how it is possible to history match the temperature and pressure together by decoupling pressure and temperature data. The analytical solutions available in the literature based on many assumptions. This is expected since to be able to obtain an analytical solution, the problem needs to be simplified. Otherwise, no analytical solution would be available. The simulator proposed do not have such limitations. Also, we do not find the analytical solutions easy to use. They are complicated and hard to follow. In fact, it is beneficial to have such a rigorous simulator to investigate the possible assumptions that could be made to simplify the solution which could lead to less complex analytical solutions.

2. Comparisons of the numerical solutions with existing analytical solutions

We do not provide any comparison with the analytical model proposed since these analytical solutions also validate their solutions with the same software which we used for comparison. Usually in the literature analytical models are not validated with field temperature measurements

3. Advantages in using numerical simulator developed compared to commercial software.

Commercial software (CMG-STARS) is not intended to simulate pressures and temperatures for a DST well test in which the measurements are obtained in the wellbore at a certain gauge location above the producing horizon. CMG-STARS wellbore model aims to provide solutions only when there exists one to one correspondence between wellbore and reservoir gridblocks. At the locations where the gauges are placed for a conventional well test, there is no reservoir adjacent to the wellbore. To the best of our knowledge, there exists no commercial simulator for coupling reservoir and wellbore to solve transient temperatures and pressures both in wellbore and reservoir simultaneously. One the other hand, industry standard commercial simulators solve enthalpy thus the change of enthalpy with respect to pressure and temperature need to be defined properly for the hydrocarbon mixture. For

instance, if pressure dependence of enthalpy is neglected, no J-T effect would be observed. Instead, the simulator developed presented solves temperature not enthalpy. Thermal parameters such as J-T coefficient explicitly defined. Thus, through history matching, these parameters could be obtained. As it is shown in this study, we have successfully estimated J-T coefficient from field temperature measurements. This parameter is not an input for the commercial simulators since it is implicitly integrated through dependence of enthalpy to pressure and temperature.

4. Sensitivity analysis for J-T coefficient is not provided.

We do not provide sensitivity to J-T coefficient since changing J-T coefficient and fixing all other thermodynamic parameters physically impossible. In order for J-T coefficient parameter to differ, composition needs to be different changing all the other parameters. At least, there should be a consistency between J-T coefficient and isentropic expansion coefficient in order to honor the thermodynamic laws. Therefore, isentropic expansion coefficient is estimated using J-T coefficient through thermodynamic relations where we keep isobaric thermal expansion coefficient fixed. Now, we provide two unrealistic cases just for clarification. Firstly, please refer to Figure 2.12 in which the effect of change in permeability is clearly observed in the temperature response. Now, when we keep J-T coefficient constant only in the wellbore, Figure 2.43 shows the effect of different J-T coefficients (changing only in the reservoir) on drawdown wellbore temperatures at a higher gauge location (z = 110 m). Thus, in this figure, below up to the point where the curves separate, the change in temperature is due to wellbore phenomena. Later, the curves deviate due to J-T effect in the reservoir. Note that the J-T phenomena in the wellbore leads to a different signature shifts the curve up and down. In the second unrealistic case, J-T coefficient is fixed in the reservoir and different J-T coefficients are used just in the wellbore plotted in Figure 2.44.

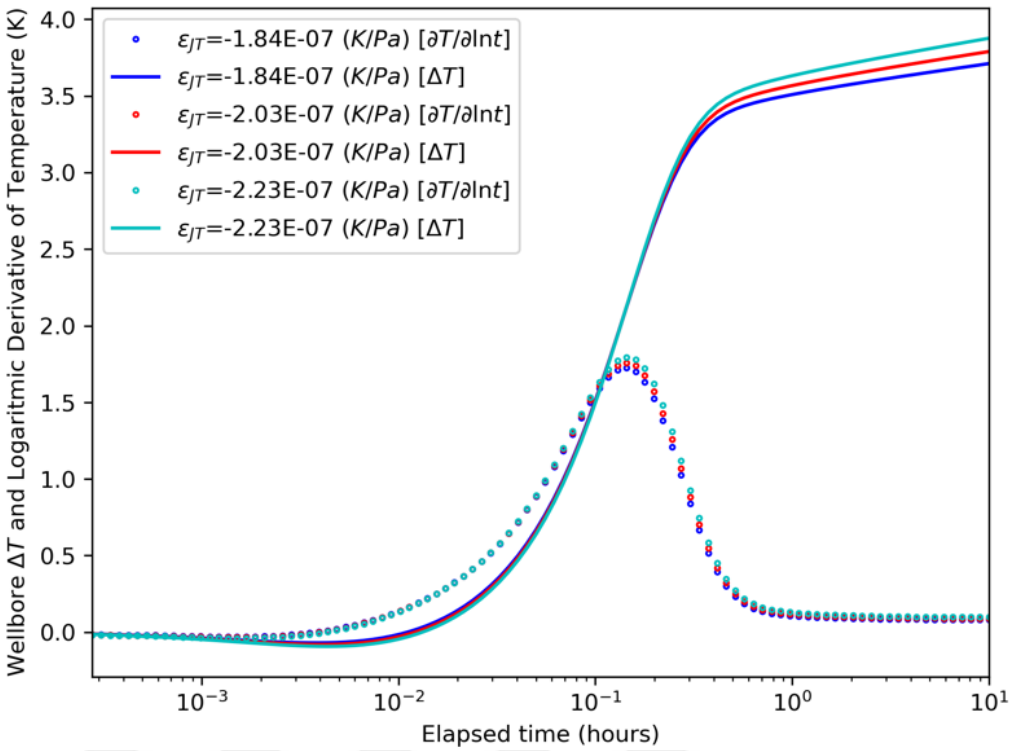

Figure 2.43: Effect of J-T coefficient (changing only in the reservoir) on drawdown wellbore temperatures (z=110m).

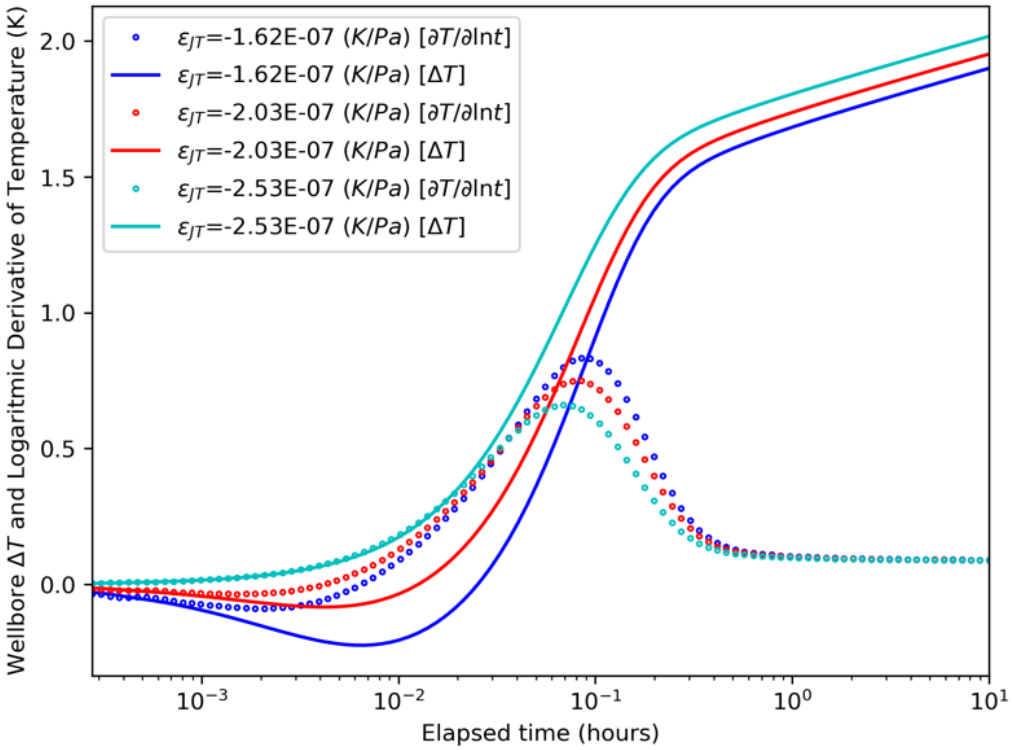

Figure 2.44: Effect of J-T coefficient (changing only in the wellbore) on drawdown wellbore temperatures (z=30m).

5. Comments on computational time during parameter estimation.

The computational time would depend on the computer used and the number of cores assigned. Using a standard PC with one core the forward runs in the synthetic examples are about 3 seconds. During parameter estimation it is about 5 minutes. However, time step selection and EOS plays crucial role. For instance, when IAPWS (2018) used for water, it is not feasible to perform regression in such a short duration. We recommend creating a proxy model to represent EOS.

6. Comments on gauge placement in a DST test design.

As it is explained in the section of impact of gauge distances, when the gauge is placed further away from the producing horizon the wellbore phenomena start to dominate in a larger extend. At some distance the reservoir information would be lost. It is hard to generalize and come up with a certain value since at the end it would be case depended. But based on our experience, we do not advise placing the bottom hole gauge above 100 m (above the producing horizon) if such a drawdown temperature analysis is intended.

7. Advantages of new type curves introduced in this study when compared with the one exists in literature in which absolute values of the temperature difference and its derivative on a log-log plot is used.

Firstly, it is not claimed that one could identify flow regimes associated with pressure transients using temperature transient analysis. There is no one to one correspondence. For instance, if the log-log plot of absolute temperature difference and its derivative give zero slope that does not mean that the heat flow or fluid flow is radial. During production, temperature changes are mainly due to thermodynamic phenomena, that is path independent. It is not directly related to flow geometry. The temperature models for different reservoir-well configurations are yet to be developed and manual type curve matching is a historical method as it is replaced with well testing software. One may note that the early time isentropic effects are not observed clearly in the representation suggested but this is something that could be sacrificed. If not impossible, it is extremely difficult to observe this region in the field data. Finally, it is not claimed that the new representation is the ultimate way, but an alternative is

provided. In this study, we tried to explain the physical phenomena behind the temperature changes. The plots suggested in this study are much more easily understood and not as confusing as prior representations. The aim is to provide easily understood representation with the emphasis on the plot that have significant information.

8. Comments on linear flow (1/2 slope line) on the log-log diagnostic plot of prior representation of drawdown temperature.

Figure 2.45 shows (the prior representation) absolute values of temperature difference and its derivative on log-log plot. Making the axis log-log exposes small changes in temperature and put emphasis on these small values which involves disprepancy between model and field data. Making the axis logarithmic exposes this difference as if they were important.

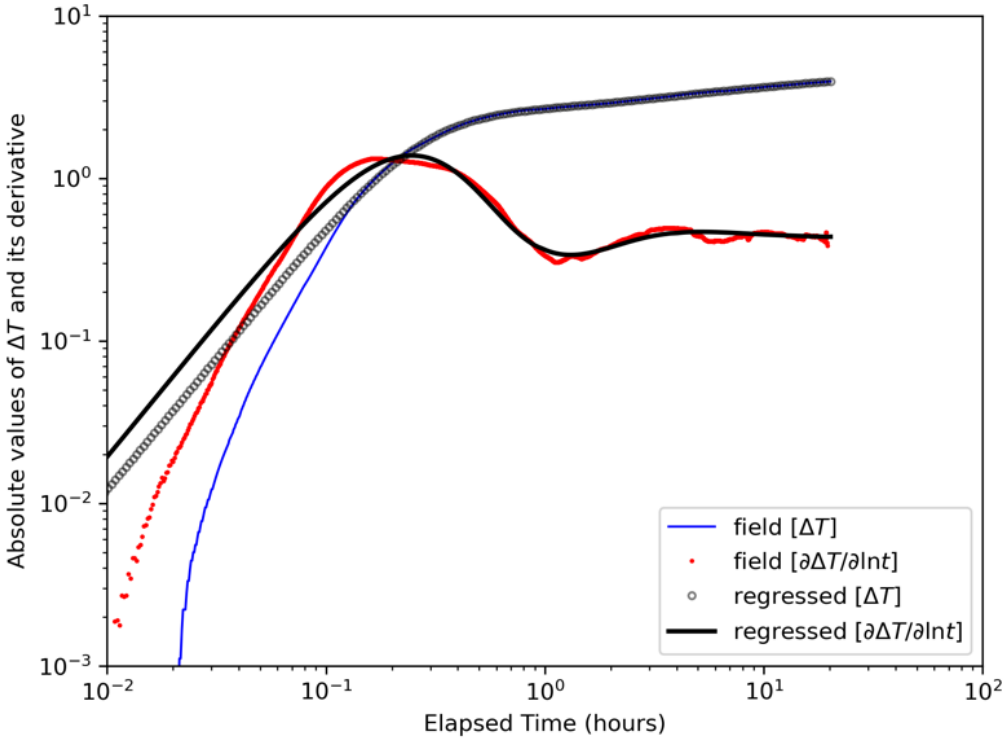

Figure 2.45: Drawdown temperatures of field data (HM case).

This is nothing to do with the reservoir response. It is wellbore phenomena, most probable due to the initial conditions. During a well test, in the drawdown period, prior to recording the measurements, there are several operations conducted. These would disturb the initial temperature distribution. No operator would wait for thermal

equilibrium to be achieved during a standard well testing operation. In the numerical simulator developed, we start (at the initial condition) by assuming thermal equilibrium in the wellbore and the temperature is distributed along the well based on the gradient. Thus, the difference it is quite normal. As we we did not conduct a detailed investigation, there could be other possible explanations but all would be within the context of wellbore phenomena.

3. NUMERICAL IMPLEMENTATION FOR SLIGHTLY COMPRESSIBLE FLUID FLOW IN A COUPLED 2-D (*r*-*z*) RESERVOIR AND 1-D (*z*) WELLBORE SYSTEM

Figure 3.1 represents the physical problem that we try to solve. Single phase fluid (oil or geothermal brine or water) flows from each open (permitted to flow or perforated) reservoir layer into the wellbore transporting associated mass and energy.

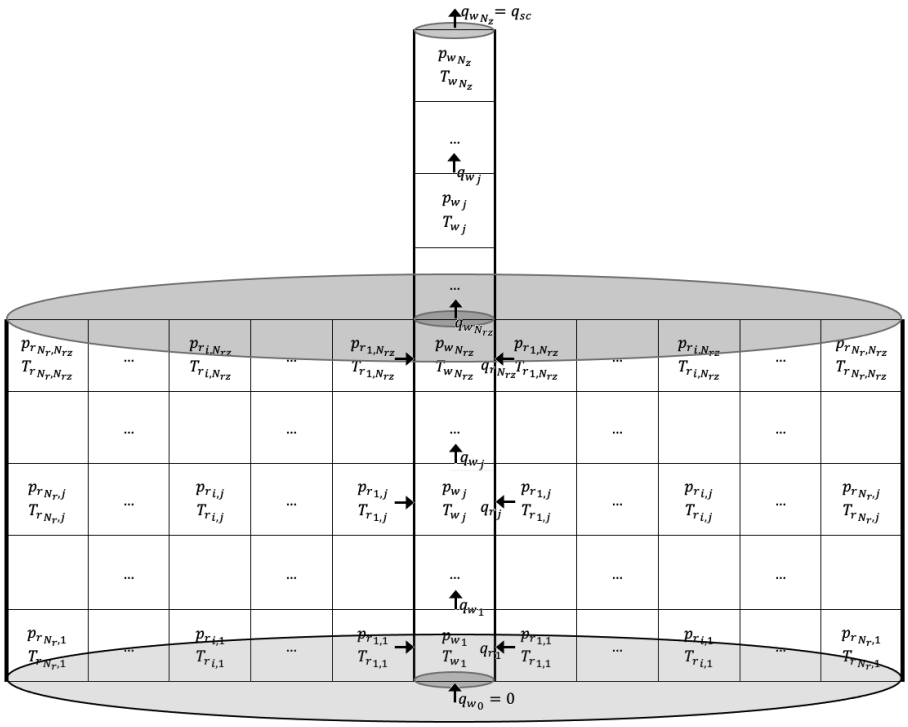

Figure 3.1: Schematic view of the coupled wellbore and reservoir gridblocks representation for multi-layer system.

Once the fluid from reservoir enters into the wellbore, it mixes with the wellbore fluid and accordingly temperature changes. As the fluid flows up the heat transfer by conduction also occurs between the fluid entering from reservoir and the fluid already in the wellbore. The temperature profile of the wellbore fluid solely depends on the mass influx from each contributing reservoir layer with its specific temperature which is determined by geothermal temperature at that corresponding depth. It also depends on the Joule-Thompson effects based on the magnitude of drawdown or buildup within that layer.

3.1 Boundary Conditions and Coupling

Derivations of 2-D (*r-z*) reservoir and 1-D (*z*) wellbore system for single phase fluid flow is presented in Appendix. We denote reservoir pressures $p_{r_{i,j}}^{n+1}$ and temperatures $T_{r_{i,j}}^{n+1}$respectively at any gridblock (*i,j*) within the reservoir system whereas we denote wellbore pressures $p_{w_j}^{n+1}$ and temperatures $T_{w_j}^{n+1}$respectively at any gridblock (*j*) within the wellbore system. In addition, N_z represents gridblock numbers in the wellbore, N_{rz} represents number of reservoir layers whereas N_r represents gridblock numbers in the radial axis in the reservoir.

As mentioned in previous chapter, in the system of wellbore equations provided in derivations, several terms in mass, momentum, and energy balance equations require boundary information at the top ($q_{w_{N_z}}^{n+1} = q_{sc}^{n}$) and at the bottom q_{w0}^{n}=0 as well as no flow bottom boundary information for temperature ($\partial T_w/\partial z=0$) and pressure ($\partial p_w/\partial z=0$). As described while discretizing the energy balance equations, temperature solution from reservoir equations at the first gridblock $T_{r_{1,j}}^{n+1}$ provides boundary information when calculating $T_{w_j}^{n+1}$ in wellbore equations. Similarly, bottom hole flowing pressure for the first reservoir gridblock calculated from reservoir equations $p_{r_{1,j}}^{n+1}$provides boundary information when calculating $p_{w_j}^{n+1}$ in wellbore equations.

For a single layer system (N_{rz}=1), one can approximate one and only (*j*=1) wellbore bottom hole flow rate variable $q_{r_j}^{n+1}$. Hence, in the constructed equations for multi-layer system, we solve the flow rate between each contributing reservoir layer (*j*) and adjacent wellbore cells. In the coupled model, since reservoir inner boundary for the contributing open interval layers is connected to the wellbore adjacent cells, flow rates for each layer in the radial direction need to be calculated from Darcy's law given in Equation 2.4. We use pressure information of reservoir flowing pressure $p_{r_{1,j}}^{n+1}$ from each contributing layer of *j* as well as wellbore flowing pressure $p_{w_j}^{n+1}$ in order to estimate the rates for layer *j*'s. The calculated $q_{r_j}^{n+1}$ values are used both in the reservoir and wellbore discretized equations. They are all updated for each iteration at any time step as the other unknown parameters in the system of equations. Therefore, the user only needs to input flow rate at surface q_{sc}^{n} which is the defined at the top of

wellbore, and initial pressure $p_{r_{1,j}}^{n+1}$ with geothermal gradient to build a representative coupled reservoir/wellbore model.

3.2 Numerical Solution

When the coupled coefficient matrix is constructed, there are 3 x N_z -1 unknowns (p_w, T_w, q_w) from wellbore ($q_{Nz}^n = q_{sc}$ is an input, thus known) and 2 x N_r x N_{rz} unknowns (p_r, T_r) from reservoir as well as N_{rz} unknowns (q_r) from all reservoir layers (either the layer is open to flow or not). Therefore, there is neither a single bottom hole pressure nor a single flowing bottomhole rate for the coupled system. In addition, 4 extra unknowns are added to account for top and bottom boundaries of wellbore.

As it is given in Equation 3.2, there are (3 x N_z - 1) + (2 x N_r x N_{rz}) + N_{rz} + 4 unknowns and the same number of equations. The system of equations from wellbore and reservoir are written altogether in matrix vector form, which is then solved by the sparse linear system solver called as "spsolve" of SciPy which is an open-source software for mathematics, science, and engineering (Pauli et al, 2020):

$$\mathbf{A}^{n+1,j}\mathbf{x}^{n+1,j+1} = \mathbf{D}^{n+1} \tag{3.1}$$

where $\mathbf{x}^{n+1}$ is the solution matrix given in Equation 3.2 consists 3 x N_z - 1 pressures, temperatures, and rates for wellbore, 2 x N_rxN_{rz} pressures, temperatures for reservoir, and N_{rz} flowing rates for all reservoir layers and 4 wellbore boundary is a 3xN_z-*1*+2xN_rxN_{rz}+N_{rz}+4 dimensional column vector whereas $\mathbf{D}^{n+1}$ is an 3xN_z-1+2xN_rxN_{rz}+N_{rz}+4 dimensional column vector which contains the terms in the right-hand side, and **A**, becomes a (3N_z-1+2N_rN_{rz}+N_{rz}+4) × (3N_z-1+2N_rN_{rz}+N_{rz}+4) nonsymmetrical highly sparse coefficient matrix. An example of this matrix is shown in Figure 3.2 resulting from system of equations for a multi-layer 2-D (*r*-*z*) system with 3 gridblocks in *r*-direction and 3 gridblocks in *z*-direction.

$$
\mathbf{x}^{n+1,j+1} = \begin{bmatrix}
q_{r_{N_{rz}}} \\
\dots \\
q_{r_j} \\
\dots \\
q_{r_1} \\
p_{r_{1,1}} \\
T_{r_{1,1}} \\
\dots \\
p_{r_{i,1}} \\
T_{r_{i,1}} \\
\dots \\
p_{r_{N_r,1}} \\
T_{r_{N_r,1}} \\
\dots \\
p_{r_{i,j}} \\
T_{r_{i,j}} \\
\dots \\
p_{r_{1,N_{rz}}} \\
T_{r_{1,N_{rz}}} \\
\dots \\
p_{r_{i,N_{rz}}} \\
T_{r_{i,N_{rz}}} \\
\dots \\
p_{r_{N_r,N_{rz}}} \\
T_{r_{N_r,N_{rz}}} \\
p_{w_{BC_1}} \\
T_{w_{BC_1}} \\
p_{w_1} \\
T_{w_1} \\
q_{w_1} \\
\dots \\
p_{w_j} \\
T_{w_j} \\
q_{w_j} \\
\dots \\
p_{w_{N_z}} \\
T_{w_{N_z}} \\
p_{w_{BC_{N_z}}} \\
T_{w_{BC_{N_z}}}
\end{bmatrix} \tag{3.2}
$$

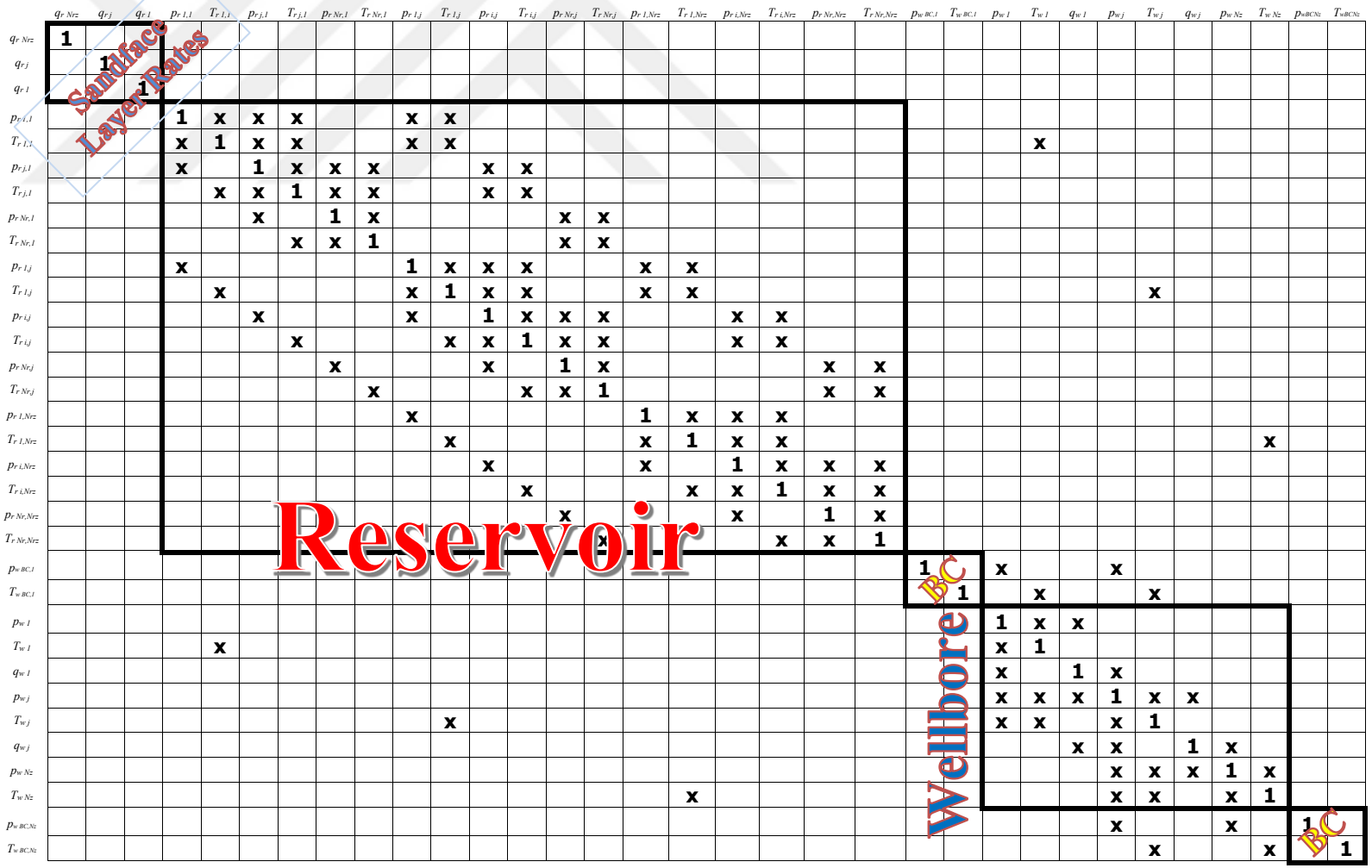

Figure 3.2: Nonsymmetrical highly sparse coefficient matrix for coupled reservoir/wellbore system (N_r=N_z=N_{rz}=3).

"spsolve" is a part of the linalg stack in SciPy which is as an open-source Python library used for scientific computing in engineering such as linear algebra, optimization, interpolation, integration. It also provides numerious tools for working with linear algebra problems such as performing matrix calculations, inverses, determinants, eigenvectors, eigenvalues, the singular value decomposition and etc.

For solving the matrix expression **Ax** = **D** in Equation 3.1, "spsolve" solver assumes the resulting matrix is sparse which costs expensive during its computation. For such a dense matrix **A**, linalg stack provides convertions to other variants to ease the overload on memory of the PC. Solving linear systems of equations is straightforward using the scipy command in linalg stack. This command expects an input matrix, **A** and a right-hand side vector, **D**. Next, the solution vector **x** is computed as in Equation 3.2. The solution vector can be solved by using a matrix inverse; however, it is extremely expensive for the problem considered in which nonsymmetrical highly sparse coefficient matrix is constructed.

3.3 Comparison of Transient Pressure and Temperature Solutions

In this section, three different partially (or fully) penetrated multi-layer reservoir/wellbore system are considered to perform the transient pressure and temperature comparison, and also to test the capabilities of the numerical simulator developed. The results obtained from the numerical solutions are compared with the commercial software (CMG-STARS). Using the input data from Table 2.1, transient sandface/wellbore pressure and temperature data is generated by nonisothermal simulator considering a drawdown/buildup test sequence for a three different type of partially penetrated well. The flow rate history consists of a 5-day production at a constant surface flow rate of 500 sm^3/D followed by a 15-day buildup. There are 9 uniformly shaped gridblocks in the *z*-direction with uniform length of 6 m whereas 200 logarithmically spaced gridblocks in the reservoir. Similarly, reservoir outer radius (r_e) is taken very large to represent an infinite acting flow throughout the entire flow history. The sandface pressures and temperatures refer to computed block pressures and temperatures of the first grid block adjacent to the wellbore grid block which is either open to flow (perforated) or closed to flow (not perforated). The location of the open interval for each case is reported in Table 3.1. Figures 3.3, 3.6 and 3.9 show the comparison of sandface and wellbore pressure of all layers from

numerical simulator developed and commercial simulator for the entire flow history in Cartesian plot whereas Figures 3.4, 3.7 and 3.10 show the same comparison for temperature in semi-log plot for drawdown and Figures 3.5, 3.8 and 3.11 for buildup, respectively. All comparisons of temperature and pressures seem to be acceptable. In commercial simulator, initial temperatures and pressures inside the wellbore are different than the sandface. In order to ensure the local equilibrium between wellbore and the surrounding rock in the commercial simulator, a minimum of 10-day production with zero surface rate is required to achieve identical wellbore and reservoir (or surrounding rock) temperatures prior to fluid flow. However, this workaround solution leads to an instability caused by convergence issues due to neglicible changes in whole system during this no-flow period. The differences observed in both pressure and temperature matches mainly caused by time stepping. Also, commercial simulator uses rigorous EOS for fluid characterization while we keep all fluid properties at initial conditions except for density. The differences in temperatures close to boundaries are due to different treatment of boundary condition. Since the commercial simulator treats heat loss effects time dependent, the shift observed in temperature matches could easily be improved by adjusting overall heat transfer coefficient, which is discussed in multi-layer cases on the following section.

Table 3.1: Description of perforations for the multi-layer system having partially/fully penetrated well.

Case No	Open Intervals	Closed Intervals
1	1,2,3,4,5,6,7,8,9	-
2	1,2,3	4,5,6,7,8,9
3	4,5,6	1,2,3,7,8,9

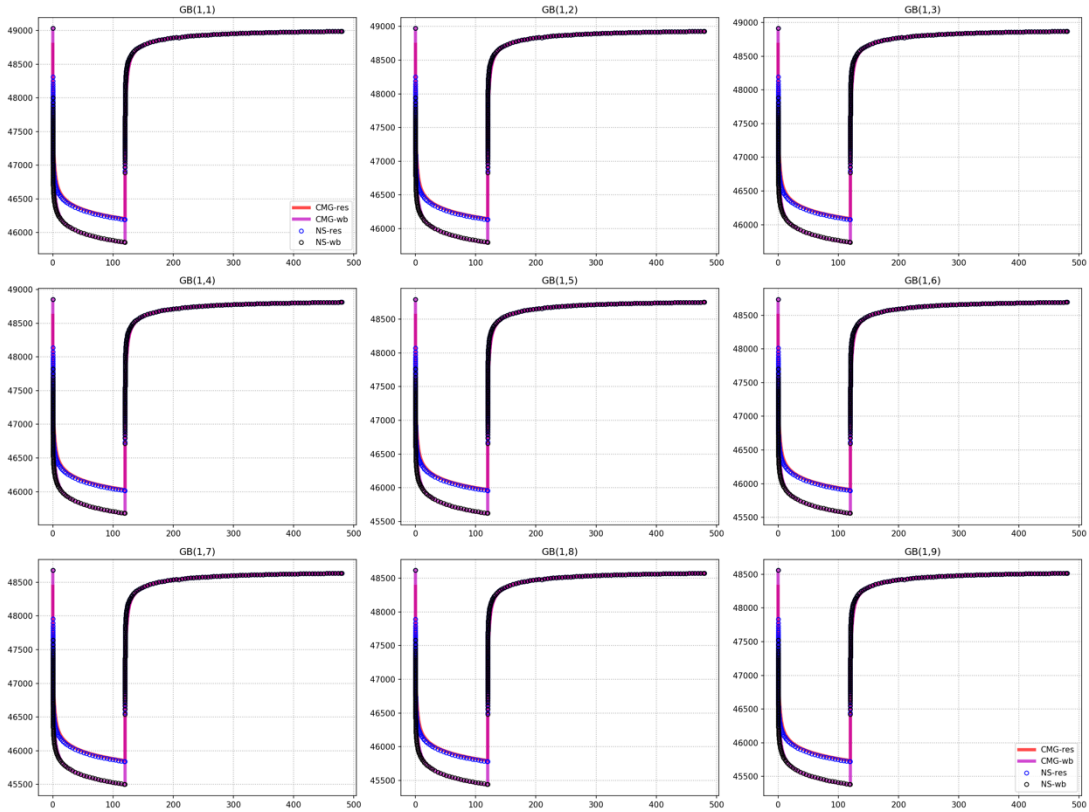

Figure 3.3: Comparison of sandface/wellbore pressures for entire history, Case 1.

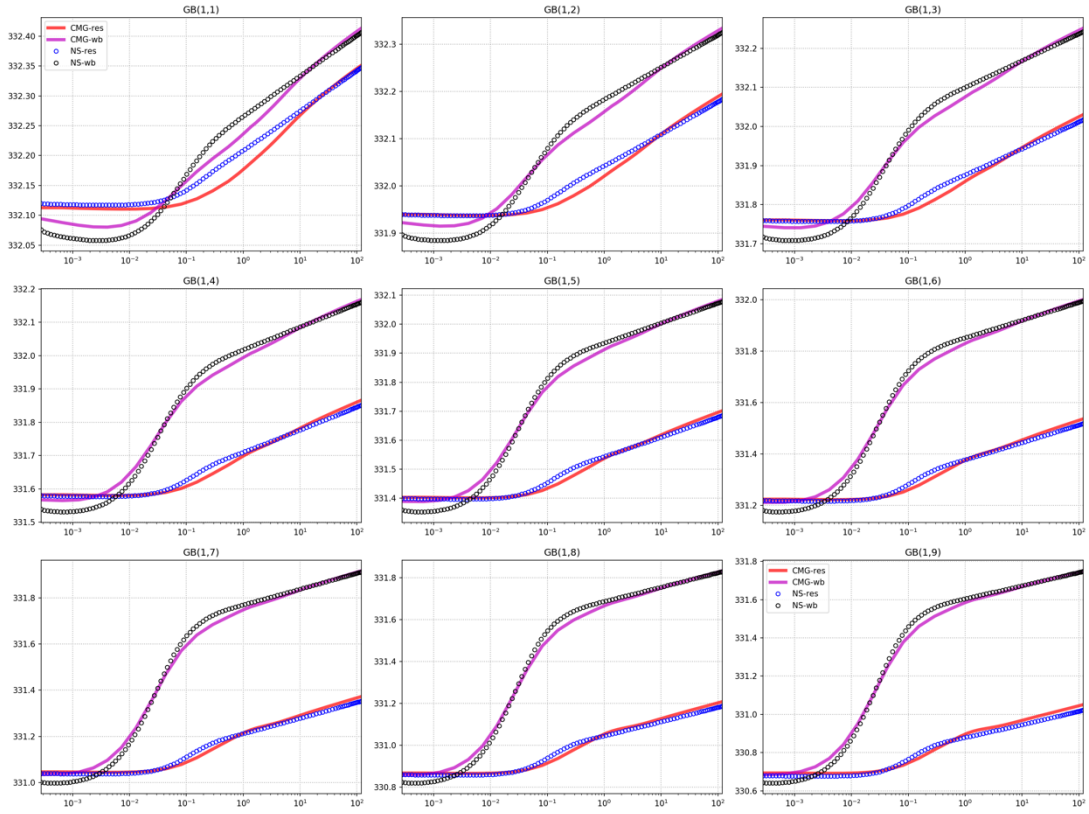

Figure 3.4: Comparison of sandface/wellbore temperatures during DD, Case 1.

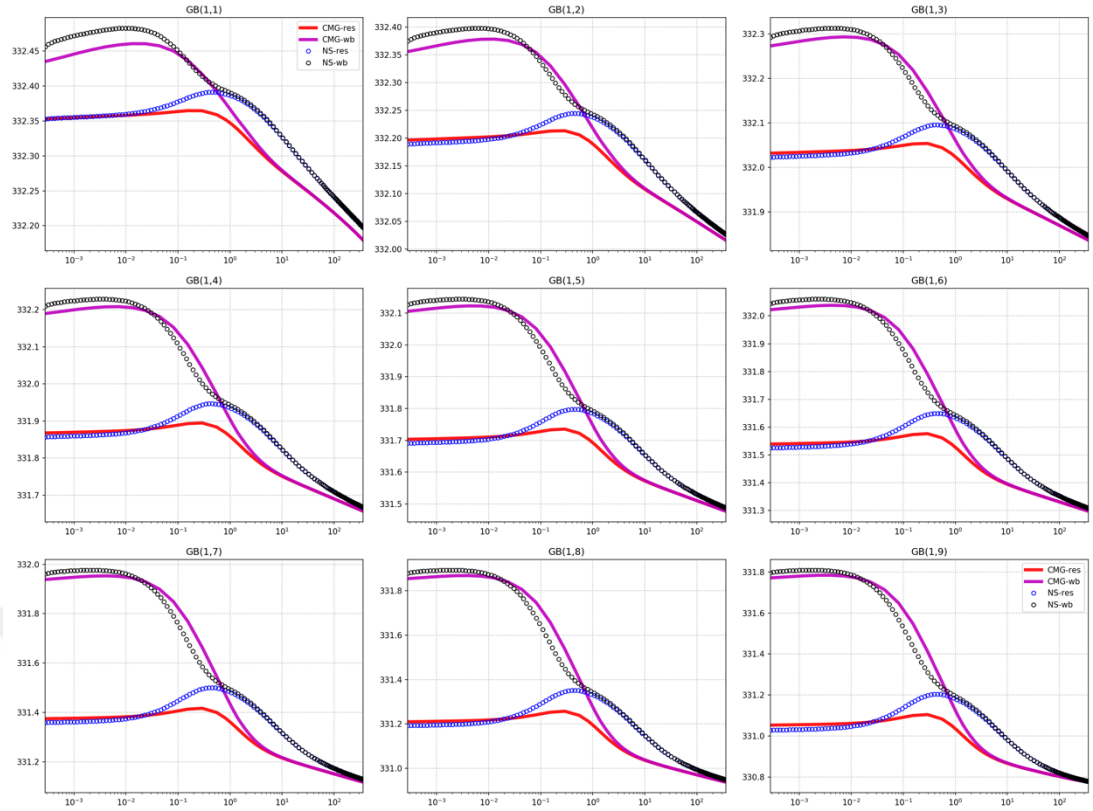

Figure 3.5: Comparison of sandface/wellbore temperatures during BU, Case 1.

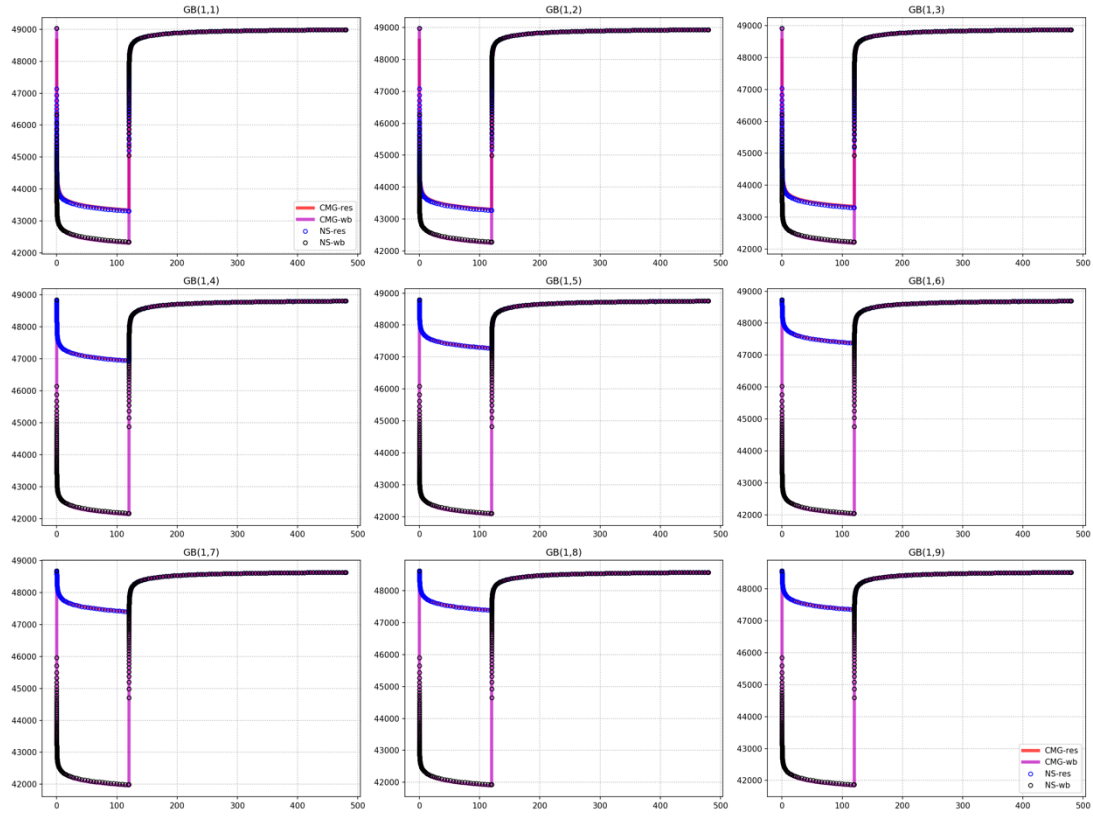

Figure 3.6: Comparison of sandface/wellbore pressures for entire history, Case 2.

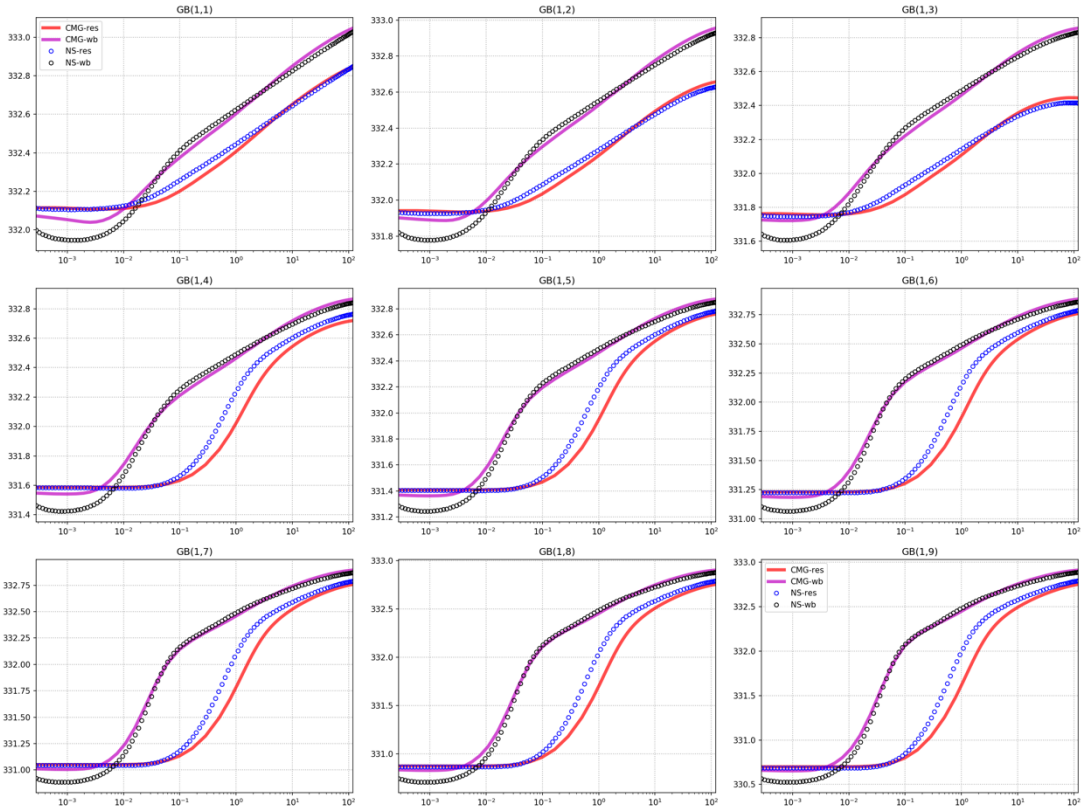

Figure 3.7: Comparison of sandface/wellbore temperatures during DD, Case 2.

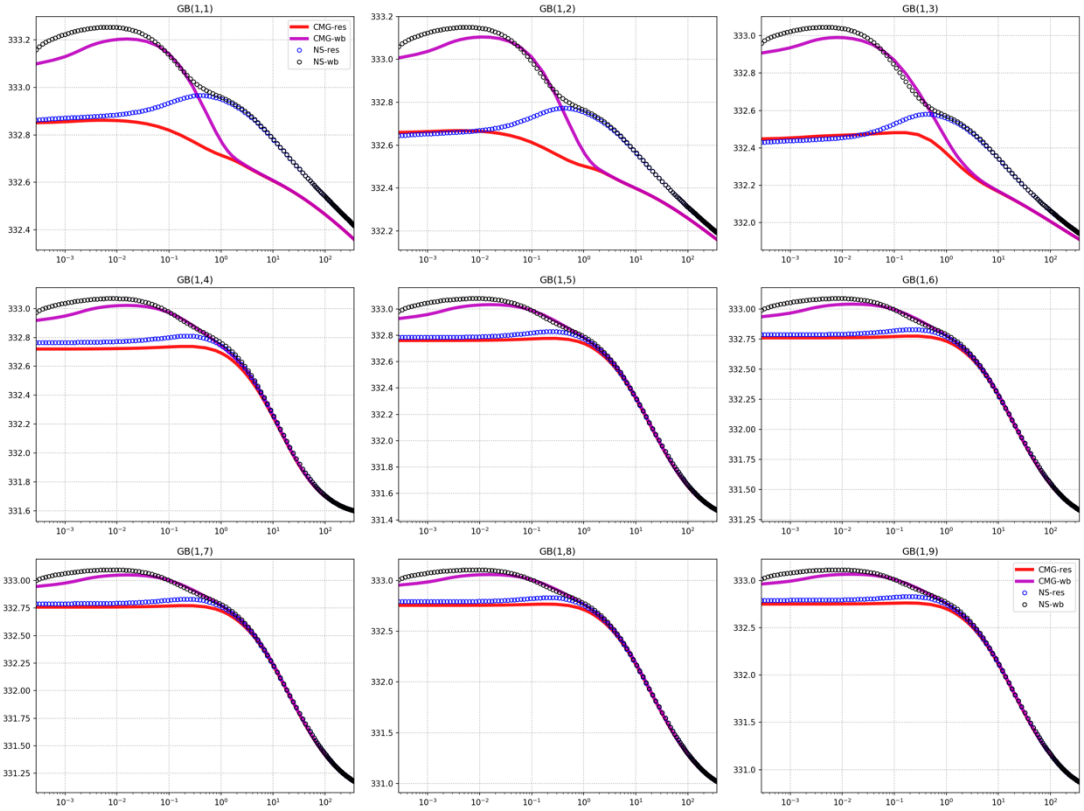

Figure 3.8: Comparison of sandface/wellbore temperatures during BU, Case 2.

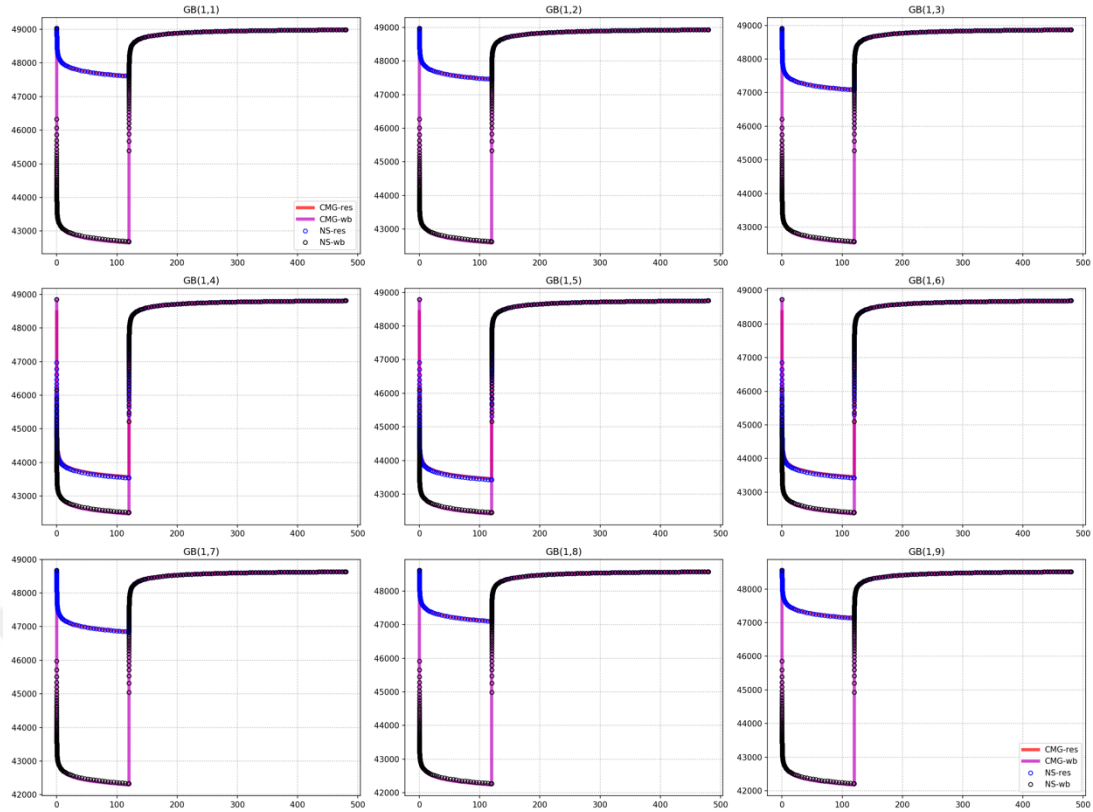

Figure 3.9: Comparison of sandface/wellbore pressures for entire history, Case 3.

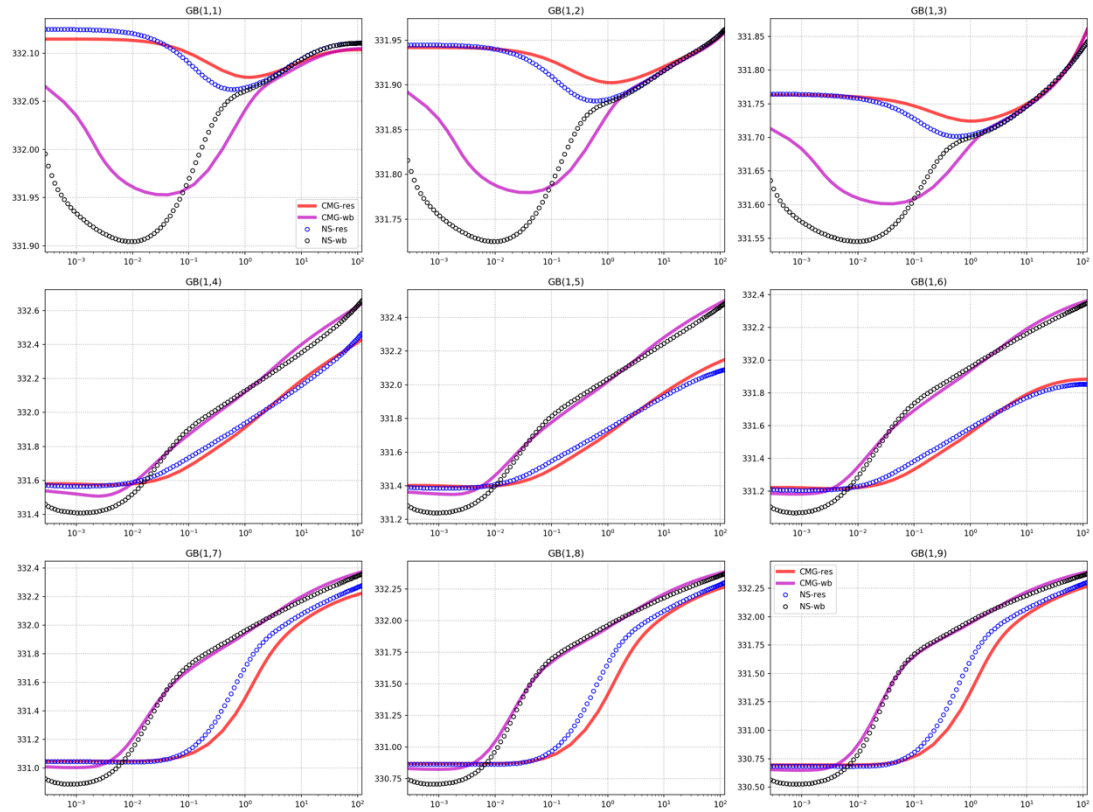

Figure 3.10: Comparison of sandface/wellbore temperatures during DD, Case 3.

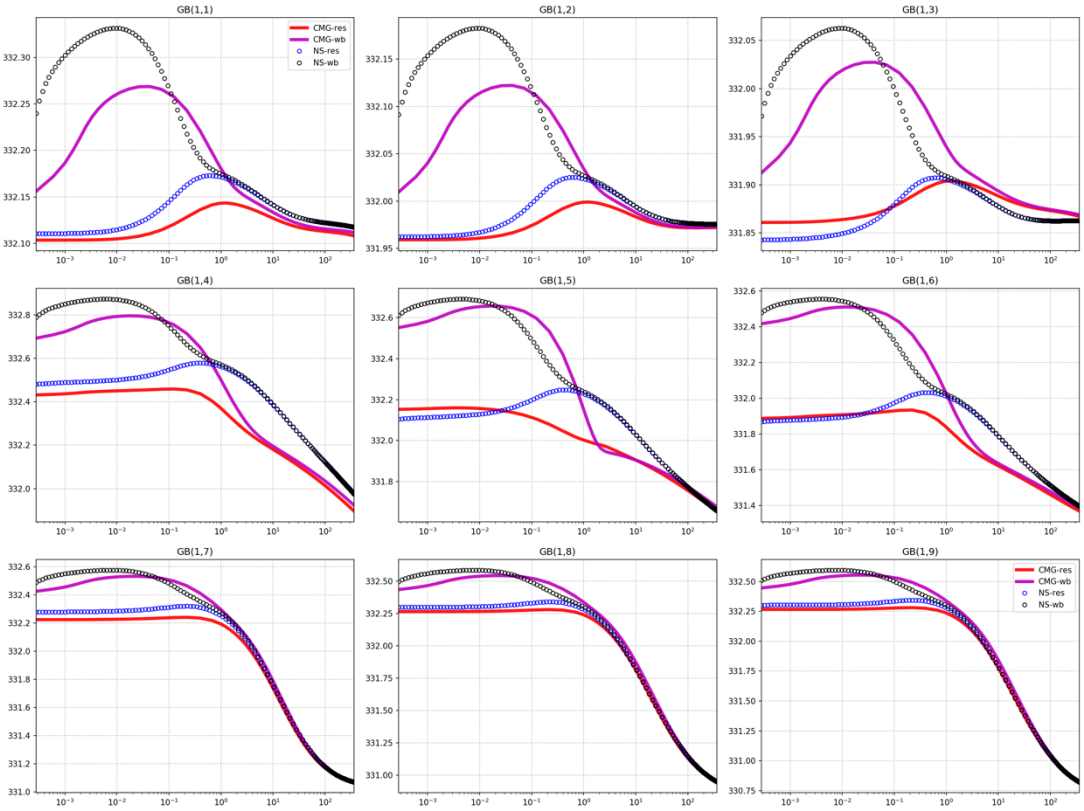

Figure 3.11: Comparison of sandface/wellbore temperatures during BU, Case 3.

3.4 Multi-Layer Reservoir and Wellbore System

3.4.1 Model initialization

Here, we consider a multi-layer system with different layer properties and compare results from numerical simulator developed with the ones computed from the commercial nonisothermal simulator (CMG-STARS). We present wellbore/reservoir temperature and pressure solutions of a vertical well producing in a radial multi-layered single phase reservoir at specified constant surface flow rate of 1000 sm^3/D for 5 days. Layer permeability and interval status (whether perforated or not) are varied for 54 layers (each having uniform height of 1 m) as listed in Table 3.3 in which the ratio of vertical permeability (k_z) and horizontal permeability (k_r) is taken a standard value of 0.1. Schematic view of layer permeability taken from the numerical simulator developed is also shown in Figure 3.12. As seen, there are five main zones in the multi-layer system in which only two of them are perforated and called as producing zones. The top, bottom and middle layers represent lower permeability regions (50 mD) which are not perforated but also not sealed as the flow is permitted in between layers (k_z/k_r=0.1). We use the input data tabulated in Table 3.2 given for all cases discussed

in the following section unless otherwise stated. All fluid and rock properties are evaluated at initial reservoir pressure and temperature. Typically, reservoir outer radius (r_e) is taken very large to model infinite acting flow throughout the drawdown period. The reservoir grid system has logarithmically spaced 200 grid blocks.

Table 3.2: Simulation input data used for comparison of multi-layer system.

Model Properties		Water Properties		Rock Properties	
r_w (m)	0.10	ρ (kg/m^3)	1003.9	ρ_m (kg/m^3)	2600
r_e (m)	25000	c_p (J/kg.K)	4088.4	$c_{p,m}$ (J/kg.K)	1000
h_{res} (m)	6	ε_{JT} (K.Pa)	-2.027×10^{-7}	λ_m (J/m.s.K)	3.67
N_z=N_{rz}	9	μ (Pa.s)	0.479×10^{-3}	c_m (Pa^{-1})	0
z_w (m)	54	λ (J/m.s.K)	0.678	β_m (K^{-1})	0
p_{in} (MPa)	50	β (K^{-1})	5×10^{-4}		
T_{in} (K)	333.15	c (Pa^{-1})	3.9×10^{-10}		
q_{sc} (sm^3/D)	1000	B (m^3/sm^3)	1		
Geo. grad. (K/m)	0.03				
U_t (W/m.s.K)	29				
ϕ	0.1				

Using all the information and the input data presented, the numerical simulator developed is able to construct various multi-layer coupled reservoir/wellbore models to generate pressures and temperatures at any given point within the reservoir as well as pressure, temperature and flow rate well profiles along the wellbore for a given flow history which may consist of numerous drawdowns and buildup periods.

Table 3.3: Description of layers for multi-layer system.

Layers (from/to)	k_r (mD)	k_z (mD)	Status
1 to 6	50	5	CLOSED
6 to 21	300	30	OPEN
21 to 31	50	5	CLOSED
31 to 41	100	10	OPEN
41 to 54	50	5	CLOSED

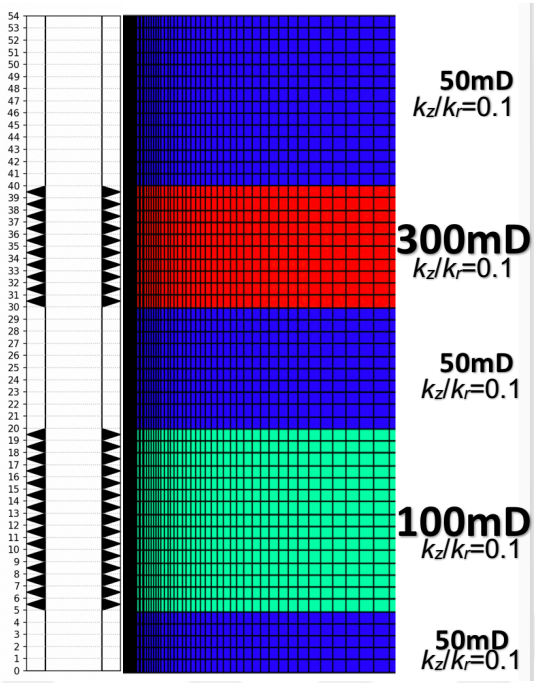

Figure 3.12: Schematic view of layer permeability on 2-D (*r*-*z*) plot for comparison case with no skin effects.

3.4.2 Comparison of drawdown pressure and temperature solutions

Figure 3.13 shows the comparison of wellbore and reservoir temperatures (left) and pressures (right) against commercial software (CMG-STARS) along the wellbore at the end of drawdown. Here, the example case verifies to prove the capability of the numerical simulator developed to further study multi-layer reservoir/wellbore systems.

Figure 3.14 shows the inflow production profile across the wellbore (also called as PLT plot) which is simply depth vs corresponding cumulative fluid contributions on Cartesian plot) from the numerical simulator developed. Production logging tools (PLTs) are used to evaluate well performance by providing high resolution measurements of the flow rates along with fluid identifications in the downhole. A typical PLT tool may consist of multiple sensors responsible of performing physical measurements in order to acquire temperatures, pressures, fluid type identification, fluid volumes and rates at individual location in the wellbore to construct a representative production or injection profile.

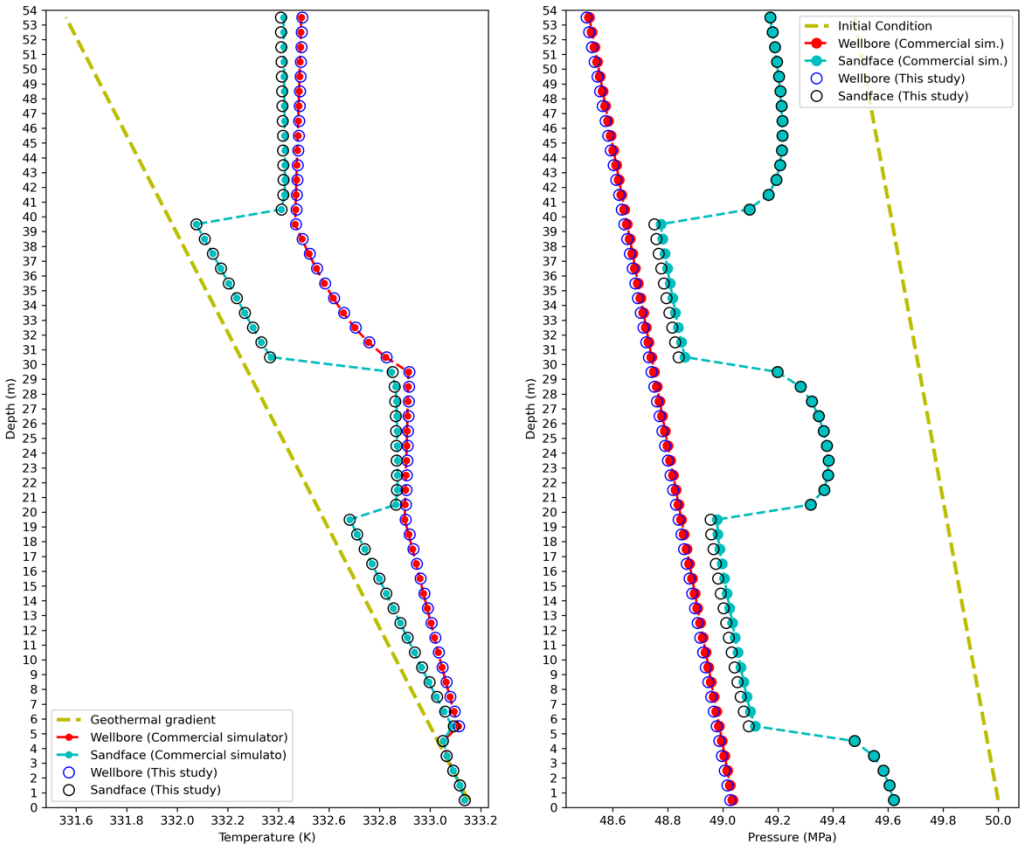

Figure 3.13: Comparison of wellbore/reservoir pressures and temperatures across the wellbore from numerical simulator developed and CMG-STARS at the end of drawdown.

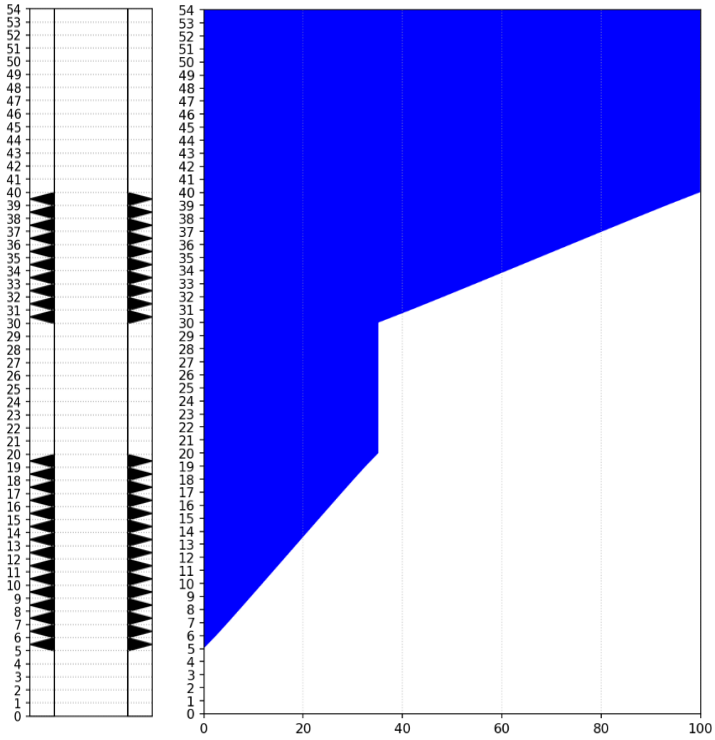

Figure 3.14: Inflow production profile across the wellbore from numerical simulator developed at the end of drawdown.

Figure 3.15 shows reservoir pressures while Figure 3.16 shows reservoir temperatures distributions on (*r*-*z*) cross sectional areal view from the numerical simulator developed at different time steps until the end of the drawdown. The interface of the numerical simulator developed is capable of visualizing pressure, temperature and flow rate distributions over space and time. Several example cases are considered for demonstrating the utility of the developed simulator and the visualization features which may enable one to conduct visual studies of well temperature and pressure transients in homogeneous reservoirs as well as heterogeneous reservoirs.

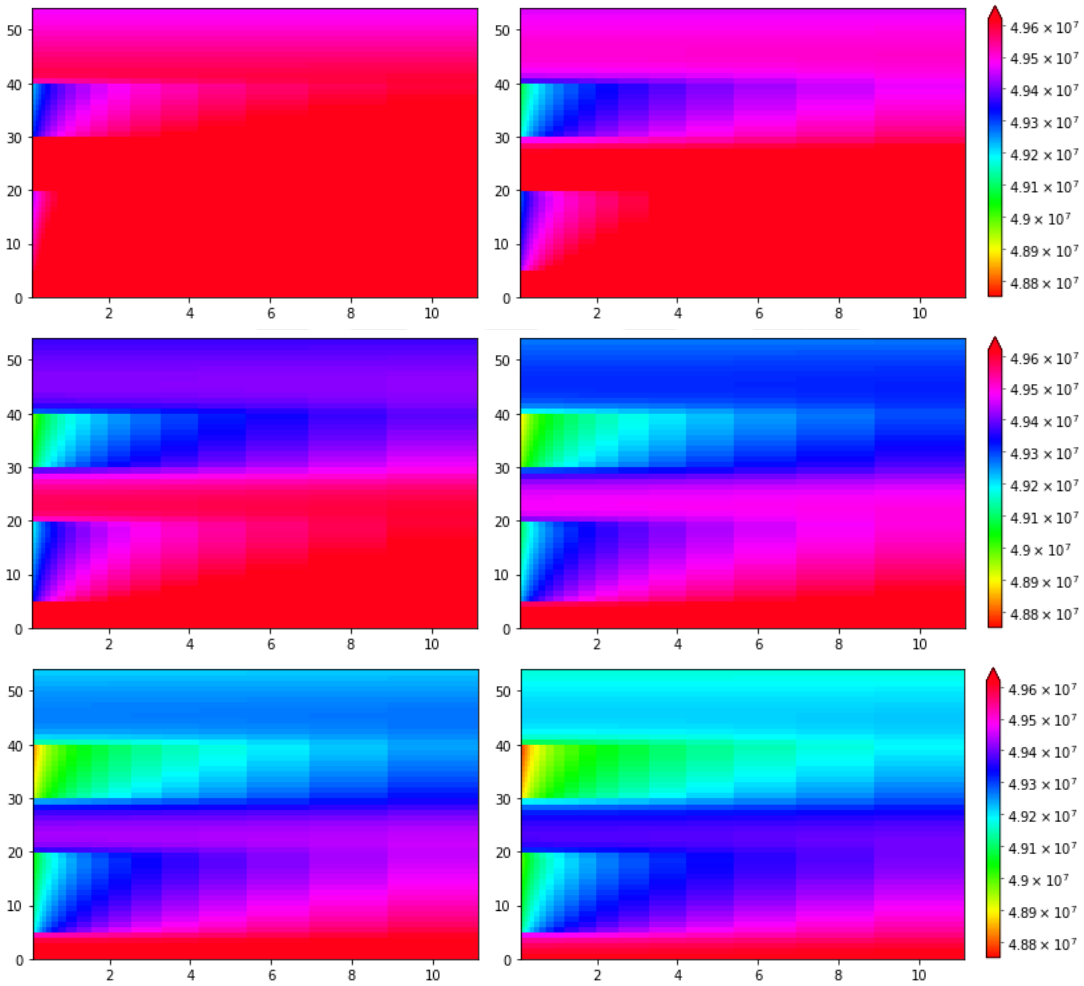

Figure 3.15: Reservoir pressure distribution (*r*-*z*) areal view from numerical simulator developed at different time steps during drawdown.

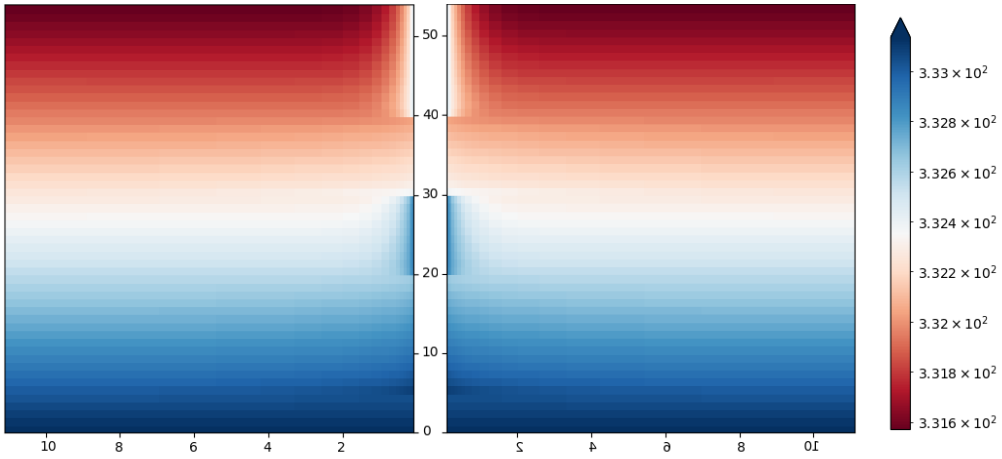

Figure 3.16: Reservoir temperature distribution (*r-z*) areal view from numerical simulator developed at the end of drawdown.

3.4.2.1 Heat loss effect on drawdown

Figure 3.17 shows the same comparison with commercial simulator as shown above in Figure 3.13 (left) with additional sandface temperature profiles for three different overall heat transfer coefficient values (U=30 W/m.s.K, U=60 W/m.s.K, U=120 W/m.s.K) used in numerical simulations. The cooling due to heat losses is obvious when the fluid travels towards the wellhead. In the treatment of numerical simulator developed, overall the heat transfer coefficient is constant. As expected, when the overall heat transfer coefficient is higher, the heat loss becomes larger, and temperature decreases at the corresponding gauge location. The drawdown sandface/wellbore temperatures show negligible changes at perforated intervals for different values at late-times of drawdown considered here. As discussed in previous chapter, the duration of the transition zone does not seem to change due to heat loss. The primary difference occurs in the buildup case such that when the overall transfer coefficient is larger, the temperature reaches the initial temperature much more quickly as expected, also leading to a shift in the temperature derivative. The speed of temperature propagation in drawdown is much faster than the temperature propagation during buildup because of convection. Conduction has negligible effects on drawdown temperatures while it becomes effective on late-time buildup sandface temperatures when the velocity of convective heat transfer inside the reservoir (u_{cr}) becomes zero.

As seen in Figure 3.17, the sandface temperature match against commercial simulator especially for unperforated layers could easily be improved by adjusting overall heat transfer coefficient in numerical simulations. However, it is not completely clear to us

how the commercial simulator treats the heat loss coefficient. Presumably, it is time-dependent.

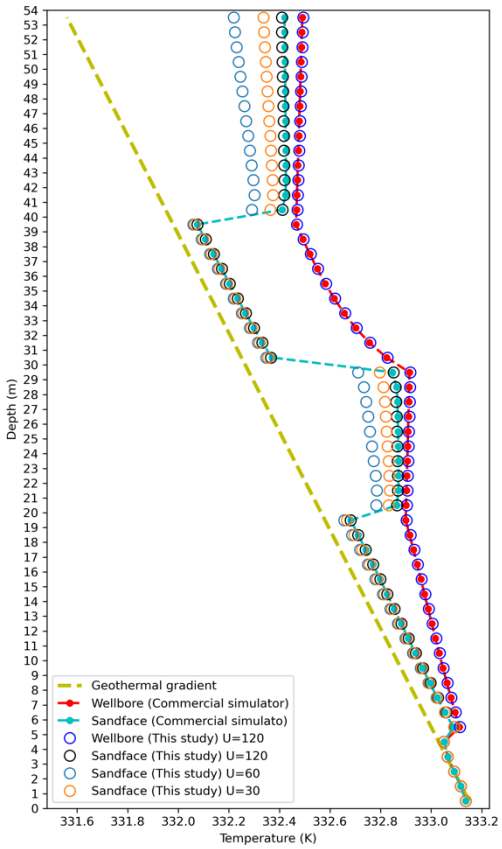

Figure 3.17: Comparison of wellbore/sandface temperatures across the wellbore for different overall heat loss coefficient values from numerical simulator developed and CMG-STARS at the end of drawdown.

3.4.3 Impact of Parameters

Now, we investigate the impact of the fluid and rock parameters on drawdown sandface and wellbore temperature responses across the wellbore using the numerical simulator developed with no skin effects. It is important to note the assumption single-phase fluid flow occurs in the place where the measurments are taken in the wellbore (from z=0 to z=54 m). Similarly, there are five main layers in the multi-layer system in which only two of them are perforated and called as producing zones. It is important to emphasize that the top, bottom and middle layers represent very low permeability regions (5 mD) which are sealed at the boundaries (k_z=0) with producing zones (flow is not permitted between producing zones and low permeability regions). We aim to imitate a typical field application in which multi reservoir zones with similar fluid and rock properties are generally open to flow across the wellbore. The important

parameters such as J-T coefficient, porosity, permeability, viscosity, flow rate, rock heat capacity, specific heat of fluid, well radius are listed in Table 3.4 to the order of magnitudes, and sensitivity to these values are inspected in detail on Cartesian plots of pressure and temperatures along with PLT plots. The distance between producing zones, mobility (kh/μ) and skin effects are also presented in this section. When investigating effects of each parameter, we keep all other parameters same as in Table 3.2. These parameters are changed either in both of the producing zones or in a single one. During sensitivity analysis, the producing zone with layers having higher permeability (300 mD) closer to wellhead is called as the upper zone whereas the producing zone with layers having lower permeability (100 mD) closer to bottom of the well is called as the lower zone.

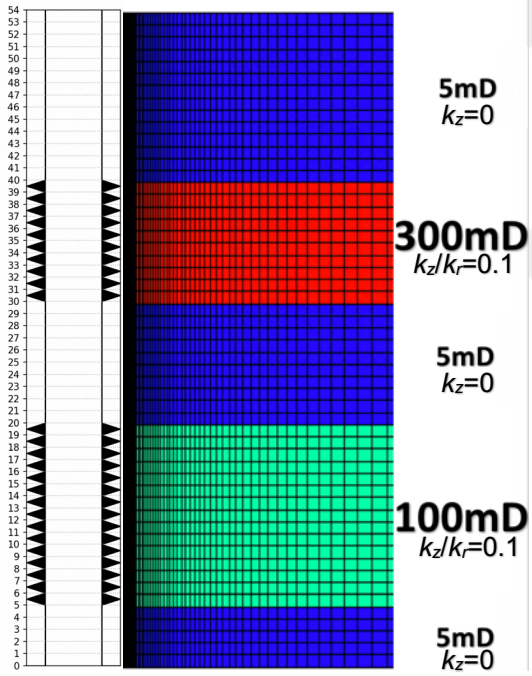

Figure 3.18: Schematic view of layer permeability on 2-D (r-z) plot for sensitivity.

Table 3.4: Parameters effecting numerical solutions for multi-layer system.

Parameters	Case 1	Case 2	Case 3
ε_{JT} (K.Pa)	-1.6×10^{-7}	-2×10^{-7}	-2.6×10^{-7}
ϕ	0.01	0.10	0.40
k (mD)	All layers$\times10^{-1}$	All layers$\times10^{0}$	All layers$\times10^{1}$
μ (Pa.s)	0.5×10^{-3}	1×10^{-3}	2×10^{-3}
q_{sc} (sm^3/D)	100	500	2500
$(\rho c_p)_m$ (J/m^3.K)	1.3×10^{6}	2.6×10^{6}	5.2×10^{6}
c_p (kg/J.K)	3073	4088	5437
r_w (m)	0.05	0.10	0.20

3.4.3.1 Effect of J-T coefficient

Figures E.1 through E.3 present wellbore (left) and sandface (right) temperature and pressure responses as well as inflow production profile across the wellbore at the end of the drawdown period for different J-T coefficient values given in Table 3.4. In Figure E.1, J-T coefficient is changed at both of the producing zones, whereas in Figures E.2 and E.3, J-T coefficient is changed only in the upper zone and only in the lower zone respectively. J-T coefficient changes occur only in reservoir model while having the same J-T coefficient (as in Case 2 of Table 3.4) in wellbore model ($\varepsilon_{JT} = -2\times10^{-7}$ K/Pa).

Clearly, significant changes in transient wellbore and sandface temperatures are observed for the entire producing horizon. Different temperature responses depending on the magnitude of the J-T coefficient which is negative for liquids, thus causing heating effect during drawdown. Although not shown here, at early-times, isentropic expansion/compression mechanism takes place where we would expect to see its physical effects as cooling during drawdown and heating during buildup.

All PLT plots seem to be identical for all cases considered for J-T coefficient as the different magnitude of J-T coefficient do not change the contribution of layers. Changes in J-T coeffients are not reflected in pressure plots as well. When the change occurs for both zones, it causes the same shift in sandface and wellbore temperatures although pressure drop in all cases seems to be same. However, when changes applied only in the upper zone, there exists no difference in wellbore temperatures until the bottom of the upper zone. This is expected since different J-T coefficients cause changes in sandface temperatures of upper zone. Thus, as higher fluid arrives at bottom of the upper zone, the effect of mixing of fluids with different temperatures are well reflected at wellbore temperatures. With higher the absolute value of J-T coefficient, cooling in the wellbore temperatures occur less. When J-T coefficient is changed only in the lower zone, the shift in wellbore temperatures starts from the bottom of the lower zone and carried out all the way to the top reflecting a slight distortion when mixing with the fluid that flows from upper zone into the wellbore. Although these cases are not realistic, they help to investigate how the fluid with different temperatures mix and move across the wellbore.

3.4.3.2 Effect of porosity

Figures E.4 through E.6 present wellbore (left) and sandface (right) temperature and pressure responses as well as inflow production profile across the wellbore at the end of the drawdown period for different porosity values given in Table 3.4. Similarly, in Figure E.4, porosity is changed for both zones, whereas in Figures E.5 and E.6, porosity is changed only in the upper zone and only in the lower zone respectively. As shown previously in derivations for sandface temperatures, increase in porosity means increase in isentropic expansion of the total system which causes more cooling for drawdown and more heating for buildup on early-time sandface temperature responses. This is followed by a slight shift on the late-time semi-log straight-line which reflects J-T coefficient effects. The wellbore temperatures indicate different behaviors when compared to sandface responses. The wellbore temperatures are mostly influenced by the effect of pressure changes due to different porosity values. Therefore, higher pressure drawdown with lower porosity values causes wellbore temperatures to decrease at early-times while increase at late-times. This is well reflected in wellbore and sandface temperatures as lower the porosity higher the increase in shift at temperature profiles are seen due to the higher pressure drops also observed at both wellbore and sandface pressure profiles.

When porosity changes for both zones, layer contributions are not affected thus all PLTs seem identical. When porosity is changed only in the lower or in the upper zone, there occurs differences in layer contributions reflected minimal in PLTs depending on the magnitude of pressure drop due to the change in porosity. When the upper zone's porosity is lower, leading to a higher drawdown, wellbore temperatures remain higher while effects on sandface temperature is negligible. When the porosity in the lower zone is smaller, leading to a higher drawdown, changes in both sandface and wellbore temperatures are almost negligible.

3.4.3.3 Effect of permeability and flow rate

Figures E.7 through E.9 present wellbore (left) and sandface (right) temperature and pressure responses as well as inflow production profile across the wellbore at the end of the drawdown period for different permeability values. The permeability for both zones (Figure E.7), only in the upper zone (Figure E.8), and only in the lower zone (Figure E.9) are multiplied by 0.1, 1, or 10 to create a contrast for surface flow of 500

sm^3/D. The magnitude of pressure drawdown determines temperature changes, i.e., higher permeabilities cause lower pressure drawdown in turn which decreases the effects of convection, isentropic expansion/compression and J-T heating/cooling on temperatures.

The layer contributions do not differ when all layer permeabilities are multipled with the same number as seen in PLT plot of Figure E.7. Wellbore pressure profiles indicate almost the same pressure drop (Δp) for each layer at the end of drawdown regardless of the layer permeability distribution. The whole system reaches to a stabilization regarding wellbore Δp that determines the amount of fluid withdrawal from individual layers. Therefore, the fluid extraction from an individual layer is directly proportional to the product of the mobility and the layer thickness. The lower zone has thickness of 15m and permeability of 100 mD while the upper zone has thickness of 10m and permeability of 300 mD. Thus, the contribution to flow from the upper zone is always expected to be double of the contribution from the lower zone when all permeabilities multipled by the same number as seen in Figure E.7. Simply, when either upper or lower zone has different permeability from the other one, fluid contribution reflected in PLT plot is controlled by the product of the mobility and the layer thickness as seen in Figures E.8 and E.9.

Although permeability in the upper zone is only changed in Figure E.8, wellbore temperatures in the lower zone indicate a clear shift because all layers are affected by the same wellbore Δp which in turn causes change in temperature. Depending on the Δp at corresponding layer, with J-T effects hotter fluid from reservoir enters into the wellbore and starts to move upwards and mixing colder reservoir fluid on the way to top. While the fluid moves upwards in the wellbore, extra pressure drop causes increase in temperature. This is clearly and always observed especially when the fluid passes through unperforated layers. When the fluid arrives to the bottom of the upper zone, mixing of fluids determines the changes in temperature from this point onwards. Therefore, the amount of fluid that enters from upper zone into the wellbore effects the temperatures. For instance, when the permeability in the upper zone is higher than the permerability in the lower zone as shown in Figure E.8, fluid contributions in the upper zone is significantly high as well, which in turn creates an exponential decrease on wellbore fluid temperature when mixing occurs at the corresponding depth. Similar behavior observed when the permeability in the lower zone is smaller than the

permeability in the upper zone as seen in Figure E.9. When the permeability in the lower zone is higher than the permeability in the upper zone, product of the mobility and the layer thickness gets higher which in turn causes higher fluid withdrawal from the lower zone when compared with withdrawal from the upper zone. Therefore, wellbore temperatures deviate slightly when mixing occurs at bottom of the upper zone.

To understand and have better insight into how flow rate effects well profiles and fluid contributions, in addition to Figures E.7 through E.9 in which surface flow rate is kept 500 sm^3/D, two additional cases with low (100 sm^3/D) and high (1000 sm^3/D) surface flow rate are considered in Figures E.10 through E.13 where permeability is similarly multiplied by 0.1, 1, or 10 to create a contrast only in the upper zone (Figures E.10 and E.12) and only in the lower zone (Figures E.11 and E.13) accordingly. On the other hand, Figure E.14 presents wellbore (left) and sandface (right) temperature and pressure responses as well as inflow production profile across the wellbore at the end of the drawdown period for different surface flow rate values (100 sm^3/D, 500 sm^3/D and 2500 sm^3/D). Similarly, as discussed previously for permeability effects, pressure drawdown becomes predominantly significant with increasing flow rates and controls the magnitude of temperature changes for drawdown.

3.4.3.4 Effect of viscosity

Figures E.15 through E.17 present wellbore (left) and sandface (right) temperature and pressure responses as well as inflow production profile across the wellbore at the end of the drawdown period for different viscosity values given in Table 3.4. Similarly, the viscosity for both zones (Figure E.15), only in the upper zone (Figure E.16), and only in the lower zone (Figure E.17) are changed. The effect of viscosity is similarly influenced by the scale of pressure changes in the opposite way of permeability effects, hence increasing viscosity increases temperatures to be observed during drawdown.

3.4.3.5 Effect of volumetric heat capacity of rock and specific heat capacity of reservoir fluid

Figures E.18 through E.20 present wellbore (left) and sandface (right) temperature and pressure responses as well as inflow production profile across the wellbore at the end of the drawdown period for different volumetric heat capacity of rock values $(\rho c_p)_m$ whereas Figures E.21 through E.23 shows the same comparison for different fluid

specific heat capacity. $(\rho c_p)_t$ product only appears in derivations as a multiplier of reservoir temperature in lumped sum product of volumetric heat capacity of fluid-saturated rock. Thus, wellbore temperatures look almost identical while sandface temperatures present some differences for the entire flow period especially for the unperforated layers. Temperature changes are quite minor for late-times of drawdown sandface temperatures when J-T coefficient effects are dominating over isentropic expansion/compression effects. When only lower or higher zone properties change for both parameters individually, changes observed in temperatures are not significant even though chosen values for investigation of the effect of these parameters are not realistic.

3.4.3.6 Effect of Well Radius

Figures E.24 through E.26 present wellbore (left) and sandface (right) temperature and pressure responses as well as inflow production profile across the wellbore at the end of the drawdown period for different well radius values at the end of drawdown. With larger well radius, the wellbore volume for the fluid to expand/compress gets bigger. The well profiles discussed here reflects the end of drawdown where J-T effects becomes dominant. Therefore, temperature shifts observed are mainly due to change in wellbore Δp. Similarly, different well radius values considered in the upper zone (Figure E.25) and lower zone (Figure E.26) to investigate complex completion designs when production is commigled from such a multi-layer system. The fluid contribution changes due to different surface area of wellbore reflected in PLT plots in minimal level. When the well radius in the upper zone is changed, the effect on wellbore Δp is much higher than when same changes of well radius applied only in the lower zone. However, it is not completely realistic to enlarge the well radius in upward direction. On the other hand, changes of well radius in the lower zone almost not exposed in wellbore temperatures of the upper zone.

3.4.3.7 Effect of the product of mobility and layer thickness (kh/μ)

We would like to emphasize the importance of the product of mobility and layer thickness on fluid contributions from each layer on PLT plots, although already discussed in detail at previous sections. Here, we consider four different completion design having the same value of the (kh/μ) product also tabulated in Table 3.5. Figures 3.19 and 3.20 present wellbore (left) and sandface (right) temperature responses,

whereas Figures 3.21 and 3.22 present wellbore (left) and sandface (right) pressure responses at the end of the drawdown period for four different completion design described in Table 3.5. Figure 3.23 presents inflow production profile across the wellbore for all cases together and indicates negligible differences regarding fluid contributions from individual layers. Furthermore, sandface temperatures follow the same linear gradient towards to the top of wellbore while wellbore temperatures show deviations depending on the different unperforated intervals in each case where J-T effects inside the wellbore observed due to pressure drop in upward direction.

Table 3.5: Description of different completions for multi-layer system.

Case No	Both layers	Lower layer		Upper layer	
	μ (cP)	k (mD)	h (m)	k (mD)	h (m)
1	0.5	100	15	150	10
2		150	10	100	15
3		75	20	300	5
4		300	5	75	20

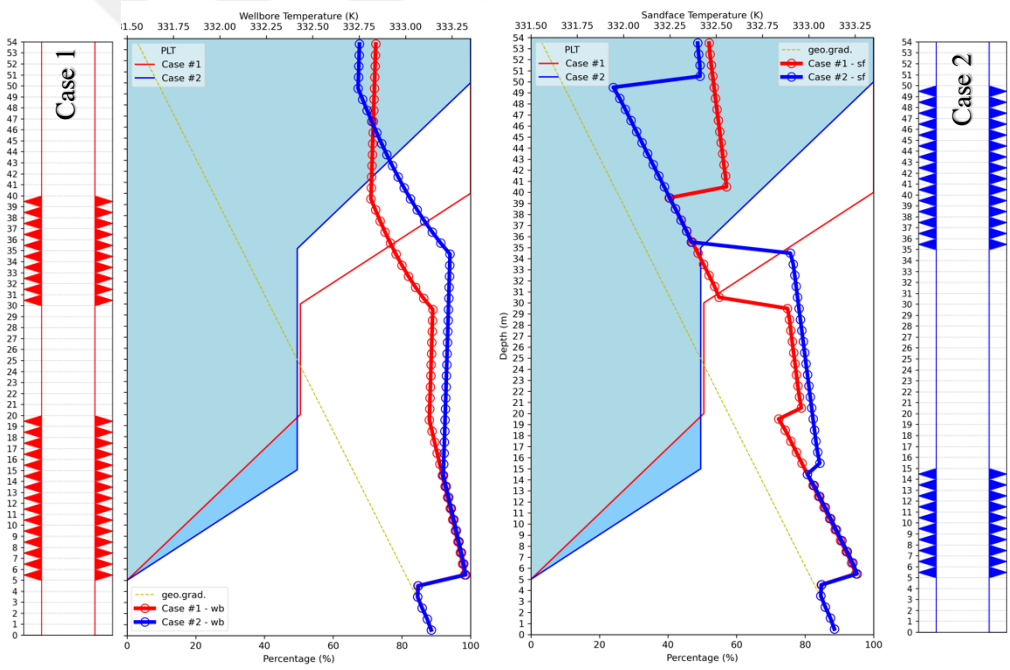

Figure 3.19: Comparison of wellbore/reservoir temperature profiles for Cases 1 and 2 at the end of drawdown.

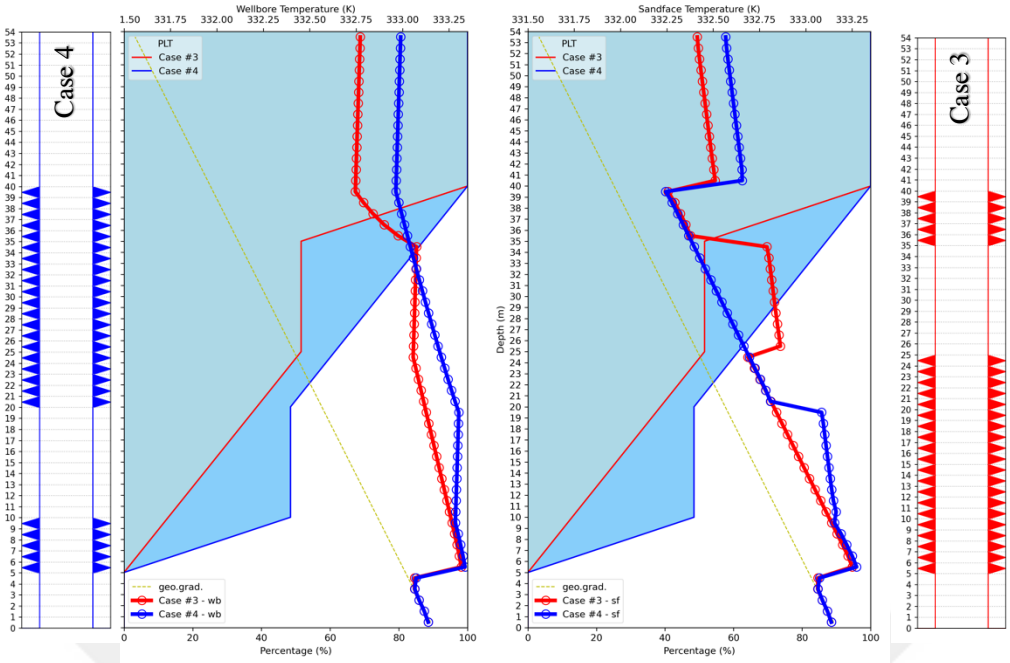

Figure 3.20: Comparison of wellbore/reservoir temperature profiles for Cases 3 and 4 at the end of drawdown.

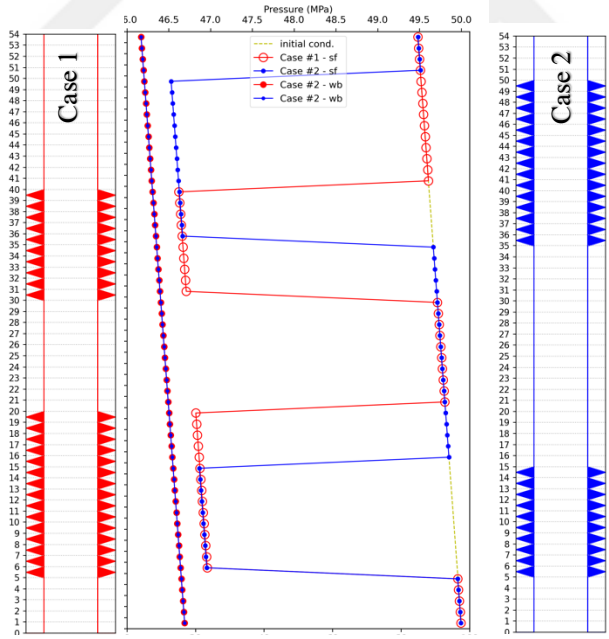

Figure 3.21: Comparison of wellbore/reservoir pressure profiles for Cases 1 and 2 at the end of drawdown.

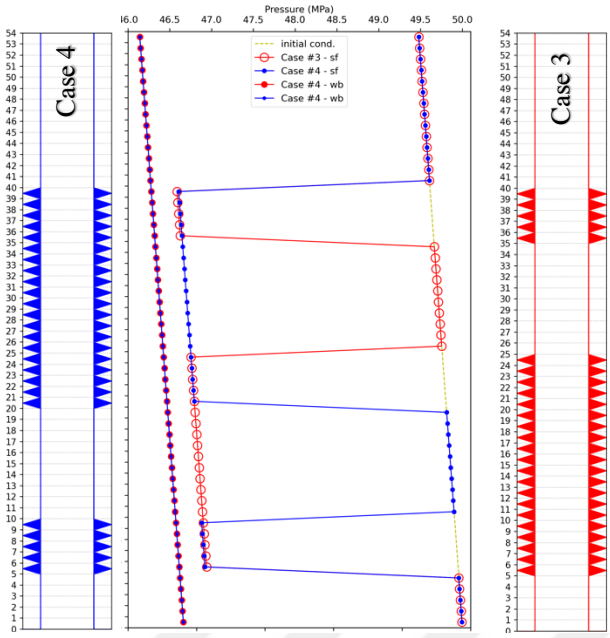

Figure 3.22: Comparison of wellbore/reservoir pressure profiles for Cases 3 and 4 at the end of drawdown.

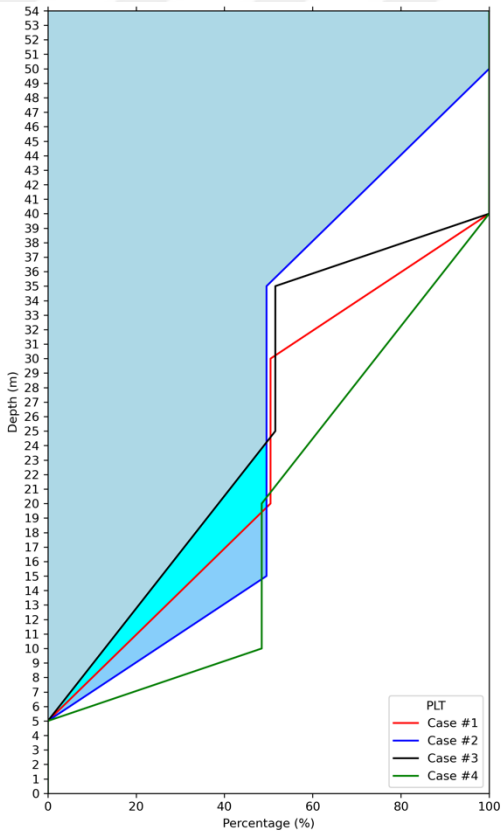

Figure 3.23: Inflow production profile across the wellbore for all cases at the end of drawdown.

3.4.3.8 Effect of distance between producing zones

Figures E.27 through E.30 present wellbore and sandface temperature (left) and pressure (right) responses as well as inflow production profile across the wellbore at the end of the drawdown period for four different distance (5 m, 10 m, 20 m and 30 m) between upper and lower zones at the end of drawdown. The properties of the upper or the lower zone such as permeability and layer thickness are taken the same values as discussed previously. Number of total layers are increased to 74 each having the same height of 1 m. Therefore, total wellbore length is also increased to 74 m. No significant changes observed except for the shift in wellbore temperatures in upward direction depending on the distance between upper and lower zones. Figure 3.24 also presents wellbore (left) and sandface (right) temperatures along with PLT plots for all cases together and indicates negligible differences when it comes to fluid contributions from individual layers. Wellbore temperatures do not differ until the fluid arrives to the bottom of the upper zone. A similar linear temperature gradient is observed clearly on sandface temperature responses. When the distance increases, the time for the fluid to travel upwards to the bottom of the upper layer increases causing higher pressure drop that is exposed in slight increase in temperature due to J-T effects in the wellbore. However, this increased is taken over by the mixing of different fluids in the wellbore starting from the bottom of the upper layer. As the upper layer gets further away from the lower zone, the fluid that enters into the wellbore at the corresponding depth is colder. Depending on the geothermal gradient, the mixing of fluids in the upper zone gets stabilized at different temperature values.

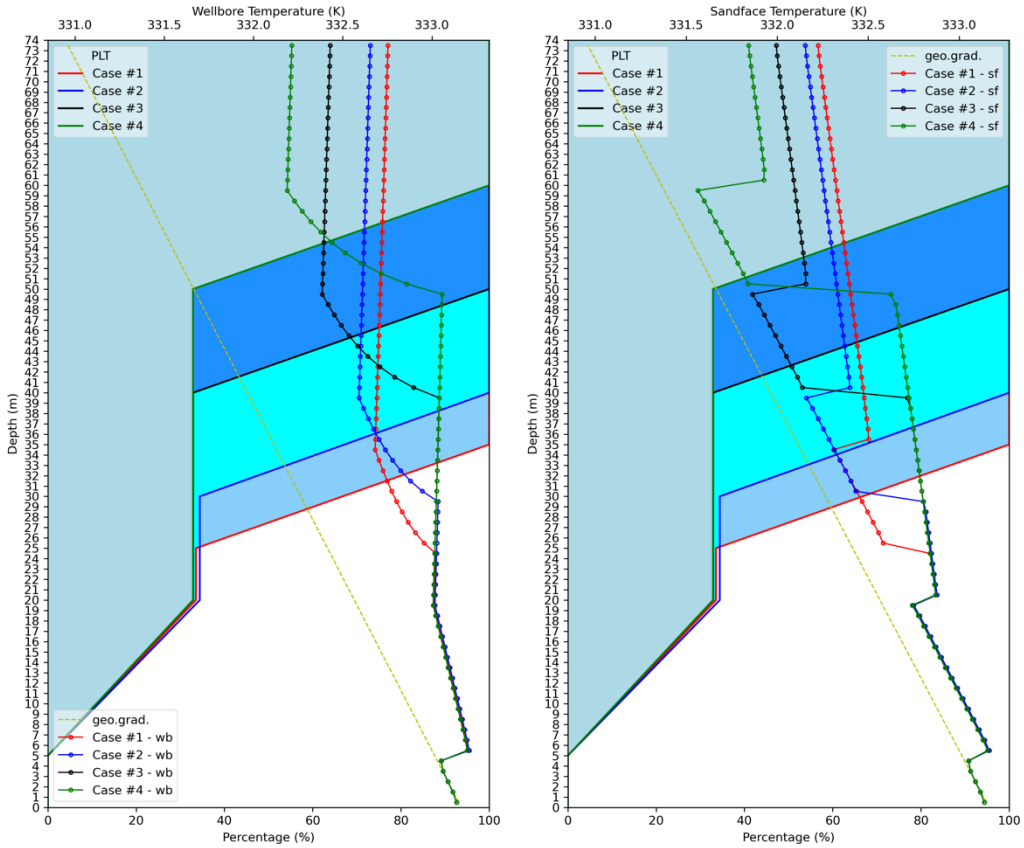

Figure 3.24: Comparison of wellbore/sandface temperatures and inflow production profile across the wellbore for all unperforated distances at the end of drawdown.

3.4.4 Impact of skin effects

As described earlier in detail, skin is modelled as a composite zone near the wellbore through the Hawkins formula (1956) given in Equation 2.6. For all skin cases considered for multi-layer system, the same skin radius is used (r_s=1m). All data used for generating pressure and temperature are kept the same as in previous section for sensitity analysis from Table 3.2 and Figure 3.18. In the presence of skin effects in which we considered s = -2, s = 5, s = 10 and s = 20, typically we assume that there is only a difference in the permeability between skin zone and non-skin zone.

3.4.4.1 Comparison of drawdown pressure and temperature solutions

Here we perform comparison for two different skin configurations. For the first skin case, the lower zone has a skin value of 5 and the upper zone has a skin value of 20 whereas for the second case, the lower zone has a negative skin value of -2 and the upper zone has a positive skin value of 10. Figures 3.25 and 3.26 shows the comparison of wellbore and reservoir temperatures (left) and pressures (right) against commercial software (CMG-STARS) along the wellbore at the end of drawdown for both skin

cases respectively. Both of the matches are almost exact. Figure 3.27 shows the inflow production profile across the wellbore from numerical simulator developed. As the skin permeability varies for both zones, flow contributions are observed accordingly in PLT plots. The lower zone both with negative skin value (Case 2) and with positive skin value (Case 1) contributes higher when compared with corresponding upper zones. Although not shown here, we investigated reservoir/wellbore temperature and pressure profiles across the wellbore at the end of drawdown for different fluid and rock properties with similar conclusions discussed so far are acquired. In general, the wellbore and sandface temperatures indicate similar behaviors as discussed previously. The intermediate and late time straight lines appear on semi-log plots after the early-time wellbore temperatures presented by different straight line with a similar slope and this extra heating mechanism that is not presented by sandface temperatures seems to dominate temperature behavior until the produced reservoir fluid reaches to the corresponding depth where we take measurements.

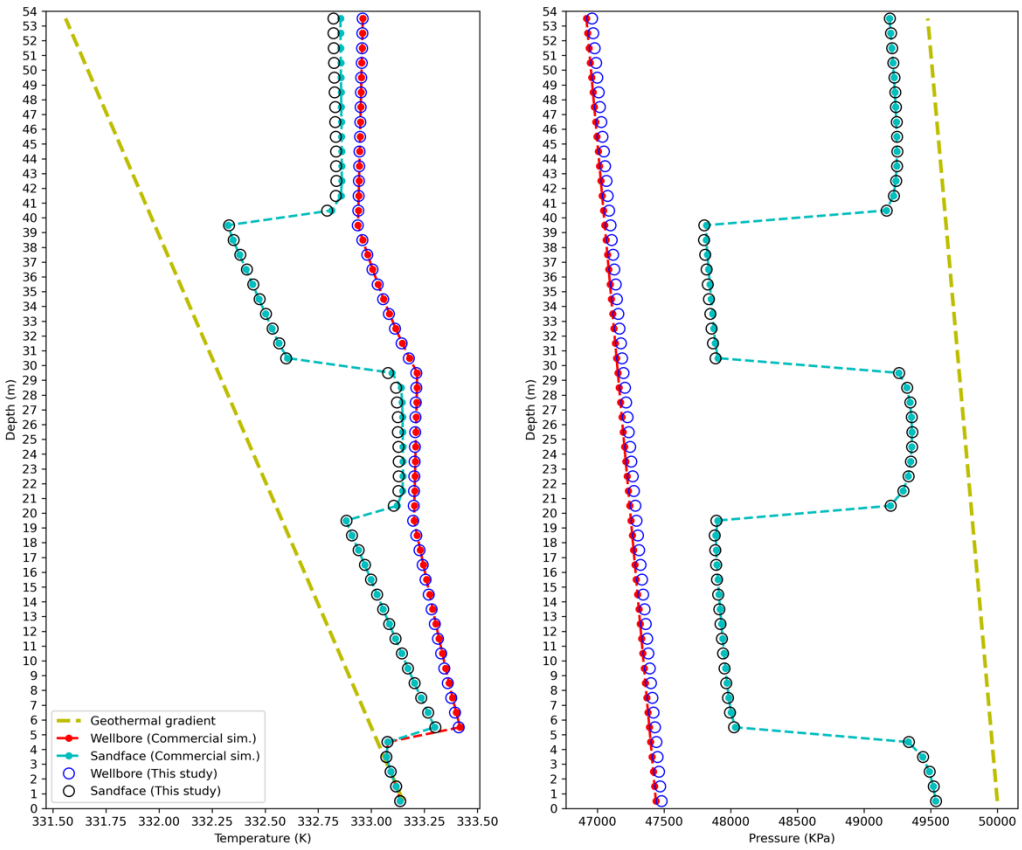

Figure 3.25: Comparison of wellbore/reservoir pressures and temperatures across the wellbore from numerical simulator developed and CMG-STARS for skin case 1 at the end of drawdown.

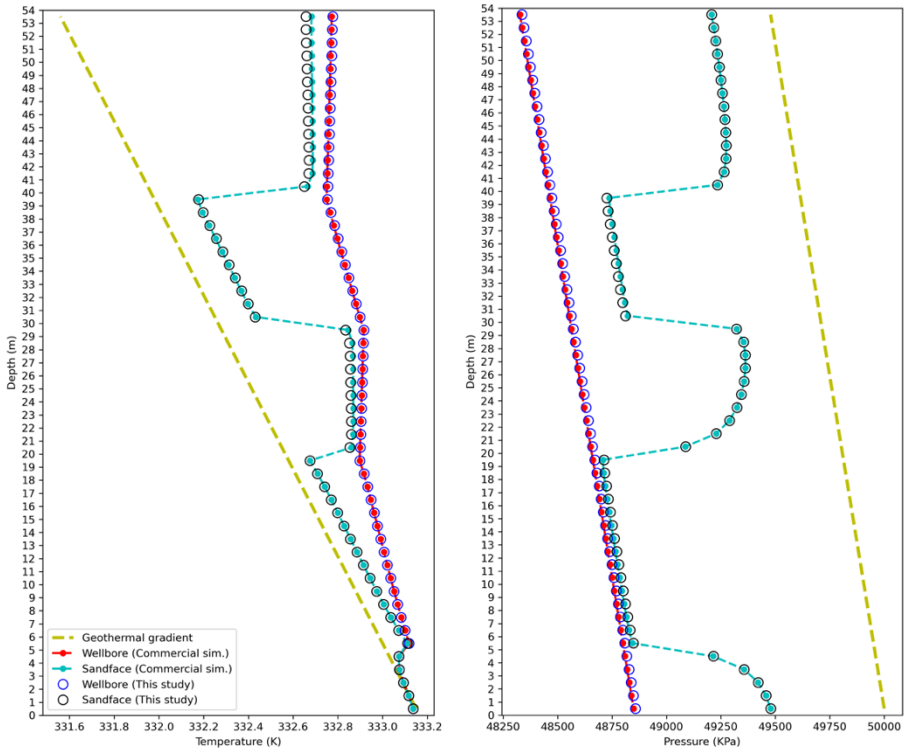

Figure 3.26: Comparison of wellbore/reservoir pressures and temperatures across the wellbore from numerical simulator developed and CMG-STARS for skin case 2 at the end of drawdown.

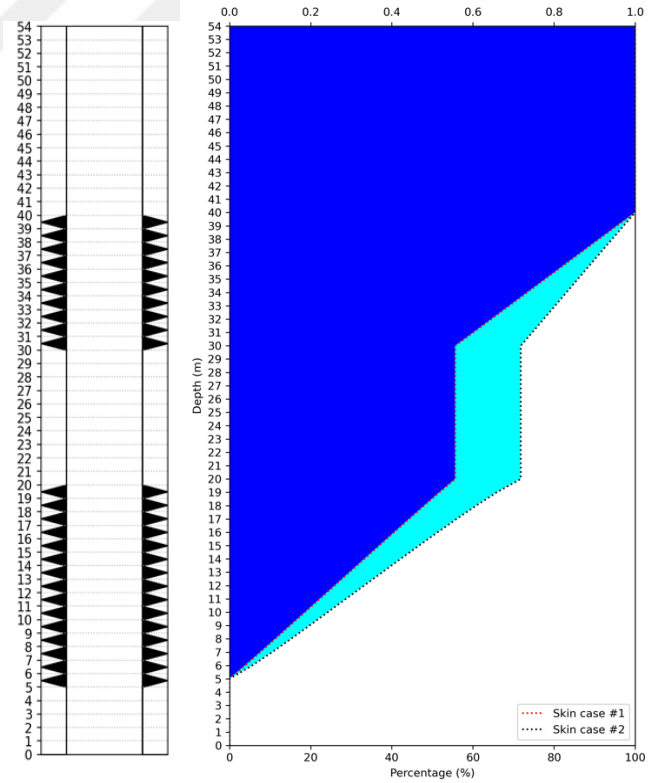

Figure 3.27: Inflow production profile across the wellbore from numerical simulator developed at the end of the drawdown for skin cases 1 and 2.

3.4.4.2 Sensitivity Analysis

Firstly, we investigate the skin effects by altering skin properties for both zones together. Figure E.31 presents wellbore (left) and sandface (right) temperature and pressure responses as well as inflow production profile across the wellbore at the end of the drawdown period for different skin values (s = -2, s = 5, s = 20 and s = 0). Then, similar to the cases discussed previously, we change skin properties only in the upper zone in Figure E.32 while keeping lower zone with no skin effects whereas Figure E.33 displays the vice versa in which skin properties in the lower zone are changed while the upper zone has no skin effects. The surface flow rate of 100 m^3/D is considered while building Figures E.31 through E.33. The same figures reproduced for the surface flow rate of 1000 sm^3/D in Figures E.34 through 3.36 to investigate different flow contributions in the presence of skin. Similar conclusions are obtained regarding different surface flow rates as discussed in detail previously. For all sensitivity cases with skin effects, there exists enough time for the intermediate and late time straight lines to appear on semi-log plots right after the early-time wellbore temperatures. The duration of drawdown may play important role especially in the presence of skin effects, which is discussed next.

3.4.4.3 Effect of drawdown time in the presence of skin effects

Figure 3.28 presents wellbore temperature profiles at different time steps starting from very early times till the end of flow whereas Figure 3.29 compares the drawdown sandface/wellbore temperatures in the lower zone (left) and upper zone (right) on semi-log plots from the numerical simulator developed as a function of shut-in time with no skin effects. The time step marked in each figure (0.123 hrs) nearly indicates the end of transition period and the reservoir response caused by the J-T phenomenon is observed and wellbore pressures seem to be stabilized around a certain wellbore Δp for all layers in the system. Figure 3.30 illustrates inflow production profiles across the wellbore at the same time steps values with no skin effects (left) and with skin effects (right) only in the upper zone (s = 20). Fluid contributions stabilizes quickly as the sandface and wellbore rates become equal. However, in the presence of skin effects, the time when the PLT measurements are taken is important as the fluid contributions varies significantly until (as marked, 6.5 hours) the second hump

(intermediate times) in the derivative disappears and the derivative becomes almost constant.

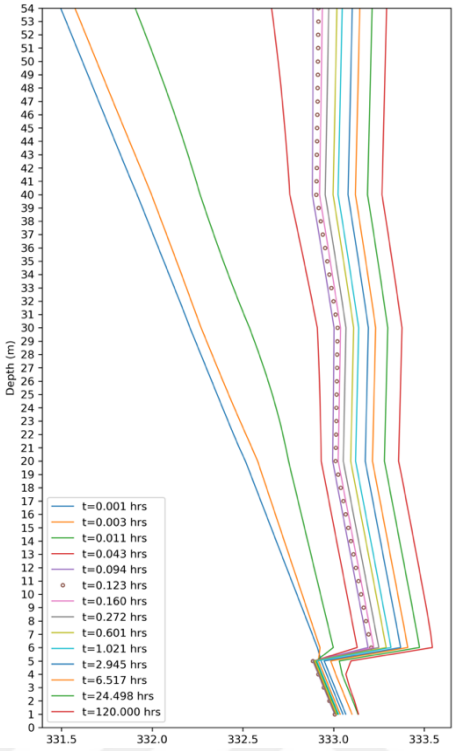

Figure 3.28: Comparison of wellbore temperature profile at different time steps during drawdown with no skin effects.

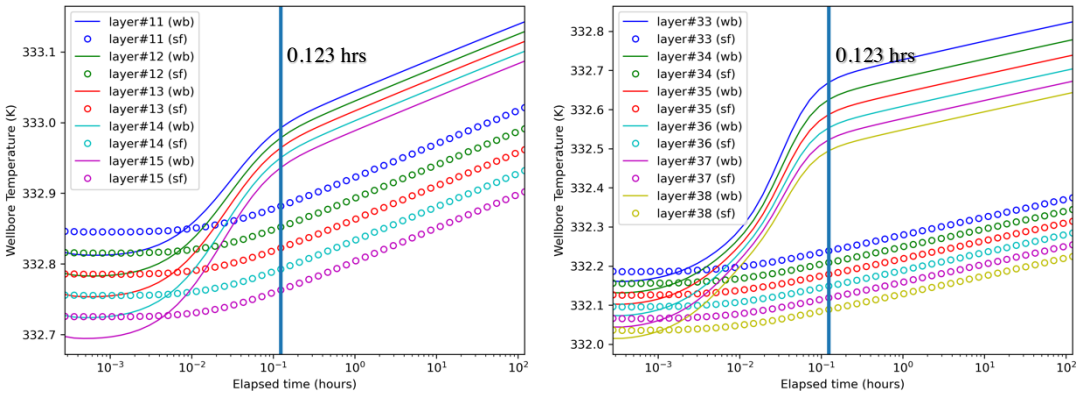

Figure 3.29: Comparison of transient wellbore and sandface temperatures in the middle layers of the lower zone (left) and the upper zone (right) in semi-log plot during drawdown with no skin effects.

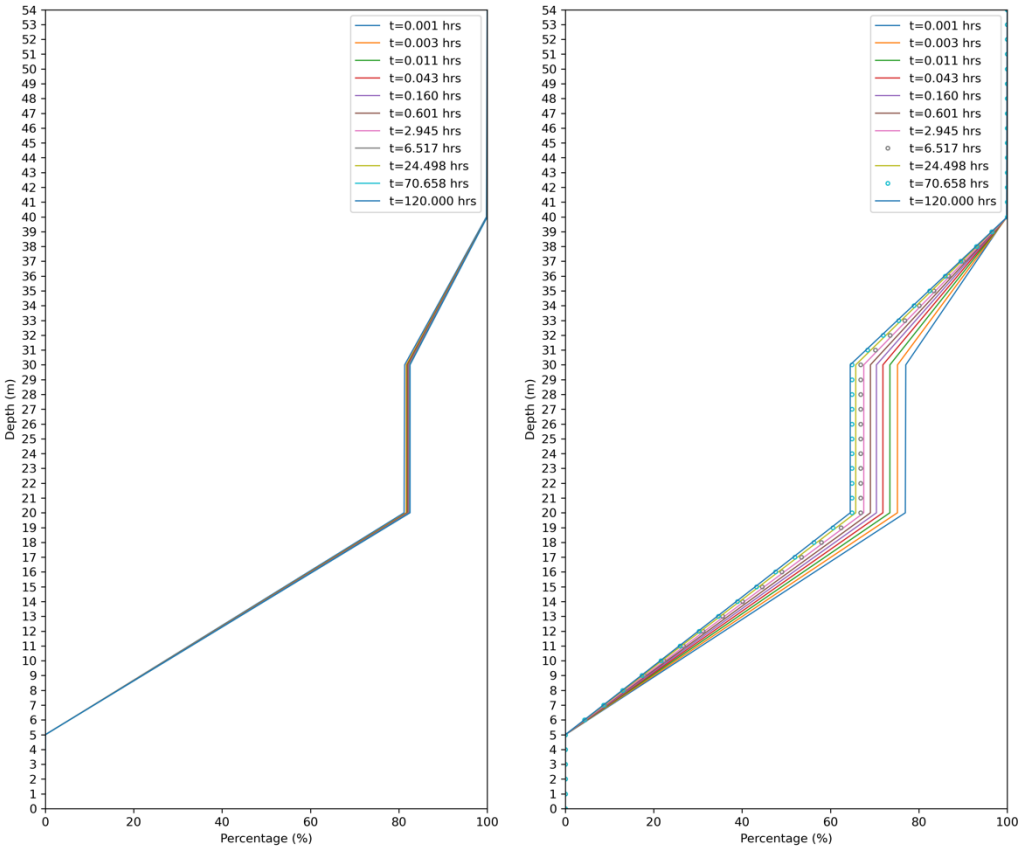

Figure 3.30: Comparison of inflow production profile across the wellbore at different time steps during drawdown for no skin effects (left) and with skin (s=20 only in the upper zone) (right).

3.4.5 Applications of multi-layer system

3.4.5.1 Variable rate test

A variable rate test is designed to demonstrate the capability of the numerical simulator developed. In Figure 3.31, flow rate history is plotted. Figure 3.32 shows wellbore pressure and temperature responses from the middle layer of upper and lower zones with respect to time on a Cartesian plot. Figure 3.33 presents wellbore temperature profiles (left) and pressure profiles (right) at the end of each drawdown period (2 days, 4 days and 8 days).

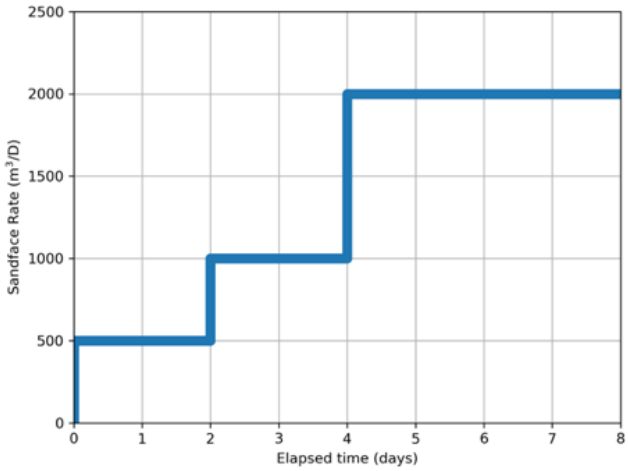

Figure 3.31: Surface flow rate history of variable rate test.

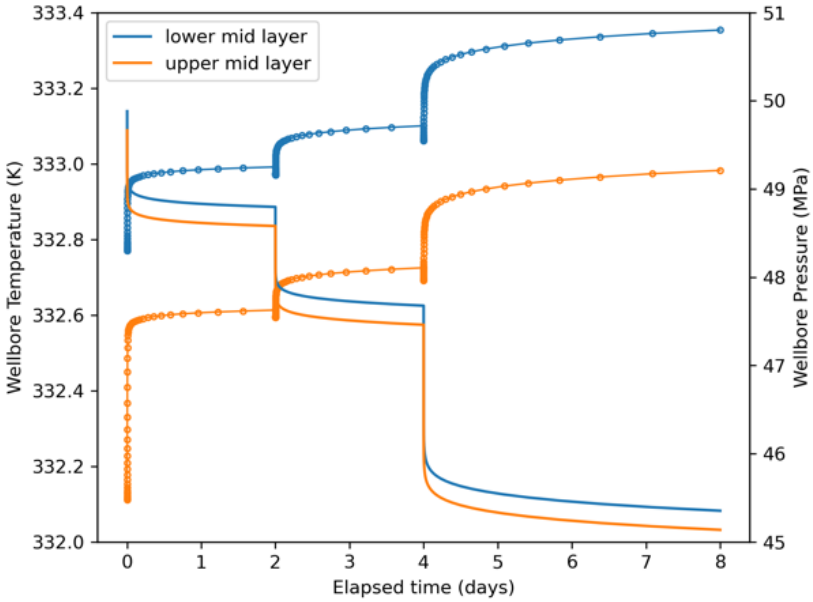

Figure 3.32: Wellbore temperatures and pressures during drawdown period of variable rate test.

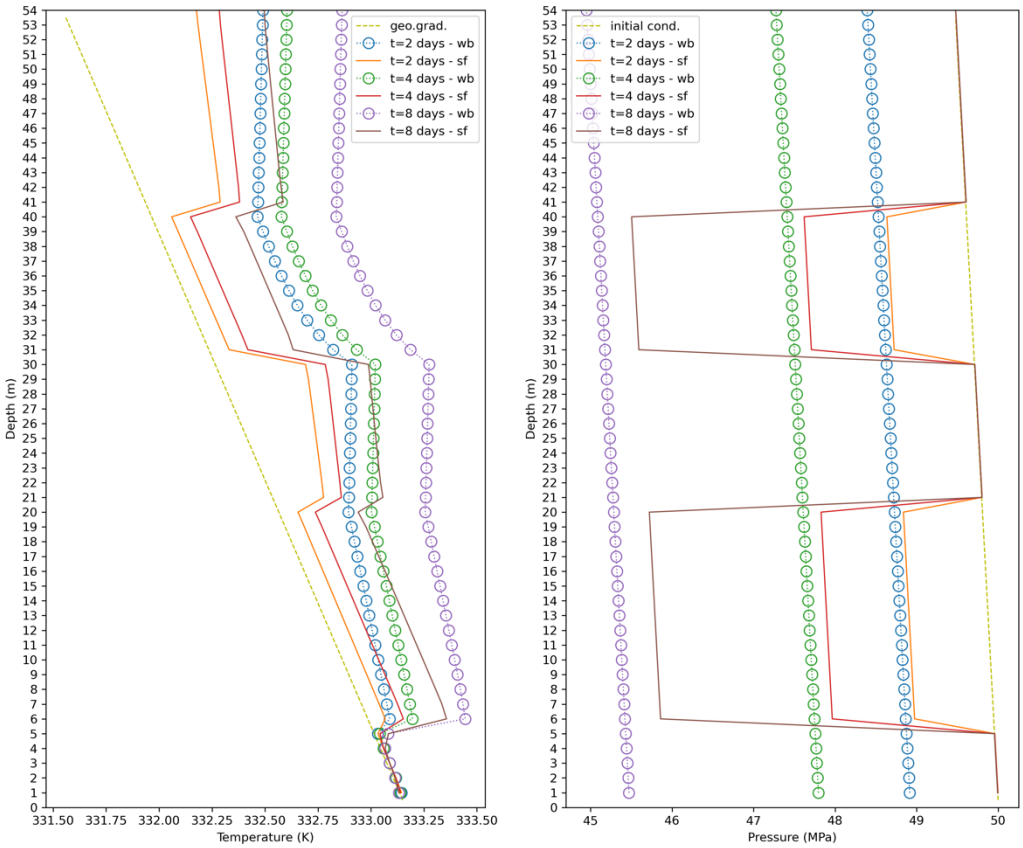

Figure 3.33: Comparison of wellbore and sandface temperature (left) and pressure (right) profile at different time steps for a variable rate test.

3.4.5.2 Plugged Perforations

During a lifetime of a well production, a number of perforations may have become plugged due to solid precipitation, scaling, build up of sand or etc. The well may need to be recompleted at above or below existing perforations. Production logging can show that wells produce from a smaller extent of the total interval due to ineffective plugged perforations. In the presence of DTS data from a well, wellbore temperature data over a vast amount of time may indicate certain behavior until the time when a significant pressure drop signal takes places and noticed. Here, a simulation model with the same properties considered for 3 years of constant production from both zones. After two years of production, one perforation (1 m of height) in the middle of the lower zone gets plugged and do not permit the flow into the wellbore until the end of simulation time. Figure 3.34 presents wellbore temperature profiles at different time steps starting from the first year followed by second year and so on. An anomaly can easily be captured at early times of the plugging and the signal is carried out thereafter.

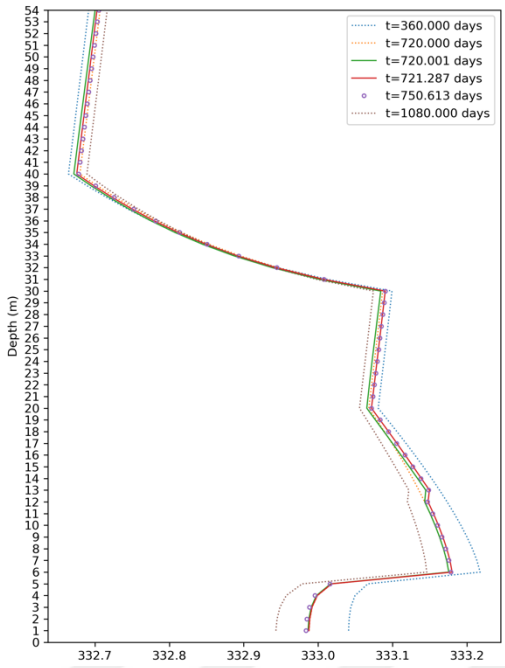

Figure 3.34: Comparison of wellbore temperature profile at different time steps during drawdown with plugged perforations after 2 years.

3.4.5.3 Parameter estimation

Levenberg-Marquardt algorithm is used to solve the nonlinear regression problem for minimizing the objective function given in Equation 2.9 in previous chapter. Here, the observed data is the wellbore temperature and pressure profile from bottom to the top of the wellbore. The model vector **m** may consist parameters as **m** = [$k_{r,j}$ s_j]. Here, we emphasis to use drawdown wellbore temperature and pressure data together for estimation of parameters that we cannot easily acquire from conventional well test applications such permeability of skin zone and non-skin zone of individual zones or layers. All input data used for generating pressure and temperature profiles are taken the same as in previous section for sensitivity analysis from Table 3.2 and Figure 3.12. The drawdown duration is decreased to 6 hours to imitate a real field PLT operation. 50 time steps are chosen for the numerical simulation. Skin radius does not change (r_s=1.06 m) and not included in the regression.

The observed data is the simulated temperature and pressure responses at all PLT data measurement locations for each pass (usually one or two consequent production period with different flow rate) across the producing horizon. The observed data used in non-linear regression may be increased if there exists more than a single drawdown during a PLT operation. We performed numerous regressions on estimating each parameter

shown in model vector **m** and the regression model generally estimated acceptably. Thus, drawdown wellbore temperature data provides good estimates when each of the layer permeability and the layer skin is investigated alone. However, in real field applications, we need to estimate most of them together. Therefore, if possible, we recommend to provide the nonlinear regression either layer permeability or the skin factor value. Therefore, the variance may be decreased in the estimated parameters as we reduce the number of parameters to estimate.

As in previous chapter, we do not discuss any procedures or graphical analyses to provide initial estimates to the nonlinear regression problem. Instead, we typically provide the bounds for each parameter to estimate as we already know the minimum and maximum values that each parameter can possibly take. Here, we investigated the importance of different initial estimates as well. Similarly, we corrupt the observed data obtained from the numerical simulation by using normally (Gaussian) distributed random errors with a standard deviation of 0.0025 K for temperature whereas 0.005 MPa for pressure.

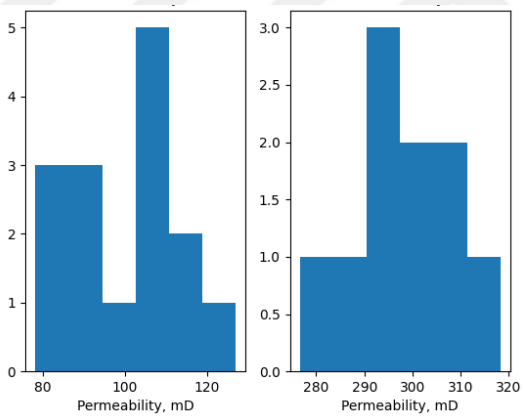

Figure 3.35: Histogram of layer permeability in the lower zone (left) and in the upper zone (right).

Regression results are listed together with cross-correlation coefficients matrix and confidence intervals when available to calculate. Figure 3.35 shows permeability histograms of lower (left) and upper (right) zones whereas Figure 3.36 presents schematic view of layer permeability on 2-D (*r*-z) plot. The mean value for permeability in the lower zone is 100 mD whereas 300 mD in the upper zone. Therefore, each layer having different permeability in the radial direction. However, we do not aim to estimate permebility and skin of each individual layer. Instead, the estimates from the regression are single permeability and single skin values for lower

and upper zones individually. Skin radius does not change (r_s=1.06 m) and not included in the regression. Typically, k_z/k_r is 0.1 and both zones are sealed, and not permiting flow from their boundaries.

There are three main cases discussed here. Each case considered the same PLT scenario in which a single pass run takes measurement with same production duration of 6 hours with constant surface flow rate of 500 sm^3/D. In the first case, layer permeabilities are regressed without any skin effects in the system whereas the second case includes skin effects with layer permeabilities and skin radius provided for regression. When intermediate radial flow occurring at the intermediate times is well observed on the derivative plot, it is possible to achieve good estimates for skin values of individual layers. The third case considers all layer properties as unknowns and perform the regression accordingly. In order to determine both layer permeability and layer skin, pressures and temperatures regressed together and results are tabulated in Table 3.11 in which the confidence intervals are not very high meaning all parameters are determined correctly.

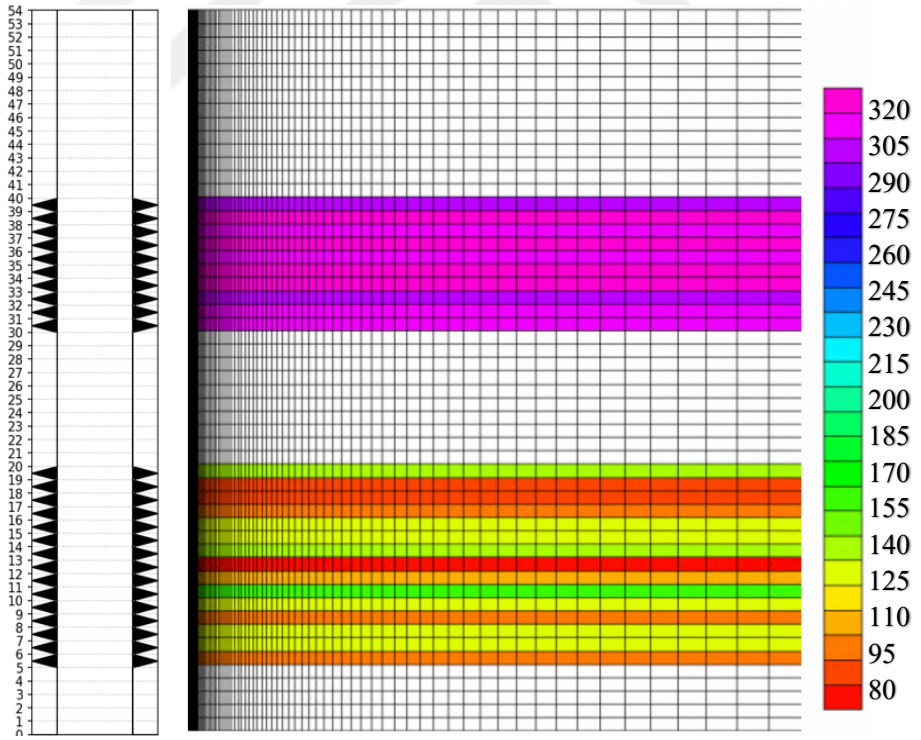

Figure 3.36: Schematic view of layer permeability on 2-D (*r-z*) plot.

For estimating only either layer permeability or layer skin, regression results using only temperature and using only pressure and using both temperature and pressure are also provided in Tables 3.6 through 3.10. Except for the regression with only pressure

in Table 3.8 and the regression of skin values in Tables 3.9 and 3.10, the estimates seem reasonable considering cross correlation coefficients and confidence intervals. Although not shown here, PLT data with multiple passes i.e., variable rate tests provide more observed data to the optimization problem, estimates did not significantly improve. Figure 3.37 presents the regressed wellbore/reservoir pressures and temperatures and inflow production profile across the wellbore in at the end of drawdown from the synthetic PLT data.

Table 3.6: Regression of layer permeability with no skin effects using temperature alone.

		Regressing *T* only					
		Initial Guess: 10 mD		Initial Guess: 100 mD		Initial Guess: 1000 mD	
	Observed Mean	Estimated	Conf. (%)	Estimated	Conf. (%)	Estimated	Conf. (%)
k_1 (mD) [Lower]	102.4	102.9	0.48	100.9	0.87	527.9	57.2
k_2 (mD) [Upper]	297.4	297.8	0.27	297.5	0.34	796.4	3.34
Cross corr. coeff.		-0.229		0.635		-0.981	

Table 3.7: Regression of layer permeability with no skin effects using both pressure and temperature together.

		Regressing *p*,*T* only					
		Initial Guess: 10 mD		Initial Guess: 100 mD		Initial Guess: 1000 mD	
	Observed Mean	Estimated	Conf. (%)	Estimated	Conf. (%)	Estimated	Conf. (%)
k_1 (mD) [Lower]	102.4	102.4	0.42	101.9	0.55	102.0	0.49
k_2 (mD) [Upper]	297.4	297.4	0.23	298.1	0.30	297.9	0.26
Cross corr. coeff.		-0.982		-0.987		-0.988	

Table 3.8: Regression of layer permeability with no skin effects using pressure only.

		Regressing *p* only					
		Initial Guess: 10 mD		Initial Guess: 100 mD		Initial Guess: 1000 mD	
	Observed Mean	Estimated	Conf. (%)	Estimated	Conf. (%)	Estimated	Conf. (%)
k_1 (mD) [Lower]	102.4	184.7	1.00	175.2	0.50	178.9	>100
k_2 (mD) [Upper]	297.4	171.0	1.56	184.9	0.74	179.7	>100
Cross corr. coeff.		-0.998		-0.994		-0.999	

Table 3.9: Regression of layer skin value using temperature alone.

		Regressing *T* only			
		Initial Guess: 30		Initial Guess: 0	
	Observed	Estimated	Conf. (%)	Estimated	Conf. (%)
s_1 [Lower]	5	8.98	8.11	0.38	>100
s_2 [Upper]	20	13.33	4.88	0.44	>100
Cross corr. coeff.		-0.869		-0.691	

Table 3.10: Regression of layer skin value using both pressure and temperature together.

		Regressing *p*,*T* together			
		Initial Guess: 30		Initial Guess: 0	
	Observed	Estimated	Conf. (%)	Estimated	Conf. (%)
s_1 [Lower]	5	4.96	0.59	4.92	0.71
s_2 [Upper]	20	19.63	0.40	19.73	0.48
Cross corr. coeff.		-0.997		-0.997	

Table 3.11: Regression of layer permeability and skin values using both pressure and temperature together.

	Observed	Estimated	Conf. (%)	Bounds	Initial guess
k_1 (mD) [Lower]	102.4	98.8	2.44	[1 to 10,000]	10,000
k_2 (mD) [Upper]	297.4	344.9	11.59	[1 to 10,000]	10,000
s_1 [Lower]	5	5.02	0.64	[0 to 30]	0
s_2 [Upper]	20	23.02	11.79	[0 to 30]	0
r_s (m)	1.06	(Not regressed)			

Cross correlation coeffients

	k_1	k_2	s_1	s_2
k_1	1	0.993	0.404	-0.989
k_2	0.993	1	-0.374	0.999
s_1	0.404	-0.374	1	-0.393
s_2	-0.989	0.999	-0.393	1

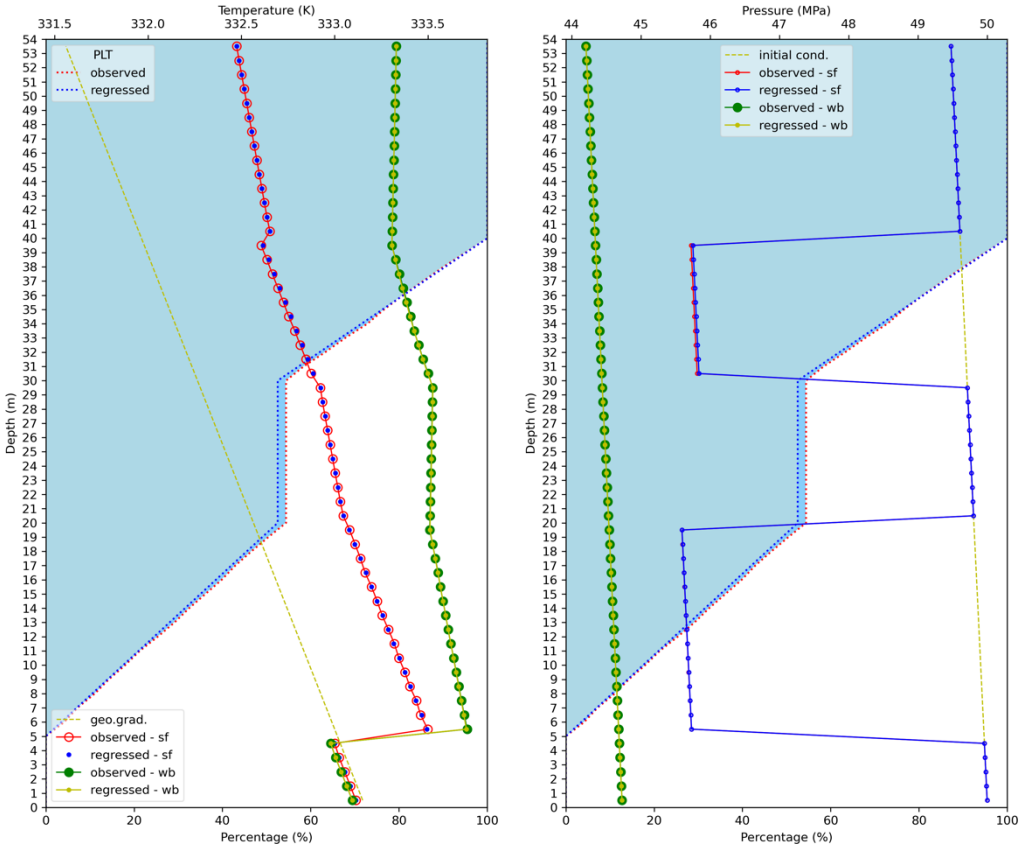

Figure 3.37: Comparison of wellbore pressures and temperatures and inflow production profile at the end of drawdown for Case 3.

4. CONCLUSIONS

This study has presented a transient single-phase, non-isothermal model that simulates the wellbore/reservoir system to resolve pressure, temperature, and rate changes within the wellbore. The wellbore model is coupled with a cylindrical reservoir simulator at the bottom of the well through the mass, momentum, and energy balance equations. The wellbore model accurately simulates the wellbore effects during transient and steady state production and shut-in periods. We have synthesized the prior knowledge based on sandface temperature responses and investigated the information content of wellbore temperature transients from the gauge depth where the actual measurements are made. A new set of diagnostic plots for the temperature transients have been presented. A semilog plot of the temperature difference and the logarithmic derivative of temperature versus time is presented to provide a diagnostic tool for model identification since both signals have the same unit and magnitude. Based on the findings, following conclusions are drawn.

- During a well testing operation where the gauge recordings are obtained at a certain distance above the producing horizon, the wellbore phenomena is indicated with a hump in temperature derivative on the proposed diagnostic plots. For typical gauge locations, after the wellbore transition period, reservoir response is observed during drawdown. Buildup temperatures are mainly influenced by the wellbore phenomena and heat losses to the surrounding formation at gauge location.
- During well test analysis, the drawdown pressure data are usually not considered due to the well-known adverse characteristics, however, drawdown temperature data could provide useful insight and help to understand the well/reservoir system analyzed together with pressure buildup as shown in the history matching of the field data.
- An effective well radius is needed for history matching due to the placement of many tools in wellbore during a conventional well testing that would reduce the fluid volume in the wellbore. This parameter is an unknown and estimated through history matching.

- Unlike the pressure transients, the temperature transients have a better resolution in the near wellbore region.
- A hybrid transient data analysis is proposed here where the temperature transient analysis (TTA) is coupled with PTA to provide a more reliable and robust characterization of the near-wellbore properties. Through nonlinear regression, the reservoir and skin-zone parameters can be estimated reliably even with some noise in history matching pressure and temperature data together.
- With visualization features of the developed simulator discussed in the study, applications to various reservoir models with different flow rate histories are excellent educational experience for petroleum engineers to have a better insight into how temperature transients move in a reservoir due to various parameters and multiple observation points in homogeneous reservoirs as well as heterogeneous.

There are numerous conclusions and concerns stated under each comparison and application cases. Some recommendations which may be used for more advanced studies outlined below as:

- Thorough sensitivity studies on multi-layer systems by constructing 2-D (r-z) coupled model indicates beneficial remarks on PLT data and well profile outputs that are mostly influenced by input parameters, such as the layer petrophysical properties and the layer thermal parameters on which rigorously modeled representative PVT plays the most significant role by controling J-T coefficient through the density variations. Several example of regression on temperature and pressure from multi-layer systems are considered for demonstrating the utility of the developed simulator. Due to high number of parameters involved in multi-layer systems, a robust characterization on thermal and rock properties are required to be able to achieve a realistic regression on temperature profiles to compute inflow rates of individual layers.
- The simulator could be used for designing a PLT operation when the field operation meets the limitation of the simulator such as single phase fluid flow having vertical well equipped with a thorough fluid characterization (EOS). Such design tests may provide a good source for:
    - Cross-check PLT plots and validate the fluid contributions from layers that are open to flow.

- Indication of wrong estimations from PLT plots acquired in field operations. There exist numerous reasons for the mechanical tool for failure during field operations. The simulator may help to recover or help to fix part of the field data. It is quite common that the spinner of the field PLT tool may not operate properly at very low flow rates. Also, the spinner may fail to calculate and construct PLT plots accurately at very high flow rates.
- AI applications to predict PLT plots from available field data such as pressure and temperature measurements by using the simulator results. Although not mentioned in this study, an AI workflow is generated and predictions are studied for validation of representative PLT data from numerous syntetic wellbore temperature and pressure data. Further study is highly recommended since there exists strong merit especially on calculation of the ratio of individual layer contributions.
- Indication of unsolicited restriction to flow from the reservoir into the wellbore caused by plugged perforations or completion failure. 2-D (*r-z*) simulator can easily capture any kind of distortions over a vast period of time. Throught sensitivity analysis is provided in this study specifically focus on the parameters that affects wellbore temperatures.

- Simulator may be improved further to obtain pressure solutions for three dimensional problems by adding the flow in the theta (θ) direction. In such case, packer-probe and probe-probe IPTT tests would be modeled entirely.
- Heterogeneity would be modeled in *r-z* cylindrical reservoirs and investigate the pressure propagations throughout the reservoir.

REFERENCES

Alves, I. N., Alhanati, F. J. S., and Shoham, O. (1992). A unified model for predicting flowing temperature distribution in wellbores and pipelines. *SPE production Engineering*, *7* (04), 363-367.

Amara, M., Capatina, D., and Lizaik, L. (2009). Coupling of Darcy–Forchheimer and compressible Navier–Stokes equations with heat transfer. *SIAM Journal on Scientific Computing*, *31* (2), 1470-1499.

App, J. F. (2010). Nonisothermal and productivity behavior of high-pressure reservoirs. *Spe Journal*, *15* (01), 50-63. doi:10.2118/114705-PA.

App, J. (2017). Permeability, skin, and inflow-profile estimation from production-logging-tool temperature traces. *Spe Journal*, *22* (04), 1123-1133. doi:10.2118/174910-PA.

Bird, R. B., Stewart, W. E., and Lightfoot, E. L. (1960). *Transport phenomena*. New York: John Wiley & Sons Inc.

Bourdet, D. (2002). *Well test analysis: the use of advanced interpretation models*. Elsevier.

Cao, H. (2002). *Development of Techniques for General Purpose Simulators* (Doctoral dissertation), Stanford University, Palo Alto, CA.

Chekalyuk, E. B. (1965). *Thermodynamics of Oil Formation, in Russian*. Nedra, Moscow.

CMG-STARS (2020). (Version 2020.10.7557.49333) [Computer Software] Advanced Process and Thermal Reservoir Simulator. Alberta, Canada: Computer Modelling Group Ltd.

Colebrook, C. F. (1939). Turbulent Flow in Pipes with Particular Reference to the Transition Region between Smooth and Rough Pipe Laws. *J Inst of Civil Engrs, 11* (4), 133-156. doi:10.1680/ijoti.1939.13150.

Curtis, M. R., and Witterholt, E. J. (1973). Use of the temperature log for determining flow rates in producing wells. In *Fall Meeting of the Society of Petroleum Engineers of AIME*, Las Vegas, Nevada, USA, 30 September-3 October. doi:10.2118/4637-MS.

Duru, O. O., and Horne, R. N. (2010a). Modeling Reservoir Temperature Transients and Reservoir-Parameter Estimation Constrained to the Model. *SPE Res Eval & Eng*, *13* (6), 873-883. doi:10.2118/115791-PA.

Duru, O. O., and Horne, R. N. (2010b). Joint inversion of temperature and pressure measurements for estimation of permeability and porosity fields. In *SPE Annual Technical Conference and Exhibition*, Florence, Italy, 19-22 September. doi:10.2118/134290-MS.

Duru, O. O., and Horne, R. N. (2011a). Simultaneous Interpretation of Pressure, Temperature, and Flow-Rate Data Using Bayesian Inversion Methods. *SPE Res Eval & Eng*, *14* (2), 225-238. doi:10.2118/124827-PA.

Duru, O. O., and Horne, R. N. (2011b). Combined Temperature and Pressure Data Interpretation: Applications to Characterization of Near-Wellbore Reservoir Structures. In *SPE Annual Technical Conference and Exhibition*, Denver, Colorado, USA, 30 October-2 November. doi:10.2118/146614-MS.

Flynn, T. (2004). *Cryogenic engineering, revised and expanded*. CRC Press.

Forouzanfar F., Pires A. P., and Reynolds A. C. (2015). Formulation of a Transient Multi-Phase Thermal Compositional Wellbore Model and its Coupling with a Thermal Compositional Reservoir Simulator. In *SPE Annual Technical Conference and Exhibition*, Houston, Texas, USA, 28-30 September 2015. doi:10.2118/174749-MS.

Galvao, M. S., Carvalho, M. S., and Barreto, A. B. Jr. (2019). A Coupled Transient-Wellbore/Reservoir Temperature Analytical Model. *SPE J.*, *24* (05), 2335–2361. doi:10.2118/195592-PA.

Garg, S. K., and Pritchett, J. W. (1977). On Pressure-Work, Viscous Dissipation and the Energy Balance Relation for Geothermal Reservoirs. *Adv Water Resour*, *1* (1), 41-47. doi:10.1016/0309-1708(77)90007-0.

Garg, S. K., and Pritchett, J. W. (1984). Pressure transient analysis for hot water geothermal wells. *Groundwater Hydraulics*, *9*, 242-255.

Hagoort, J. (2004). Ramey's wellbore heat transmission revisited. *SPE journal*, *9* (04), 465-474. doi:10.2118/87305-PA.

Han C., Delshad M., Sepehrnoori K., and Pope G.A. (2005). A fully implicit, parallel, compositional chemical flooding simulator. In *SPE Annual Technical Conference and Exhibition*, Dallas, Texas, 9–12 October 2005. doi:10.2118/97217-MS.

Hasan, A. R. and Kabir, C. S. (1994). Aspects of Wellbore Heat Transfer During Two-Phase Flow. *SPE Prod & Fac*, *9* (3), 211-216. doi:10.2118/22948-PA.

Hasan, A. R., Kabir, C. S., and Wang, X. (1997). Development and Application of a Wellbore/Reservoir Simulator for Testing Oil Wells. *SPE Form Eval, 12* (3), 182–188. doi:10.2118/ 29892-PA.

Hasan, A. R., and Kabir, C. S. (2002). *Fluid Flow and Heat Transfer in Wellbores*. Richardson, Texas, USA: SPE.

Hasan, A. R., Kabir, C. S., and Lin, D. (2005). Analytic Wellbore-Temperature Model for Transient Gas-Well Testing. *SPE Res Eval & Eng, 8* (3), 240-247. doi:10.2118/84288-PA.

Hawkins, M. F. Jr. (1956). A note on the skin effect. *J Pet Technol*, *8* (12), 65–66.

International Association for the Properties of Water and Steam (IAPWS) (2018). Revised Release (Version R6-95) on the IAPWS Formulation 1995 for the Thermodynamic Properties of Ordinary Water Substance for General and Scientific Use.

Izgec, B., Kabir, C. S., Zhu, D., and Hasan, A. R. (2007). Transient Fluid and Heat Flow Modeling in Coupled Wellbore/Reservoir Systems, *SPE Res Eval & Eng*, *10* (3), 294-301. doi:10.2118/102070-PA.

Jiang, Y. (2007). *A Flexible Computational Framework for Efficient Integrated Simulation of Advanced Wells and Unstructured Reservoir Models* (Doctoral dissertation), Stanford University, Palo Alto, CA.

Kappa (2020). (Version v5.20.03) [Computer Software] Sophia Antipolis, France: Kappa Engineering.

Livescu, S., Durlofsky, L.J., Aziz, K., and Ginestra, J.C. (2010). A fully-coupled thermal multiphase wellbore flow model for use in reservoir simulation. *J Pet Sci Eng*, *71* (3–4), 138–146. doi:10.1016/j.petrol.2009.11.022.

Newville, M., Stensitzki, T., Allen, D. B., and Ingargiola, A. (2014). LMFIT: Non-Linear Least-Square Minimization and Curve-Fitting for Python (Version 0.8.0) [Software]. Available from doi:10.5281/zenodo.11813.

Onur, M. and Cinar, M. (2016). Temperature Transient Analysis of Slightly Compressible, Single Phase Reservoirs. In *SPE Europec featured at 78th EAGE Conference and Exhibition*, Vienna, Austria, 30 May-2 June. doi:10.2118/180074-MS.

Onur, M., Palabiyik, Y., Tureyen, O. I., and Cinar, M. (2016a). Transient temperature behavior and analysis of single-phase liquid-water geothermal reservoirs during drawdown and buildup tests: Part II. Interpretation and analysis methodology with applications, *J Pet Sci Eng, 146*, 657-669. doi:10.1016/j.petrol.2016.08.002.

Onur, M., Ulker, G., Kocak, S., and Gok I. M. (2016b). Interpretation and Analysis of Transient Sandface and Wellbore Temperature Data. In *SPE Annual Technical Conference and Exhibition*, Dubai, United Arab Emirates, 26-28 September. doi:10.2118/181710-MS.

Onur, M. (2017). Modeling and Interpretation of the Bottomhole Temperature Transient Data. In *SPE Latin America and Caribbean Petroleum Engineering Conference*, Buenos Aires, Argentina, 18-19 May 2017. SPE-185586-MS. doi:10.2118/185586-MS.

Onur, M., Ulker, G., Kocak, S., and Gok I. M. (2017). Interpretation and Analysis of Transient-Sandface and Wellbore-Temperature Data. *SPE J.*, *22* (4), 1156–1177. doi:10.2118/181710-PA.

Onur, M. and Cinar, M. (2017a). Analysis of Sandface-Temperature-Transient Data for Slightly Compressible, Single-Phase Reservoirs. *SPE J.*, *22* (4): 1134–1155. doi:10.2118/180074-PA.

Onur, M. and Cinar, M. (2017b). Modeling and analysis of Temperature Transient Sandface and Wellbore Temperature Data from Variable Rate Well Test Data. In *SPE Europec featured at 79th EAGE Conference and Exhibition*, Paris, France, 12-15 June. doi:10.2118/185802-MS.

Onur, M., Galvao M., Bircan D. E., Carvalho M., and Barreto A. (2019). Analytical Models for Interpretation and Analysis of Transient Sandface and Wellbore Temperature Data. In *SPE Annual Technical Conference and Exhibition*, Calgary, Alberta, Canada, September 2019. doi:10.2118/195991-MS.

Palabiyik, Y., Tureyen, O. I., and Onur M. (2013). A study on Pressure and Temperature Behaviors of Geothermal Wells in Single-Phase Liquid Reservoirs. In *38th Workshop on Geothermal Reservoir Engineering*, Stanford University, Stanford, California, USA, 11-13 February.

Palabiyik, Y., Tureyen, O. I., and Onur M. (2015). Pressure and Temperature Behaviors of Single-Phase Liquid Water Geothermal Reservoirs under Various Production/Injection Schemes. In *World Geothermal Congress*, Melbourne, Australia, 19-25 April.

Palabiyik, Y., Onur, M., Tureyen, O. I., and Cinar, M. (2016). Transient temperature behavior and analysis of single-phase liquid-water geothermal reservoirs during drawdown and buildup tests: Part I. Theory, new analytical and approximate solutions, *J Pet Sci Eng*, *146*, 637-656. doi:10.1016/j.petrol.2016.08.003.

Panini, F., and Onur, M. (2018). Parameter Estimation from Sandface Drawdown Temperature Transient Data in the Presence of a Skin Zone Near the Wellbore. In *SPE Europec featured at 80th EAGE Conference and Exhibition*, Copenhagen, Denmark, 11-14 June. doi:10.2118/190773-MS.

Pauli Virtanen, Ralf Gommers, Travis E. Oliphant, Matt Haberland, ……. SciPy 1.0 Contributors (2020). Fundamental Algorithms for Scientific Computing in Python. *Nature Methods, 17* (3), 261-272.

Peng, D. Y., and Robinson, D. B. (1976). A new two-constant equation of state. *Industrial & Eng Chemistry Fundamentals*, *15* (1), 59-64.

Pourafshary, P., Varavei, A., Sepehrnoori, K., and Podio, L. (2009). A compositional wellbore/reservoir simulator to model multiphase flow and temperature distribution. *J Pet Sci Eng,* 69 (1–2), 40–52. doi:10.1016/j.petrol.2009.02.012.

Pruess, K., Oldenburg, C. M., and Moridis, G. J. (1999). *TOUGH2 user's guide version 2* (No. LBNL-43134). Lawrence Berkeley National Lab.(LBNL), Berkeley, CA, United States.

Ramazanov, A. S., and Nagimov, V. M. (2007). Analytical model for the calculation of temperature distribution in the oil reservoir during unsteady fluid inflow. *Oil and Gas Business Journal*, *1* (1), 1-8.

Ramey, H. J. Jr. (1962). Wellbore Heat Transmission. *J Pet Technol*, *14* (4), 427-435. doi:10.2118/96-PA.

Semenova, A., Livescu, S., Durlofsky, L.J., and Aziz, K. (2010). Modeling of Multisegmented Thermal Wells in Reservoir Simulation. In *SPE EUROPEC/EAGE Annual Conference and Exhibition*, Barcelona, Spain, 14–17 June. doi:10.2118/130371-MS.

Sidorova, M., Theuveny, B., Pimenov, V., Shako, V., and Guzman-Garcia, A. G. (2014). Do Not Let Temperature Transients Hinder Your Build-up Pressure Interpretation - Proper Gauge Placement in Highly Productive Reservoirs in Well Testing Operations. In *SPE Annual Caspian Technical Conference and Exhibition*. doi:10.2118/172278-MS.

Sidorova, M., Shako V., and Pimenov V. (2015). The value of transient temperature responses in testing operations. In *SPE Middle East Oil & Gas Show and Conference*, Manama, Bahrain, 8-11 March.

Spindler, R. (2011). Analytical Models for Wellbore-Temperature Distribution. *SPE J.*, *16* (1), 125-133. doi:10.2118/140135-PA.

Sui, W., Zhu, D., and Hill, A. D. (2008). Model for Transient Temperature and Pressure Behavior in Commingled Vertical Wells. In *SPE Russian Oil & Gas Technical Conference and Exhibition*, Moscow, Russia, 28-30 October. doi:10.2118/115200-MS.

Timmerhaus, Klaus D., and Thomas M. Flynn. (1989). *Cryogenic process engineering*. Springer Science & Business Media.

Wang, P., Yotov, I., Wheeler, M., Arbogast, T., Dawson, C., Parashar, M., and Sepehrnoori, K. (1997). A new generation EOS compositional reservoir simulator: Part I—formulation and discretization. In *SPE Reservoir Simulation Symposium*, Dallas, TX, 8–11 June. doi:10.2118/37979-MS.

Wang, P., Balay, S., Sepehrnoori, K., Wheeler, J., Abate, J., Smith, B. and Pope, G.A. (1999). A fully implicit parallel EOS compositional simulator for large scale reservoir simulation. In *SPE Reservoir Simulation Symposium*, Houston, Texas, United States, 14–17 February. doi:10.2118/51885-MS.

Willhite, G. P. (1967). Overall Heat Transfer Coefficients in Steam and Hot Water Injection Wells. *J Pet Technol*, *19* (5), 607-615. doi:10.2118/1449-PA.

Wu, Y. S., and Pruess, K. (1990). An analytical solution for wellbore heat transmission in layered formations. *SPE Reservoir Engineering, 5* (04), 531-538. doi:10.2118/17497-PA.

APPENDICES

APPENDIX A: Model Formulation 2-D (*r*-*z*) Reservoir
APPENDIX B: Discretization of 2-D (*r*-*z*) Reservoir Equations
APPENDIX C: Model Formulation 1-D (*z*) Wellbore
APPENDIX D: Discretization of 1-D (*z*) Wellbore Equations
APPENDIX E: Figures of Chapter 3

APPENDIX A: Model Formulation 2-D (*r-z*) Reservoir

Mass Balance: 2-D (*r-z*) single-phase non-isothermal flow of slightly compressible fluid (water or oil) is considered for the reservoir. The generalized continuity equation for mass conservation in the porous media is given by:

$$\frac{\partial}{\partial t}(\rho\phi) + \nabla \cdot (\rho \mathbf{v}) = 0 \tag{A.1}$$

where the terms from the left to right represent the mass-accumulation and convective flux term respectively. There is no sink/source term used in derivations. The first term in Equation A.1 considered as:

$$\frac{\partial}{\partial t}(\rho\phi) = \rho\frac{\partial \phi}{\partial t} + \phi\frac{\partial \rho}{\partial t} \tag{A.2}$$

Using the chain rule for time derivative of density and porosity gives:

$$\rho\frac{\partial \phi}{\partial t} = \rho\left(\frac{\partial p_r}{\partial t}\frac{\partial \phi}{\partial p_r} + \frac{\partial T_r}{\partial t}\frac{\partial \phi}{\partial T_r}\right) \tag{A.3}$$

$$\phi\frac{\partial \rho}{\partial t} = \phi\left(\frac{\partial p_r}{\partial t}\frac{\partial \rho}{\partial p_r} + \frac{\partial T_r}{\partial t}\frac{\partial \rho}{\partial T_r}\right) \tag{A.4}$$

The effective isothermal compressibility coefficients for the rock and fluid are represented respectively by:

$$c_m = \frac{1}{\phi}\frac{\partial \phi}{\partial p_r} \tag{A.5}$$

$$c = \frac{1}{\rho}\frac{\partial \rho}{\partial p_r} \tag{A.6}$$

The effective isobaric thermal expansion coefficients for the rock and fluid are represented respectively by:

$$\beta_m = -\frac{1}{\phi}\frac{\partial \phi}{\partial T_r} \tag{A.7}$$

$$\beta = -\frac{1}{\rho}\frac{\partial \rho}{\partial T_r} \tag{A.8}$$

The rearrangement of terms in Equation A.2 gives:

$$\frac{\partial(\rho\phi)}{\partial t} = \rho\left(\phi \underbrace{\frac{1}{\phi}\frac{\partial \phi}{\partial p_r}}_{c_m}\frac{\partial p_r}{\partial t} + \phi\frac{\partial T_r}{\partial t}\underbrace{\frac{1}{\phi}\frac{\partial \phi}{\partial T_r}}_{-\beta_m}\right) + \phi\left(\rho\frac{\partial p_r}{\partial t}\underbrace{\frac{1}{\rho}\frac{\partial \rho}{\partial p_r}}_{c} + \rho\frac{\partial T_r}{\partial t}\underbrace{\frac{1}{\rho}\frac{\partial \rho}{\partial T_r}}_{-\beta}\right) \tag{A.9}$$

The rearrangement of terms in above equation yields:

$$\frac{\partial}{\partial t}(\rho\phi) = \rho\phi c_m\frac{\partial p_r}{\partial t} - \rho\phi\beta_m\frac{\partial T_r}{\partial t} + \rho\phi c\frac{\partial p_r}{\partial t} - \rho\phi\beta\frac{\partial T_r}{\partial t} \tag{A.10}$$

We can finalize evaluating Equation A.2:

$$\frac{\partial}{\partial t}(\rho\phi) = \rho\phi\left((c_m + c)\frac{\partial p_r}{\partial t} - (\beta_m + \beta)\frac{\partial T_r}{\partial t}\right) \tag{A.11}$$

Now we evaluate the second term in Equation A.1:

$$\nabla\cdot(\rho\mathbf{v}) = \mathbf{v}\cdot\nabla\rho + \rho(\nabla\cdot\mathbf{v}) \tag{A.12}$$

We start with the first term in Equation A.12. the gradient of density in *r-z* system is given by:

$$\mathbf{v}\cdot\nabla\rho = \mathbf{v}\cdot\left(\frac{\partial\rho}{\partial r} + \frac{\partial\rho}{\partial z}\right) \tag{A.13}$$

Using Equations A.5 through A.8, we can express Equation A.13 as:

$$\mathbf{v}\cdot\nabla\rho = \mathbf{v}\cdot\left(\rho\underbrace{\frac{1}{\rho}\frac{\partial\rho}{\partial p_r}}_{c}\frac{\partial p_r}{\partial r} + \rho\underbrace{\frac{1}{\rho}\frac{\partial\rho}{\partial T_r}}_{-\beta}\frac{\partial T_r}{\partial r} + \rho\underbrace{\frac{1}{\rho}\frac{\partial\rho}{\partial p_r}}_{c}\frac{\partial p_r}{\partial z} + \rho\underbrace{\frac{1}{\rho}\frac{\partial\rho}{\partial T_r}}_{-\beta}\frac{\partial T_r}{\partial z}\right) \tag{A.14}$$

$$\mathbf{v} \cdot \nabla\rho = \mathbf{v} \cdot \left[\rho c \underbrace{\left(\frac{\partial p_r}{\partial r} + \frac{\partial p_r}{\partial z} \right)}_{\nabla p_r} - \rho \underbrace{\left(\frac{\partial T_r}{\partial r} + \frac{\partial T_r}{\partial z} \right)}_{\nabla T_r} \right] \tag{A.15}$$

$$\mathbf{v} \cdot \nabla = \mathbf{v} \cdot (\rho c \nabla p_r - \rho \beta \nabla T_r) \tag{A.16}$$

The rearrangement of terms in Equation A.12 gives:

$$\nabla \cdot (\rho \mathbf{v}) = \rho[\mathbf{v} \cdot (c \nabla p_r - \beta \nabla T_r) + (\nabla \cdot \mathbf{v})] \tag{A.17}$$

We evaluate the last term in the above equation as:

$$\nabla \cdot \mathbf{v} = \frac{1}{r} \frac{\partial}{\partial r} (r v_r) + \frac{\partial}{\partial z} (v_z) \tag{A.18}$$

The semi-empirical momentum equation of Darcy expresses vector of fluid velocity as:

$$\mathbf{v} = -\frac{\mathbf{K}}{\mu} (\nabla p_r - \rho g \nabla z) \tag{A.19}$$

Where **K** is the diagonal permeability vector, which is given as below for a *r-z* system:

$$\mathbf{K} = \begin{bmatrix} k_r & 0 \\ 0 & k_z \end{bmatrix} \tag{A.20}$$

and the gradient of z is a 2-dimensional vector given by:

$$\nabla z = \begin{bmatrix} \frac{\partial z}{\partial r} \\ \frac{\partial z}{\partial z} \end{bmatrix} = \begin{bmatrix} 0 \\ 1 \end{bmatrix} \tag{A.21}$$

The partial derivative of z with respect to radial coordinate is zero because we assume a horizontal *r-z* reservoir system where v_r and v_z given in a horizontal *r-z* system by:

$$v_r = -\frac{k_r}{\mu} \frac{\partial p_r}{\partial r} \tag{A.22}$$

$$v_z = -\frac{k_z}{\mu}\frac{\partial p_r}{\partial z} + \frac{k_z}{\mu}\rho g \tag{A.23}$$

Using Equations A.22 and A.23 in A.18 gives:

$$\begin{aligned}\nabla \cdot \mathbf{v} &= -\frac{1}{r}\frac{\partial}{\partial r}\left(r\frac{k_r}{\mu}\frac{\partial p_r}{\partial r}\right) - \frac{\partial}{\partial z}\left(\frac{k_z}{\mu}\frac{\partial p_r}{\partial z} - \frac{k_z}{\mu}\rho g\right) \\ &= -\frac{1}{r}\frac{\partial}{\partial r}\left(r\frac{k_r}{\mu}\frac{\partial p_r}{\partial r}\right) - \frac{\partial}{\partial z}\left(\frac{k_z}{\mu}\frac{\partial p_r}{\partial z}\right) + \frac{\partial}{\partial z}\left(\frac{k_z}{\mu}\rho g\right) \\ &= -\frac{1}{r}\frac{\partial}{\partial r}\left(r\frac{k_r}{\mu}\frac{\partial p_r}{\partial r}\right) - \frac{\partial}{\partial z}\left(\frac{k_z}{\mu}\frac{\partial p_r}{\partial z}\right) + g\frac{\partial}{\partial z}\left(\frac{k_z}{\mu}\rho\right)\end{aligned} \tag{A.24}$$

The rearrangement of terms yields:

$$\begin{aligned}\nabla \cdot \mathbf{v} &= -\frac{1}{r}\frac{\partial}{\partial r}\left(r\frac{k_r}{\mu}\frac{\partial p_r}{\partial r}\right) - \frac{\partial}{\partial z}\left(\frac{k_z}{\mu}\frac{\partial p_r}{\partial z}\right) + g\left[\rho\frac{\partial}{\partial z}\left(\frac{k_z}{\mu}\right) + \frac{k_z}{\mu}\frac{\partial}{\partial z}(\rho)\right] \\ &= -\frac{1}{r}\frac{\partial}{\partial r}\left(r\frac{k_r}{\mu}\frac{\partial p_r}{\partial r}\right) - \frac{\partial}{\partial z}\left(\frac{k_z}{\mu}\frac{\partial p_r}{\partial z}\right) \\ &\quad + g\left[\rho\frac{\partial}{\partial z}\left(\frac{k_z}{\mu}\right) + \frac{k_z}{\mu}\rho\left(c\frac{\partial p_r}{\partial z} - \beta\frac{\partial T_r}{\partial z}\right)\right]\end{aligned} \tag{A.25}$$

Finally:

$$\begin{aligned}\nabla \cdot \mathbf{v} &= -\frac{1}{r}\frac{\partial}{\partial r}\left(r\frac{k_r}{\mu}\frac{\partial p_r}{\partial r}\right) - \frac{\partial}{\partial z}\left(\frac{k_z}{\mu}\frac{\partial p_r}{\partial z}\right) \\ &\quad + g\rho\left[\frac{\partial}{\partial z}\left(\frac{k_z}{\mu}\right) + \frac{k_z}{\mu}\left(c\frac{\partial p_r}{\partial z} - \beta\frac{\partial T_r}{\partial z}\right)\right]\end{aligned} \tag{A.26}$$

If we rewrite Equation A.1 again:

$$\rho\phi\left[(c_m + c)\frac{\partial p_r}{\partial t} - (\beta_m + \beta)\frac{\partial T_r}{\partial t}\right] + \rho[\mathbf{v} \cdot (c\nabla p_r - \beta\nabla T_r) + (\nabla \cdot \mathbf{v})] = 0 \tag{A.27}$$

$$\rho\phi\left[(c_m + c)\frac{\partial p_r}{\partial t} - (\beta_m + \beta)\frac{\partial T_r}{\partial t}\right] + \rho[(c\mathbf{v} \cdot \nabla p_r - \beta\mathbf{v} \cdot \nabla T_r) + (\nabla \cdot \mathbf{v})] = 0 \tag{A.28}$$

Diving each side with ρ gives:

$$\phi\left[(c_m + c)\frac{\partial p_r}{\partial t} - (\beta_m + \beta)\frac{\partial T_r}{\partial t}\right] + (c\mathbf{v} \cdot \nabla p_r - \beta\mathbf{v} \cdot \nabla T_r) + (\nabla \cdot \mathbf{v}) = 0 \tag{A.29}$$

Rewriting above equation with gradient of pressure and temperature gives:

$$\phi\left[(c_m + c)\frac{\partial p_r}{\partial t} - (\beta_m + \beta)\frac{\partial T_r}{\partial t}\right] + c\left[-\frac{\mathbf{K}}{\mu}(\nabla p_r - \rho g \nabla z)\cdot\nabla p_r\right] \\ -\beta\left[-\frac{\mathbf{K}}{\mu}(\nabla p_r - \rho g \nabla z)\cdot\nabla T_r\right] + (\nabla\cdot\mathbf{v}) = 0 \tag{A.30}$$

Or

$$\phi\left[(c_m + c)\frac{\partial p_r}{\partial t} - (\beta_m + \beta)\frac{\partial T_r}{\partial t}\right] \\ + \left\{c\left[-\frac{\mathbf{K}}{\mu}\left(\nabla p_r\cdot\nabla p_r - \rho g(\nabla z\cdot\nabla p_r)\right)\right]\right. \\ \left. -\beta\left[-\frac{\mathbf{K}}{\mu}\left(\nabla p_r\cdot\nabla T_r - \rho g(\nabla z\cdot\nabla T_r)\right)\right] + (\nabla\cdot\mathbf{v})\right\} = 0 \tag{A.31}$$

Note that we will expand the dot products in the equation above by considering the *r*-*z* coordinate system as:

$$\frac{\mathbf{K}}{\mu}\left(\nabla p_r\cdot\nabla p_r - \rho g(\nabla z\cdot\nabla p_r)\right) = \frac{k_r}{\mu}\left(\frac{\partial p_r}{\partial r}\right)^2 + \frac{k_z}{\mu}\left(\frac{\partial p_r}{\partial z}\right)^2 - \rho g\frac{k_z}{\mu}\left(\frac{\partial p_r}{\partial z}\right) \tag{A.32}$$

and

$$\frac{\mathbf{K}}{\mu}\left(\nabla p_r\cdot\nabla T_r - \rho g(\nabla z\cdot\nabla T_r)\right) = \frac{k_r}{\mu}\frac{\partial p_r}{\partial r}\frac{\partial T_r}{\partial r} + \frac{k_z}{\mu}\frac{\partial p_r}{\partial z}\frac{\partial T_r}{\partial z} - \rho g\frac{k_z}{\mu}\left(\frac{\partial T_r}{\partial z}\right) \tag{A.33}$$

Replacing vector of fluid velocity in Equation A.33 gives:

$$-\phi\left[(c_m + c)\frac{\partial p_r}{\partial t} - (\beta_m + \beta)\frac{\partial T_r}{\partial t}\right] \\ + c\left[\frac{k_r}{\mu}\left(\frac{\partial p_r}{\partial r}\right)^2 + \frac{k_z}{\mu}\left(\frac{\partial p_r}{\partial z}\right)^2 - \rho g\frac{k_z}{\mu}\left(\frac{\partial p_r}{\partial z}\right)\right] \\ -\beta\left[\frac{k_r}{\mu}\frac{\partial p_r}{\partial r}\frac{\partial T_r}{\partial r} + \frac{k_z}{\mu}\frac{\partial p_r}{\partial z}\frac{\partial T_r}{\partial z} - \rho g\frac{k_z}{\mu}\left(\frac{\partial T_r}{\partial z}\right)\right] \\ + \frac{1}{r}\frac{\partial}{\partial r}\left(r\frac{k_r}{\mu}\frac{\partial p_r}{\partial r}\right) + \frac{\partial}{\partial z}\left(\frac{k_z}{\mu}\frac{\partial p_r}{\partial z}\right) \\ -g\rho\left[\frac{\partial}{\partial z}\left(\frac{k_z}{\mu}\right) + \frac{k_z}{\mu}\left(c\frac{\partial p_r}{\partial z} - \beta\frac{\partial T_r}{\partial z}\right)\right] = 0 \tag{A.34}$$

Or

$$
\begin{aligned}
-\phi\left[(c_m + c)\frac{\partial p_r}{\partial t} - (\beta_m + \beta)\frac{\partial T_r}{\partial t}\right] \\
+ c\left[\frac{k_r}{\mu}\left(\frac{\partial p_r}{\partial r}\right)^2 + \frac{k_z}{\mu}\left(\frac{\partial p_r}{\partial z}\right)^2 - 2\rho g\frac{k_z}{\mu}\left(\frac{\partial p_r}{\partial z}\right)\right] \\
- \beta\left[\frac{k_r}{\mu}\frac{\partial p_r}{\partial r}\frac{\partial T_r}{\partial r} + \frac{k_z}{\mu}\frac{\partial p_r}{\partial z}\frac{\partial T_r}{\partial z} - 2\rho g\frac{k_z}{\mu}\left(\frac{\partial T_r}{\partial z}\right)\right] \\
+ \frac{1}{r}\frac{\partial}{\partial r}\left(r\frac{k_r}{\mu}\frac{\partial p_r}{\partial r}\right) + \frac{\partial}{\partial z}\left(\frac{k_z}{\mu}\frac{\partial p_r}{\partial z}\right) - g\rho\frac{\partial}{\partial z}\left(\frac{k_z}{\mu}\right) = 0
\end{aligned}
\tag{A.35}
$$

We define u_{c_r} and u_{c_z} as below:

$$u_{c_r} = -\frac{k_r}{\mu}\frac{\partial p_r}{\partial r} \tag{A.36}$$

$$u_{c_z} = -\frac{k_z}{\mu}\frac{\partial p_r}{\partial z} \tag{A.37}$$

And, update Equation A.35:

$$
\begin{aligned}
-\phi\left[\underbrace{(c_m + c)}_{c_t}\frac{\partial p_r}{\partial t} - \underbrace{(\beta_r + \beta)}_{\beta_t}\frac{\partial T_r}{\partial t}\right] \\
- c\left[u_{c_r}\left(\frac{\partial p_r}{\partial r}\right) + u_{c_z}\left(\frac{\partial p_r}{\partial}\right) - 2\rho g u_{c_z}\right] \\
+ \beta\left[u_{c_r}\frac{\partial T_r}{\partial r} + u_{c_z}\frac{\partial T_r}{\partial z} + 2\rho g\frac{k_z}{\mu}\left(\frac{\partial T_r}{\partial z}\right)\right] - \frac{1}{r}\frac{\partial}{\partial r}\left(r u_{c_r}\right) \\
- \frac{\partial}{\partial z}\left(u_{c_z}\right) - g\rho\frac{\partial}{\partial z}\left(\frac{k_z}{\mu}\right) = 0
\end{aligned}
\tag{A.38}
$$

The fluid-saturated rock isothermal compressibility (c_t) and thermal expansion (β_t) terms may be simply defined as below:

$$c_t = c_m + c \tag{A.39}$$

$$\beta_t = \beta_m + \beta \tag{A.40}$$

Energy Balance: When we assume local thermal equilibrium between the solid matrix and the fluid, we can consider thermal energy balance equation as:

$$\frac{\partial}{\partial t}[\phi\rho U + (1-\phi)\rho_m U_m] + \nabla\cdot(\rho U\mathbf{v}) + \nabla\cdot(p_r\mathbf{v}) - \nabla\cdot(\boldsymbol{\lambda_t}\nabla T_r) = 0 \quad \text{(A.41)}$$

An alternative form of the thermal energy balance equation given by Equation A.41 can be obtained by expressing specific internal energy U in terms of specific enthalpy H by using the thermo-dynamic relationship:

$$\rho U = \rho H - p_r \quad \text{(A.42)}$$

and using the standard assumption that specific internal energy of the solid matrix is equal to its specific enthalpy,

$$U_m = H_m \quad \text{(A.43)}$$

Using Equations A.42 and A.43 in A.41 gives:

$$\frac{\partial}{\partial t}[\phi(\rho H - p_r) + (1-\phi)\rho_m H_m] + \nabla\cdot[(\rho H - p_r)\mathbf{v}] + \nabla\cdot(p_r\mathbf{v}) - \nabla\cdot(\boldsymbol{\lambda_t}\nabla T_r) = 0 \quad \text{(A.44)}$$

Performing algebra yields:

$$\frac{\partial}{\partial t}(\phi\rho H) - \frac{\partial}{\partial t}(\phi p_r) + \frac{\partial}{\partial t}[(1-\phi)\rho_m H_m] + \nabla\cdot(\rho H\mathbf{v}) - \nabla\cdot(\boldsymbol{\lambda_t}\nabla T_r) = 0 \quad \text{(A.45)}$$

We evaluate mass balance equation for solid matrix as below with the assumption of solid matrix's being rigid so that it has zero velocity:

$$\frac{\partial}{\partial t}[(1-\phi)\rho_m H_m] = (1-\phi)\rho_m\frac{\partial H_m}{\partial t} + H_m\underbrace{\frac{\partial}{\partial t}[(1-\phi)\rho_m]}_{0} \quad \text{(A.46)}$$

And, update Equation A.44:

$$\frac{\partial}{\partial t}(\phi\rho H) - \frac{\partial}{\partial t}(\phi p_r) + (1-\phi)\rho_m\frac{\partial H_m}{\partial t} + \nabla\cdot(\rho H\mathbf{v}) - \nabla\cdot(\boldsymbol{\lambda_t}\nabla T_r) = 0 \quad \text{(A.47)}$$

We can further express some terms in Equation A.47 as:

$$\frac{\partial}{\partial t}(\phi\rho H) = H\frac{\partial}{\partial t}(\phi\rho) + \phi\rho\frac{\partial H}{\partial t} \quad \text{(A.48)}$$

$$\nabla \cdot (\rho H \mathbf{v}) = \rho \mathbf{v} \cdot \nabla H + H \nabla \cdot (\rho \mathbf{v}) \tag{A.49}$$

And, we update Equations A.47 using A.48 and A.49:

$$\begin{aligned} &\left[H \frac{\partial}{\partial t}(\phi \rho) + \phi \rho \frac{\partial H}{\partial t}\right] - \frac{\partial}{\partial t}(\phi p_r) + (1-\phi)\rho_m \frac{\partial H_m}{\partial t} \\ &+[\rho \mathbf{v} \cdot \nabla H + H \nabla \cdot (\rho \mathbf{v})] - \nabla \cdot (\boldsymbol{\lambda_t} \nabla T_r) = 0 \end{aligned} \tag{A.50}$$

By multiplying both sides of the continuity equation given by Equation A.1 by specific enthalpy of the reservoir fluid leaving due to the production, H, and the rearranging of terms gives:

$$H \frac{\partial}{\partial t}(\rho \phi) = -H \nabla \cdot (\rho \mathbf{v}) \tag{A.51}$$

Using Equations A.51 in A.50:

$$\begin{aligned} &\left[-H \nabla \cdot (\rho \mathbf{v}) + \phi \rho \frac{\partial H}{\partial t}\right] - \frac{\partial}{\partial t}(\phi p_r) + (1-\phi)\rho_m \frac{\partial H_m}{\partial t} \\ &+[\rho \mathbf{v} \cdot \nabla H + H \nabla \cdot (\rho \mathbf{v})] - \nabla \cdot (\boldsymbol{\lambda_t} \nabla T_r) = 0 \end{aligned} \tag{A.52}$$

Further rearrangement of terms yields:

$$\phi \rho \frac{\partial H}{\partial t} - \frac{\partial}{\partial t}(\phi p_r) + (1-\phi)\rho_m \frac{\partial H_m}{\partial t} + (\rho \mathbf{v} \cdot \nabla H) - \nabla \cdot (\boldsymbol{\lambda_t} \nabla T_r) = 0 \tag{A.53}$$

Dividing both sides by ϕ gives:

$$\begin{aligned} &\rho \frac{\partial H}{\partial t} - \frac{1}{\phi}\left[\frac{\partial}{\partial t}(\phi p_r)\right] + \left(\frac{(1-\phi)\rho_m}{\phi}\right)\frac{\partial H_m}{\partial t} + \frac{1}{\phi}(\rho \mathbf{v} \cdot \nabla H) \\ &- \frac{1}{\phi}[\nabla \cdot (\boldsymbol{\lambda_t} \nabla T_r)] = 0 \end{aligned} \tag{A.54}$$

We can express following thermodynamic relationships for solid matrix and the fluid where we assume c_p, $c_{p,m}$ and ε_{JT} independent of temperature and pressure:

$$\frac{\partial H}{\partial t} = c_p \left(\frac{\partial T_r}{\partial t} - \varepsilon_{JT} \frac{\partial p_r}{\partial t}\right) \tag{A.55}$$

$$\frac{\partial H_m}{\partial t} = c_{p_m} \frac{\partial T_r}{\partial t} \tag{A.56}$$

And, update Equation A.54:

$$\rho c_p \left(\frac{\partial T_r}{\partial t} - \varepsilon_{JT} \frac{\partial p_r}{\partial t}\right) - \frac{1}{\phi}\left[\frac{\partial}{\partial t}(\phi p_r)\right] + \left(\frac{(1-\phi)\rho_m c_{p_m}}{\phi}\right)\frac{\partial T_r}{\partial t} + \frac{1}{\phi}(\rho \mathbf{v} \cdot \nabla H) - \frac{1}{\phi}[\nabla \cdot (\boldsymbol{\lambda_t} \nabla T_r)] = 0 \tag{A.57}$$

We can express the second term in the above equation as:

$$\frac{1}{\phi}\left[\frac{\partial}{\partial t}(\phi p_r)\right] = \frac{1}{\phi}\left(\phi \frac{\partial p_r}{\partial t} + p_r \frac{\partial \phi}{\partial t}\right) = \frac{\partial p_r}{\partial t} + p_r \left[\underbrace{\frac{1}{\phi}\frac{\partial \phi}{\partial p_r}}_{c_m} \frac{\partial p_r}{\partial t} + \underbrace{\frac{1}{\phi}\frac{\partial \phi}{\partial T_r}}_{-\beta_m} \frac{\partial T_r}{\partial t}\right] = (1 + p_r c_m)\frac{\partial p_r}{\partial t} - p_r \beta_m \frac{\partial T_r}{\partial t} \tag{A.58}$$

And, update Equation A.57:

$$\rho c_p \left(\frac{\partial T_r}{\partial t} - \varepsilon_{JT} \frac{\partial p_r}{\partial t}\right) - (1 + p_r c_m)\frac{\partial p_r}{\partial t} + p_r \beta_m \frac{\partial T_r}{\partial t} + \left(\frac{(1-\phi)\rho_m c_{p_m}}{\phi}\right)\frac{\partial T_r}{\partial t} + \frac{1}{\phi}(\rho \mathbf{v} \cdot \nabla H) - \frac{1}{\phi}[\nabla \cdot (\boldsymbol{\lambda_t} \nabla T_r)] = 0 \tag{A.59}$$

Dividing both sides by ρc_p gives:

$$\left(\frac{\partial T_r}{\partial t} - \varepsilon_{JT} \frac{\partial p_r}{\partial t}\right) - \left(\frac{1 + p_r c_m}{\rho c_p}\right)\frac{\partial p_r}{\partial t} + \frac{p_r \beta_m}{\rho c_p}\frac{\partial T_r}{\partial t} + \left(\frac{(1-\phi)\rho_m c_{p_m}}{\phi \rho c_p}\right)\frac{\partial T_r}{\partial t} + \frac{1}{\phi c_p}(\mathbf{v} \cdot \nabla H) - \frac{1}{\phi \rho c_p}[\nabla \cdot (\boldsymbol{\lambda_t} \nabla T_r)] = 0 \tag{A.60}$$

We evaluate gradient term in *r-z* system as below where we assume c_p and ε_{JT} independent of temperature and pressure:

$$\nabla H = c_p\left(\nabla T_r - \varepsilon_{JT} \nabla p_r\right) \tag{A.61}$$

And then multiply by velocity:

$$\mathbf{v}\cdot\nabla H=\nabla H\cdot\mathbf{v}=c_p\left(\nabla T_r\cdot\mathbf{v}-\varepsilon_{JT}\nabla p_r\cdot\mathbf{v}\right)=c_p\left(\mathbf{v}\cdot\nabla T_r-\varepsilon_{JT}\mathbf{v}\cdot\nabla p_r\right) \quad \text{(A.62)}$$

Note that we will expand the dot products of velocity in the equation above by considering the *r-z* coordinate system as:

$$\begin{aligned}\mathbf{v}\cdot\nabla p_r&=-\frac{\mathbf{K}}{\mu}\left(\nabla p_r\cdot\nabla p_r-\rho g(\nabla z\cdot\nabla p_r)\right)\\&=-\frac{k_r}{\mu}\left(\frac{\partial p_r}{\partial r}\right)^2-\frac{k_z}{\mu}\left(\frac{\partial p_r}{\partial z}\right)^2+\rho g\frac{k_z}{\mu}\left(\frac{\partial p_r}{\partial z}\right)\end{aligned} \quad \text{(A.63)}$$

$$\begin{aligned}\mathbf{v}\cdot\nabla T_r&=-\frac{\mathbf{K}}{\mu}\left(\nabla p_r\cdot\nabla T_r-\rho g(\nabla z\cdot\nabla T_r)\right)\\&=-\frac{k_r}{\mu}\frac{\partial p_r}{\partial r}\frac{\partial T_r}{\partial r}-\frac{k_z}{\mu}\frac{\partial p_r}{\partial z}\frac{\partial T_r}{\partial z}+\rho g\frac{k_z}{\mu}\left(\frac{\partial T_r}{\partial z}\right)\end{aligned} \quad \text{(A.64)}$$

So, we have:

$$\begin{aligned}\mathbf{v}\cdot\nabla H=\nabla H\cdot\mathbf{v}&=c_p\left(\mathbf{v}\cdot\nabla T_r-\varepsilon_{JT}\mathbf{v}\cdot\nabla p_r\right)\\&=-c_p\left\{\frac{k_r}{\mu}\frac{\partial p_r}{\partial r}\frac{\partial T_r}{\partial r}+\frac{k_z}{\mu}\frac{\partial p_r}{\partial z}\frac{\partial T_r}{\partial z}-\rho g\frac{k_z}{\mu}\left(\frac{\partial T_r}{\partial z}\right)\right.\\&\left.-\varepsilon_{JT}\left[\frac{k_r}{\mu}\left(\frac{\partial p_r}{\partial r}\right)^2+\frac{k_z}{\mu}\left(\frac{\partial p_r}{\partial z}\right)^2-\rho g\frac{k_z}{\mu}\left(\frac{\partial p_r}{\partial z}\right)\right]\right\}\end{aligned} \quad \text{(A.65)}$$

And, update Equation A.60:

$$\begin{aligned}&\left(\frac{\partial T_r}{\partial t}-\varepsilon_{JT}\frac{\partial p_r}{\partial t}\right)-\left(\frac{1+p_r c_m}{\rho c_p}\right)\frac{\partial p_r}{\partial t}+\frac{p_r\beta_m}{\rho c_p}\frac{\partial T_r}{\partial t}+\left(\frac{(1-\phi)\rho_m c_{p_m}}{\phi\rho c_p}\right)\frac{\partial T_r}{\partial t}\\&-\frac{1}{\phi}\left\{\begin{array}{c}\dfrac{k_r}{\mu}\dfrac{\partial p_r}{\partial r}\dfrac{\partial T_r}{\partial r}+\dfrac{k_z}{\mu}\dfrac{\partial p_r}{\partial z}\dfrac{\partial T_r}{\partial z}-\rho g\dfrac{k_z}{\mu}\left(\dfrac{\partial T_r}{\partial z}\right)\\-\varepsilon_{JT}\left[\dfrac{k_r}{\mu}\left(\dfrac{\partial p_r}{\partial r}\right)^2+\dfrac{k_z}{\mu}\left(\dfrac{\partial p_r}{\partial z}\right)^2-\rho g\dfrac{k_z}{\mu}\left(\dfrac{\partial p_r}{\partial z}\right)\right]\end{array}\right\}\\&-\frac{1}{\phi\rho c_p}\left[\nabla\cdot(\boldsymbol{\lambda_t}\nabla T_r)\right]=0\end{aligned} \quad \text{(A.66)}$$

In Equation A.41, $\boldsymbol{\lambda_t}$ is a diagonal thermal conductivity of fluid-saturated rock tensor given by:

$$\boldsymbol{\lambda_t} = \begin{bmatrix} \lambda_{t_r} & 0 \\ 0 & \lambda_{t_z} \end{bmatrix} \tag{A.67}$$

We evaluate the gradient term in *r*-*z* system as below:

$$\nabla \cdot (\boldsymbol{\lambda_t} \nabla T) = \frac{1}{r}\frac{\partial}{\partial r}\left(r\lambda_{t_r}\frac{\partial T_r}{\partial r}\right) + \frac{\partial}{\partial z}\left(\lambda_{t_z}\frac{\partial T_r}{\partial z}\right) \tag{A.68}$$

Then we update Equation A.66:

$$\begin{aligned} &\left(\frac{\partial T_r}{\partial t} - \varepsilon_{JT}\frac{\partial p_r}{\partial t}\right) - \left(\frac{1 + p_r c_m}{\rho c_p}\right)\frac{\partial p_r}{\partial t} + \frac{p_r \beta_m}{\rho c_p}\frac{\partial T_r}{\partial t} + \left(\frac{(1-\phi)\rho_m c_{p_m}}{\phi \rho c_p}\right)\frac{\partial T_r}{\partial t} \\ &\quad - \frac{1}{\phi}\left\{\frac{k_r}{\mu}\frac{\partial p_r}{\partial r}\frac{\partial T_r}{\partial r} + \frac{k_z}{\mu}\frac{\partial p_r}{\partial z}\frac{\partial T_r}{\partial z} - \rho g\frac{k_z}{\mu}\left(\frac{\partial T_r}{\partial z}\right)\right. \\ &\quad \left. - \varepsilon_{JT}\left[\frac{k_r}{\mu}\left(\frac{\partial p_r}{\partial r}\right)^2 + \frac{k_z}{\mu}\left(\frac{\partial p_r}{\partial z}\right)^2 - \rho g\frac{k_z}{\mu}\left(\frac{\partial p_r}{\partial z}\right)\right]\right\} \\ &\quad - \frac{1}{\phi \rho c_p}\left[\frac{1}{r}\frac{\partial}{\partial r}\left(r\lambda_{t_r}\frac{\partial T_r}{\partial r}\right) + \frac{\partial}{\partial z}\left(\lambda_{t_z}\frac{\partial T_r}{\partial z}\right)\right] = 0 \end{aligned} \tag{A.69}$$

Rearrangement of terms in Equation A.66 using Equations A.36 and A.37 and also defining isentropic thermal expansion coefficient (φ) as:

$$\begin{aligned} &\left[1 + \frac{(1-\phi)\rho_m c_{p_m}}{\phi \rho c_p} + \frac{p_r \beta_m}{\rho c_p}\right]\frac{\partial T_r}{\partial t} - \left(\underbrace{\varepsilon_{JT} + \frac{1}{\rho c_p}}_{\varphi} + \frac{p_r c_m}{\rho c_p}\right)\frac{\partial p_r}{\partial t} \\ &= \frac{1}{\phi}\left\{-u_{c_r}\left(\frac{\partial T_r}{\partial r}\right) - u_{c_z}\left(\frac{\partial T_r}{\partial z}\right) - \rho g\frac{k_z}{\mu}\left(\frac{\partial T_r}{\partial z}\right)\right. \\ &\quad \left. - \varepsilon_{JT}\left[-u_{c_r}\left(\frac{\partial p_r}{\partial r}\right) - u_{c_z}\left(\frac{\partial p_r}{\partial z}\right) + \rho g u_{c_z}\right]\right\} \\ &\quad + \frac{1}{\phi \rho c_p}\left[\frac{1}{r}\frac{\partial}{\partial r}\left(r\lambda_{t_r}\frac{\partial T_r}{\partial r}\right) + \frac{\partial}{\partial z}\left(\lambda_{t_z}\frac{\partial T_r}{\partial z}\right)\right] \end{aligned} \tag{A.70}$$

Or multiplying both sides by porosity

$$\left[\phi + \frac{(1-\phi)\rho_m c_{p_m}}{\rho c_p} + \frac{\phi p_r \beta_m}{\rho c_p}\right]\frac{\partial T_r}{\partial t} - \phi\varphi\frac{\partial p_r}{\partial t} + \left(\frac{p_r c_m}{\rho c_p}\right)\frac{\partial p_r}{\partial t}$$
$$= \left\{\begin{array}{l} -u_{c_r}\left(\frac{\partial T_r}{\partial r}\right) - u_{c_z}\left(\frac{\partial T_r}{\partial z}\right) - \rho g\frac{k_z}{\mu}\left(\frac{\partial T_r}{\partial z}\right) \\ -\varepsilon_{JT}\left[-u_{c_r}\left(\frac{\partial p_r}{\partial r}\right) - u_{c_z}\left(\frac{\partial p_r}{\partial z}\right) + \rho g u_{c_z}\right] \end{array}\right\} \quad \text{(A.71)}$$
$$+ \frac{1}{\rho c_p}\left[\frac{1}{r}\frac{\partial}{\partial r}\left(r\lambda_{t_r}\frac{\partial T_r}{\partial r}\right) + \frac{\partial}{\partial z}\left(\lambda_{t_z}\frac{\partial T_r}{\partial z}\right)\right]$$

Now we define the volumetric heat capacity of the fluid-saturated rock as:

$$\left(\rho c_p\right)_t = \phi\rho c_p + (1-\phi)\rho_m c_{p_m} \quad \text{(A.72)}$$

And also, we define thermal conductivity of the fluid-saturated rock as:

$$\lambda_t = \phi\lambda + (1-\phi)\lambda_m \quad \text{(A.73)}$$

If we multiply both sides in Equation B.71 by the term described as:

$$\varsigma = \frac{\rho c_p}{\left(\rho c_p\right)_t + \phi p_r \beta_m} \quad \text{(A.74)}$$

Equation A.71 becomes:

$$\frac{\partial T_r}{\partial t} - \varsigma\phi\left[\varphi + \frac{p_r c_m}{\rho c_p}\right]\frac{\partial p_r}{\partial t}$$
$$= -\varsigma u_{c_r}\left(\frac{\partial T_r}{\partial r}\right) - \varsigma u_{c_z}\left(\frac{\partial T_r}{\partial z}\right) - \varsigma\rho g\frac{k_z}{\mu}\left(\frac{\partial T_r}{\partial z}\right)$$
$$+ \varsigma\varepsilon_{JT}\left[u_{c_r}\left(\frac{\partial p_r}{\partial r}\right) + u_{c_z}\left(\frac{\partial p_r}{\partial z}\right) - \rho g u_{c_z}\right] \quad \text{(A.75)}$$
$$+ \frac{\varsigma}{\rho c_p}\left[\frac{1}{r}\frac{\partial}{\partial r}\left(r\lambda_{t_r}\frac{\partial T_r}{\partial r}\right) + \frac{\partial}{\partial z}\left(\lambda_{t_z}\frac{\partial T_r}{\partial z}\right)\right]$$

Note that Equation A.75 is still a nonlinear PDE as λ_t, ε_{JT}, ρ, μ left-hand side as well as c_p, c_m in the right hand side are dependent on pressure and temperature.

The coefficient of isentropic expansion of the fluid (φ) is related to the J-T coefficient of the fluid by the following relationship:

$$\varphi = \varepsilon_{JT} + \frac{1}{\rho c_p} \tag{A.76}$$

When pressure is reduced, the fluid expands. Expansion of the fluid creates a change in temperature as it is indicated by the second and sixth terms of Equation A.75 in which the second term represents the isentropic expansion and the fifth term represents the J-T expansion. In fact, both terms represent the effect of isentropic expansion on temperature, however, the adiabatic expansion could either be reversible or irreversible in a thermodynamic sense. By definition, an isentropic process is adiabatic and reversible. On the other hand, the J-T expansion is adiabatic and irreversible. This is also observed through the thermodynamic definition of the coefficients (Equations A.77 and A.78) that multiply the pressure derivative terms. That is the fundamental difference between these expansion terms. The J-T coefficient multiplies the spatial derivative of pressure since the throttling process occurs along the spatial dimension. The thermodynamic relation between the isentropic expansion coefficient and J-T coefficient (Equation A.8) should not be interpreted as a J-T effect since these terms multiply the time derivative (Timmerhaus and Flynn, 1989; Flynn, 2004).

$$\varphi = \left(\frac{\partial T}{\partial p}\right)_S \tag{A.77}$$

$$\varepsilon_{JT} = \left(\frac{\partial T}{\partial p}\right)_H \tag{A.78}$$

When enthalpy is considered as a function of pressure and temperature $H(p,T)$, this suggests that the total differential dH can be expressed as:

$$dH = \left(\frac{\partial H}{\partial p}\right)_T dp + \left(\frac{\partial H}{\partial T}\right)_p dT \tag{A.79}$$

Note that:

$$\left(\frac{\partial H}{\partial p}\right)_T = V(1 - T\beta) \tag{A.80}$$

$$\left(\frac{\partial H}{\partial T}\right)_p = c_p \tag{A.81}$$

J-T coefficient can be acquired as in Equation A.82 by substituting Equations A.80 and A.81 in Equation A.79:

$$\varepsilon_{JT} = \frac{V}{c_p}(T\beta - 1) = \frac{(T\beta - 1)}{\rho c_p} \tag{A.82}$$

Furthermore, when we consider entropy as a function of pressure and temperature $S(p,T)$, this suggests that the total differential dS can be expressed and must be equal to zero:

$$dS = \left(\frac{\partial S}{\partial p}\right)_T dp + \left(\frac{\partial S}{\partial T}\right)_p dT \tag{A.83}$$

Following thermodynamic relations apply:

$$\left(\frac{\partial S}{\partial p}\right)_T = -\left(\frac{\partial V}{\partial T}\right)_p = -V\beta \tag{A.84}$$

$$\left(\frac{\partial S}{\partial T}\right)_p = \frac{c_p}{T} \tag{A.85}$$

Using Equations A.84 and A.85 in A.83 gives Equation A.86 as:

$$\left(\frac{\partial T}{\partial p}\right)_S = \frac{T\left(\frac{\partial V}{\partial T}\right)_p}{c_p} = \frac{TV\beta}{c_p} \tag{A.86}$$

APPENDIX B: Discretization of 2-D (*r*-*z*) Reservoir Equations

Mathematical model and governing equations to solve the two-dimensional flow of slightly compressible fluid flow in porous media are derived in the previous section. Block-centered grid system used contains properties of reservoir, which are assigned to each grid block. In order to set up the grid blocks in radial coordinates for two-dimensional study in the *r* and *z* directions, we define N_r to denote the number of grid blocks in the *r*-direction and N_{rz} to denote the number of grid blocks in the *z*-direction within the reservoir domain. As we consider two-dimensional *r*-*z* flow, only one grid block having 360° in θ direction is considered. Simulator always uses a "block centered grid" with the grid points in the *r*-direction geometrically spaced whereas in the *z*-direction user defined spaced. If not specified, as default, simulator uses equally spaced grid blocks in *z*-direction, which may not be realistic in some cases where the well is not fully penetrated. For the problem considered in this work the top and bottom boundaries and the outer boundary are no flow (Neumann type). A general view of the grids used is shown in Figure 3.1.

The coordinate system can be defined with *i* and *j* "dummy" index, where the *i* index defines the coordinate in the *r*-direction whereas the index *j* defines the coordinate in the *z*-direction. Coordinate axes for block-centered grid with defining dummy index are shown also in Figure 3.1. The reservoir pressure and temperature defined at grid points of the form (r_i,z_j) and the subrectangles represent grid blocks. Note that $r_{½}$ is equal to the wellbore radius r_w and $r_{Nr+½}$ is equal to the reservoir drainage radius r_e whereas $z_{½}$ is equal to zero which represents the bottom boundary and $z_{Nrz+½}$ is equal to the reservoir thickness h_{res}. The *z*-grid points are specified by first defining the block heights, Δz_j, j=1,2,…,N_{rz}. Thus, taking the top boundary definition as $z_{½}$=0 when the first gridblock in *z*-direction is considered as j=1, the *z*-direction block boundaries $z_{j+½}$, for j=1,2,…,N_{rz} are defined by:

$$z_{j+\frac{1}{2}} = z_{j-\frac{1}{2}} + \Delta z_j \tag{B.1}$$

The grid points z_j , for j=1,2,…,N_{rz} are then defined by:

$$z_j = z_{j-\frac{1}{2}} + \frac{\Delta z_j}{2} \tag{B.2}$$

Given that the terminology block centered grid is used, it may be noted that z_j is the center of each grid block at the vertical direction and can also be expressed as the halfway between:

$$z_j = \frac{z_{j+\frac{1}{2}} + z_{j-\frac{1}{2}}}{2} \tag{B.3}$$

Mass Balance: Recalling Equation B.38 with taking into consideration of derivatives in both side of the equation at any grid block points (r_i, z_j) for the finite difference formulation and multiply each side by control volume defined as $c_v = \pi \Delta z_j \left(r^2_{i+\frac{1}{2}} - r^2_{i-\frac{1}{2}} \right)$ gives:

$$\begin{aligned} -c_v \left[\phi c_t \frac{\partial p_r}{\partial t} - \phi \beta_t \frac{\partial T_r}{\partial t} \right]^{n+1}_{i,j} \\ - c_v \left[c u_{c_r} \left(\frac{\partial p_r}{\partial r} \right) + c \left[u_{c_z} + 2\rho g \frac{k_z}{\mu} \right] \left(\frac{\partial p_r}{\partial z} \right) \right]^{n+1}_{i,j} \\ + c_v \left[\beta u_{c_r} \left(\frac{\partial T_r}{\partial r} \right) + \beta \left[u_{c_z} + 2\rho g \frac{k_z}{\mu} \right] \left(\frac{\partial T_r}{\partial z} \right) \right]^{n+1}_{i,j} \\ + c_v \left[\frac{1}{r} \frac{\partial}{\partial r} \left(r \frac{k_r}{\mu} \frac{\partial p_r}{\partial r} \right) + \frac{\partial}{\partial z} \left(\frac{k_z}{\mu} \frac{\partial p_r}{\partial z} \right) - g\rho \frac{\partial}{\partial z} \left(\frac{k_z}{\mu} \right) \right]^{n+1}_{i,j} = 0 \end{aligned} \tag{B.4}$$

Each term is evaluated separately here. Therefore, the conduction term can be defined by central difference formulation due to second order derivative:

$$\begin{aligned} &\left[\frac{1}{r} \frac{\partial}{\partial r} \left(r \frac{k_r}{\mu} \frac{\partial p_r}{\partial r} \right) + \frac{\partial}{\partial z} \left(\frac{k_z}{\mu} \frac{\partial p_r}{\partial z} \right) - g\rho \frac{\partial}{\partial z} \left(\frac{k_z}{\mu} \right) \right]^{n+1}_{i,j} = \\ &\frac{1}{r_i} \left[r_{i+\frac{1}{2}} \left(\frac{k_r}{\mu} \frac{\partial p_r}{\partial r} \right)^{n+1}_{i+\frac{1}{2},j} - r_{i-\frac{1}{2}} \left(\frac{k_r}{\mu} \frac{\partial p_r}{\partial r} \right)^{n+1}_{i-\frac{1}{2},j} \right] \\ &+ \left[\left(\frac{k_z}{\mu} \frac{\partial p_r}{\partial z} \right)^{n+1}_{i,j+\frac{1}{2}} - \left(\frac{k_z}{\mu} \frac{\partial p_r}{\partial z} \right)^{n+1}_{i,j-\frac{1}{2}} - g\rho \left(\frac{k_z}{\mu} \right)^{n+1}_{i,j+\frac{1}{2}} + g\rho \left(\frac{k_z}{\mu} \right)^{n+1}_{i,j-\frac{1}{2}} \right] \end{aligned} \tag{B.5}$$

Consequently, derivation of $\partial p_r/\partial r$ and $\partial p_r/\partial z$, in above equations can be evaluated with upwind and downwind finite difference formulation at the boundaries as:

$$\left(\frac{\partial p_r}{\partial r}\right)_{i+\frac{1}{2},j}^{n+1} = \frac{{p_r}_{i+1,j}^{n+1} - {p_r}_{i,j}^{n+1}}{r_{i+1} - r_i} \tag{B.6}$$

$$\left(\frac{\partial p_r}{\partial r}\right)_{i-\frac{1}{2},j}^{n+1} = \frac{{p_r}_{i,j}^{n+1} - {p_r}_{i-1,j}^{n+1}}{r_i - r_{i-1}} \tag{B.7}$$

$$\left(\frac{\partial p_r}{\partial z}\right)_{i,j+\frac{1}{2}}^{n+1} = \frac{{p_r}_{i,j+1}^{n+1} - {p_r}_{i,j}^{n+1}}{z_{j+1} - z_j} \tag{B.8}$$

$$\left(\frac{\partial p_r}{\partial z}\right)_{i,j-\frac{1}{2}}^{n+1} = \frac{{p_r}_{i,j}^{n+1} - {p_r}_{i,j-1}^{n+1}}{z_j - z_{j-1}} \tag{B.9}$$

Convective terms can be defined by either upwind or downwind scheme formulation depending on the direction of the flow in each iteration at any time steps. It is important to note that, one must check the direction of the flow to take a representative derivative for convective term. If ${p_r}_{i+1,j}^{n+1} \geq {p_r}_{i,j}^{n+1}$ then we use upwind scheme in the *r*-direction shown as below:

$$\begin{aligned}\left[u_{c_r}\left(\frac{\partial p_r}{\partial r}\right)\right]_{i,j}^{n+1} &= \left[-\frac{k_r}{\mu}\left(\frac{\partial p_r}{\partial r}\right)\left(\frac{\partial p_r}{\partial r}\right)\right]_{i,j}^{n+1} \\ &= -\left(\frac{k_r}{\mu}\right)_{i,j}^{n+1}\left(\frac{{p_r}_{i+1,j}^{n+1} - {p_r}_{i,j}^{n+1}}{r_{i+1} - r_i}\right)^2\end{aligned} \tag{B.10}$$

$$\begin{aligned}\left[u_{c_r}\left(\frac{\partial T_r}{\partial r}\right)\right]_{i,j}^{n+1} &= \left[-\frac{k_r}{\mu}\left(\frac{\partial p_r}{\partial r}\right)\left(\frac{\partial T_r}{\partial r}\right)\right]_{i,j}^{n+1} \\ &= -\left(\frac{k_r}{\mu}\right)_{i,j}^{n+1}\left(\frac{{p_r}_{i+1,j}^{n+1} - {p_r}_{i,j}^{n+1}}{r_{i+1} - r_i}\right)\left(\frac{{T_r}_{i+1,j}^{n+1} - {T_r}_{i,j}^{n+1}}{r_{i+1} - r_i}\right)\end{aligned} \tag{B.11}$$

If ${p_r}_{i+1,j}^{n+1} < {p_r}_{i,j}^{n+1}$, then we switch convective term to downwind scheme shown as below:

$$\left[u_{c_r}\left(\frac{\partial p_r}{\partial r}\right)\right]_{i,j}^{n+1} = \left[-\frac{k_r}{\mu}\left(\frac{\partial p_r}{\partial r}\right)\left(\frac{\partial p_r}{\partial r}\right)\right]_{i,j}^{n+1}$$
$$= -\left(\frac{k_r}{\mu}\right)_{i,j}^{n+1}\left(\frac{p_{r_{i,j}}^{n+1} - p_{r_{i-1,j}}^{n+1}}{r_i - r_{i-1}}\right)^2 \tag{B.12}$$

$$\left[u_{c_r}\left(\frac{\partial T_r}{\partial r}\right)\right]_{i,j}^{n+1} = \left[-\frac{k_r}{\mu}\left(\frac{\partial p_r}{\partial r}\right)\left(\frac{\partial T_r}{\partial r}\right)\right]_{i,j}^{n+1}$$
$$= -\left(\frac{k_r}{\mu}\right)_{i,j}^{n+1}\left(\frac{p_{r_{i,j}}^{n+1} - p_{r_{i-1,j}}^{n+1}}{r_i - r_{i-1}}\right)\left(\frac{T_{r_{i,j}}^{n+1} - T_{r_{i-1,j}}^{n+1}}{r_i - r_{i-1}}\right) \tag{B.13}$$

Similarly, for z-direction, if $p_{r_{i,j+1}}^{n+1} \geq p_{r_{i,j}}^{n+1}$ then we use upwind scheme shown as below:

$$\left[u_{c_z}\left(\frac{\partial p_r}{\partial z}\right)\right]_{i,j}^{n+1} = \left[-\frac{k_z}{\mu}\left(\frac{\partial p_r}{\partial z}\right)\left(\frac{\partial p_r}{\partial z}\right)\right]_{i,j}^{n+1}$$
$$= -\left(\frac{k_r}{\mu}\right)_{i,j}^{n+1}\left(\frac{p_{r_{i,j+1}}^{n+1} - p_{r_{i,j}}^{n+1}}{z_{i+1} - z_i}\right)^2 \tag{B.14}$$

$$\left[u_{c_z}\left(\frac{\partial T_r}{\partial z}\right)\right]_{i,j}^{n+1} = \left[-\frac{k_z}{\mu}\left(\frac{\partial p_r}{\partial z}\right)\left(\frac{\partial T_r}{\partial z}\right)\right]_{i,j}^{n+1}$$
$$= -\left(\frac{k_z}{\mu}\right)_{i,j}^{n+1}\left(\frac{p_{r_{i,j+1}}^{n+1} - p_{r_{i,j}}^{n+1}}{z_{i+1} - z_i}\right)\left(\frac{T_{r_{i,j+1}}^{n+1} - T_{r_{i,j}}^{n+1}}{z_{i+1} - z_i}\right) \tag{B.15}$$

Similarly, for z-direction, if $p_{r_{i,j+1}}^{n+1} < p_{r_{i,j}}^{n+1}$ then we use downwind scheme shown as below:

$$\left[u_{c_z}\left(\frac{\partial p_r}{\partial z}\right)\right]_{i,j}^{n+1} = \left[-\frac{k_z}{\mu}\left(\frac{\partial p_r}{\partial z}\right)\left(\frac{\partial p_r}{\partial z}\right)\right]_{i,j}^{n+1}$$
$$= -\left(\frac{k_r}{\mu}\right)_{i,j}^{n+1}\left(\frac{p_{r_{i,j}}^{n+1} - p_{r_{i,j-1}}^{n+1}}{z_i - z_{i-1}}\right)^2 \tag{B.16}$$

$$\left[u_{c_z}\left(\frac{\partial T_r}{\partial z}\right)\right]_{i,j}^{n+1} = \left[-\frac{k_z}{\mu}\left(\frac{\partial p_r}{\partial z}\right)\left(\frac{\partial T_r}{\partial z}\right)\right]_{i,j}^{n+1}$$
$$= -\left(\frac{k_z}{\mu}\right)_{i,j}^{n+1}\left(\frac{p_{r_{i,j}}^{n+1} - p_{r_{i,j-1}}^{n+1}}{z_i - z_{i-1}}\right)\left(\frac{T_{r_{i,j}}^{n+1} - T_{r_{i,j-1}}^{n+1}}{z_i - z_{i-1}}\right) \tag{B.17}$$

Using this definition for any time steps, we wish to consider the backward difference in time derivative, and then finalize differencing the equation as below;

$$c_v\phi c_t\left(\frac{p_{r_{i,j}}^{n+1} - p_{r_{i,j}}^{n}}{\Delta t}\right) - c_v\phi\beta_t\left(\frac{T_{r_{i,j}}^{n+1} - T_{r_{i,j}}^{n}}{\Delta t}\right) - g\rho\left[\left(\frac{k_z}{\mu}\right)_{i,j+\frac{1}{2}}^{n+1} - \left(\frac{k_z}{\mu}\right)_{i,j-\frac{1}{2}}^{n+1}\right] =$$

$$-c_v c u_{c_r}\left(\frac{p_{r_{i+1,j}}^{n+1} - p_{r_{i,j}}^{n+1}}{r_{i+1} - r_i}\right) - c_v c\left[u_{c_z} + 2\rho g\frac{k_z}{\mu}\right]\left(\frac{p_{r_{i,j+1}}^{n+1} - p_{r_{i,j}}^{n+1}}{z_{j+1} - z_j}\right)$$

$$+c_v\beta u_{c_r}\left(\frac{T_{r_{i+1,j}}^{n+1} - T_{r_{i,j}}^{n+1}}{r_{i+1} - r_i}\right) + c_v\beta\left[u_{c_z} + 2\rho g\frac{k_z}{\mu}\right]\left(\frac{T_{r_{i,j+1}}^{n+1} - T_{r_{i,j}}^{n+1}}{z_{j+1} - z_j}\right)$$

$$+2\pi\Delta z_j\left[\frac{r_{i+\frac{1}{2}}}{(r_{i+1} - r_i)}\right]\left(\frac{k_r}{\mu}\right)_{i+\frac{1}{2},j}\left(p_{r_{i+1,j}}^{n+1} - p_{r_{i,j}}^{n+1}\right)$$

$$+2\pi\Delta z_j\left[\frac{r_{i-\frac{1}{2}}}{(r_i - r_{i-1})}\right]\left(\frac{k_r}{\mu}\right)_{i-\frac{1}{2},j}\left(p_{r_{i,j}}^{n+1} - p_{r_{i-1,j}}^{n+1}\right)$$

$$+\frac{\pi\left(r_{i+\frac{1}{2}}^2 - r_{i-\frac{1}{2}}^2\right)}{(z_{j+1} - z_j)}\left(\frac{k_z}{\mu}\right)_{i,j+\frac{1}{2}}\left(p_{r_{i,j+1}}^{n+1} - p_{r_{i,j}}^{n+1}\right)$$

$$-\frac{\pi\left(r_{i+\frac{1}{2}}^2 - r_{i-\frac{1}{2}}^2\right)}{(z_j - z_{j-1})}\left(\frac{k_z}{\mu}\right)_{i,j-\frac{1}{2}}\left(p_{r_{i,j}}^{n+1} - p_{r_{i,j-1}}^{n+1}\right)$$

(B.18)

Transmissibility terms in *r*-direction at a grid block, (r_i, z_j)'s boundaries can be defined as:

$$\zeta_{i-\frac{1}{2},j}^{n+1} = 2\pi\Delta z_j\left[\frac{r_{i-\frac{1}{2}}}{(r_i - r_{i-1})}\right]\left(\frac{k_r}{\mu}\right)_{i-\frac{1}{2},j} \tag{B.19}$$

$$\zeta_{i+\frac{1}{2},j}^{n+1} = 2\pi\Delta z_j \left[\frac{r_{i+\frac{1}{2}}}{(r_{i+1} - r_i)}\right]\left(\frac{k_r}{\mu}\right)_{i+\frac{1}{2},j} \tag{B.20}$$

Transmissibility terms in z-direction at a grid block, (r_i, z_j)'s boundaries can be defined as:

$$\zeta_{i,j-\frac{1}{2}}^{n+1} = \left[\frac{\pi\left(r_{i+\frac{1}{2}}^2 - r_{i-\frac{1}{2}}^2\right)}{\left(z_j - z_{j-1}\right)}\right]\left(\frac{k_z}{\mu}\right)_{i,j-\frac{1}{2}} \tag{B.21}$$

$$\zeta_{i,j+\frac{1}{2}}^{n+1} = \left[\frac{\pi\left(r_{i+\frac{1}{2}}^2 - r_{i-\frac{1}{2}}^2\right)}{\left(z_{j+1} - z_j\right)}\right]\left(\frac{k_z}{\mu}\right)_{i,j+\frac{1}{2}} \tag{B.22}$$

where convective term defined respectively in r-direction and z-direction at a grid block, (r_i, z_j)'s center as:

$$\omega_{r\,i,j}^{n+1} = \left(\frac{c_v}{r_{i+1} - r_i}\right)\left(u_{c_r}\right)_{i,j}^{n+1} \tag{B.23}$$

$$\omega_{z\,i,j}^{n+1} = \left(\frac{c_v}{z_{j+1} - z_j}\right)\left(u_{c_z} + 2\rho g\frac{k_z}{\mu}\right)_{i,j}^{n+1} \tag{B.24}$$

The gravity term on the right-hand side of the equation also defined as:

$$\psi_{i,j}^{n+1} = g\rho\left(\frac{\left(\frac{k_z}{\mu}\right)_{i,j+1}^{n+1} - \left(\frac{k_z}{\mu}\right)_{i,j}^{n+1}}{z_{j+1} - z_j}\right) \tag{B.25}$$

Furthermore, the volumetric term at a grid block, (r_i, z_j) is defined as:

$$Q_{i,j}^{n+1} = \frac{c_v}{\Delta t}\phi c_t \tag{B.26}$$

$$R_{i,j}^{n+1} = \frac{c_v}{\Delta t}\phi\beta_t \tag{B.27}$$

Thus, using the preceding definitions of transmissibility and volumetric terms, Equation B.18 can be rewritten for i=2,...,N_r-1 and j=2,...,N_{rz}-1:

$$\begin{aligned} Q_{i,j}^{n+1}\left(p_{r_{i,j}}^{n+1}-p_{r_{i,j}}^{n}\right)-R_{i,j}^{n+1}\left(T_{r_{i,j}}^{n+1}-T_{r_{i,j}}^{n}\right)+\psi_{i,j}^{n+1} \\ =-c\omega_{r_{i,j}}^{n+1}\left(p_{r_{i+1,j}}^{n+1}-p_{r_{i,j}}^{n+1}\right) \\ -c\omega_{z_{i,j}}^{n+1}\left(p_{r_{i,j+1}}^{n+1}-p_{r_{i,j}}^{n+1}\right)+\beta\omega_{r_{i,j}}^{n+1}\left(T_{r_{i+1,j}}^{n+1}-T_{r_{i,j}}^{n+1}\right) \\ +\beta\omega_{z_{i,j}}^{n+1}\left(T_{r_{i,j+1}}^{n+1}-T_{r_{i,j}}^{n+1}\right)+\zeta_{i+\frac{1}{2},j}^{n+1}\left(p_{r_{i+1,j}}^{n+1}-p_{r_{i,j}}^{n+1}\right) \\ -\zeta_{i-\frac{1}{2},j}^{n+1}\left(p_{r_{i,j}}^{n+1}-p_{r_{i-1,j}}^{n+1}\right)+\zeta_{i,j+\frac{1}{2}}^{n+1}\left(p_{r_{i,j+1}}^{n+1}-p_{r_{i,j}}^{n+1}\right) \\ -\zeta_{i,j-\frac{1}{2}}^{n+1}\left(p_{r_{i,j}}^{n+1}-p_{r_{i,j-1}}^{n+1}\right) \end{aligned} \tag{B.28}$$

It is important to note that transmissibility terms in r-direction, i=N_r as well as in z-direction, when j=1 and j=N_{rz} are all set to zero in order to incorporate a no flow outer as well as top and bottom pressure boundary condition. For coupling purposes, the inner boundary condition (when i=1) is given in Equation 2.1.

$$\left(\frac{\partial p_r}{\partial r}\right)_{i-\frac{1}{2},j}^{n+1}=\frac{p_{r_{1,j}}^{n+1}-p_{w_j}^{n+1}}{r_1} \quad , \quad \left(\frac{\partial p_r}{\partial r}\right)_{N_r+\frac{1}{2},j}^{n+1}=0 \tag{B.29}$$

$$\left(\frac{\partial p_r}{\partial z}\right)_{i,\frac{1}{2}}^{n+1}=0 \quad , \quad \left(\frac{\partial p_r}{\partial z}\right)_{i,N_{rz}+\frac{1}{2}}^{n+1}=0 \tag{B.30}$$

Thus, all corresponding transmissibility terms for pressure yields:

$$\zeta_{\frac{1}{2},j}^{n+1}=0 \qquad \zeta_{N_r+\frac{1}{2},j}^{n+1}=0 \tag{B.31}$$

$$\zeta_{i,\frac{1}{2}}^{n+1}=0 \qquad \zeta_{i,N_{rz}+\frac{1}{2}}^{n+1}=0 \tag{B.32}$$

Thus, convective terms for pressure are also set to zero where the direction of the flow hits the boundaries:

$$\omega_{r_{1,j}}^{n+1}=0 \qquad \omega_{r_{N_r,j}}^{n+1}=0 \tag{B.33}$$

$$\omega_{z_{i,1}}^{n+1}=0 \qquad \omega_{z_{i,N_{rz}}}^{n+1}=0 \tag{B.34}$$

Recalling the outer boundary condition for temperature, when $i=N_r$, $T_{r_{N_r+1,j}}^{n+1} = T_e^n$ and it is a known term thus goes to right hand side of the equation.

$$\zeta_{N_r+\frac{1}{2},j}^{n+1} = 2\pi h\left[\frac{r_e}{(r_e - r_{N_r})}\right]\left(\frac{k_r}{\mu}\right)_{N_r+\frac{1}{2},j} \tag{B.35}$$

It is also important to note that when $i=N_r$, the convective term for temperature is defined as a known parameter and goes to right hand side of the equation as:

$$\omega_{Nr,j}^{n+1} = \left(\frac{c_v}{r_e - r_{N_r}}\right)\left(u_{c_r}\right)_{N_r,j}^{n+1} \tag{B.36}$$

Recalling the outer boundary conditions for temperature, when $j=1$, $T_{r_{i,0}}^{n+1} = T_e^n$,and when $j=N_{rz}$, $T_{r_{i,N_{rz}+1}}^{n+1} = T_e^n$ and as known terms go to right hand side of the equation.

$$\zeta_{i,\frac{1}{2}}^{n+1} = \left[\frac{\pi\left(r_{i+\frac{1}{2}}^2 - r_{i-\frac{1}{2}}^2\right)}{z_1}\right]\left(\frac{k_z}{\mu}\right)_{i,\frac{1}{2}} \tag{B.37}$$

$$\zeta_{i,N_{rz}+\frac{1}{2}}^{n+1} = \left[\frac{\pi\left(r_{i+\frac{1}{2}}^2 - r_{i-\frac{1}{2}}^2\right)}{h_{res} - z_{N_{rz}}}\right]\left(\frac{k_z}{\mu}\right)_{i,N_{rz}+\frac{1}{2}} \tag{B.38}$$

it is also important to note that when $j=N_{rz}$, the convective term for temperature is defined as a known parameter and goes to right hand side of the equation as:

$$\omega_{z\,i,N_{rz}}^{n+1} = \left(\frac{c_v}{h_{res} - z_{N_{rz}}}\right)\left(u_{c_z} + 2\rho g\frac{k_z}{\mu}\right)_{i,N_{rz}}^{n+1} \tag{B.39}$$

Recalling Equation B.28, we can finalize the mass balance equation by putting unknown terms one side and pressure terms to the other side as:

$$
\begin{aligned}
&\left(-Q_{i,j}^{n+1}\right)p_{r}{}_{i,j}^{n} + \left(R_{i,j}^{n+1}\right)T_{r}{}_{i,j}^{n} + \psi_{i,j}^{n+1} = \\
&\left[-Q_{i,j}^{n+1} + \left(-\zeta_{i+\frac{1}{2},j}^{n+1} + c\omega_{r}{}_{i,j}^{n+1}\right) + \left(-\zeta_{,j+\frac{1}{2}}^{n+1} + c\omega_{z}{}_{i,j}^{n+1}\right) - \zeta_{i-\frac{1}{2},j}^{n+1}\right. \\
&\qquad \left. - \zeta_{i,j-\frac{1}{2}}^{n+1}\right] p_{r}{}_{i,j}^{n+1} + \left(R_{i,j}^{n+1} - \beta\omega_{r}{}_{i,j}^{n+1} - \beta\omega_{z}{}_{i,j}^{n+1}\right) T_{r}{}_{i,j}^{n+1} \\
&+ \left(\zeta_{i+\frac{1}{2},j}^{n+1} - c\omega_{r}{}_{i,j}^{n+1}\right) p_{r}{}_{i+1,j}^{n+1} + \left(\zeta_{i-\frac{1}{2},j}^{n+1}\right) p_{r}{}_{i-1,j}^{n+1} + \left(\zeta_{i,j+\frac{1}{2}}^{n+1} - c\omega_{z}{}_{i,j}^{n+1}\right) p_{r}{}_{i,j+1}^{n+1} \\
&+ \left(\zeta_{i,j-\frac{1}{2}}^{n+1}\right) p_{r}{}_{i,j-1}^{n+1} + \left(\beta\omega_{r}{}_{i,j}^{n+1}\right) T_{r}{}_{i+1,j}^{n+1} + \left(\beta\omega_{z}{}_{i,j}^{n+1}\right) T_{r}{}_{i,j+1}^{n+1}
\end{aligned}
\tag{B.40}
$$

Energy Balance: Recalling Equation A.75 with taking into consideration of derivatives in both side of the equation at any grid block points (r_i, z_j) for the finite difference formulation and multiply each side by control volume yields:

$$
\begin{aligned}
&c_v\left(\frac{\partial T_r}{\partial t}\right)_{i,j}^{n+1} - c_v\left[\varsigma\phi\left(\varphi + \frac{p_r c_m}{\rho c_p}\right)\left(\frac{\partial p_r}{\partial t}\right)\right]_{i,j}^{n+1} = \\
&-c_v\left[\varsigma u_{c_r}\left(\frac{\partial T_r}{\partial r}\right)\right]_{i,j}^{n+1} - c_v\left[\varsigma\left(u_{c_z} + \rho g\frac{k_z}{\mu}\right)\left(\frac{\partial T_r}{\partial z}\right)\right]_{i,j}^{n+1} \\
&+c_v\left[\varsigma\varepsilon_{JT}u_{c_r}\left(\frac{\partial p_r}{\partial r}\right)\right]_{i,j}^{n+1} + c_v\left[\varsigma\varepsilon_{JT}\left(u_{c_z} + \rho g\frac{k_z}{\mu}\right)\left(\frac{\partial p_r}{\partial z}\right)\right]_{i,j}^{n+1} \\
&+c_v\left[\frac{\varsigma}{\rho c_p}\left(\frac{1}{r}\frac{\partial}{\partial r}\left(r\lambda_{t_r}\frac{\partial T_r}{\partial r}\right) + \frac{\partial}{\partial z}\left(\lambda_{t_z}\frac{\partial T_r}{\partial z}\right)\right)\right]_{i,j}^{n+1}
\end{aligned}
\tag{B.41}
$$

Each term is evaluated separately here. Therefore, the conduction term can be defined by central difference formulation:

$$
\begin{aligned}
&\left[\frac{1}{r}\frac{\partial}{\partial r}\left(r\lambda_{t_r}\frac{\partial T_r}{\partial r}\right) + \frac{\partial}{\partial z}\left(\lambda_{t_z}\frac{\partial T_r}{\partial z}\right)\right]_{i,j}^{n+1} = \left(\lambda_{t_z}\frac{\partial T_r}{\partial z}\right)_{i,j+\frac{1}{2}}^{n+1} - \left(\lambda_{t_z}\frac{\partial T_r}{\partial z}\right)_{i,j-\frac{1}{2}}^{n+1} \\
&+\frac{1}{r_i}\left[r_{i+\frac{1}{2}}\left(\lambda_{t_r}\frac{\partial T_r}{\partial r}\right)_{i+\frac{1}{2},j}^{n+1} - r_{i-\frac{1}{2}}\left(\lambda_{t_r}\frac{\partial T_r}{\partial r}\right)_{i-\frac{1}{2},j}^{n+1}\right]
\end{aligned}
\tag{B.42}
$$

Consequently, derivation of $\partial p/\partial r$ and $\partial p/\partial z$ in Equation A.68 should be evaluated with central finite difference formulation. Convective terms can be defined by either

upwind or downwind scheme formulation depending on the direction of the flow in each iteration at any time step. One must check the direction of the flow to take a representative derivative for convective term as explained for mass balance equation. Using this definition for any time steps, we wish to consider the backward difference in time derivative, and then finalize differencing the equation as below:

$$c_v\left(\frac{T_{r_{i,j}}^{n+1}-T_{r_{i,j}}^{n}}{\Delta t}\right)-c_v\underbrace{\varsigma\phi\left(\varphi+\frac{p_{r_{i,j}}^{n+1}c_m}{\rho c_p}\right)}_{\varrho}\left(\frac{p_{r_{i,j}}^{n+1}-p_{r_{i,j}}^{n}}{\Delta t}\right)=$$

$$-c_v\varsigma u_{c_r}\left(\frac{T_{r_{i+1,j}}^{n+1}-T_{r_{i,j}}^{n+1}}{r_{i+1}-r_i}\right)-c_v\varsigma\left(u_{c_z}+\rho g\frac{k_z}{\mu}\right)\left(\frac{T_{r_{i,j+1}}^{n+1}-T_{r_{i,j}}^{n+1}}{z_{j+1}-z_j}\right)$$

$$+c_v\varsigma\varepsilon_{JT}u_{c_r}\left(\frac{p_{r_{i+1,j}}^{n+1}-p_{r_{i,j}}^{n+1}}{r_{i+1}-r_i}\right)+c_v\varsigma\varepsilon_{JT}\left(u_{c_z}+\rho g\frac{k_z}{\mu}\right)\left(\frac{p_{r_{i,j+1}}^{n+1}-p_{r_{i,j}}^{n+1}}{z_{j+1}-z_j}\right)$$

$$+2\pi\Delta z_j\left[\frac{r_{i+\frac{1}{2}}}{(r_{i+1}-r_i)}\right]\left(\frac{\varsigma}{\rho c_p}\right)_{i,j}^{n+1}\lambda_{t_{r_{i+\frac{1}{2},j}}}\left(T_{r_{i+1,j}}^{n+1}-T_{r_{i,j}}^{n+1}\right)$$

$$-2\pi\Delta z_j\left[\frac{r_{i-\frac{1}{2}}}{(r_i-r_{i-1})}\right]\left(\frac{\varsigma}{\rho c_p}\right)_{i,j}^{n+1}\lambda_{t_{r_{i-\frac{1}{2},j}}}\left(T_{r_{i,j}}^{n+1}-T_{r_{i-1,j}}^{n+1}\right)$$

$$+\left[\frac{\pi\left(r_{i+\frac{1}{2}}^2-r_{i-\frac{1}{2}}^2\right)}{\left(z_{j+1}-z_j\right)}\right]\left(\frac{\varsigma}{\rho c_p}\right)_{i,j}^{n+1}\lambda_{t_{z_{i,j+\frac{1}{2}}}}\left(T_{r_{i,j+1}}^{n+1}-T_{r_{i,j}}^{n+1}\right)$$

$$-\left[\frac{\pi\left(r_{i+\frac{1}{2}}^2-r_{i-\frac{1}{2}}^2\right)}{\left(z_j-z_{j-1}\right)}\right]\left(\frac{\varsigma}{\rho c_p}\right)_{i,j}^{n+1}\lambda_{t_{z_{i,j-\frac{1}{2}}}}\left(T_{r_{i,j}}^{n+1}-T_{r_{i,j-1}}^{n+1}\right)$$

(B.43)

Using the definition of α in Coats gridding in the radial direction described in previous section, transmissibility terms in *r*-direction at a grid block, (r_i, z_j)'s boundaries can be defined as:

$$\xi_{i-\frac{1}{2},j}^{n+1}=2\pi\Delta z_j\left(\frac{r_{i-\frac{1}{2}}}{r_i-r_{i-1}}\right)\left(\frac{\varsigma}{\rho c_p}\right)_{i,j}^{n+1}\lambda_{t_{r_{i-\frac{1}{2},j}}} \tag{B.44}$$

$$\xi_{i+\frac{1}{2},j}^{n+1} = 2\pi\Delta z_j \left(\frac{r_{i+\frac{1}{2}}}{r_{i+1} - r_i}\right)\left(\frac{\varsigma}{\rho c_p}\right)_{i,j}^{n+1} \lambda_{t_{r_{i+\frac{1}{2},j}}} \tag{B.45}$$

It is important to note that transmissibility term for conduction in *r*-direction as given in Equation B.44, when *i*=1, is the representative section of the wellbore adjacent to the formation and inner boundary condition for temperature should be applied from given Equation 2.3 in terms of overall heat transfer coefficient:

$$\xi_{i-\frac{1}{2},j}^{n+1} = 2\pi\Delta z_j r_w U_t \left(\frac{\varsigma}{\rho c_p}\right)_{i,j}^{n+1} \tag{B.46}$$

Transmissibility terms in *z*-direction at a grid block, (r_i, z_j)'s boundaries can be defined as:

$$\xi_{i,j-\frac{1}{2}}^{n+1} = \left[\frac{\pi\left(r_{i+\frac{1}{2}}^2 - r_{i-\frac{1}{2}}^2\right)}{\left(z_j - z_{j-1}\right)}\right]\left(\frac{\varsigma}{\rho c_p}\right)_{i,j}^{n+1} \lambda_{t_{z_{i,j-\frac{1}{2}}}} \tag{B.47}$$

$$\xi_{i,j+\frac{1}{2}}^{n+1} = \left[\frac{\pi\left(r_{i+\frac{1}{2}}^2 - r_{i-\frac{1}{2}}^2\right)}{\left(z_{j+1} - z_j\right)}\right]\left(\frac{\varsigma}{\rho c_p}\right)_{i,j}^{n+1} \lambda_{t_{z_{i,j+\frac{1}{2}}}} \tag{B.48}$$

where convective term defined respectively in *r*-direction and *z*-direction at a grid block, (r_i, z_j)'s center as:

$$\theta_{r_{i,j}}^{n+1} = \left(\frac{c_v\varsigma}{r_{i+1} - r_i}\right)\left(u_{c_r}\right)_{i,j}^{n+1} \tag{B.49}$$

$$\theta_{z_{i,j}}^{n+1} = \left(\frac{c_v\varsigma}{z_{j+1} - z_j}\right)\left(u_{c_z} + \rho g\frac{k_z}{\mu}\right)_{i,j}^{n+1} \tag{B.50}$$

Furthermore, and also rewrite the volumetric term at a grid block, (r_i, z_j) is defined as:

$$V_{i,j}^{n+1} = \frac{c_v}{\Delta t} \tag{B.51}$$

Thus, using the preceding definitions of transmissibility and volumetric terms, Equation B.43 can be rewritten for i=2,...,N_{rz}-1 and i=2,...,N_{rz}-1:

$$\begin{aligned} V_{i,j}^{n+1}\left(T_{r_{i,j}}^{n+1}-T_{r_{i,j}}^{n}\right)-V_{i,j}^{n+1}\varrho_{i,j}^{n+1}\left(p_{r_{i,j}}^{n+1}-p_{r_{i,j}}^{n}\right) \\ =-\theta_{r_{i,j}}^{n+1}\left(T_{r_{i+1,j}}^{n+1}-T_{r_{i,j}}^{n+1}\right)-\theta_{z_{i,j}}^{n+1}\left(T_{r_{i,j+1}}^{n+1}-T_{r_{i,j}}^{n+1}\right) \\ +\varepsilon_{JT}\theta_{r_{i,j}}^{n+1}\left(p_{r_{i+1,j}}^{n+1}-p_{r_{i,j}}^{n+1}\right) \\ +\varepsilon_{JT}\theta_{z_{i,j}}^{n+1}\left(p_{r_{i,j+1}}^{n+1}-p_{r_{i,j}}^{n+1}\right)+\xi_{i+\frac{1}{2},j}^{n+1}\left(T_{r_{i+1,j}}^{n+1}-T_{r_{i,j}}^{n+1}\right) \\ -\xi_{i-\frac{1}{2},j}^{n+1}\left(T_{r_{i,j}}^{n+1}-T_{r_{i-1,j}}^{n+1}\right)+\xi_{i,j+\frac{1}{2}}^{n+1}\left(T_{r_{i,j+1}}^{n+1}-T_{r_{i,j}}^{n+1}\right) \\ -\xi_{i,j-\frac{1}{2}}^{n+1}\left(T_{r_{i,j}}^{n+1}-T_{r_{i,j-1}}^{n+1}\right) \end{aligned} \tag{B.52}$$

Recalling the outer boundary condition for temperature, when i=N_r, $T_{N_r+1,j}^{n+1}=T_e^n$ and when j=1, $T_{i,0}^{n+1}=T_e^n$ and when j=N_{rz}, $T_{i,N_{rz}+1}^{n+1}=T_e^n$, as known terms go to right hand side of the equation and recalculated as respectively:

$$\xi_{N_r+\frac{1}{2},j}^{n+1}=2\pi\Delta z_j\left[\frac{r_e}{\left(r_e-r_{N_r}\right)}\right]\left(\frac{\varsigma}{\rho c_p}\right)_{N_r,j}^{n+1}\lambda_{t_{r_{N_r+\frac{1}{2},j}}} \tag{B.53}$$

$$\xi_{i,\frac{1}{2}}^{n+1}=\left[\frac{\pi\left(r_{i+\frac{1}{2}}^2-r_{i-\frac{1}{2}}^2\right)}{z_1}\right]\left(\frac{\varsigma}{\rho c_p}\right)_{i,1}^{n+1}\lambda_{t_{z_{i,\frac{1}{2}}}} \tag{B.54}$$

$$\xi_{i,N_{rz}+\frac{1}{2}}^{n+1}=\left[\frac{\pi\left(r_{i+\frac{1}{2}}^2-r_{i-\frac{1}{2}}^2\right)}{\left(h_{res}-z_{N_{rz}}\right)}\right]\left(\frac{\varsigma}{\rho c_p}\right)_{i,N_{rz}}^{n+1}\lambda_{t_{z_{i,N_{rz}+\frac{1}{2}}}} \tag{B.55}$$

Recalling the boundary conditions, it is important to note that when i=N_r, in order to incorporate a no flow outer boundary condition, the convective term for pressure is also set to zero if the direction of flow requires upwind scheme:

$$\theta_{r_{i,N_{rz}}}^{n+1}=0 \tag{B.56}$$

whereas the convective term for temperature is defined as a known parameter and goes to right hand side of the equation:

$$\theta_{r}{}_{N_r,j}^{n+1} = \left(\frac{c_v \varsigma}{r_e - r_{N_r}}\right)\left(u_{c_r}\right)_{N_r,j}^{n+1} \tag{B.57}$$

Recalling the boundary conditions, it is important to note that when $j=N_z$, in order to incorporate a no flow bottom boundary condition, the convective term for pressure is also set to zero if the direction of flow requires upwind scheme:

$$\theta_{z}{}_{i,N_{rz}}^{n+1} = 0 \tag{B.58}$$

Whereas the convective term for temperature is defined as a known parameter and goes to right hand side of the equation:

$$\theta_{z}{}_{i,N_{rz}}^{n+1} = \left(\frac{c_v \varsigma}{h - z_{N_{rz}}}\right)\left(u_{c_z} + \rho g \frac{k_z}{\mu}\right)_{i,N_{rz}}^{n+1} \tag{B.59}$$

Recalling Equation B.52, we can finalize the energy balance equation by putting unknown terms one side and pressure terms to the other side as:

$$\begin{aligned}
&\left[-V_{i,j}^{n+1} + \left(\theta_{r}{}_{i,j}^{n+1} - \xi_{i+\frac{1}{2},j}^{n+1}\right) + \left(\theta_{z}{}_{i,j}^{n+1} - \xi_{i,j+\frac{1}{2}}^{n+1}\right) - \xi_{i-\frac{1}{2},j}^{n+1} - \xi_{i,j-\frac{1}{2}}^{n+1}\right] T_{r}{}_{i,j}^{n+1} \\
&+ \left(V_{i,j}^{n+1}\varrho_{i,j}^{n+1} - \varepsilon_{JT}\theta_{r}{}_{i,j}^{n+1} - \varepsilon_{JT}\theta_{z}{}_{i,j}^{n+1}\right) p_{r}{}_{i,j}^{n+1} + \left(-\theta_{r}{}_{i,j}^{n+1} + \xi_{i+\frac{1}{2},j}^{n+1}\right) T_{r}{}_{i+1,j}^{n+1} \\
&+ \left(-\theta_{z}{}_{i,j}^{n+1} + \xi_{i,j+\frac{1}{2}}^{n+1}\right) T_{r}{}_{i,j+1}^{n+1} + \left(\xi_{i-\frac{1}{2},j}^{n+1}\right) T_{r}{}_{i-1,j}^{n+1} + \left(\xi_{i,j-\frac{1}{2}}^{n+1}\right) T_{r}{}_{i,j-1}^{n+1} \\
&+ \left(\varepsilon_{JT}\theta_{r}{}_{i,j}^{n+1}\right) p_{r}{}_{i+1,j}^{n+1} + \left(\varepsilon_{JT}\theta_{z}{}_{i,j}^{n+1}\right) p_{r}{}_{i,j+1}^{n+1} \\
&= \left(-V_{i,j}^{n+1}\right) T_{i,j}^{n} + \left(V_{i,j}^{n+1}\varrho_{i,j}^{n+1}\right) p_{r}{}_{i,j}^{n}
\end{aligned} \tag{B.60}$$

Here, we evaluate all transmissibility terms in *r*-direction and *z*-direction. We use the harmonic averages for the permeability. Therefore, permeability in *r*-direction for all layers can be derived as:

$$(k_r)_{i+\frac{1}{2},j} = \frac{(k_r)_{i,j}(k_r)_{i+1,j} ln\left(\frac{r_{i+1}}{r_i}\right)}{(k_r)_{i,j} ln\left(\frac{r_{i+1}}{r_{i+\frac{1}{2}}}\right) + (k_r)_{i+1,j} ln\left(\frac{r_{i+\frac{1}{2}}}{r_i}\right)} \tag{B.61}$$

whereas permeability in *z*-direction for all grids in the *r*-direction can be derived as:

$$(k_z)_{i,j+\frac{1}{2}} = \frac{(k_z)_{i,j}(k_z)_{i,j+1}\left(\Delta z_j + \Delta z_{j+1}\right)}{(k_z)_{i,j}\Delta z_{j+1} + (k_z)_{i,j+1}\Delta z_j} \tag{B.62}$$

viscosity and thermal conductivity terms need to be evaluated by using a simple averaging consequently as:

$$\mu^{n+1}_{i+\frac{1}{2},j} = \frac{\mu^{n+1}_{i+1,j} + \mu^{n+1}_{i,j}}{2}, \quad \mu^{n+1}_{i-\frac{1}{2},j} = \frac{\mu^{n+1}_{i,j} + \mu^{n+1}_{i-1,j}}{2} \tag{B.63}$$

$$\mu^{n+1}_{i,j+\frac{1}{2}} = \frac{\mu^{n+1}_{i,j+1} + \mu^{n+1}_{i,j}}{2}, \quad \mu^{n+1}_{i,j-\frac{1}{2}} = \frac{\mu^{n+1}_{i,j} + \mu^{n+1}_{i,j-1}}{2} \tag{B.64}$$

$$\lambda_{t_r}{}^{n+1}_{i+\frac{1}{2},j} = \frac{\lambda_{t_r}{}^{n+1}_{i+1,j} + \lambda_{t_r}{}^{n+1}_{i,j}}{2}, \quad \lambda_{t_r}{}^{n+1}_{i-\frac{1}{2},j} = \frac{\lambda_{t_r}{}^{n+1}_{i,j} + \lambda_{t_r}{}^{n+1}_{i-1,j}}{2} \tag{B.65}$$

$$\lambda_{t_z}{}^{n+1}_{i,j+\frac{1}{2}} = \frac{\lambda_{t_z}{}^{n+1}_{i,j+1} + \lambda_{t_z}{}^{n+1}_{i,j}}{2}, \quad \lambda_{t_z}{}^{n+1}_{i,j-\frac{1}{2}} = \frac{\lambda_{t_z}{}^{n+1}_{i,j} + \lambda_{t_z}{}^{n+1}_{i,j-1}}{2} \tag{B.66}$$

A skin factor is incorporated into the finite difference model by the use of the thick skin concept as given in Equation 2.6 in which a skin region is presented as a zone of altered permeability adjacent to the producing interval. The horizontal permeability of the skin zone, $k_{r,s}$ is defined by specifying the radius of the skin region, r_s, the skin factor, s, and the vertical permeability in the skin region $k_{z,s}$ is assigned by requiring that:

$$\frac{k_{z,s}}{k_{r,s}} = \frac{k_z}{k_r} \tag{B.67}$$

APPENDIX C: Model Formulation 1-D (*r-z*) Wellbore

Mass, momentum, and energy balance equations are used to generate the constitutive equations for a control volume with the surface area A_r and cross-sectional area A_w within the wellbore. The basis of methodology followed here is to derive equations in the (*r-z*) wellbore system so that the wellbore gridblock that is adjacent to the reservoir may contain terms in the radial direction for coupling purposes. Other than that, single phase fluid flow in the wellbore occurs only in the axial direction.

Mass Balance: The generalized continuity equation for mass conservation for a differential depth of the well in a pipe, in terms of wellbore fluid density ρ, velocity in the axial direction v, and velocity in the radial direction u is written as:

$$\frac{\partial \rho}{\partial t} + \frac{1}{r}\frac{\partial (\rho r u)}{\partial r} + \frac{\partial (\rho v)}{\partial z} = 0 \tag{C.1}$$

If we express derivatives in the second and in the third term as below:

$$\frac{\partial \rho}{\partial t} + \frac{1}{r}\left[ru\left(\frac{\partial \rho}{\partial r}\right) + \rho\frac{\partial (ru)}{\partial r}\right] + \left[\frac{\partial \rho}{\partial z}v + \rho\frac{\partial v}{\partial z}\right] = 0 \tag{C.2}$$

The third derivative term can be expressed as:

$$\frac{\partial (ru)}{\partial r} = \frac{\partial r}{\partial r}u + r\frac{\partial u}{\partial r} \tag{C.3}$$

Using Equation C.3 in C.2 yields:

$$\frac{\partial \rho}{\partial t} + \left(\frac{\partial \rho}{\partial r}u + \rho\left(\frac{u}{r} + \frac{\partial u}{\partial r}\right)\right) + \left(\frac{\partial \rho}{\partial z}v + \rho\frac{\partial v}{\partial z}\right) = 0 \tag{C.4}$$

Using the equation introduced in the previous mass balance derivations gives:

$$\left[\rho c\frac{\partial p_w}{\partial t}-\rho\beta\frac{\partial T_w}{\partial t}\right]+\left[\left(\rho c\frac{\partial p_w}{\partial r}-\rho\beta\frac{\partial T_w}{\partial r}\right)u+\rho\left(\frac{u}{r}+\frac{\partial u}{\partial r}\right)\right]+\left[\left(\rho c\frac{\partial p_w}{\partial z}-\rho\beta\frac{\partial T_w}{\partial z}\right)v+\rho\frac{\partial v}{\partial z}\right]=0 \tag{C.5}$$

Dividing both sides by ρc yields:

$$\left[\frac{\partial p_w}{\partial t}-\frac{\beta}{c}\frac{\partial T_w}{\partial t}\right]+\left[\left(\frac{\partial p_w}{\partial r}-\frac{\beta}{c}\frac{\partial T_w}{\partial r}\right)u+\frac{1}{c}\left(\frac{u}{r}+\frac{\partial u}{\partial r}\right)\right]+\left[\left(\frac{\partial p_w}{\partial z}-\frac{\beta}{c}\frac{\partial T_w}{\partial z}\right)+\frac{1}{c}\frac{\partial v}{\partial z}\right]=0 \tag{C.6}$$

If we express in terms of volumetric rates given as $v=q_w/A_w$ and $u=q_r/A_r$:

$$\left[\frac{\partial p_w}{\partial t}-\frac{\beta}{c}\frac{\partial T_w}{\partial t}\right]+\left[\left(\frac{\partial p_w}{\partial r}-\frac{\beta}{c}\frac{\partial T_w}{\partial r}\right)\frac{q_r}{A_r}+\frac{1}{A_r c}\left(\frac{q_r}{r}+\frac{\partial q_r}{\partial r}\right)\right]+\left[\left(\frac{\partial p_w}{\partial z}-\frac{\beta}{c}\frac{\partial T_w}{\partial z}\right)\frac{q_w}{A_w}+\frac{1}{A_w c}\frac{\partial q_w}{\partial z}\right]=0 \tag{C.7}$$

Rearranging Equation C.7 yields:

$$\frac{\partial p_w}{\partial t}-\frac{\beta}{c}\frac{\partial T_w}{\partial t}+\left(\frac{q_w}{A_w}\left(\frac{\partial p_w}{\partial z}\right)-\frac{\beta}{c}\frac{q_w}{A_w}\left(\frac{\partial T_w}{\partial z}\right)+\frac{1}{A_w c}\left(\frac{\partial q_w}{\partial z}\right)\right)+\left[\frac{q_r}{A_r}\left(\frac{\partial p_w}{\partial r}\right)-\frac{\beta}{c}\frac{q_r}{A_r}\left(\frac{\partial T_w}{\partial r}\right)+\left(\frac{1}{A_r c}\right)\left(\frac{\partial q_r}{\partial r}+\frac{q_r}{r}\right)\right]=0 \tag{C.8}$$

The volumetric rate at the well in the radial direction (q_r at $r=r_w$) appears only at the face of bottom-most wellbore gridblocks that are adjacent to the first reservoir gridblocks, and is calculated by Darcy's Law given in Equation 2.4. This may also be called as the bottomhole flow rate from reservoir into the wellbore at corresponding depth and should be used in the mass, momentum and energy balance equations with a negative sign because the volumetric rate leaving the system q_{sc} is defined positive for a producing well at the top of the wellbore. Hence, the last term in the squared brackets does not appear ($q_r=0$) for the wellbore gridblocks that are neither unperforated nor not adjacent to the reservoir.

Energy Balance: The transient thermal energy equation is given in a general form by Bird et al. (1960) in terms of internal energy:

$$\frac{D(\rho U\mathbf{v})}{Dt} = -p_w(\nabla \cdot \mathbf{v}) + \nabla \cdot (\boldsymbol{\lambda}\nabla T_w) + (\boldsymbol{\tau}\colon \nabla \mathbf{v}) \tag{C.9}$$

The work done by viscous dissipation given as last term in the right-hand side is replaced by the term that corresponds to friction heat dissipated due to viscous shear. The second term in the right-hand side of Equation C.9 is the diagonal thermal conductivity tensor which models the conduction phenomena in the wellbore. When the wellbore is in thermal equilibrium with the formation, the thermal energy balance equation for the (*r*-*z*) system in a conservative form where velocity components are included in the derivatives is given by:

$$\begin{aligned}\left(\frac{\partial(\rho U)}{\partial t} + \frac{\partial(\rho U u)}{\partial r} + \frac{\partial(\rho U v)}{\partial z}\right) \\ = -\left(\frac{\partial(p_w u)}{\partial r} + \frac{\partial(p_w v)}{\partial z}\right) + \nabla \cdot (\boldsymbol{\lambda}\nabla T_w) + \rho\frac{f v^2 |v|}{2D}\end{aligned} \tag{C.10}$$

Expressing specific internal energy U in terms of specific enthalpy H by using the thermodynamic relationship of $\rho U = \rho H - p_w$, and rearranging, the final alternative form of the thermal energy balance equation can be obtained as:

$$\begin{aligned}&\frac{\partial(\rho H - p_w)}{\partial t} + \left(u\frac{\partial(\rho H - p_w)}{\partial r} + (\rho H - p_w)\frac{\partial u}{\partial r}\right) + \left(u\frac{\partial p_w}{\partial r} + p_w\frac{\partial u}{\partial r}\right) \\ &+ \left(v\frac{\partial(\rho H - p_w)}{\partial z} + (\rho H - p_w)\frac{\partial v}{\partial z}\right) + \left(v\frac{\partial p_w}{\partial z} + p_w\frac{\partial v}{\partial z}\right) - \nabla \cdot (\boldsymbol{\lambda}\nabla T_w) = 0\end{aligned} \tag{C.11}$$

In terms of volumetric rates, it becomes:

$$\begin{aligned}&\frac{\partial(\rho H - p_w)}{\partial t} + \left(\frac{q_r}{A_r}\frac{\partial(\rho H - p_w)}{\partial r} + \frac{(\rho H - p_w)}{A_r}\left(\frac{\partial q_r}{\partial r}\right)\right) \\ &\quad + \left(\frac{q_r}{A_r}\frac{\partial p_w}{\partial r} + \frac{p_w}{A_r}\frac{\partial q_r}{\partial r}\right) \\ &\quad + \left(\frac{q_w}{A_w}\frac{\partial(\rho H - p_w)}{\partial z} + \frac{(\rho H - p_w)}{A_w}\frac{\partial q_w}{\partial z}\right) \\ &\quad + \left(\frac{q_w}{A_w}\frac{\partial p_w}{\partial z} + \frac{p_w}{A_w}\frac{\partial q_w}{\partial z}\right) - \nabla \cdot (\boldsymbol{\lambda}\nabla T_w) = 0\end{aligned} \tag{C.12}$$

The sum of some terms shown below is equal to zero as:

$$\frac{\partial(\rho H)}{\partial t}-\frac{\partial p_w}{\partial t}+\left\{\left(\frac{q_r}{A_r}\frac{\partial(\rho H)}{\partial r}-\frac{q_r}{A_r}\frac{\partial p_w}{\partial r}+\frac{(\rho H)}{A_r}\frac{\partial q_r}{\partial r}-\frac{p_w}{A_r}\frac{\partial q_r}{\partial r}\right)+\left(\frac{q_r}{A_r}\frac{\partial p_w}{\partial r}+\frac{p_w}{A_r}\frac{\partial q_r}{\partial r}\right)\right\}+\left\{\begin{array}{l}\frac{q_w}{A_w}\frac{\partial(\rho H)}{\partial z}-\frac{q_w}{A_w}\frac{\partial p_w}{\partial z}+\frac{(\rho H)}{A_w}\frac{\partial q_w}{\partial z}\\ -\frac{p_w}{A_w}\frac{\partial q_w}{\partial z}+\frac{q_w}{A_w}\frac{\partial p_w}{\partial z}+\frac{p_w}{A_w}\frac{\partial q_w}{\partial z}\end{array}\right\}-\nabla\cdot(\boldsymbol{\lambda}\nabla T_w)=0 \tag{C.13}$$

Rearrangement of terms gives:

$$\frac{\partial(\rho H)}{\partial t}-\frac{\partial p_w}{\partial t}+\left\{\left(\frac{q_r}{A_r}\frac{\partial(\rho H)}{\partial r}+\frac{(\rho H)}{A_r}\frac{\partial q_r}{\partial r}\right)\right\}+\left\{\frac{q_w}{A_w}\frac{\partial(\rho H)}{\partial z}+\frac{(\rho H)}{A_w}\frac{\partial q_w}{\partial z}\right\}-\nabla\cdot(\boldsymbol{\lambda}\nabla T_w)=0 \tag{C.14}$$

If we express remaining derivatives, it becomes:

$$\left[H\frac{\partial\rho}{\partial t}+\rho\frac{\partial H}{\partial t}\right]-\frac{\partial p_w}{\partial t}+\left\{\left(\frac{q_r}{A_r}\left(H\frac{\partial\rho}{\partial r}+\rho\frac{\partial H}{\partial r}\right)+\frac{(\rho H)}{A_r}\frac{\partial q_r}{\partial r}\right)\right\}+\left\{\frac{q_w}{A_w}\left(H\frac{\partial\rho}{\partial z}+\rho\frac{\partial H}{\partial z}\right)+\frac{(\rho H)}{A_w}\frac{\partial q_w}{\partial z}\right\}-\nabla\cdot(\boldsymbol{\lambda}\nabla T_w)=0 \tag{C.15}$$

Rearrangement of terms yields due to conservation of mass:

$$H\left\{\underbrace{\frac{\partial\rho}{\partial t}+\left[\frac{q_r}{A_r}\frac{\partial\rho}{\partial r}+\rho\left(\frac{1}{r}\frac{q_r}{A_r}+\frac{1}{A_r}\frac{\partial q_r}{\partial r}\right)\right]+\left[\frac{q_w}{A_w}\frac{\partial\rho}{\partial z}+\rho\frac{1}{A_w}\frac{\partial q_w}{\partial z}\right]}_{=0}\right\}+\rho\frac{\partial H}{\partial t}-\frac{\partial p_w}{\partial t}+\left(\frac{q_r}{A_r}\rho\frac{\partial H}{\partial r}\right)+\left(\frac{q_w}{A_w}\rho\frac{\partial H}{\partial z}\right)-\nabla\cdot(\boldsymbol{\lambda}\nabla T_w)=0 \tag{C.16}$$

Further rearrangement of terms yields:

$$\rho\frac{\partial H}{\partial t}-\frac{\partial p_w}{\partial t}+\left[\frac{q_r}{A_r}\left(\rho\frac{\partial H}{\partial r}\right)\right]+\left[\frac{q_w}{A_w}\left(\rho\frac{\partial H}{\partial z}\right)\right]-\nabla\cdot(\boldsymbol{\lambda}\nabla T_w)=0 \tag{C.17}$$

Dividing each side by ρ gives:

$$\frac{\partial H}{\partial t}-\frac{1}{\rho}\frac{\partial p_w}{\partial t}+\left[\frac{q_r}{A_r}\left(\frac{\partial H}{\partial r}\right)\right]+\left[\frac{q_w}{A_w}\left(\frac{\partial H}{\partial z}\right)\right]-\left(\frac{1}{\rho}\right)\nabla\cdot(\boldsymbol{\lambda}\nabla T_w)=0 \tag{C.18}$$

We define some thermodynamic relations where we assume c_p and ε_{JT} independent of pressure and temperature as:

$$\frac{\partial H}{\partial t} = c_p\left(\frac{\partial T_w}{\partial t} - \varepsilon_{JT}\frac{\partial p_w}{\partial t}\right) \tag{C.19}$$

$$\frac{\partial H}{\partial r} = c_p\left(\frac{\partial T_w}{\partial r} - \varepsilon_{JT}\frac{\partial p_w}{\partial r}\right) \tag{C.20}$$

$$\frac{\partial H}{\partial z} = c_p\left(\frac{\partial T_w}{\partial z} - \varepsilon_{JT}\frac{\partial p_w}{\partial z}\right) \tag{C.21}$$

Using Equations C.19 through C.21 in C.18 gives:

$$\begin{aligned} c_p\left(\frac{\partial T_w}{\partial t} - \varepsilon_{JT}\frac{\partial p_w}{\partial t}\right) - \frac{1}{\rho}\frac{\partial p_w}{\partial t} + \left[\frac{q_r}{A_r}c_p\left(\frac{\partial T_w}{\partial r} - \varepsilon_{JT}\frac{\partial p_w}{\partial r}\right)\right] \\ + \left[\frac{q_w}{A_w}c_p\left(\frac{\partial T_w}{\partial z} - \varepsilon_{JT}\frac{\partial p_w}{\partial z}\right)\right] - \left(\frac{1}{\rho}\right)\nabla\cdot(\boldsymbol{\lambda}\nabla T_w) = 0 \end{aligned} \tag{C.22}$$

Dividing each side by c_p gives:

$$\begin{aligned} \left(\frac{\partial T_w}{\partial t} - \varepsilon_{JT}\frac{\partial p_w}{\partial t}\right) - \frac{1}{\rho c_p}\frac{\partial p_w}{\partial t} + \left[\frac{q_r}{A_r}\left(\frac{\partial T_w}{\partial r} - \varepsilon_{JT}\frac{\partial p_w}{\partial r}\right)\right] \\ + \left[\frac{q_w}{A_w}\left(\frac{\partial T_w}{\partial z} - \varepsilon_{JT}\frac{\partial p_w}{\partial z}\right)\right] - \left(\frac{1}{\rho c_p}\right)\nabla\cdot(\boldsymbol{\lambda}\nabla T_w) = 0 \end{aligned} \tag{C.23}$$

Rearrangement of the terms and also using isentropic expansion coefficient φ gives:

$$\begin{aligned} \left\{\frac{\partial T_w}{\partial t} - \underbrace{\left(\varepsilon_{JT} + \frac{1}{\rho c_p}\right)}_{\varphi}\frac{\partial p_w}{\partial t}\right\} + \left\{-\varepsilon_{JT}\left(\frac{q_r}{A_r}\right)\frac{\partial p_w}{\partial r} - \varepsilon_{JT}\left(\frac{q_w}{A_w}\right)\frac{\partial p_w}{\partial z}\right\} \\ + \left\{\left(\frac{q_r}{A_r}\right)\frac{\partial T_w}{\partial r} + \left(\frac{q_w}{A_w}\right)\frac{\partial T_w}{\partial z}\right\} - \left(\frac{1}{\rho c_p}\right)\nabla\cdot(\boldsymbol{\lambda}\nabla T_w) = 0 \end{aligned} \tag{C.24}$$

In Equation C.9, $\boldsymbol{\lambda}$ is a diagonal thermal conductivity of fluid tensor given same as in the previous sections by:

$$\boldsymbol{\lambda} = \begin{bmatrix} \lambda_r & 0 \\ 0 & \lambda_z \end{bmatrix} \tag{C.25}$$

Conduction term is described where λ_r and λ_z represents thermal conductivity of the wellbore fluid as:

$$\nabla \cdot (\boldsymbol{\lambda} \nabla T) = \frac{1}{r}\frac{\partial}{\partial r}\left(r\lambda_r \frac{\partial T_w}{\partial r}\right) + \frac{\partial}{\partial z}\left(\lambda_z \frac{\partial T_w}{\partial z}\right) \tag{C.26}$$

Final equation can be obtained as:

$$\begin{aligned} &\frac{\partial T_w}{\partial t} - \underbrace{\left(\varepsilon_{JT} + \frac{1}{\rho c_p}\right)}_{\varphi}\frac{\partial p_w}{\partial t} + \left(\frac{q_w}{A_w}\right)\frac{\partial T_w}{\partial z} - \varepsilon_{JT}\left(\frac{q_w}{A_w}\right)\frac{\partial p_w}{\partial z} \\ &\quad + \left[\left(\frac{q_r}{A_r}\right)\frac{\partial T_w}{\partial r} - \varepsilon_{JT}\left(\frac{q_r}{A_r}\right)\frac{\partial p_w}{\partial r}\right] \\ &\quad - \frac{1}{\rho c_p}\left(\frac{1}{r}\frac{\partial}{\partial r}\left(\lambda_r \frac{\partial T_w}{\partial r}\right) + \frac{\partial}{\partial z}\left(\lambda_z \frac{\partial T_w}{\partial z}\right)\right) = \rho \frac{f|(q_w)^3|}{2D(A_w)^3} \end{aligned} \tag{C.27}$$

The last term of the left-hand side of Equation C.27 involves the component on the radial axis (λ_r) that accounts for the wellbore heat losses to the surrounding formation by conduction, while the component on the axial axis (λ_z) represents conductivity of the fluid in axial direction along the wellbore which may be neglected as it indicates no effects due to convection dominated free flow in the wellbore. Partial derivatives with respect to axial and radial direction multiplied by volumetric rates account for the convection in the corresponding direction. As mentioned in mass balance, convective terms in radial axis does not exist except for the bottommost gridblocks that are adjacent to the reservoir.

Momentum Balance: The equation of motion is given in general form by Bird et al. (1960) as:

$$\rho \frac{D\mathbf{v}}{Dt} = -\nabla p_w - [\nabla \cdot \boldsymbol{\tau}] + \rho g \tag{C.28}$$

where g is the gravitational force. For cylindrical coordinates, when axial and radial directions are considered only, momentum balance equation for the fluid flow given in Equation C.28 can be written in non-conservative form as:

$$\rho\left(\frac{\partial v}{\partial t}+u\frac{\partial v}{\partial r}+v\frac{\partial v}{\partial z}\right) = -\frac{\partial p_w}{\partial z}-\mu\left[-\frac{1}{r}\frac{\partial}{\partial r}\left(r\frac{\partial v}{\partial r}\right)-\frac{\partial^2 v}{\partial z^2}\right]+\rho g+\frac{f v|v|}{2D} \tag{C.29}$$

where the last term in right hand side accounts for the continuous friction pressure drop along a pipe segment due to viscous shear. When the change in fluid velocities in axial direction across the radial axis are taken as zero *(∂v/∂r*=0) in Equation C.29, the final form of the momentum balance equation can be obtained as:

$$\frac{1}{A_w}\left(\frac{\partial q_z}{\partial t}\right)+\frac{q_w}{(A_w)^2}\left(\frac{\partial q_w}{\partial z}\right)+\frac{1}{\rho}\left(\frac{\partial p_w}{\partial z}\right)-\frac{1}{(A_w)^2}\frac{\mu}{\rho}\left(\frac{\partial^2 q_w}{\partial z^2}\right)+g + \frac{f q_w|q_w|}{2D(A_w)^2}=0 \tag{C.30}$$

where *f* represents the well-known Darcy-Weishbach friction factor. For laminar flow in the wellbore, it is given as:

$$f=\frac{64\mu}{\rho v D}=\frac{64}{R_e} \tag{C.31}$$

where R_e is the Reynolds number defined by:

$$R_e=\frac{\rho v D}{\mu}=\frac{\rho}{\mu}\frac{q_w}{A_w}D \tag{C.32}$$

When R_e is calculated higher than 4000, turbulent flow occurs in wellbore and Equation C.31 becomes no longer valid. Therefore, friction factor developed by Colebrook (1939) is used:

$$\frac{1}{\sqrt{f}}=-2log\left(\frac{\frac{\vartheta}{D}}{3.7}+\frac{2.51}{R_e\sqrt{f}}\right) \tag{C.33}$$

where ϑ represents the pipe roughness and *D* represents the pipe diameter. Note that Equation C.33 has to be solved iteratively.

APPENDIX D: Discretization of 1-D (z) Wellbore Equations

Mass Balance: Recalling Equation C.8 for mass balance with taking into consideration of derivatives in both side of the equation at any grid block points (z_j) for the finite difference formulation gives:

$$\frac{{p_w}_j^{n+1} - {p_w}_j^{n}}{\Delta t} - \frac{\beta}{c}\left(\frac{{T_w}_j^{n+1} - {T_w}_j^{n}}{\Delta t}\right) + \frac{{q_w}_j^{n+1}}{A_w}\left(\frac{{p_w}_{j+1}^{n+1} - {p_w}_j^{n+1}}{z_{j+1} - z_j}\right) \tag{D.1}$$

$$-\frac{\beta}{c}\frac{{q_w}_j^{n+1}}{A_w}\left(\frac{{T_w}_j^{n+1} - {T_w}_{j-1}^{n+1}}{z_j - z_{j-1}}\right) + \frac{1}{cA_w}\left(\frac{{q_w}_j^{n+1} - {q_w}_{j-1}^{n+1}}{\Delta z_j}\right)$$

$$+\frac{{q_r}_j^{n+1}}{A_r}\left(\frac{{p_r}_{1,j}^{n+1} - {p_w}_j^{n+1}}{r_1 - \frac{r_w}{2}}\right) - \frac{\beta}{c}\frac{{q_r}_j^{n+1}}{A_r}\left(\frac{{T_r}_{1,j}^{n+1} - {T_w}_j^{n+1}}{r_1 - \frac{r_w}{2}}\right) + \left(\frac{1}{cA_r}\right)\left(\frac{{q_r}_j^{n+1}}{\frac{r_w}{2}}\right) = 0$$

Multiplying each side with Δt^{n+1} and placing the known terms to right hand side of the equation:

$${p_w}_j^{n} - \frac{\beta}{c}{T_w}_j^{n} = {p_w}_j^{n+1} - \frac{\beta}{c}t_j^{n+1} + \frac{\Delta t^{n+1}}{\left(z_{j+1} - z_j\right)}\left(\frac{{q_w}_{j+\frac{1}{2}}^{n+1}}{A_w}\right)\left({p_w}_{j+1}^{n+1} - {p_w}_j^{n+1}\right)$$

$$+\left(-\frac{\beta}{c}\right)\frac{\Delta t^{n+1}}{\left(z_j - z_{j-1}\right)}\left(\frac{{q_w}_{j-\frac{1}{2}}^{n+1}}{A_w}\right)\left({T_w}_j^{n+1} - {T_w}_{j-1}^{n+1}\right) + \frac{\Delta t^{n+1}}{cA_w\Delta z_j}\left({q_w}_{j+\frac{1}{2}}^{n+1} - {q_w}_{j-\frac{1}{2}}^{n+1}\right)$$

$$+\Delta t^{n+1}\frac{{q_r}_j^{n+1}}{A_r\left(r_1 - \frac{r_w}{2}\right)}\left({p_r}_{1,j}^{n+1} - {p_w}_j^{n+1}\right) - \Delta t^{n+1}\frac{\beta}{c}\frac{{q_r}_j^{n+1}}{A_r\left(r_1 - \frac{r_w}{2}\right)}\left({T_r}_{1,j}^{n+1} - {T_w}_j^{n+1}\right)$$

$$+\frac{\Delta t^{n+1}}{cA_r\frac{r_w}{2}}\left({q_r}_j^{n+1}\right) \tag{D.2}$$

Energy Balance: We evaluate the conduction terms for axial and radial directions separately since they need to be defined by central difference formulation due to second order derivatives. We need to use averaging technique for thermal conductivity

of fluid (given in Equation C.26) in order to define at boundaries. We start with the conduction term in the radial direction as:

$$\frac{1}{r}\frac{\partial}{\partial r}\left(r\lambda_r\frac{\partial T_w}{\partial r}\right)=\frac{1}{r_i}\left(\frac{r_{i+\frac{1}{2}}\lambda_{r\,i+\frac{1}{2}}\left(\frac{\partial T_w}{\partial r}\right)_{i+\frac{1}{2}}-r_{i-\frac{1}{2}}\lambda_{r\,i-\frac{1}{2}}\left(\frac{\partial T_w}{\partial r}\right)_{i-\frac{1}{2}}}{\underbrace{r_{i+\frac{1}{2}}-r_{i-\frac{1}{2}}}_{r_w}}\right) \tag{D.3}$$

Here, the subscript with ½ refers to boundaries. For instance, i+½ points the boundary between gridblock i and i+1 whereas i-½ points the boundary between gridblock i and i-1. Note that conduction component in Equation D.3 contains terms only for the boundary (at $r=r_w$) where the wellbore cell is adjacent to its surrounding rock or the first gridblock of reservoir. Therefore, the inner boundary condition (at r=0) is taken as:

$$\left(\frac{\partial T_w}{\partial r}\right)_{i-\frac{1}{2}}=0 \tag{D.4}$$

Recalling the Equation 2.2 in which the thermal conductivity of the fluid at the boundary (at $r=r_w$) between wellbore gridblock and its surrounding rock ($j>N_{rz}$) or the first gridblock of reservoir ($j<=N_{rz}$) is replaced by overall coefficient of heat transfer (U_t) to apply for the conduction in radial direction in Equation D.3 yields:

$$\begin{aligned}\frac{1}{r}\frac{\partial}{\partial r}\left(r\lambda_r\frac{\partial T_w}{\partial r}\right)&=\frac{\lambda_{r_{i+\frac{1}{2}}}}{\underbrace{\Delta r}_{U_t}}\left(\frac{{T_e}_j^{\,n}-{T_w}_j^{\,n+1}}{r_w-\frac{r_w}{2}}\right) && if\ j>N_{rz}\\ \frac{1}{r}\frac{\partial}{\partial r}\left(r\lambda_r\frac{\partial T_w}{\partial r}\right)&=\frac{\lambda_{r_{i+\frac{1}{2}}}}{\underbrace{\Delta r}_{U_t}}\left(\frac{{T_r}_{1,j}^{\,n+1}-{T_w}_j^{\,n+1}}{r_1-\frac{r_w}{2}}\right) && if\ j\le N_{rz}\end{aligned} \tag{D.5}$$

Here, ${T_e}_j^{\,n}$ depends on geothermal gradient and changes at each corresponding depth conduction term exists for the wellbore cells that are adjacent to the reservoir. The conduction term in the axial direction is written as:

$$\frac{\partial}{\partial z}\left(\lambda_z \frac{\partial}{\partial z}\right) = \frac{\lambda_{z_{j+\frac{1}{2}}}\left(\frac{\partial T_w}{\partial z}\right)_{j+\frac{1}{2}} - \lambda_{z_{j-\frac{1}{2}}}\left(\frac{\partial T_w}{\partial z}\right)_{j-\frac{1}{2}}}{\Delta z_j}$$
$$= \frac{\lambda_{z_{j+\frac{1}{2}}}\left(\frac{T_{w_{j+1}}^{n+1} - T_{w_j}^{n+1}}{z_{j+1} - z_j}\right) - \lambda_{z_{j-\frac{1}{2}}}\left(\frac{T_{w_j}^{n+1} - T_{w_{j-1}}^{n+1}}{z_j - z_{j-1}}\right)}{\Delta z_j} \tag{D.6}$$

It is important to note that top and bottom outer boundaries should be set to zero respectively because of the insulated wellbore boundary condition:

$$\left(\frac{\partial T_w}{\partial z}\right)_{\frac{1}{2}} = 0 \tag{D.7}$$

$$\left(\frac{\partial T_w}{\partial z}\right)_{Nz+\frac{1}{2}} = 0 \tag{D.8}$$

Recalling Equation C.27, for energy balance with taking into consideration of derivatives in both side of the equation at any grid block points (z_j) for the finite difference formulation gives:

$$\left(\frac{T_{w_j}^{n+1} - T_{w_j}^{n}}{\Delta t}\right) - \varphi\left(\frac{p_{w_j}^{n+1} - p_{w_j}^{n}}{\Delta t}\right) + \frac{q_{w_j}^{n+1}}{A_w}\left(\frac{T_{w_j}^{n+1} - T_{w_{j-1}}^{n+1}}{z_j - z_{j-1}}\right)$$
$$- \varepsilon_{JT}\frac{q_{w_j}^{n+1}}{A_w}\left(\frac{p_{w_{j+1}}^{n+1} - p_{w_j}^{n+1}}{z_{j+1} - z_j}\right) + \frac{q_{r_j}^{n+1}}{A_r}\left(\frac{T_{r_{1,j}}^{n+1} - T_{w_j}^{n+1}}{r_1 - \frac{r_w}{2}}\right)$$
$$- \varepsilon_{JT}\frac{q_{r_j}^{n+1}}{A_r}\left(\frac{p_{r_{1,j}}^{n+1} - p_{w_j}^{n+1}}{r_1 - \frac{r_w}{2}}\right)$$
$$- \frac{1}{\rho c_p}\left(\frac{U_t}{r_1 - \frac{r_w}{2}}\left(T_{r_{1,j}}^{n+1} - T_{w_j}^{n+1}\right)\right.$$
$$+ \frac{\lambda_{z_{j+\frac{1}{2}}}}{\Delta z_j\left(z_{j+1} - z_j\right)}\left(T_{w_{j+1}}^{n+1} - T_{w_j}^{n+1}\right)$$
$$\left. - \frac{\lambda_{z_{j-\frac{1}{2}}}}{\Delta z_j\left(z_j - z_{j-1}\right)}\left(T_{w_j}^{n+1} - T_{w_{j-1}}^{n+1}\right)\right) = \rho\frac{f\left|\left(q_{w_j}^{n+1}\right)^3\right|}{2D(A_w)^3} \tag{D.9}$$

Multiplying each side with Δt^{n+1} and placing the known terms to right hand side of the equation:

$$T_{w_j}^{\ n} - \varphi p_{w_j}^{\ n} = T_{w_j}^{\ n+1} - \varphi p_{w_j}^{\ n+1} + \Delta t^{n+1} \frac{q_{w_j}^{\ n+1}}{A_w} \left(\frac{T_{w_j}^{\ n+1} - T_{w_{j-1}}^{\ n+1}}{z_j - z_{j-1}} \right)$$

$$-\Delta t^{n+1} \varepsilon_{JT} \frac{q_{w_j}^{\ n+1}}{A_w} \left(\frac{p_{w_{j+1}}^{\ n+1} - p_{w_j}^{\ n+1}}{z_{j+1} - z_j} \right) + \Delta t^{n+1} \frac{q_{r_j}^{\ n+1}}{A_r} \left(\frac{T_{r_{1,j}}^{\ n+1} - T_{w_j}^{\ n+1}}{r_1 - \frac{r_w}{2}} \right)$$

$$-\Delta t^{n+1} \varepsilon_{JT} \frac{q_{r_j}^{\ n+1}}{A_r} \left(\frac{p_{r_{1,j}}^{\ n+1} - p_{w_j}^{\ n+1}}{r_1 - \frac{r_w}{2}} \right) - \Delta t^{n+1} \rho \frac{f \left| \left(q_{w_j}^{\ n+1} \right)^3 \right|}{2D(A_w)^3} \qquad \text{(D.10)}$$

$$-\frac{\Delta t^{n+1}}{\rho c_p} \left(\frac{U_t}{r_1 - \frac{r_w}{2}} \left(T_{r_{1,j}}^{\ n+1} - T_{w_j}^{\ n+1} \right) + \frac{\lambda_{z_{j+\frac{1}{2}}}}{\Delta z_j \left(z_{j+1} - z_j \right)} \left(T_{w_{j+1}}^{\ n+1} - T_{w_j}^{\ n+1} \right) \right.$$

$$\left. - \frac{\lambda_{z_{j-\frac{1}{2}}}}{\Delta z_j \left(z_j - z_{j-1} \right)} \left(T_{w_j}^{\ n+1} - T_{w_{j-1}}^{\ n+1} \right) \right)$$

Momentum Balance: Recalling Equation C.30, for momentum balance with taking into consideration of derivatives in both side of the equation at any grid block points (z_j) for the finite difference formulation gives:

$$\frac{q_{w_j}^{\ n+1} - q_{w_j}^{\ n}}{\Delta t} + \frac{q_{w_j}^{\ n+1}}{(A_w)^2} \left(\frac{q_{w_j}^{\ n+1} - q_{w_{j-1}}^{\ n+1}}{\Delta z_j} \right) + \frac{1}{\rho} \left(\frac{p_{w_{j+1}}^{\ n+1} - p_{w_j}^{\ n+1}}{z_{j+1} - z_j} \right)$$

$$-\frac{1}{(A_w)^2} \left(\frac{\mu}{\rho} \right)_j^{n+1} \frac{\left(\frac{q_{w_{j+1}}^{\ n+1} - q_{w_j}^{\ n+1}}{\Delta z_{j+1}} \right) - \left(\frac{q_{w_j}^{\ n+1} - q_{w_{j-1}}^{\ n+1}}{\Delta z_j} \right)}{\Delta z_{i+1} + \Delta z_i} + g \qquad \text{(D.11)}$$

$$+\frac{f q_{w_j}^{\ n+1} \left| q_{w_j}^{\ n+1} \right|}{2D(A_w)^2} = 0$$

Multiplying each side with Δt^{n+1} and placing known terms to right hand side of the equation:

$$q_{w_j}^{n+1} + \Delta t^{n+1} \frac{q_{w_j}^{n+1}}{(A_w)^2}\left(\frac{q_{w_j}^{n+1} - q_{w_{j-1}}^{n+1}}{\Delta z_j}\right) + \frac{\Delta t^{n+1}}{\rho}\left(\frac{p_{w_{j+1}}^{n+1} - p_{w_j}^{n+1}}{z_{j+1} - z_j}\right)$$

$$-\frac{\Delta t^{n+1}}{(A_w)^2}\left(\frac{\mu}{\rho}\right)_j^{n+1}\left[\frac{\left(\frac{q_{w_{j+1}}^{n+1} - q_{w_j}^{n+1}}{\Delta z_{j+1}}\right) - \left(\frac{q_{w_j}^{n+1} - q_{w_{j-1}}^{n+1}}{\Delta z_j}\right)}{\Delta z_{i+1} + \Delta z_i}\right] \qquad \text{(D.12)}$$

$$+\Delta t^{n+1} g + \Delta t^{n+1} \frac{f q_{w_j}^{n+1} \left|q_{w_j}^{n+1}\right|}{2D(A_w)^2} = q_{w_j}^{n}$$

APPENDIX E: Figures of Chapter 3

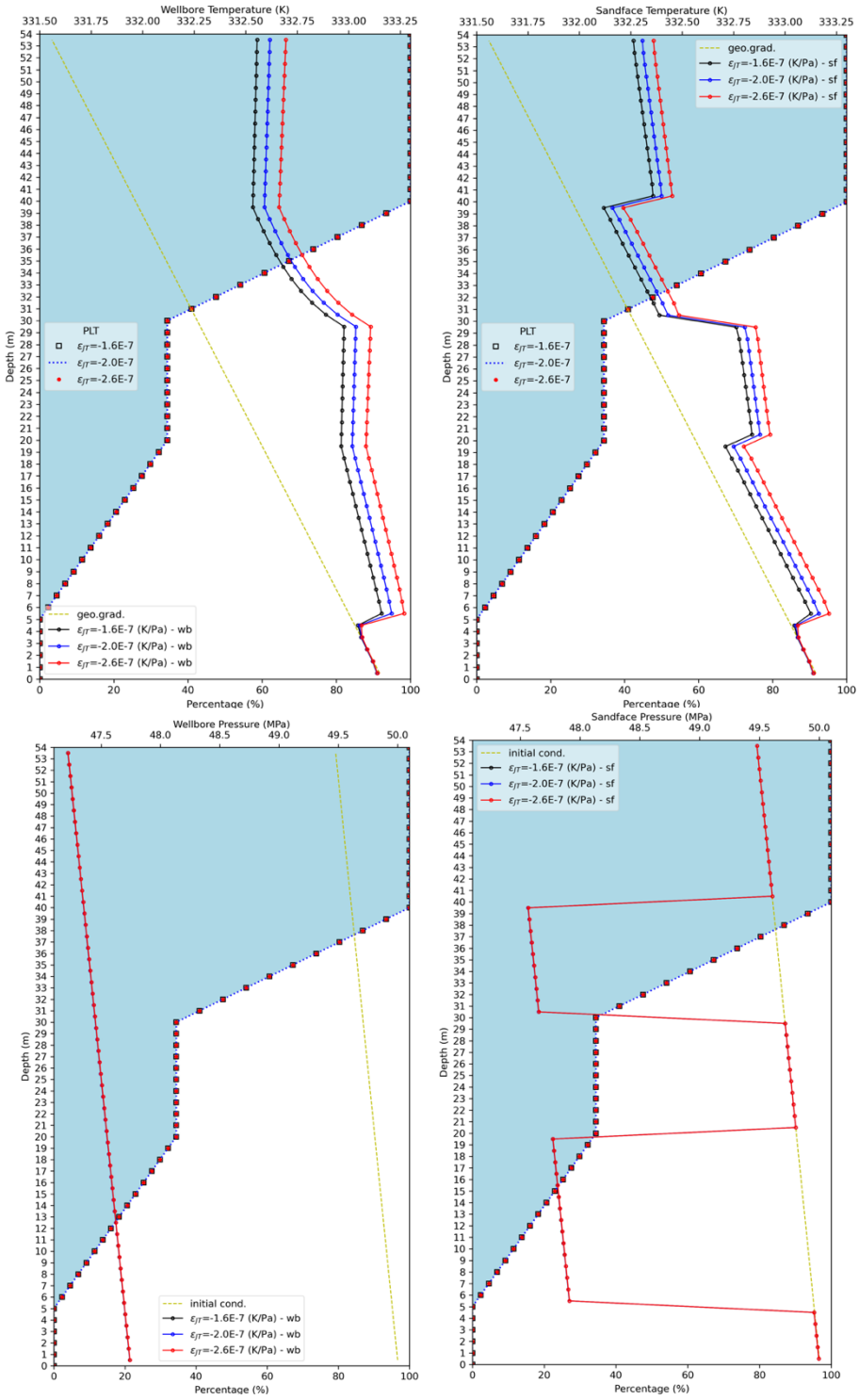

Figure E.1: Comparison of wellbore/sandface temperatures and pressures for different J-T coefficient values for **both zones** at the end of drawdown.

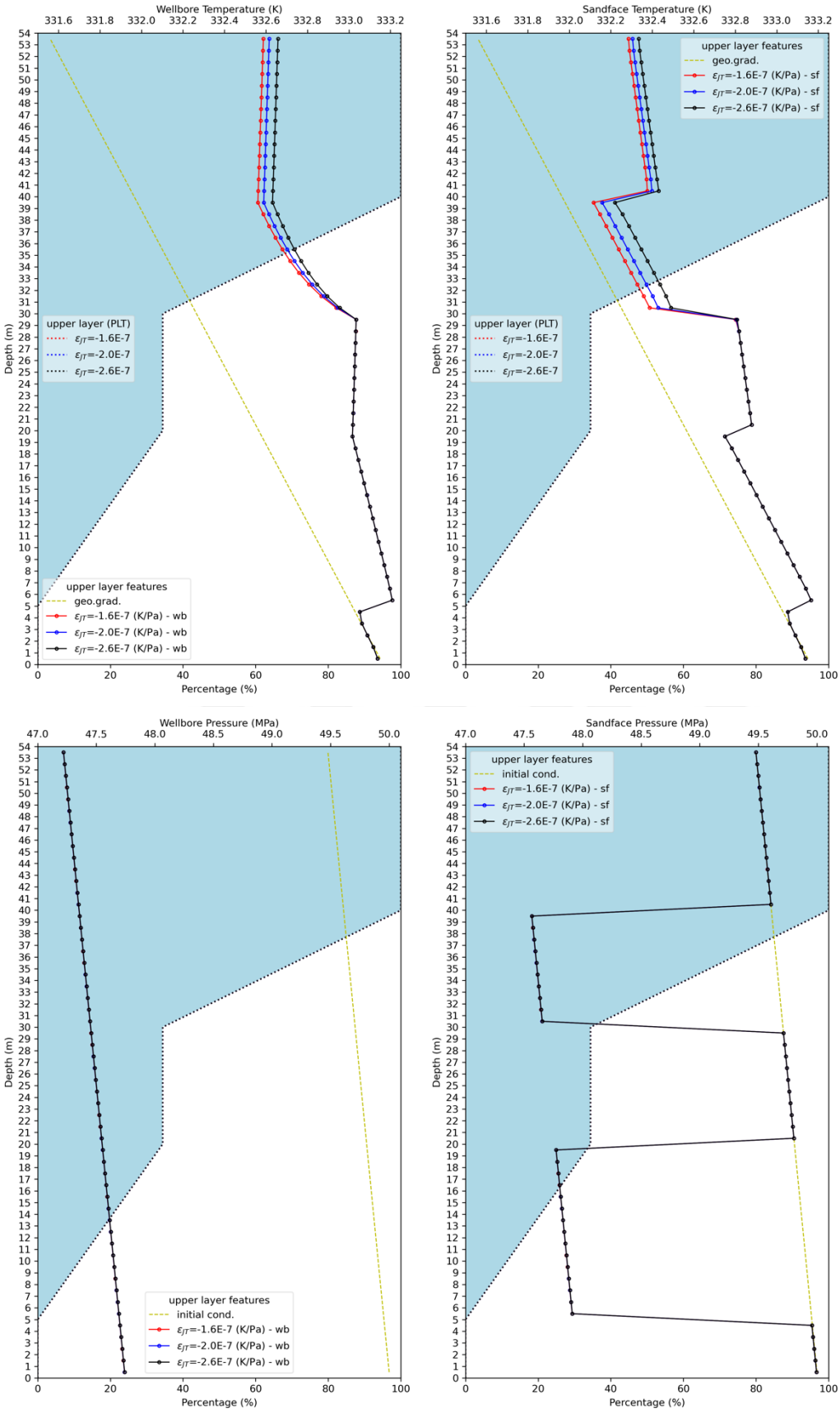

Figure E.2: Comparison of wellbore/sandface temperatures and pressures for different J-T coefficient values in the **upper zone** at the end of drawdown.

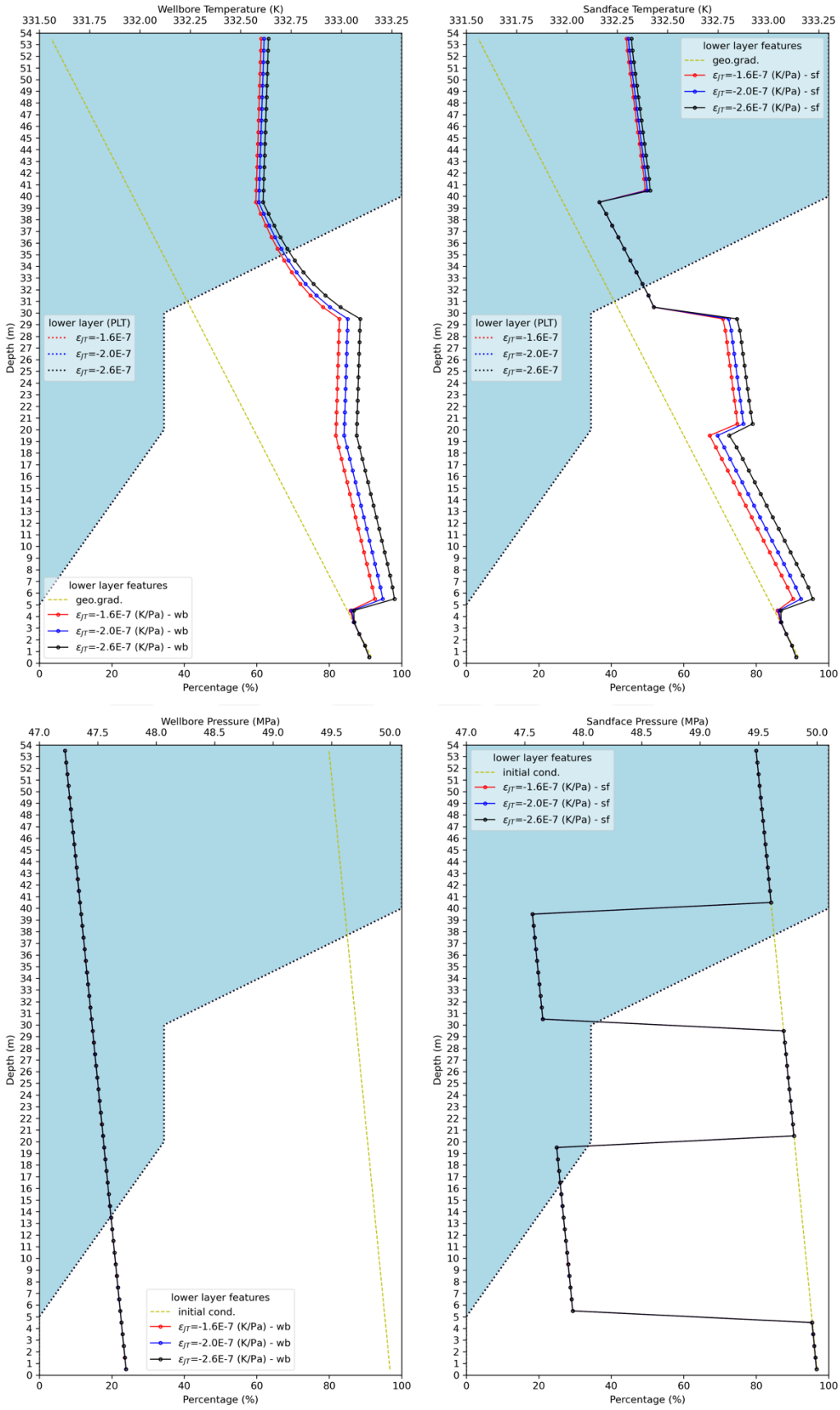

Figure E.3: Comparison of wellbore/sandface temperatures and pressures for different J-T coefficient values in the **lower zone** at the end of drawdown.

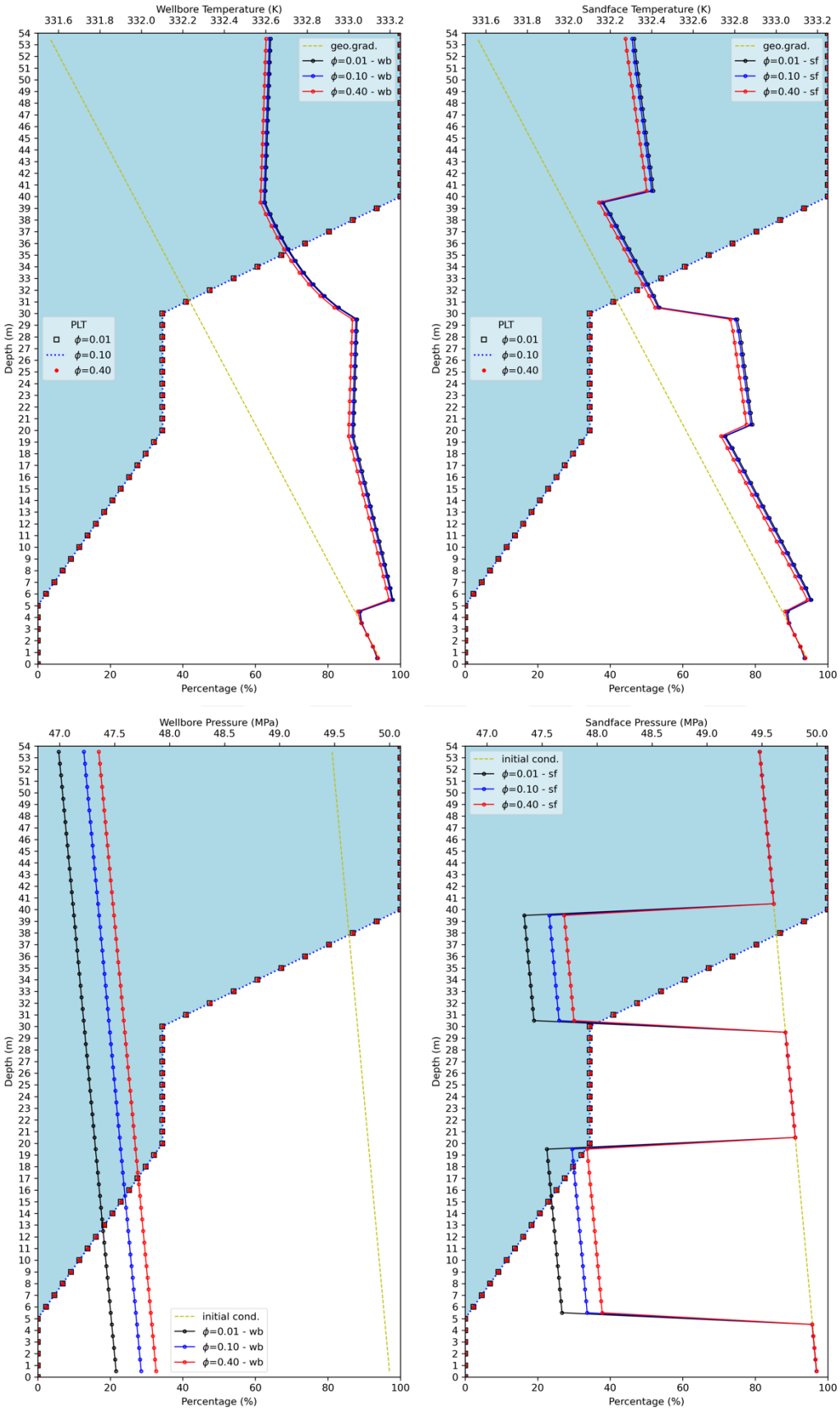

Figure E.4: Comparison of wellbore/sandface temperatures and pressures for different porosity values for **both zone** at the end of drawdown.

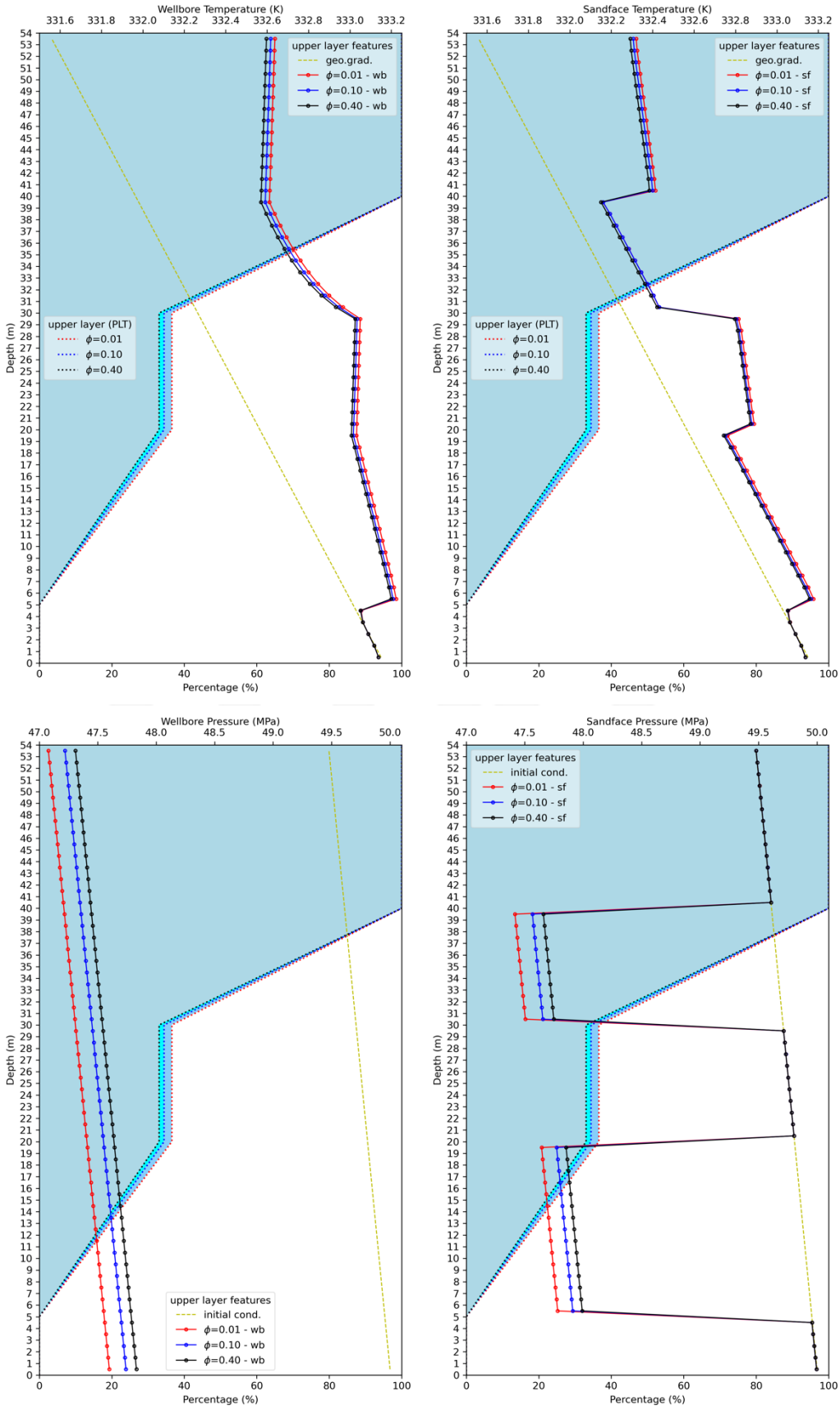

Figure E.5: Comparison of wellbore/sandface temperatures and pressures for different porosity values in the **upper zone** at the end of drawdown.

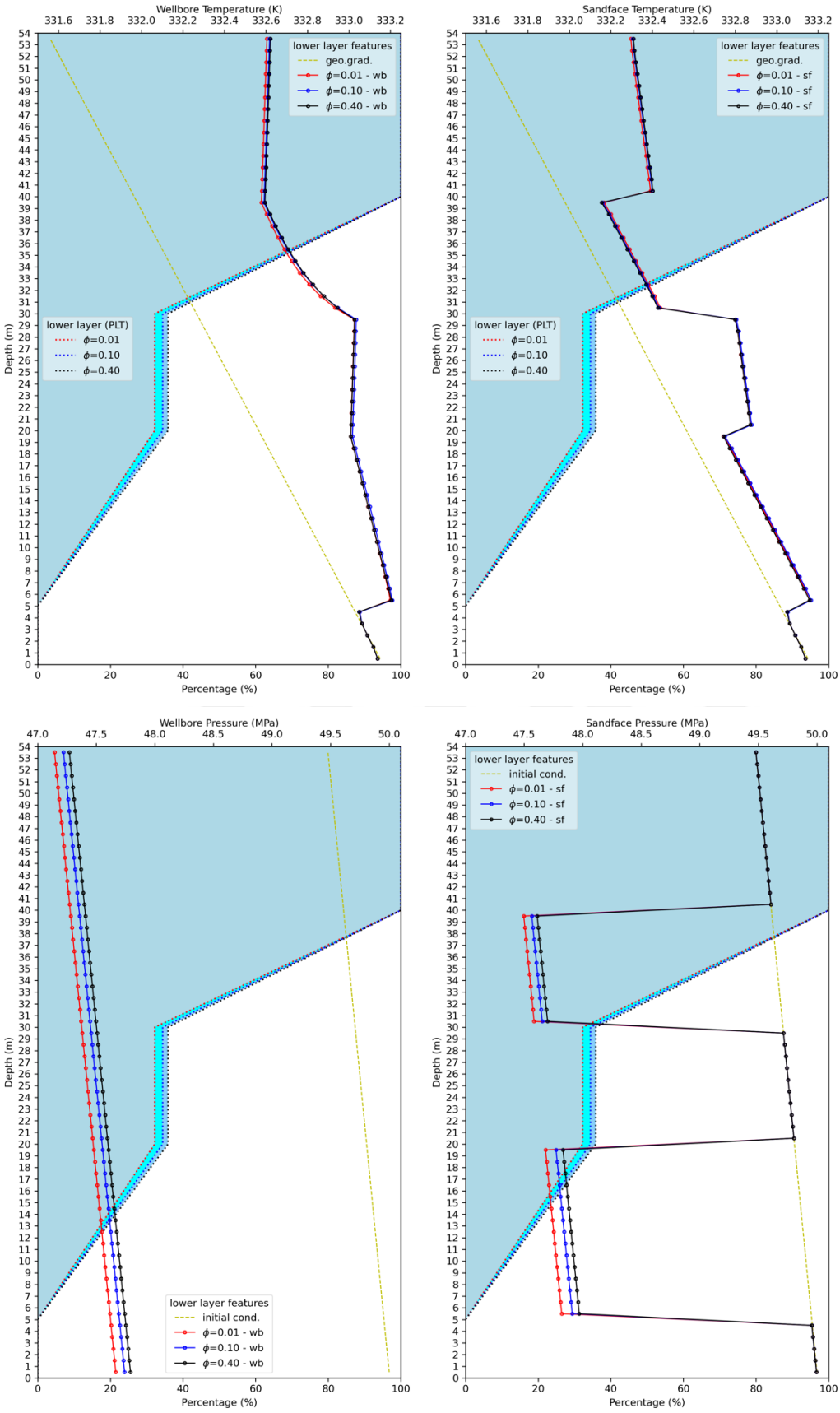

Figure E.6: Comparison of wellbore/sandface temperatures and pressures for different porosity values in the **lower zone** at the end of drawdown.

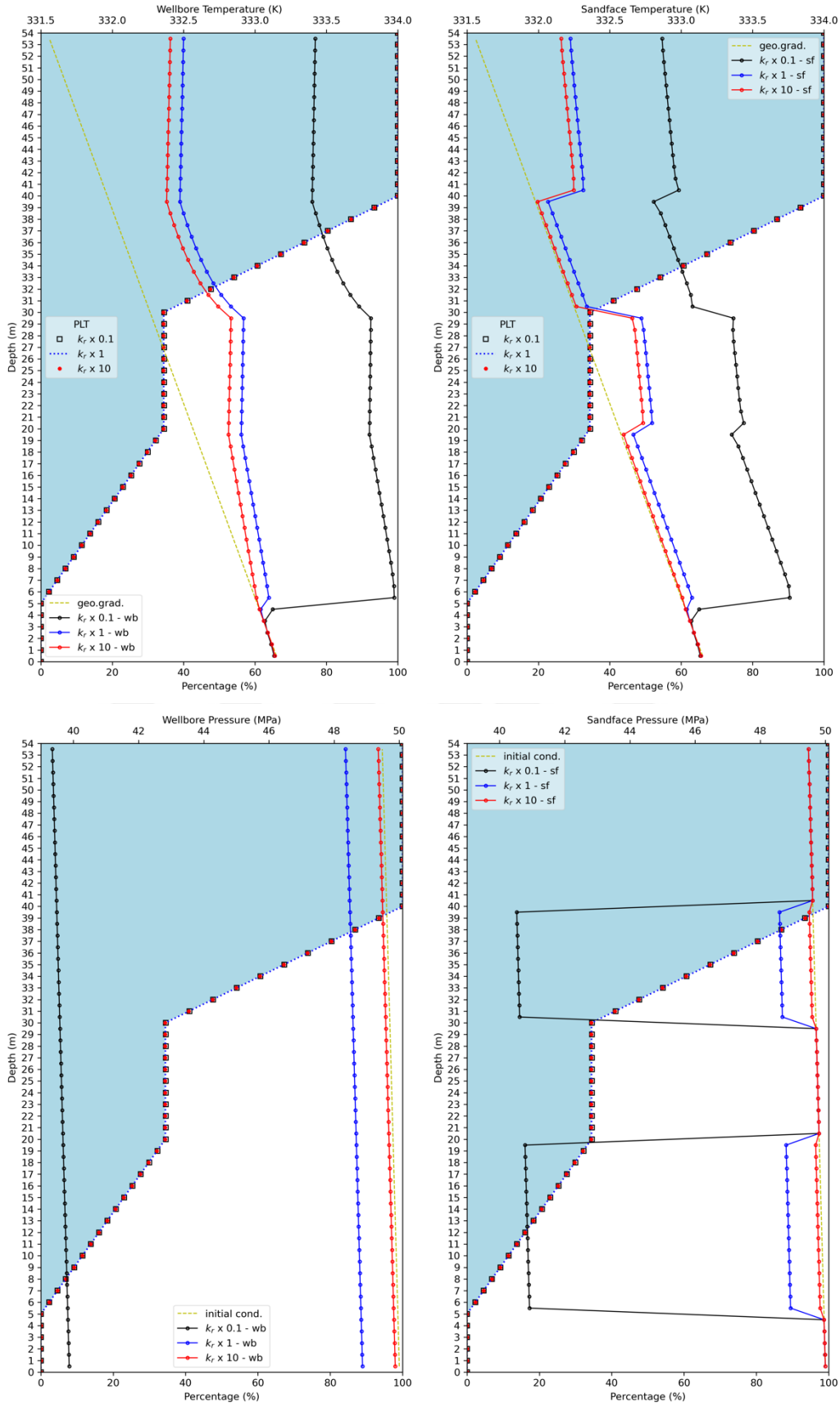

Figure E.7: Comparison of wellbore/sandface temperatures and pressures for different permeability values for **both zones** at the end of drawdown (q_{sc}=500 sm^3/D).

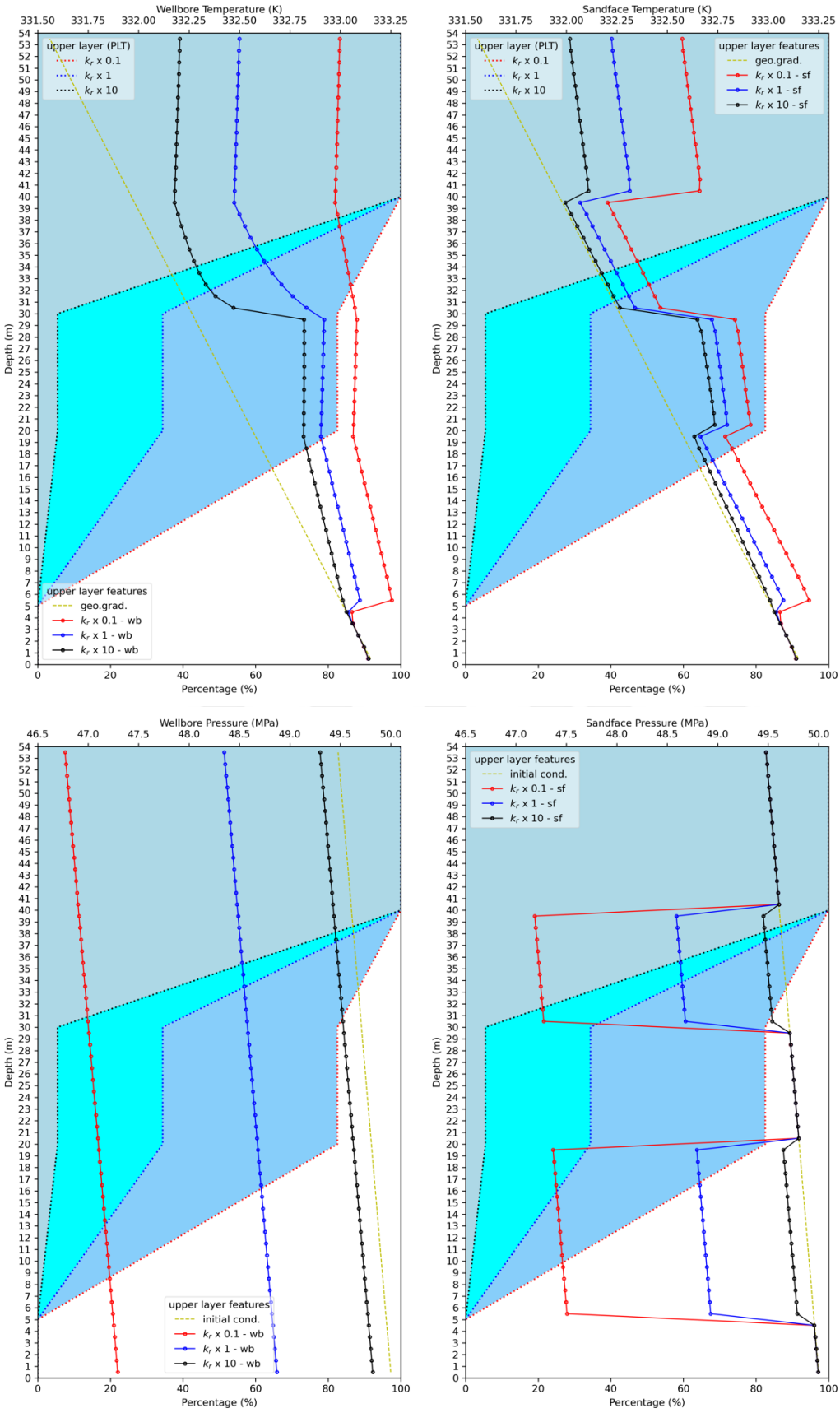

Figure E.8: Comparison of wellbore/sandface temperatures and pressures for different permeability values in the **upper zone** at the end of drawdown(q_{sc}=500sm^3/D).

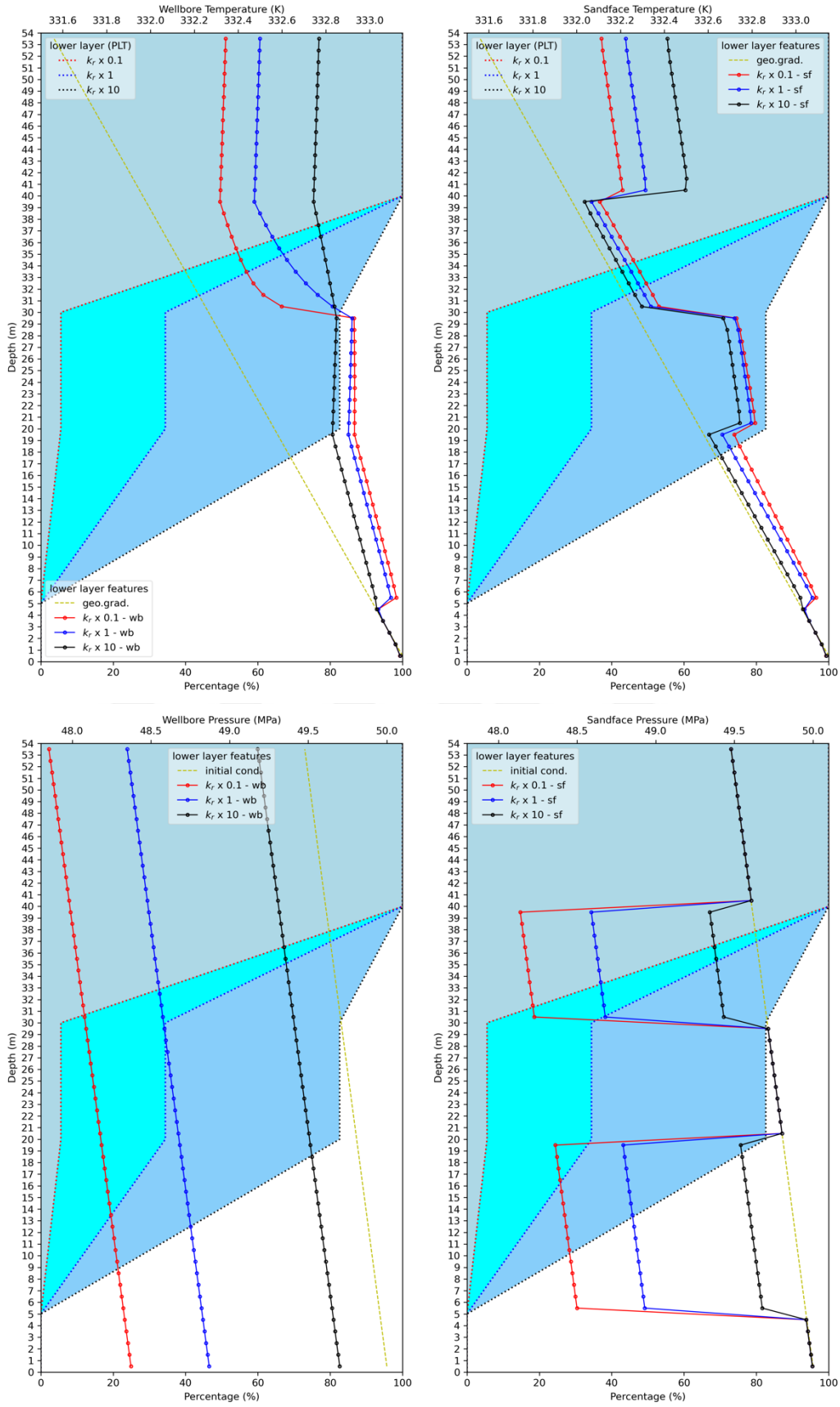

Figure E.9: Comparison of wellbore/sandface temperatures and pressures for different permeability values in the **lower zone** at the end of drawdown (q_{sc}=500sm^3/D).

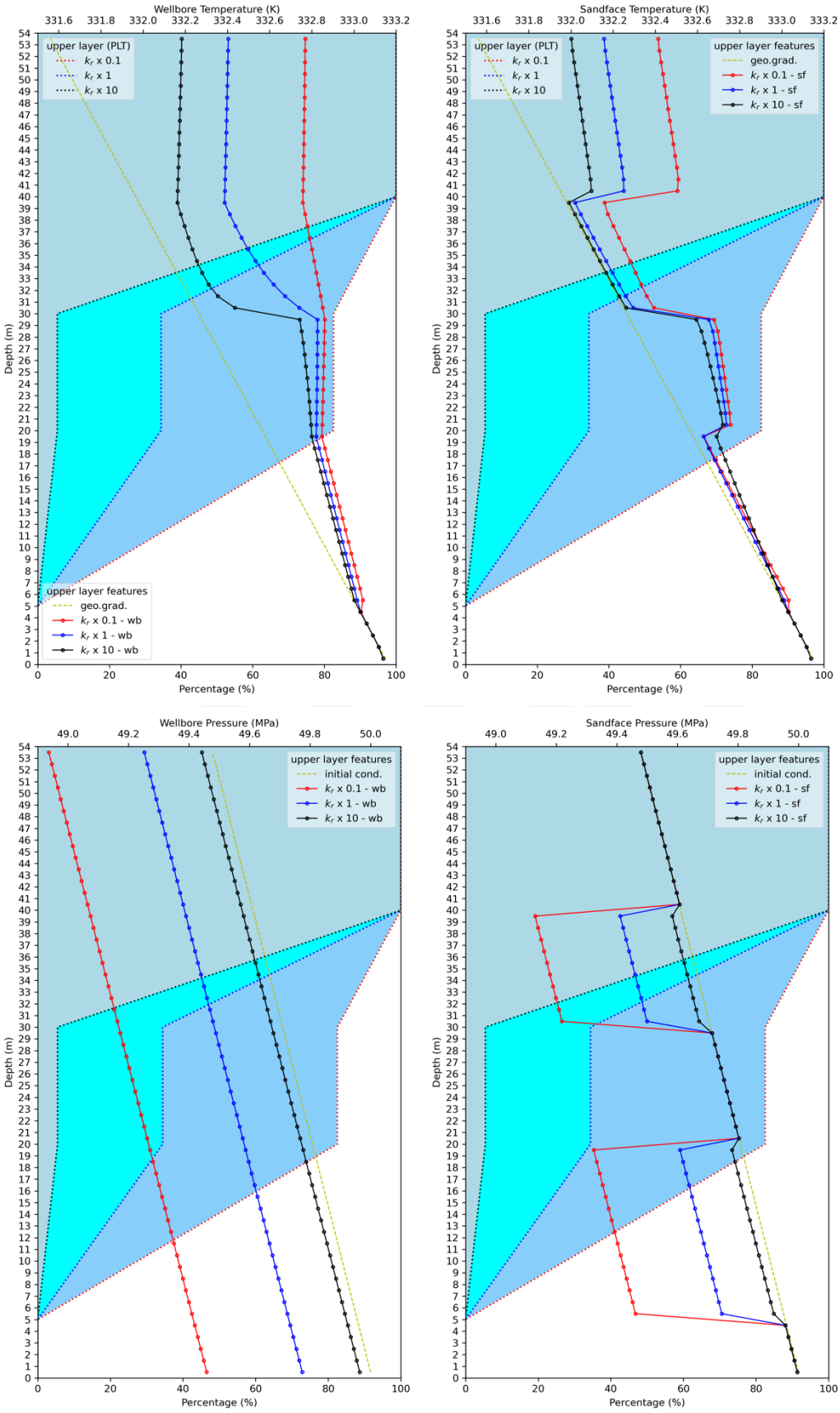

Figure E.10: Comparison of wellbore/sandface temperatures and pressures for different permeability values in the **upper zone** at the end of drawdown (q_{sc}=100sm^3/D).

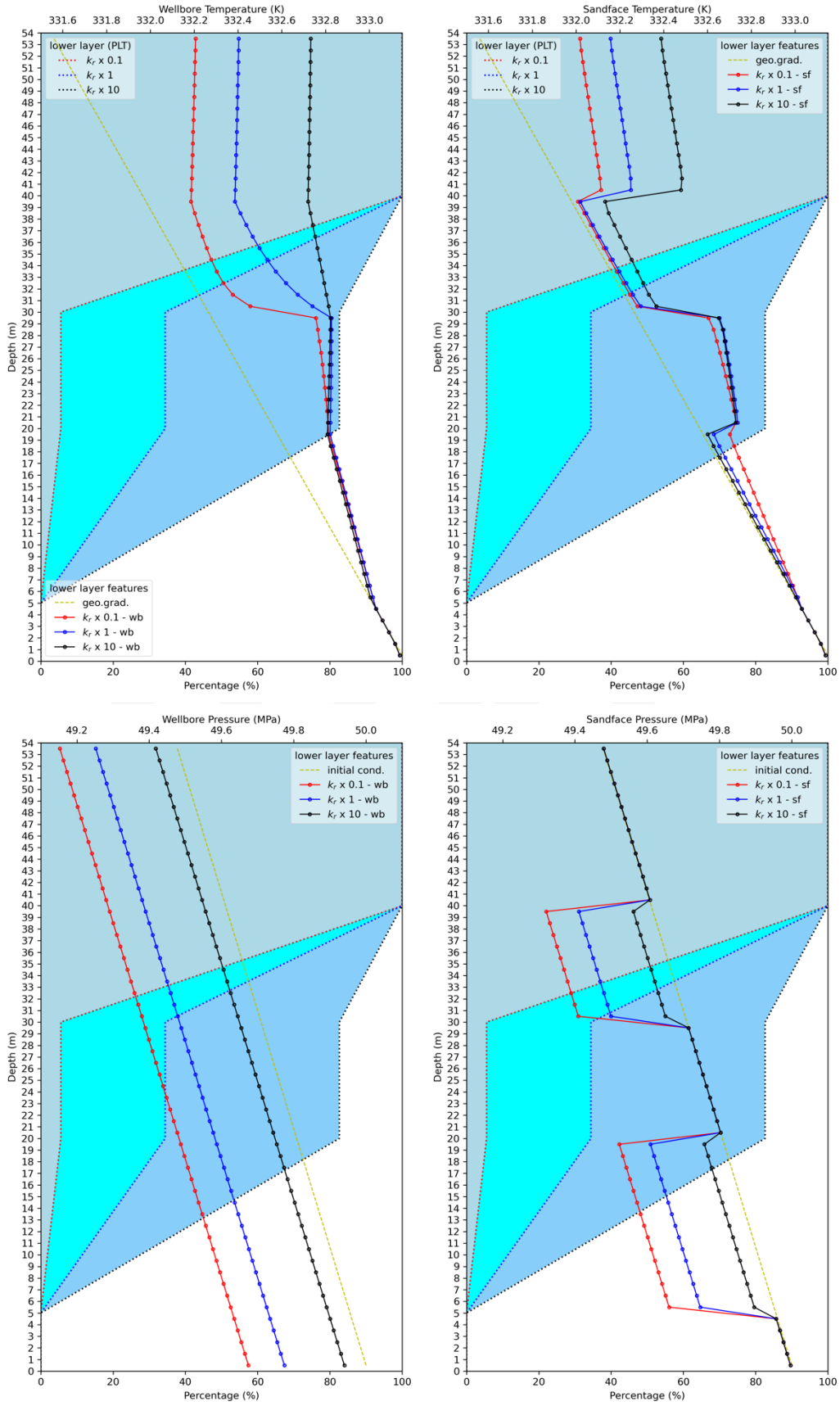

Figure E.11: Comparison of wellbore/sandface temperatures and pressures for different permeability values in the **lower zone** at the end of drawdown (q_{sc}=100sm^3/D).

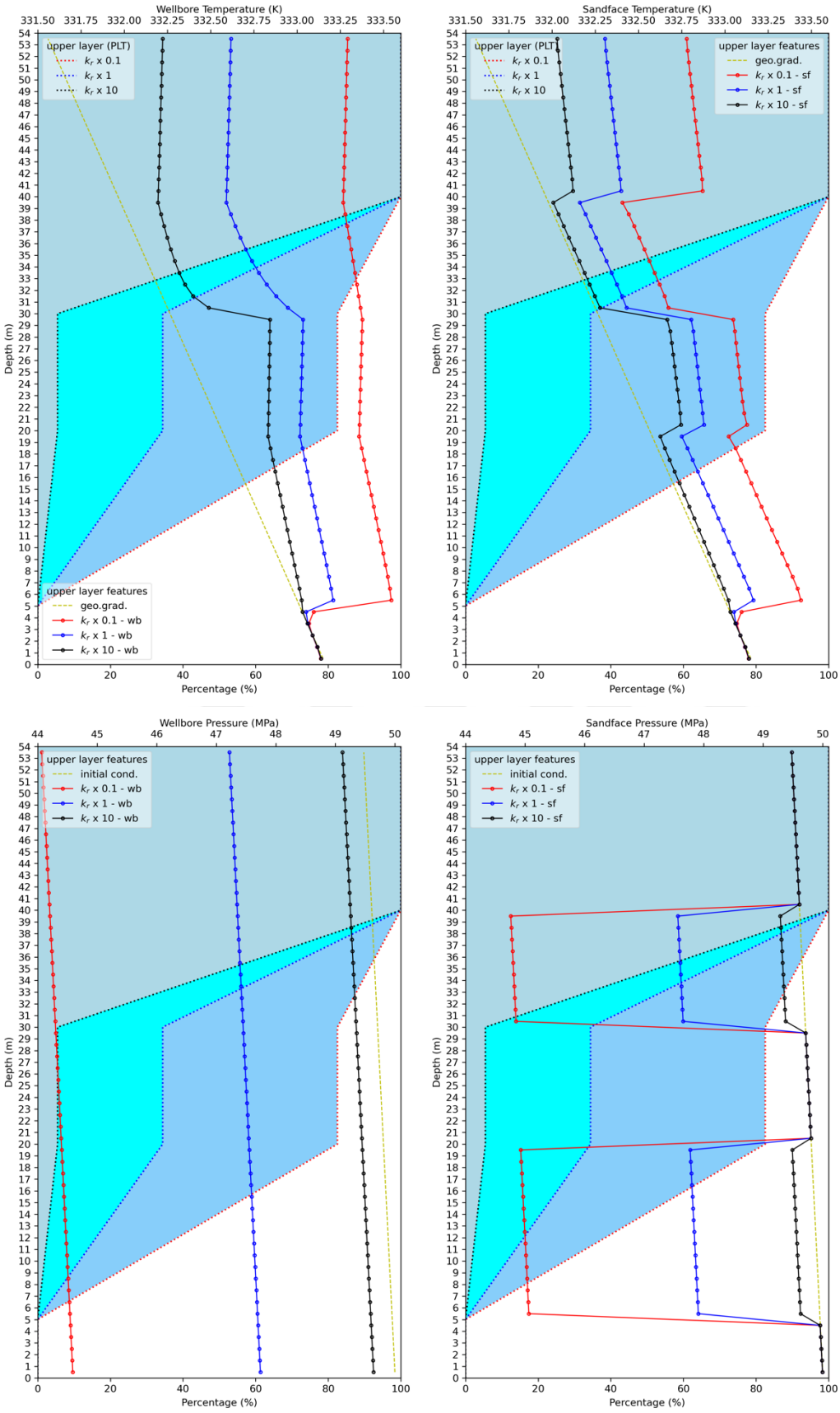

Figure E.12: Comparison of wellbore/sandface temperatures and pressures for different permeability values in the **upper zone** at the end of drawdown (q_{sc}=1000sm^3/D).

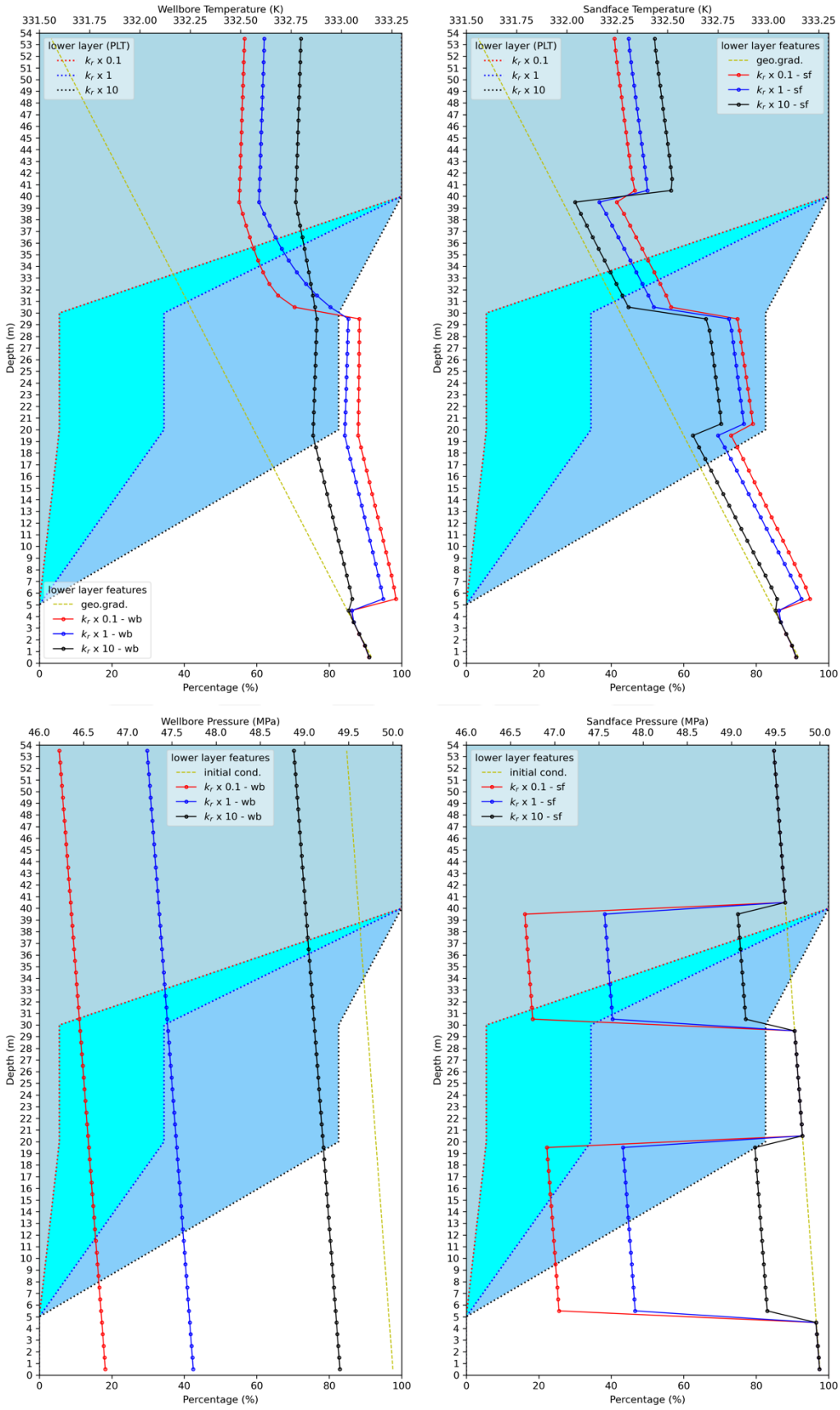

Figure E.13: Comparison of wellbore/sandface temperatures and pressures for different permeability values in the **lower zone** at the end of drawdown(q_{sc}=1000sm^3/D).

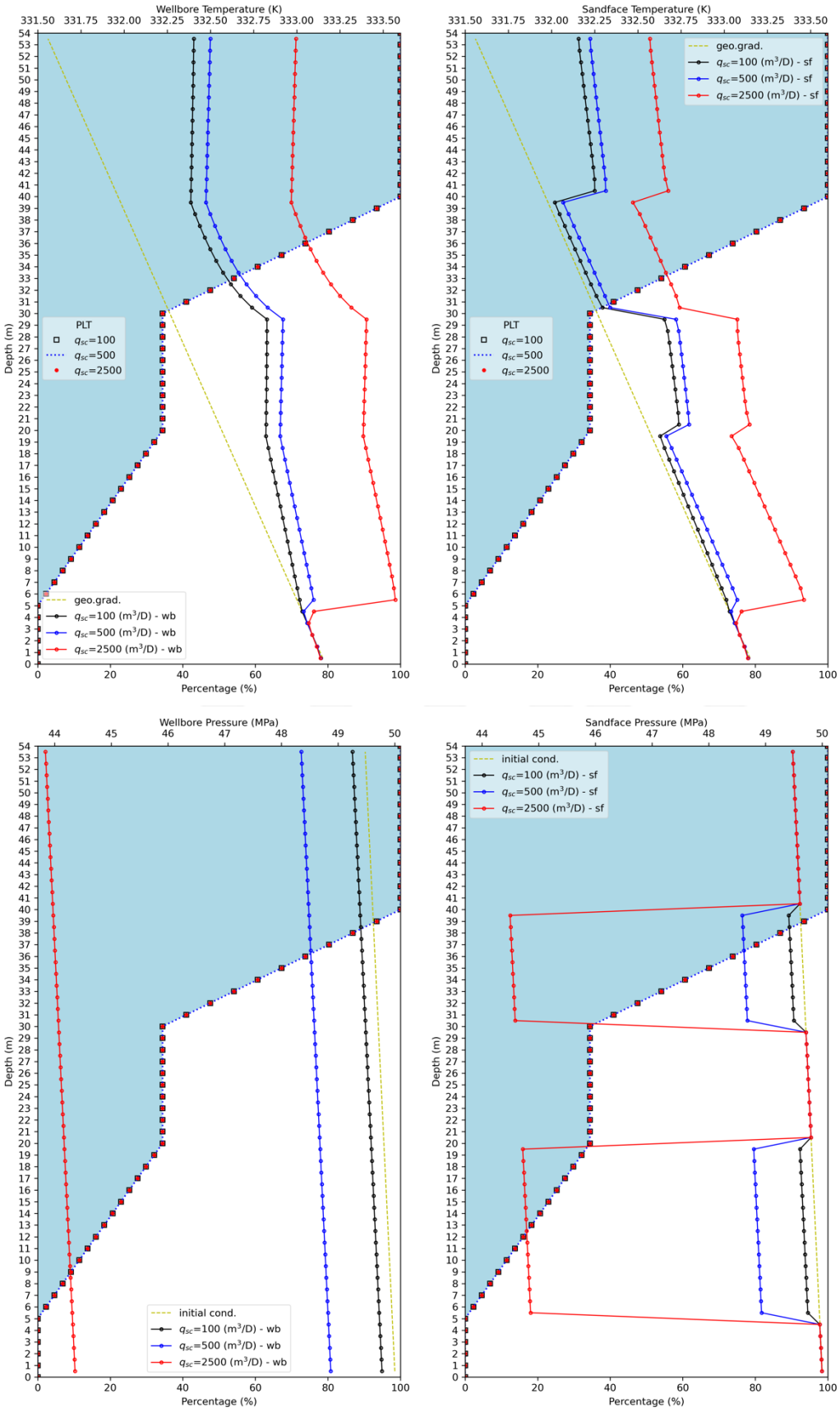

Figure E.14: Comparison of wellbore/sandface temperatures and pressures for different surface flow rates at the end of drawdown.

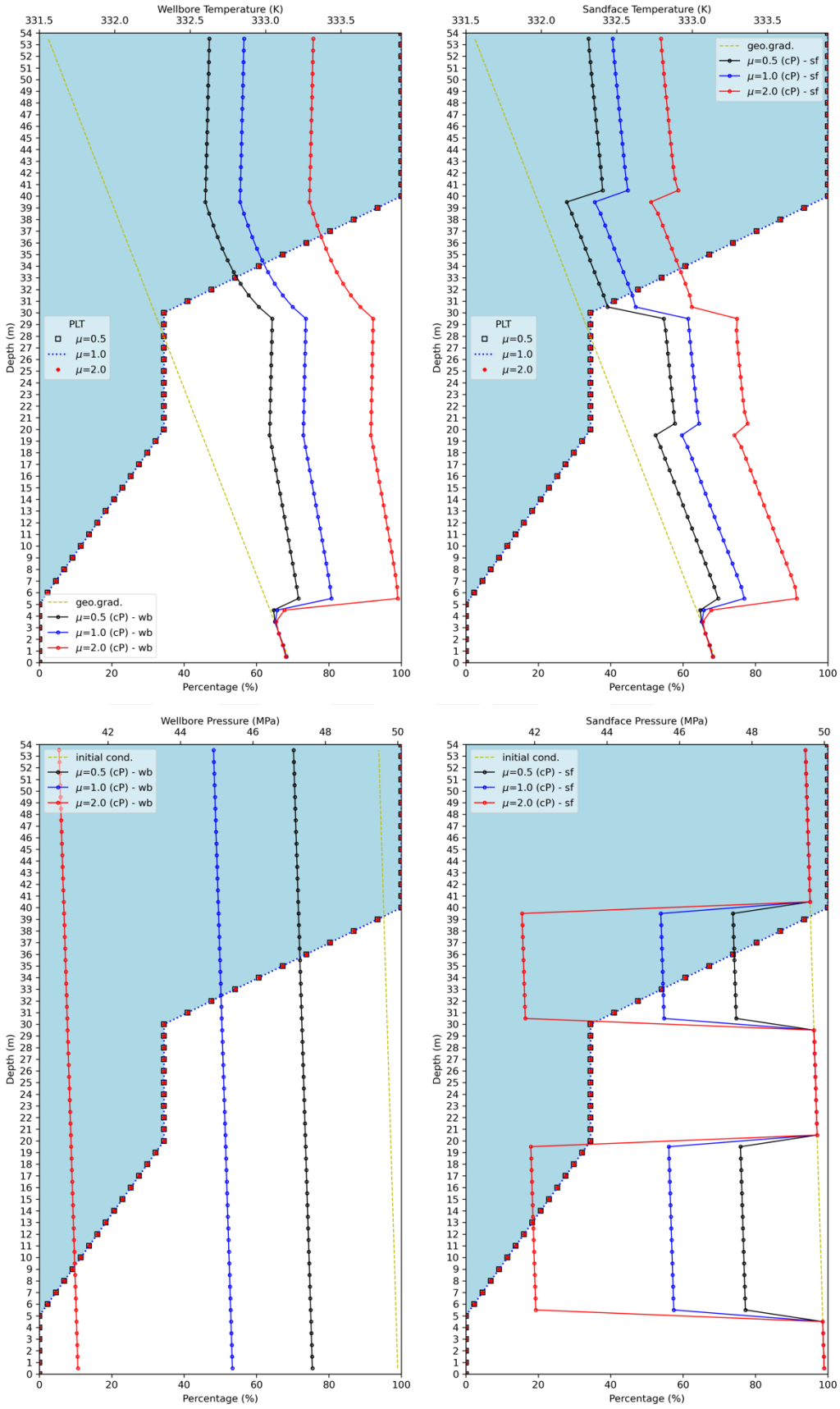

Figure E.15: Comparison of wellbore/sandface temperatures and pressures for different viscosity values for **both zones** at the end of drawdown.

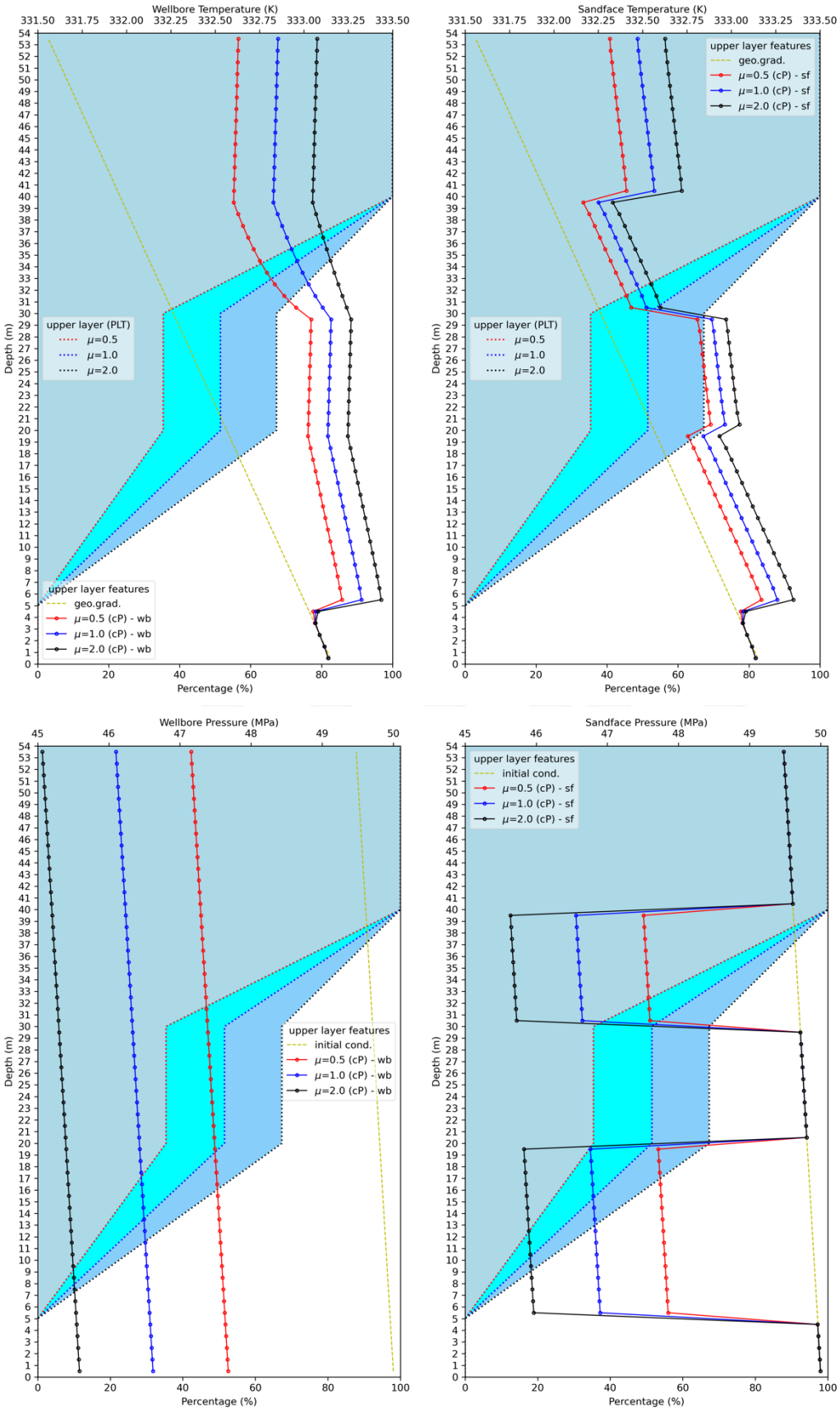

Figure E.16: Comparison of wellbore/sandface temperatures and pressures for different viscosity values in the **upper zone** at the end of drawdown.

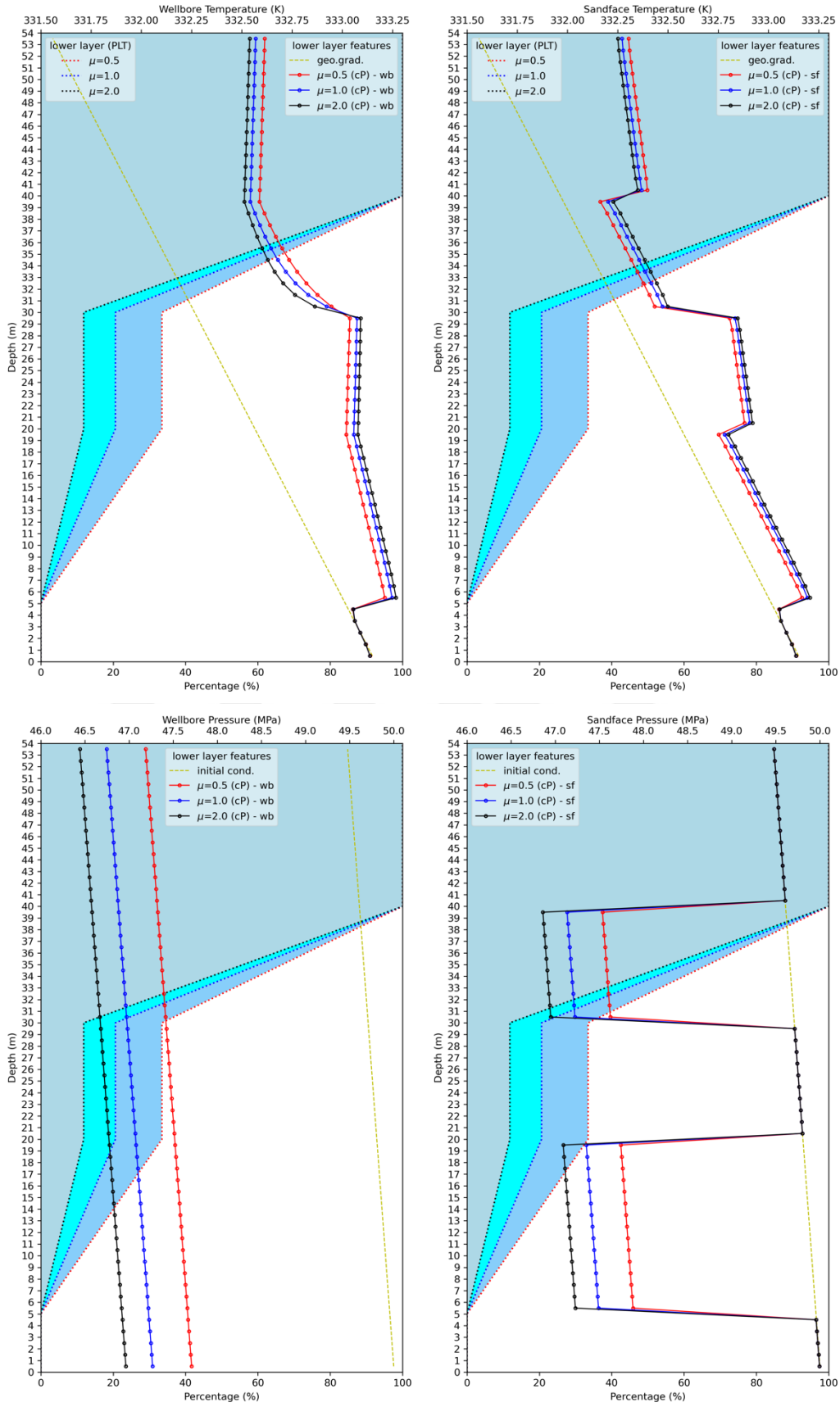

Figure E.17: Comparison of wellbore/sandface temperatures and pressures for different viscosity values in the **lower zone** at the end of drawdown.

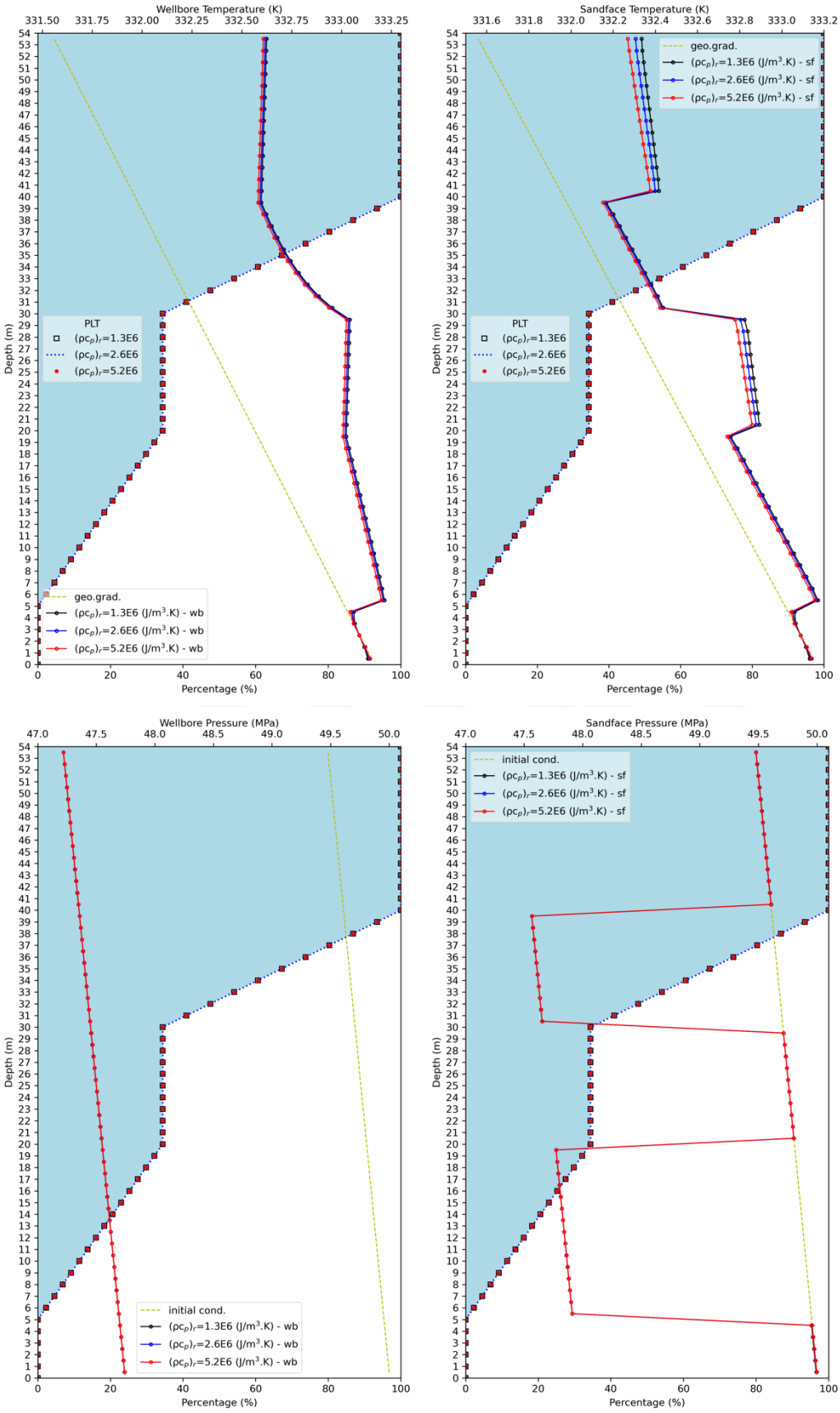

Figure E.18: Comparison of wellbore/sandface temperatures and pressures for different volumetric heat capacity of rock values for **both zones** at the end of drawdown.

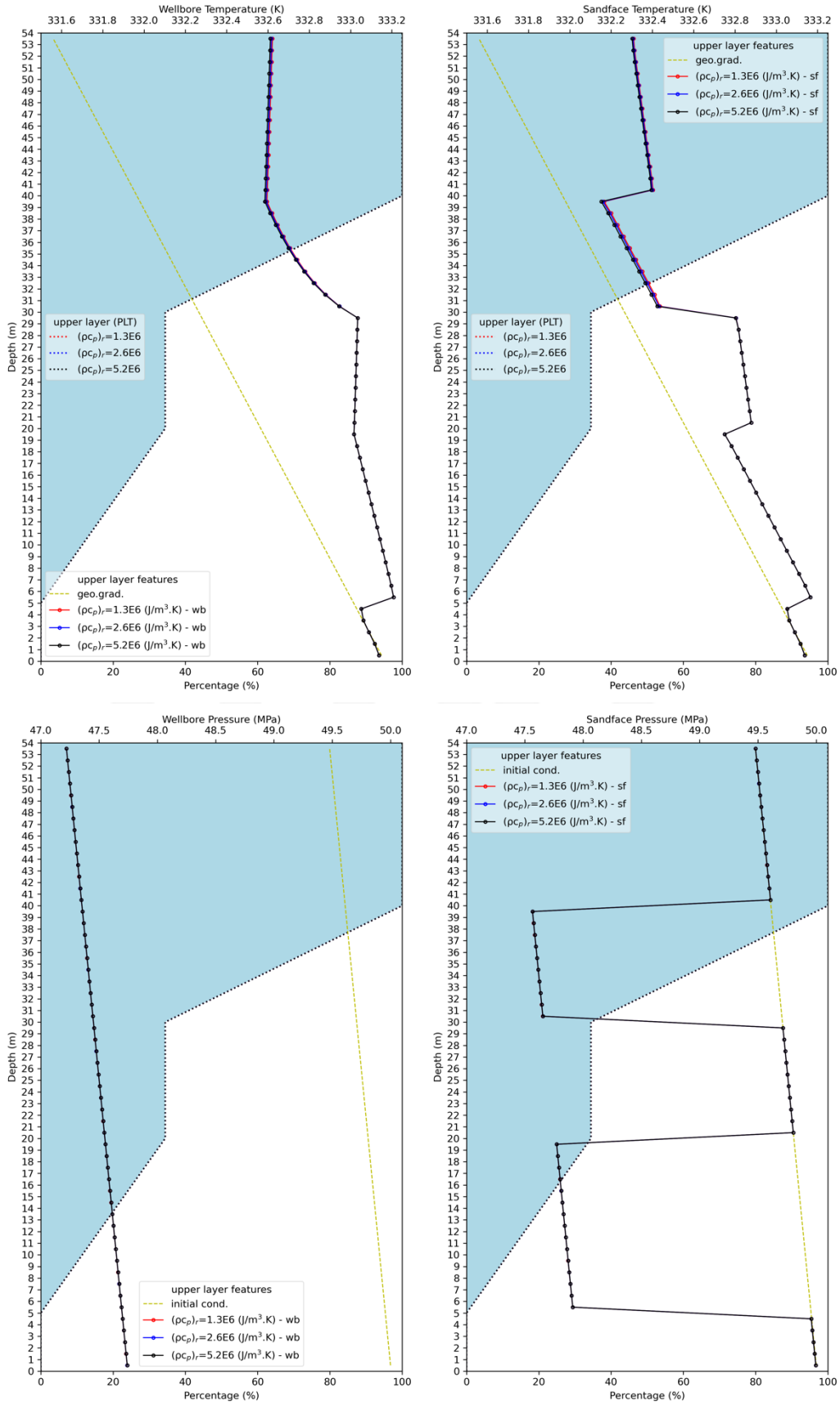

Figure E.19: Comparison of wellbore/sandface temperatures and pressures for different volumetric heat capacity of rock values in the **upper zone** at the end of drawdown.

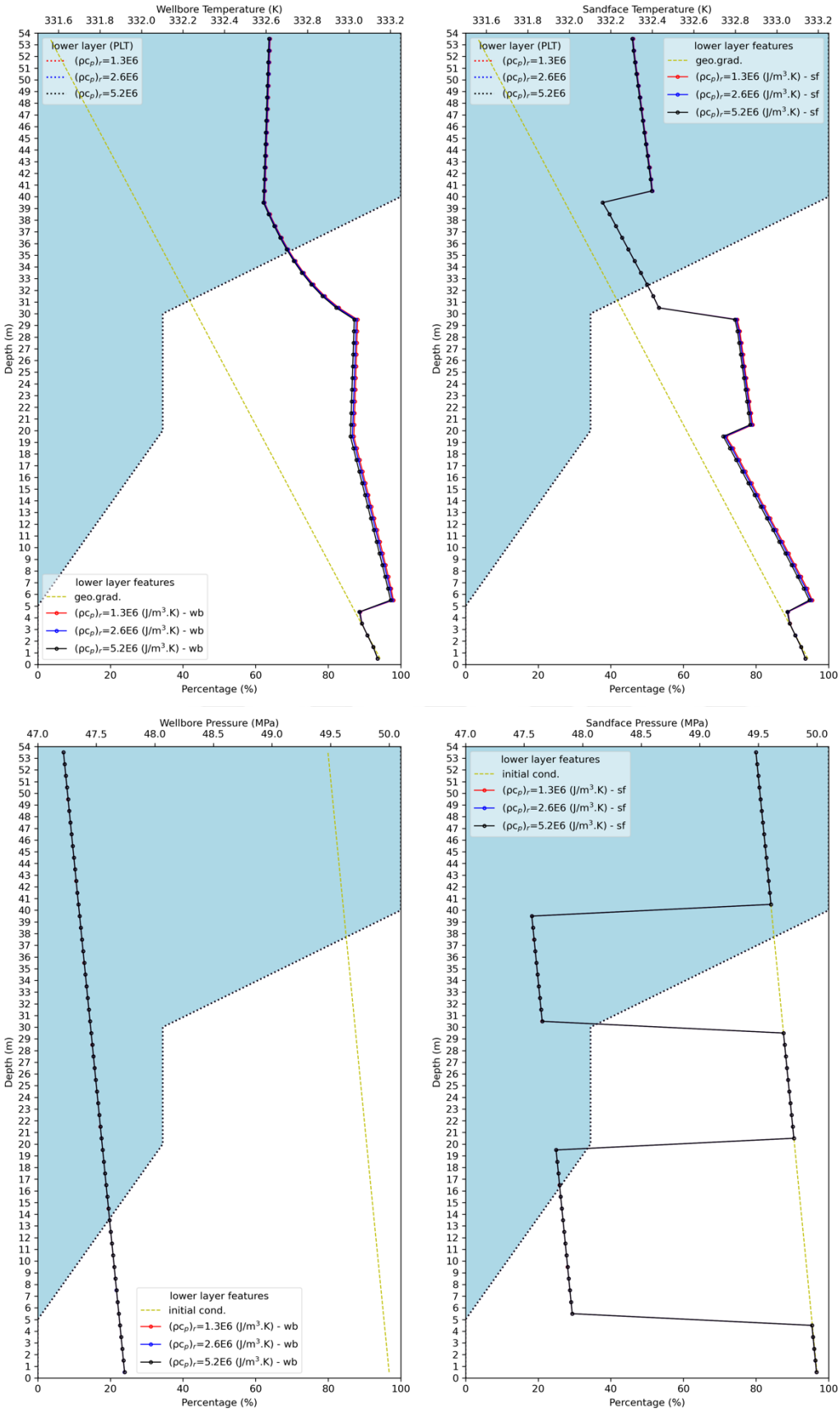

Figure E.20: Comparison of wellbore/sandface temperatures and pressures for different volumetric heat capacity of rock values in the **lower zone** at the end of drawdown.

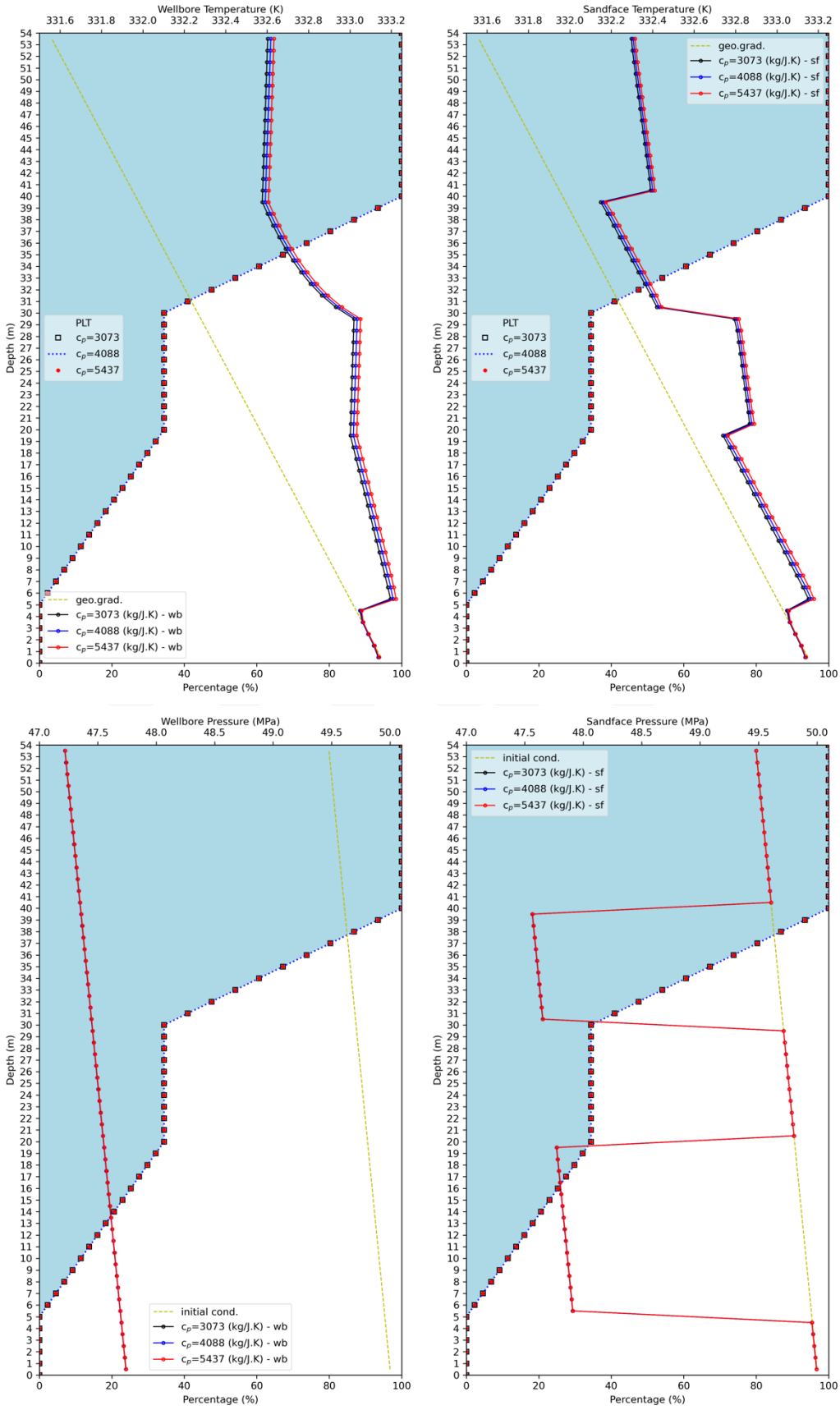

Figure E.21: Comparison of wellbore/sandface temperatures and pressures for different fluid specific heat capacity values for **both zones** at the end of drawdown.

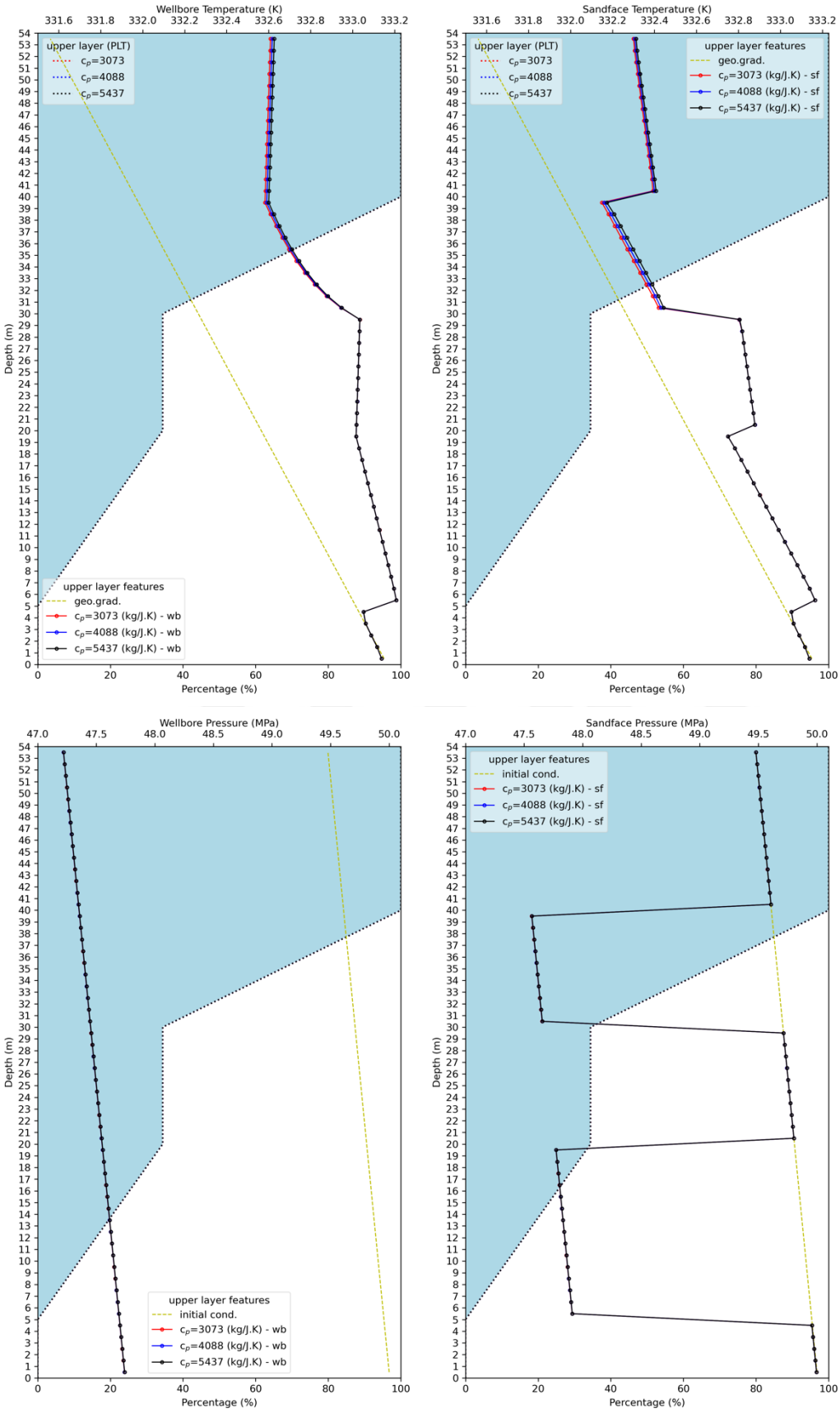

Figure E.22: Comparison of wellbore/sandface temperatures and pressures for different fluid specific heat capacity values in the **upper zone** at the end of drawdown.

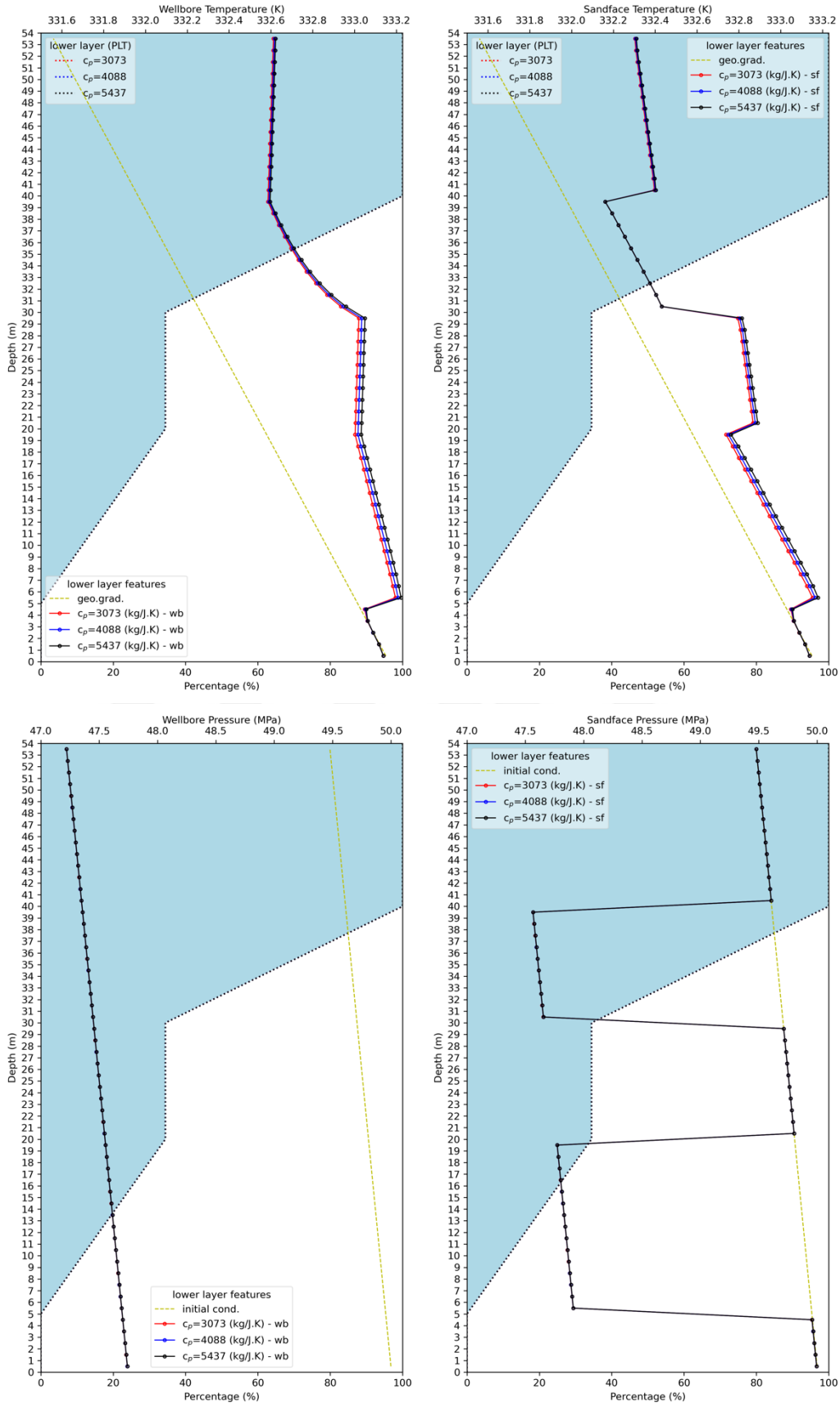

Figure E.23: Comparison of wellbore/sandface temperatures and pressures for different fluid specific heat capacity values in the **lower zone** at the end of drawdown.

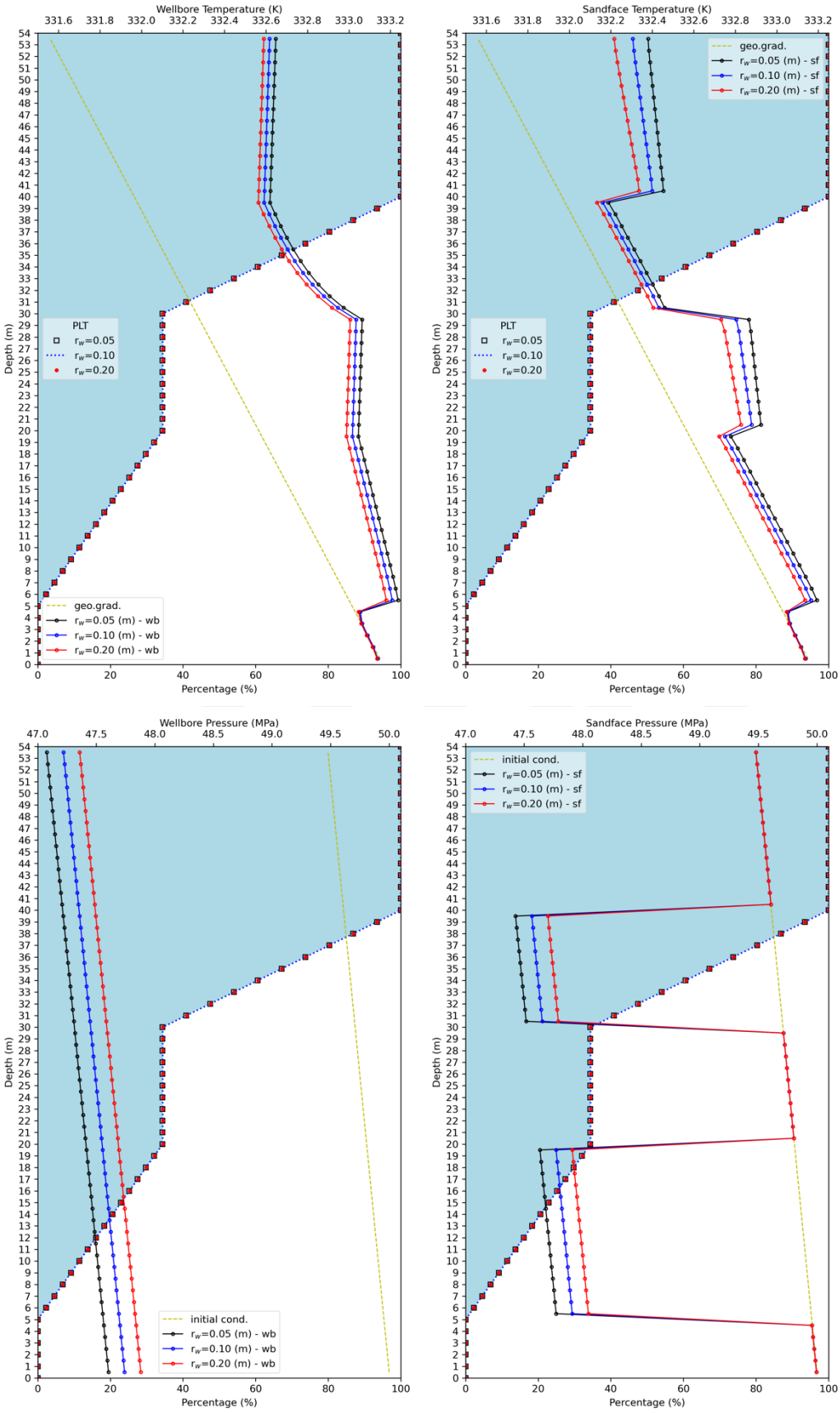

Figure E.24: Comparison of wellbore/sandface temperatures and pressures for different well radius values for **both zones** at the end of drawdown.

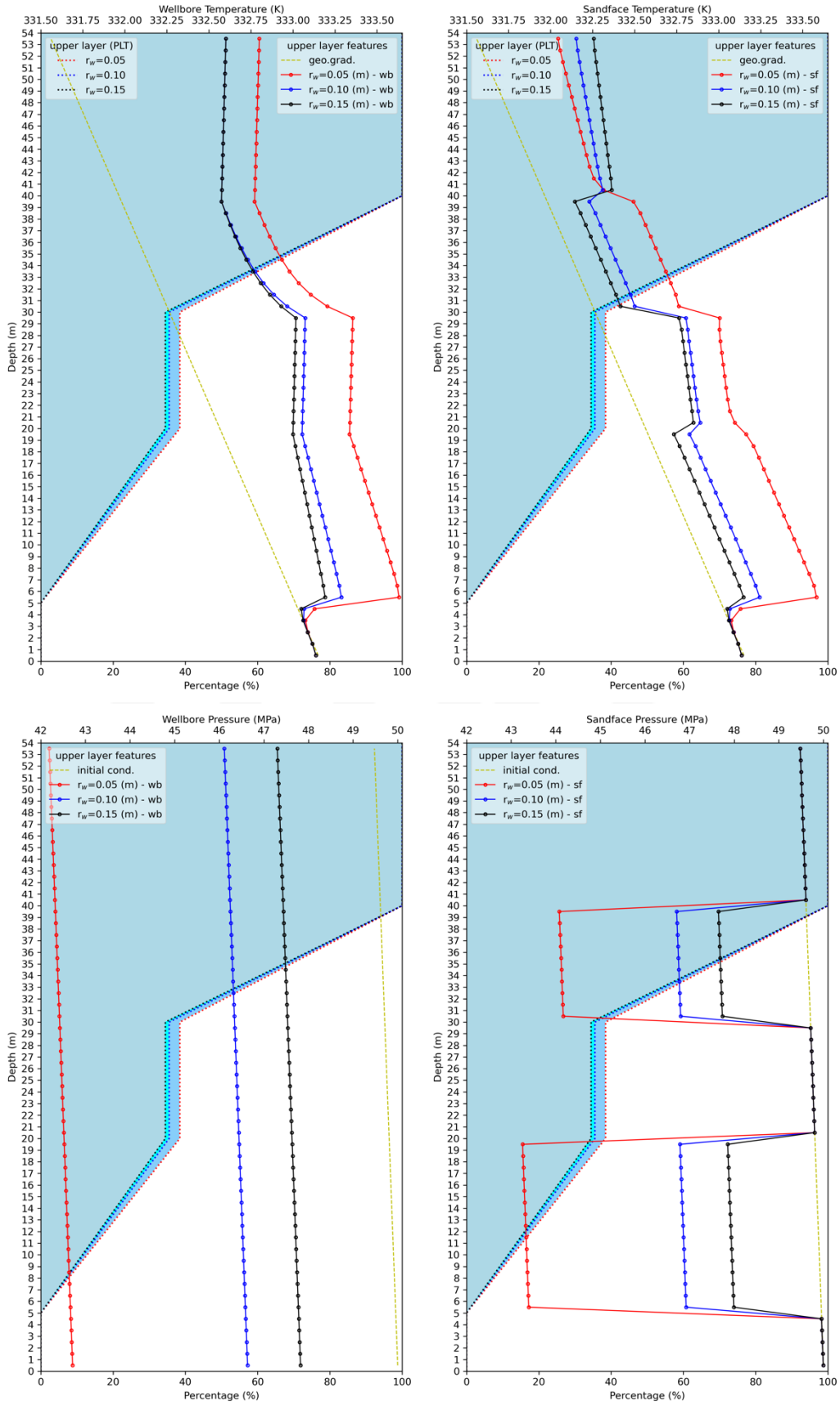

Figure E.25: Comparison of wellbore/sandface temperatures and pressures for different well radius values in the **upper zone** at the end of drawdown.

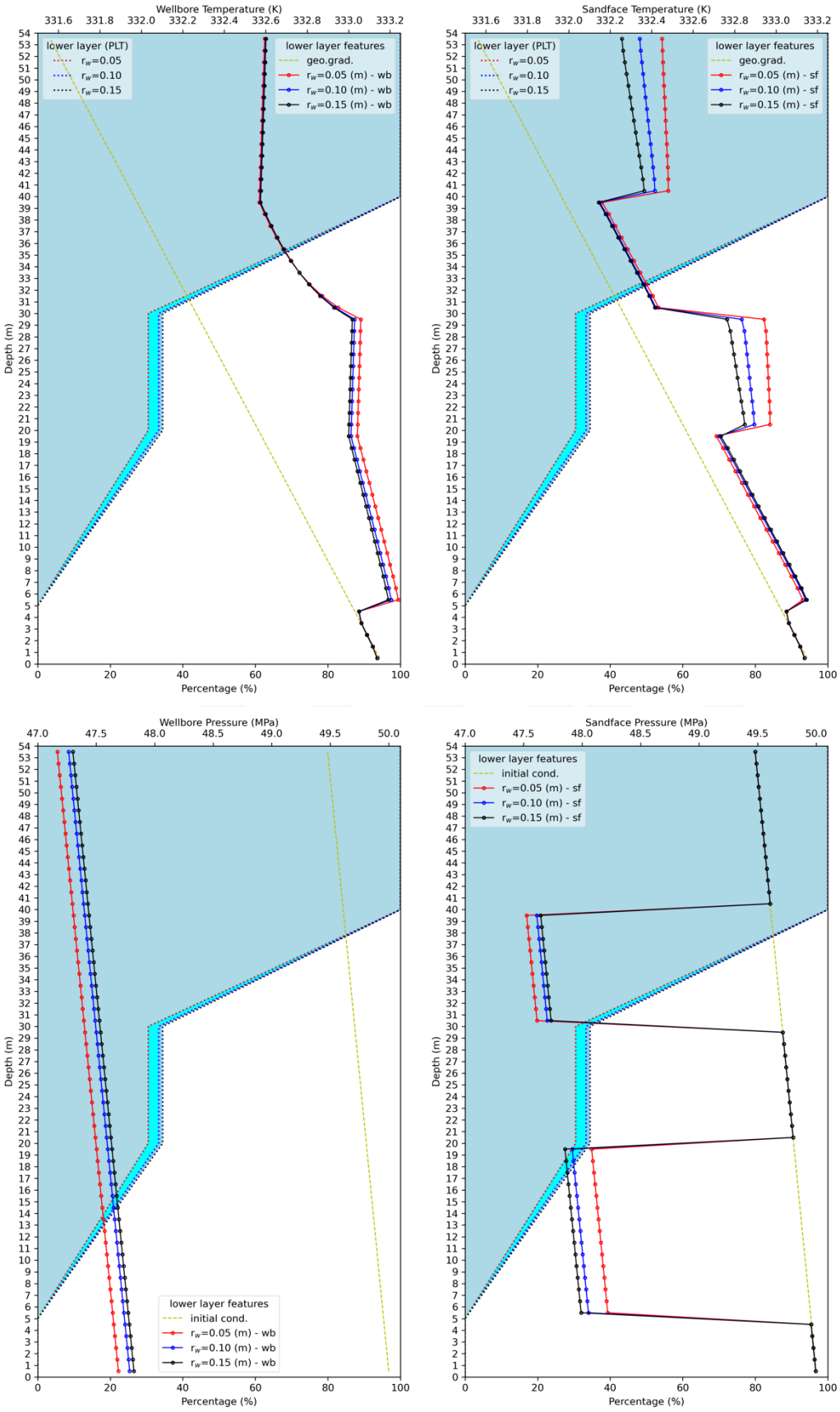

Figure E.26: Comparison of wellbore/sandface temperatures and pressures for different well radius values in the **lower zone** at the end of drawdown.

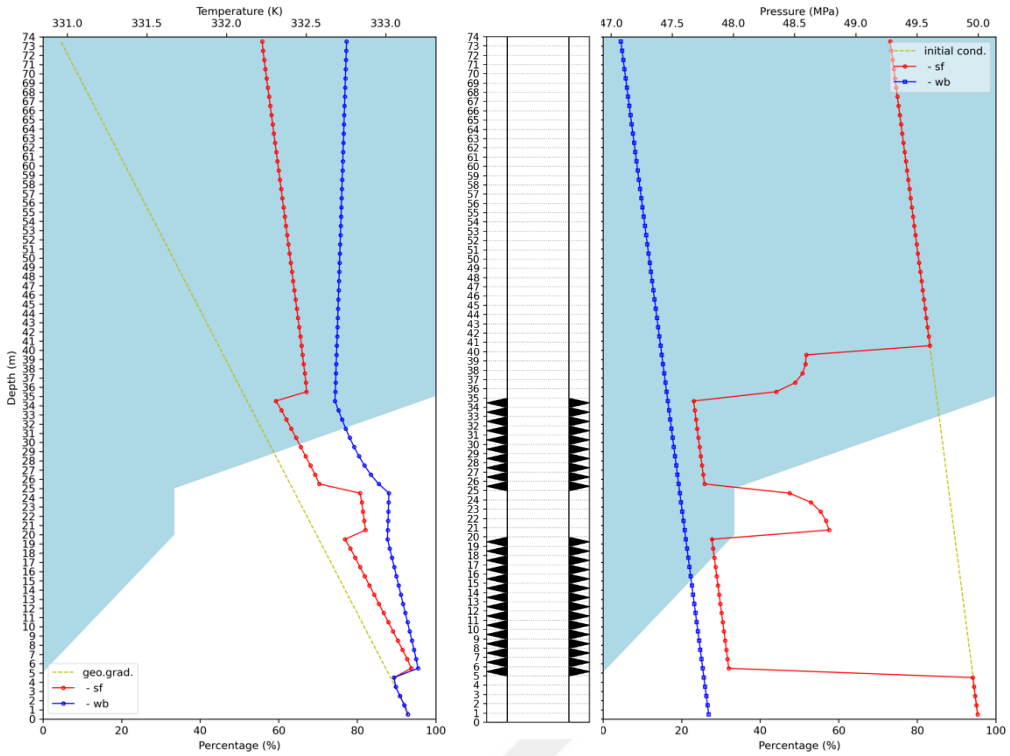

Figure E.27: Comparison of wellbore/sandface temperatures and pressures for unperforated distance of **5 m** between producing zones at the end of drawdown.

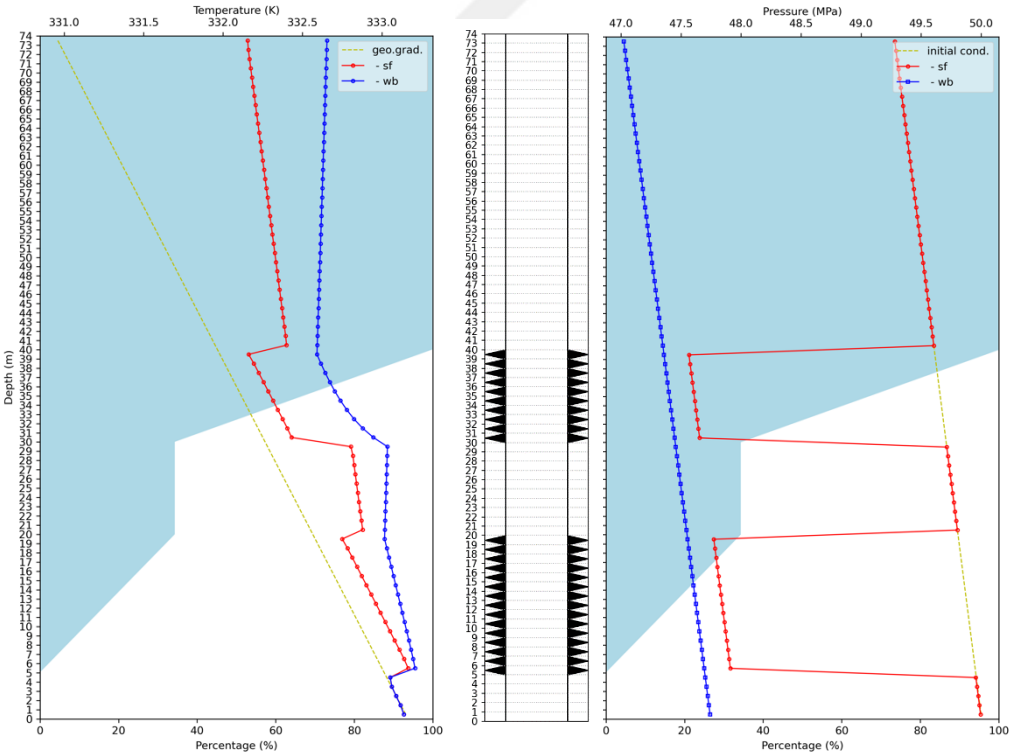

Figure E.28: Comparison of wellbore/sandface temperatures and pressures for unperforated distance of **10 m** between producing zones at the end of drawdown.

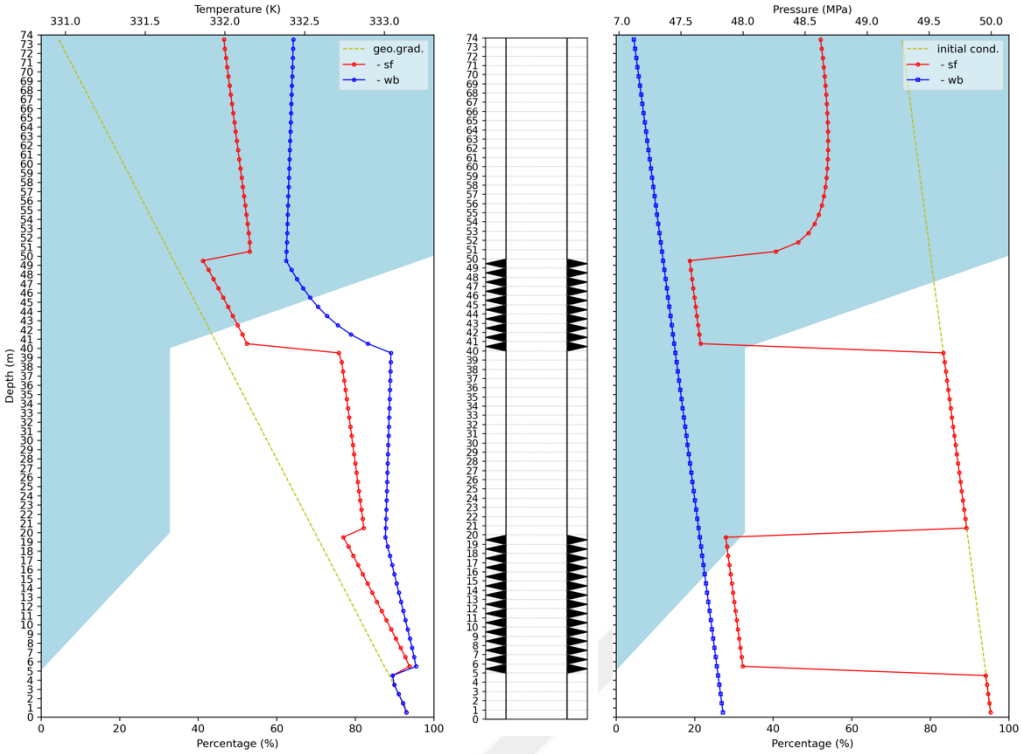

Figure E.29: Comparison of wellbore/sandface temperatures and pressures for unperforated distance of **20 m** between producing zones at the end of drawdown.

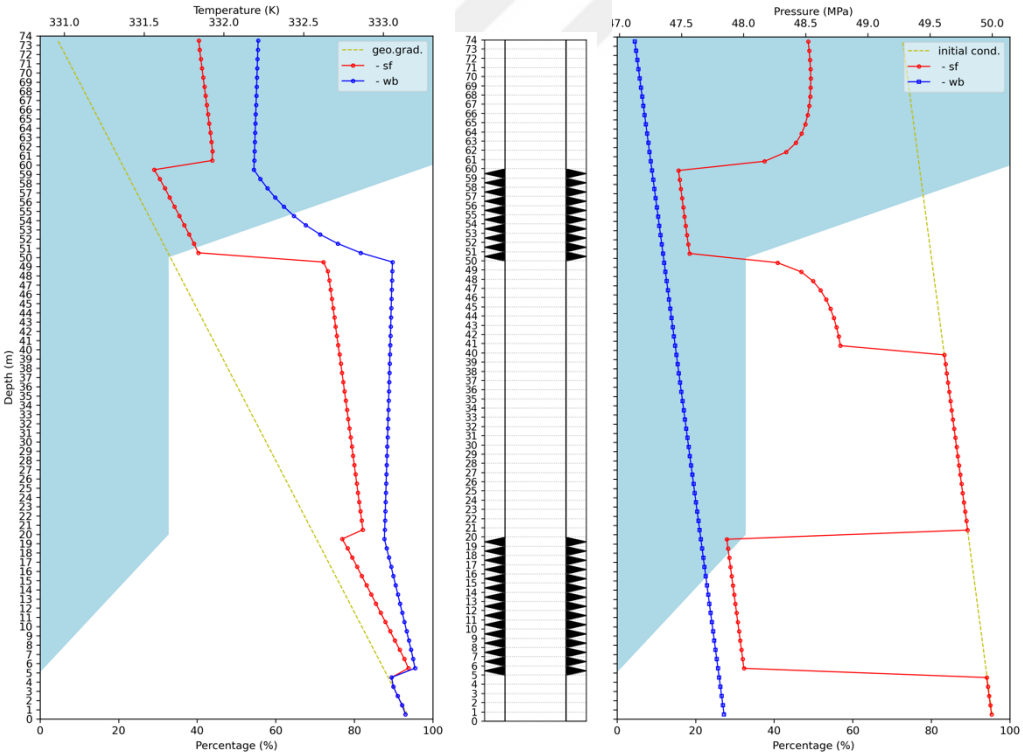

Figure E.30: Comparison of wellbore/sandface temperatures and pressures for unperforated distance of **30 m** between producing zones at the end of drawdown.

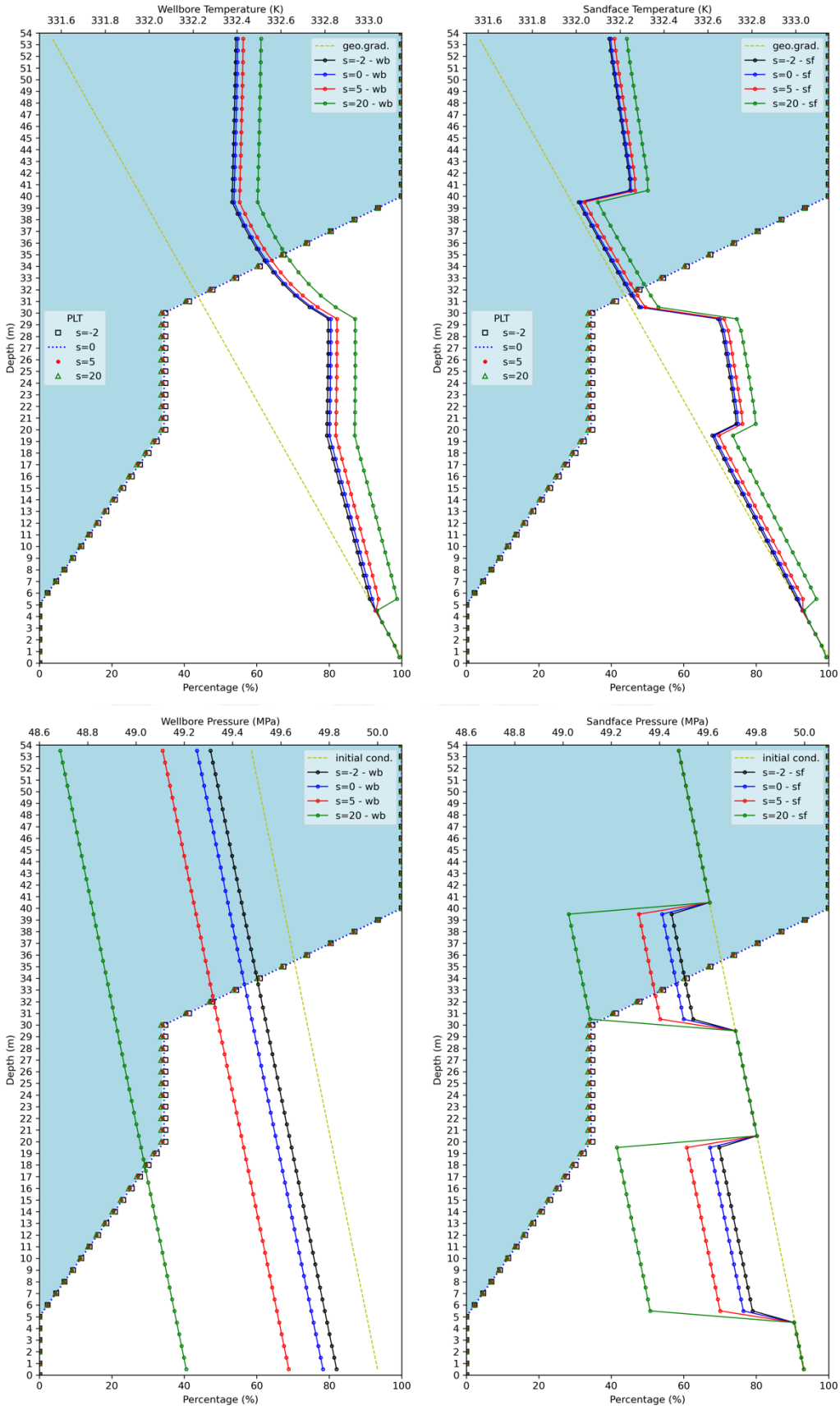

Figure E.31: Comparison of wellbore/reservoir pressures and temperatures for different skin values for **both zones** at the end of drawdown (q_{sc} = 100 sm^3/D).

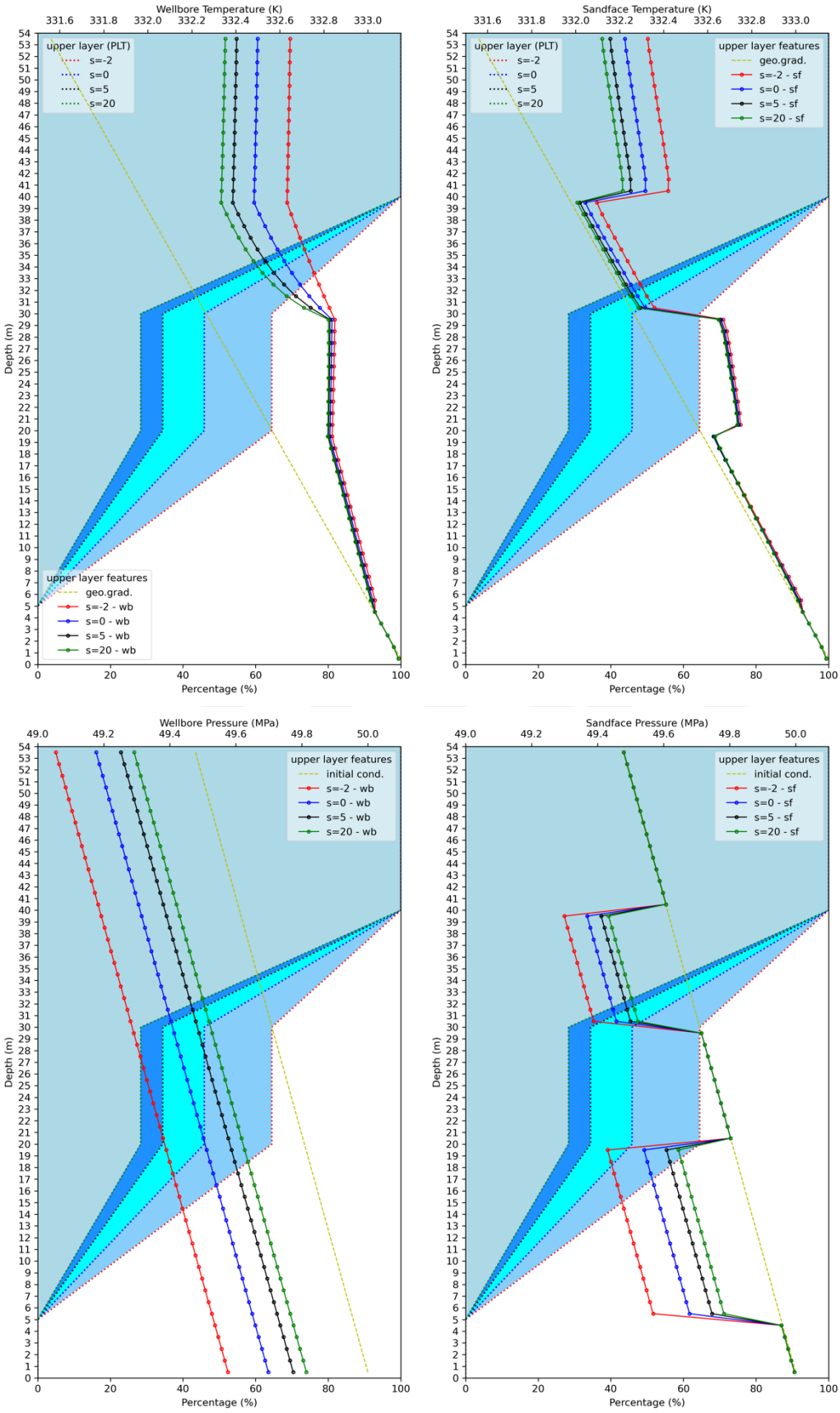

Figure E.32: Comparison of wellbore/reservoir pressures and temperatures for different skin values in the **upper zone** at the end of drawdown (q_{sc} = 100 sm^3/D).

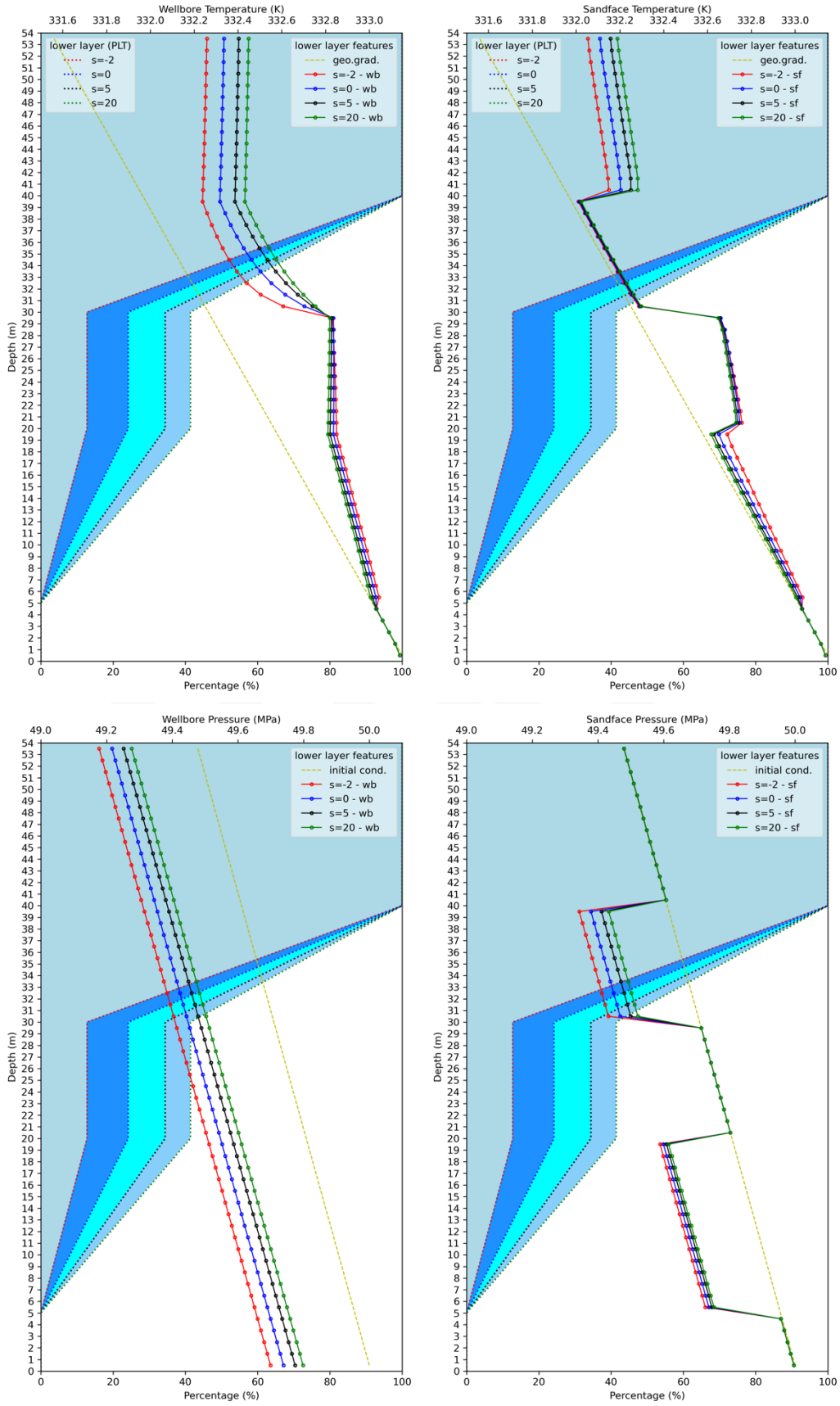

Figure E.33: Comparison of wellbore/reservoir pressures and temperatures for different skin values in the **lower zone** at the end of drawdown (q_{sc} = 100 sm^3/D).

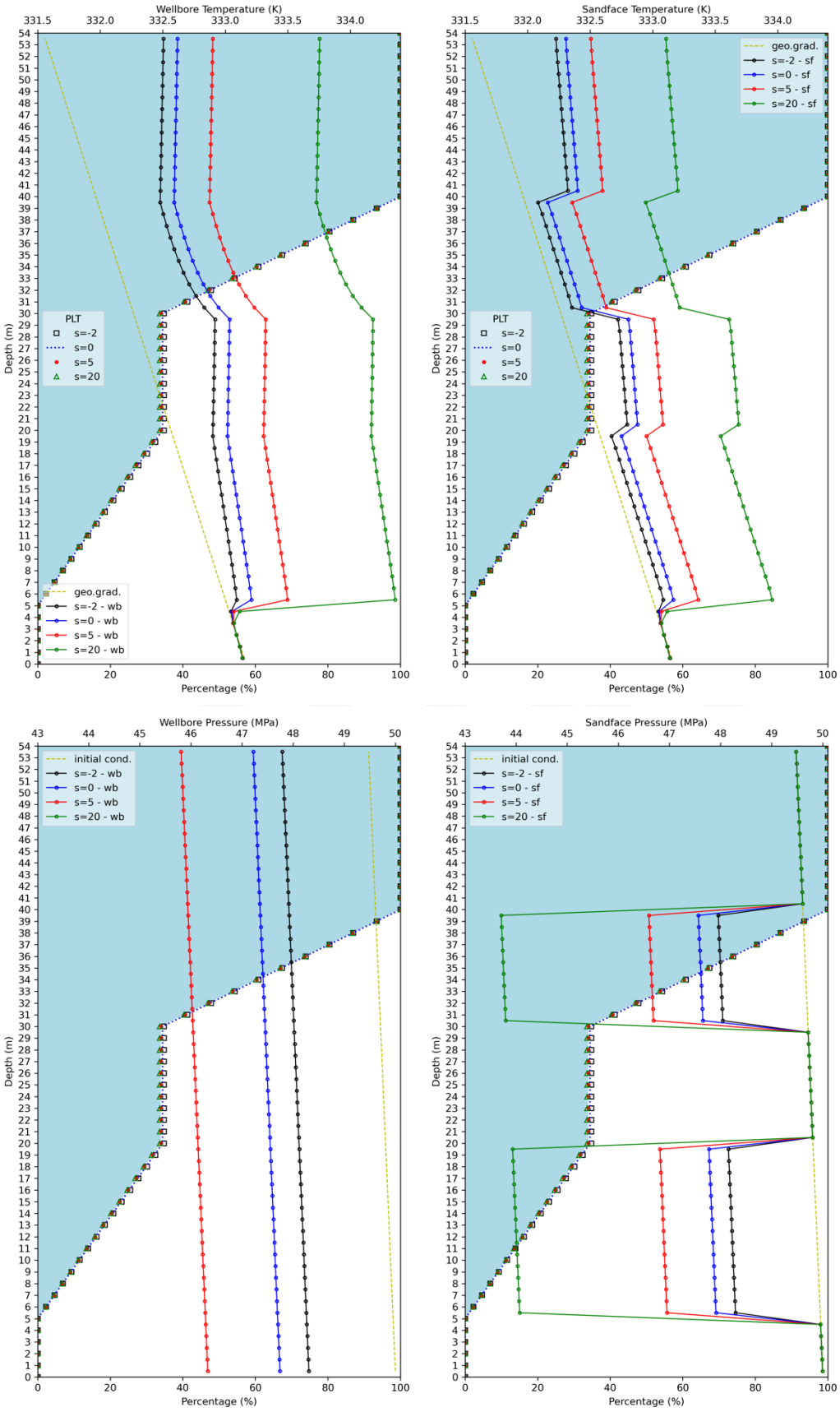

Figure E.34: Comparison of wellbore/reservoir pressures and temperatures for different skin values for **both zones** at the end of drawdown (q_{sc} = 1000 sm^3/D).

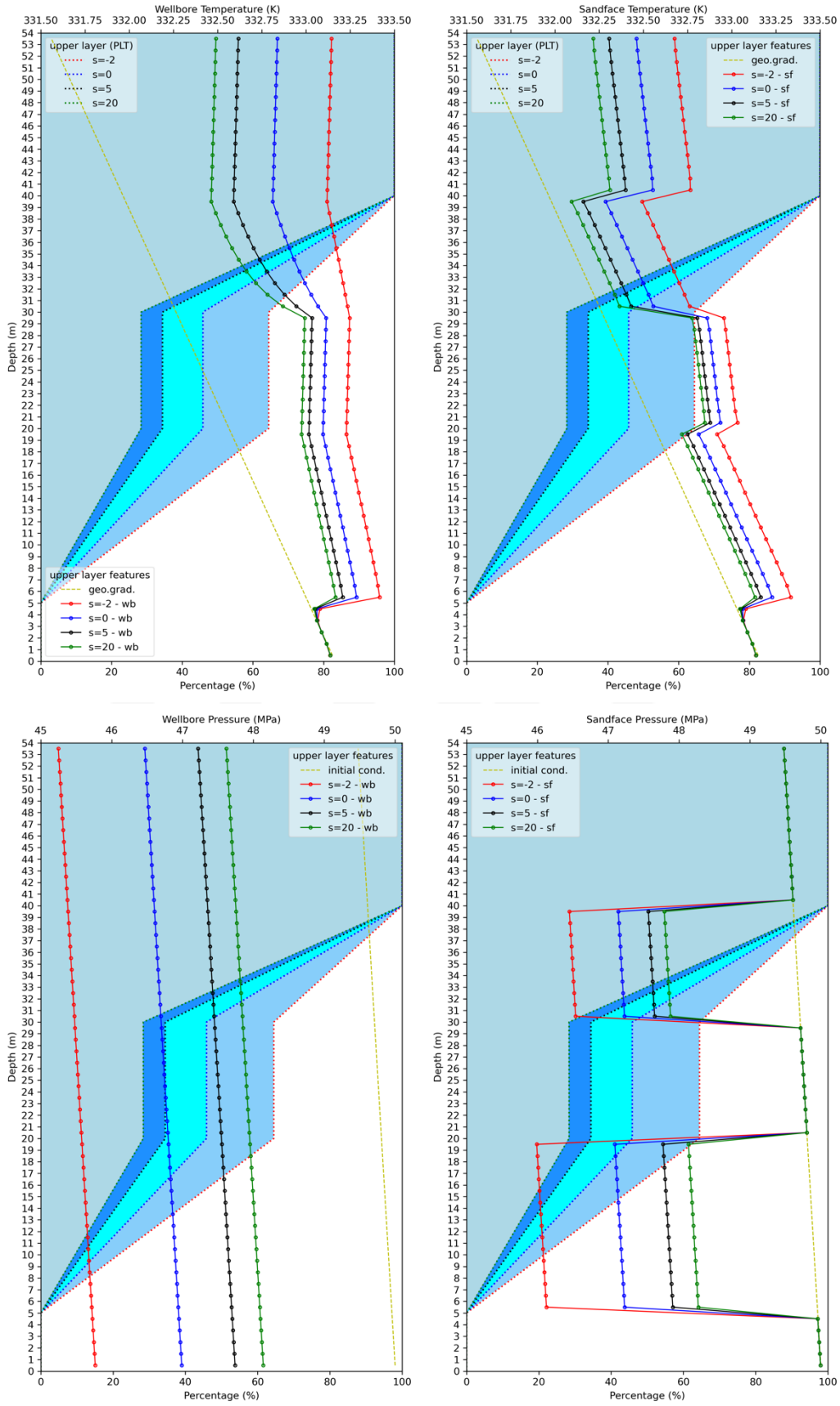

Figure E.35: Comparison of wellbore/reservoir pressures and temperatures for different skin values in the **upper zone** at the end of drawdown (q_{sc} = 1000 sm^3/D).

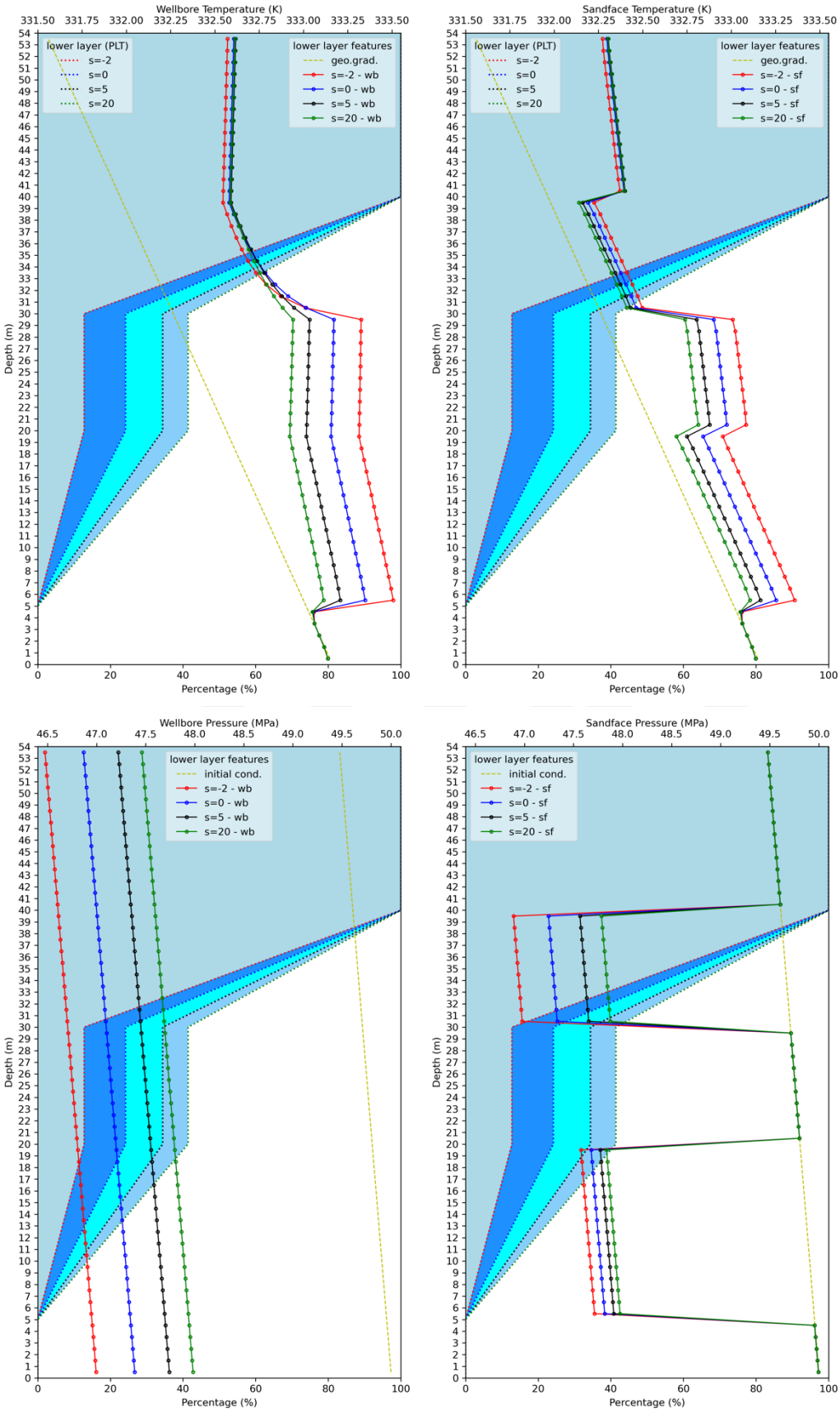

Figure E.36: Comparison of wellbore/reservoir pressures and temperatures for different skin values in the **lower zone** at the end of drawdown (q_{sc} = 1000 sm^3/D).

CURRICULUM VITAE

Name Surname **:** Cihan ALAN

EDUCATION:

- **B.Sc.** **:** 2006, Istanbul Technical University, Petroleum and Natural Gas Engineering
- **M.Sc.** **:** 2012, Istanbul Technical University Petroleum and Natural Gas Engineering

PROFESSIONAL EXPERIENCE:

- Schlumberger, Field Engineer, Well Testing Department, **Saudi Arabia** (2007-2010).
- I.T.U, Research Assistant, Petroleum and Natural Gas Engineering Department (2010-2012).
- Core Laboratories International B.V., PVT Analysis Engineer, Abu Dhabi, **UAE** (2012-2014)
- Saudi Aramco, Reservoir Simulation Engineer, Dhahran, **Saudi Arabia** (2014-2018).

REWARDS:

- SPE 2006 European Student Paper Contest Undergraduate & Masters Section, **Second Place Winner**, Intelligent Energy Conf. and Exh., Amsterdam, **Holland**
- SPE 2013 European Student Paper Contest PhD Section, **Finalist**, Offshore Mediterranean Conf. & Exh., Ravenna, **Italy**
- SPE 2020 European Student Paper Contest PhD Section, **Finalist**, Annual Student Energy Congress, Zagreb, **Croatia**

PROFESSIONAL CERTIFICATIONS:

- Microsoft Certified Professional (MCP), 2005.
- Microsoft Certified Application Developer (MCAD.NET), 2005.
- Microsoft Certified Solution Developer (MCAD.NET), 2005.

JOURNAL PAPERS AND PRESENTATIONS ON THE THESIS:

- Presented in 19th International Petroleum and Natural Gas Congress and Exhibition of Turkey, Istanbul, 22/Jun/2018.

- Presented in Annual Student Energy Congress, Zagreb, **Croatia**, 04/Mar/2020

- Presented in Turkey IV. Scientific and Technical Petroleum Congress (Virtual), 18/Nov/2020.

- **Alan, C.** and Cinar, M. (2022). Interpretation of Temperature Transient Data From Coupled Reservoir and Wellbore Model for Single Phase Fluids, *J Pet Sci Eng*, *209*, 109913. doi:10.1016/j.petrol.2021.109913

OTHER PUBLICATIONS, PRESENTATIONS AND PATENTS:

- **Alan, C.**, Tureyen, O. I. and Onur, M. (2013). A Numerical Study of the Pressure Behavior of a Vertical Well in a Dry Gas Reservoir. In *19th International Petroleum and Natural Gas Congress and Exhibition of Turkey*, Ankara, Turkey, 15-17 May. doi:10.3997/2214-4609-pdb.380.35

- U.S. Patent, US10697283B2, Saudi Aramco, granted on June, 2020. **Alan, C.** et al. (2020). Methods, systems, and computer medium having computer programs stored thereon to optimize reservoir management decisions based on reservoir properties. *U.S. Patent No. 10,697,283*, Washington, DC: U.S. Patent and Trademark Office.